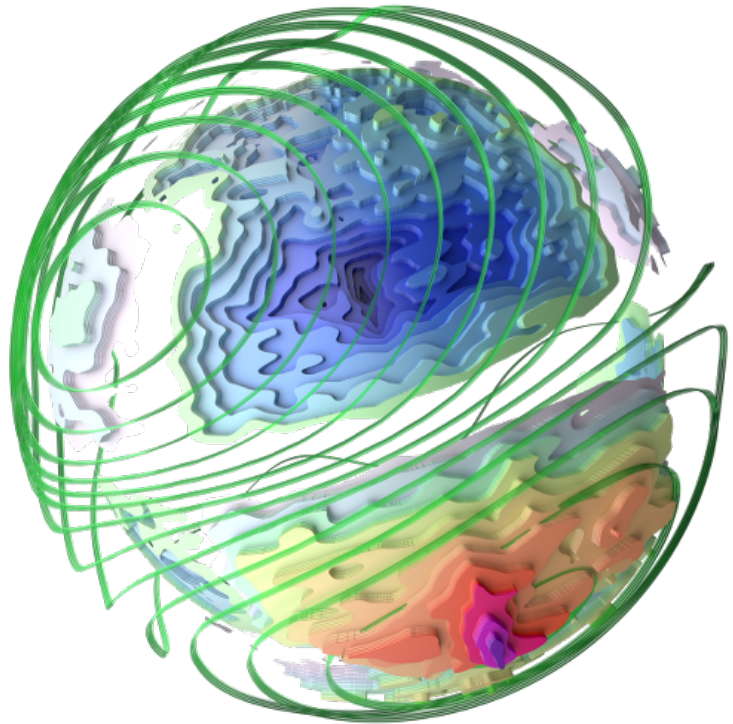


VERA: VERTical coupling in Earth's Atmosphere at mid and high latitudes

Final Report

Yosuke Yamazaki, Claudia Stolle, Tarique Siddiqui,
Jan Laštovička, Zbyšek Mošna, Michal Kozubek,
William Ward, David Themens, Samuel Kristoffersen



25 September 2020

ESA Contract No. 4000126709/19/NL/IA

Table of Contents

1	Introduction	5
1.1	Scientific Background.....	5
1.2	Project Background	5
1.3	Project Aim.....	6
1.4	Main scientific Questions.....	7
1.5	Meetings	8
1.6	Project-related Publications.....	8
1.7	Conference/Workshop Presentations.....	8
1.8	Structure of This Document.....	9
2	Scientific Requirement Consolidation	11
2.1	Scope and Outline	11
2.2	External Drivers of the Ionosphere/Thermosphere (IT) System.....	11
2.2.1	Ionospheric electrodynamics	11
2.2.2	Ionosphere-thermosphere coupling	13
2.2.3	External Sources of IT Variability.....	13
2.3	Sudden Stratospheric Warming (SSW)	15
2.3.1	External Sources of IT Variability.....	15
2.3.2	SSW effects on the ionosphere	15
2.3.3	SSW effects on the thermosphere.....	16
2.4	List of the Literature Concerning SSW Influence on the IT System.....	17
2.4.1	Ionosphere.....	17
2.4.2	Thermosphere	21
2.4.3	Modeling.....	21
2.5	Conclusions	23
3	Data Collection	26
3.1	Scope and Outline	26
3.2	Stratospheric data	26
3.3	Sudden stratospheric warmings during 2000–2019.....	27
3.4	European/global TEC data	29
3.5	European ionosonde data	30
3.6	Canadian ionospheric data.....	32
3.6.1	General information.....	32
3.6.2	Ionosondes	34
3.6.3	GNSS receivers.....	35
3.7	Vernadsky Antarctic ionosonde.....	36
3.8	Incoherent scatter radar.....	36
3.9	Swarm data	37
3.9.1	Electron density	38
3.9.2	Total electron content	39
3.9.3	Equatorial electrojet/equatorial electric field.....	39
3.9.4	Field-aligned current.....	40
3.10	CHAMP data.....	41
3.10.1	Electron density.....	41
3.10.2	Equatorial electrojet/equatorial electric field	42
3.11	Canadian MLT data from Eureka	42
3.11.1	Aura satellite data.....	44

3.12	Conclusions	44
4	Models and Data Analysis Methods	46
4.1	Scope and Outline	46
4.2	Models	46
4.2.1	Physics-based models	46
4.2.1.1	TIE-GCM.....	46
4.2.1.2	WACCM-X.....	48
4.2.1.3	TIE-GCM/WACCM-X.....	49
4.2.2	Empirical model.....	50
4.2.2.1	E-CHAIM	50
4.3	Data Analysis Technique	50
4.3.1	Ionosphere data analysis	50
4.3.2	Wave analysis of Eureka data.....	51
4.3.3	Wave analysis of satellite and model data	52
4.3.3.1	Zonal wavenumber analysis.....	52
4.3.3.2	Lunar tidal analysis for Swarm and CHAMP data	53
4.4	Conclusions	54
5	Model Validation and Comparison with Observations	56
5.1	Scope and Outline	56
5.2	Validation of the TIE-GCM and WACCM-X	56
5.2.1	Simulating the 2009 SSW with SD-WACCM-X	56
5.2.2	Using WACCM-X outputs as input to the TIE-GCM lower boundary.....	57
5.2.2.1	Semidiurnal tides from WACCM-X and TIE-GCM simulations.....	58
5.2.2.2	Vertical E×B drifts from WACCM-X and TIE-GCM simulations	61
5.2.2.3	TEC from TIE-GCM simulations and GPS observations.....	61
5.2.3	Simulating the 2018 and 2019 NH major SSWs using WACCM-X.....	62
5.2.4	WACCM-X vs GPS observations of TEC for 2018 and 2019 SSWs	62
5.2.5	WACCM-X vs Eureka data for 2009 SSW	64
5.3	E-CHAIM, TIE-GCM and Data Comparisons	67
5.4	Poker Flat Incoherent Scatter Radar Validations of TIE-GCM	71
5.5	Conclusions	73
6	Final Findings and Results of Impact Assessment	75
6.1	Scope and Outline	75
6.2	January 2009 SSW	75
6.2.1	Description of SSW	75
6.2.2	High-latitude MLT region	76
6.2.3	High-latitude ionosphere	77
6.2.4	Mid-latitude ionosphere.....	78
6.2.5	Low-latitude ionosphere	80
6.3	January 2015 SSW	81
6.3.1	Description of SSW	81
6.3.2	Low-latitude response.....	82
6.4	February 2018 SSW	84
6.4.1	Description of SSW	84
6.4.2	High-latitude MLT region	85
6.4.3	Mid-latitude ionosphere.....	86
6.4.4	Low-latitude ionosphere	88
6.5	January 2019 SSW	88
6.5.1	Description of SSW	88

6.5.2	High-latitude MLT region	89
6.5.3	High-latitude ionosphere	91
6.5.4	Mid-latitude ionosphere.....	93
6.5.5	Low-latitude ionosphere	94
6.6	September 2019 SSW.....	95
6.6.1	Description of SSW	95
6.6.2	MLT region.....	96
6.6.3	High-latitude ionosphere	97
6.6.4	Low-latitude ionosphere	99
6.7	Impact Assessment and Conclusions.....	101
6.7.1	Re-statement of VERA scientific questions	101
6.7.2	Answers to the VERA scientific questions.....	101
6.7.3	Conclusions.....	102
7	Scientific Roadmap	104
7.1	Scope and Outline	104
7.2	Recommendations: Follow-on research activities.....	104
7.2.1	Numerical modelling of the high-latitude ionosphere	104
7.2.2	Mechanism for the ionospheric response to SSW at middle and high latitudes.....	105
7.2.3	Changes in gravity wave activity.....	105
7.2.4	Antarctic SSW	106
7.3	Recommendations: Broader context.....	106
7.3.1	SSW effects on small-scale ionospheric structures	106
7.3.2	Ionospheric response to other meteorological phenomena.....	107
7.3.3	Upper limit of geomagnetic activity for SSW-ionosphere coupling studies	107
7.3.4	Neutral vs plasma density response to SSW.....	108
7.3.5	Optimum stratospheric parameters for SSW-ionosphere coupling studies	109
7.3.6	Acquisition of more comprehensive and global data	109
	Applicable Documents	111
	References	111
	List of Abbreviations.....	135

Citation: Yamazaki, Y., Stolle, C., Siddiqui, T., Laštovička, J., Mošna, Z., Kozubek, M., Ward, W., Themens, D. R., & Kristoffersen, S. (2020) VERA: VERTICAL coupling in Earth's Atmosphere at mid and high latitudes – Final Report, Potsdam, German Research Centre for Geosciences GFZ, pp 138, <https://doi.org/10.2312/GFZ.2.3.2020.001>.

Chapter 1

Introduction

1 Introduction

1.1 Scientific Background

Understanding the Earth's ionosphere, the ionized part of the upper atmosphere (80-600 km), is increasingly important, as society becomes more and more dependent on space-based technologies. The ionosphere hosts vital infrastructure, such as low-Earth-orbit satellites and the international space station. Also, ionospheric plasmas disrupt electromagnetic signals that travel through the region, which can influence radio communication, navigation and GNSS (Global Navigation Satellite Systems) including positioning. The ionosphere is highly variable, and the prediction of its weather is a real challenge.

The ionosphere is subject to various forcing mechanisms from external sources. The most important source of ionospheric variability is energetic solar radiation at 0.1-100 nm wavelengths (X-ray and EUV), which causes the 11-year solar-cycle variation of the ionosphere. The ionospheric peak plasma density, for example, is approximately 100% higher during solar maximum compared to solar minimum. For the short-term (day-to-day) variability (~20-30%), two other processes are also equally important, namely forcing from the magnetosphere and forcing from the lower atmosphere (e.g., Fang et al., 2018). In the VERA (vertical coupling in Earth's atmosphere at mid and high latitudes) project, we focus on the ionospheric variability associated with lower-atmospheric forcing. Special attention is paid to the ionospheric response to sudden stratospheric warmings (SSWs) (e.g., Andrews, 1987; Labitzke, 1999; see also 2.3), during which the middle atmosphere (10-85 km) is highly disturbed. The response of the ionosphere to SSWs has previously been studied for low latitude regions, where forcing from the magnetosphere is indirect and relatively modest (Chau et al., 2012; Pedatella et al., 2018). VERA attempts to assess the importance of vertical atmospheric coupling at mid- and high- latitudes, using observations from low Earth orbit (LEO) satellites and ground-based radars, as well as state-of-the-art numerical models.

1.2 Project Background

European Space Agency (ESA) published Invitation to Tender (ITT) for Swarm+ Coupling: High-Low Atmosphere Interactions [AD-1] on 19 September 2018. The accompanying Statement of Work (SoW) document [AD-2] addressed the effect of SSWs on the low-latitude ionosphere among other latest important topics; “... various papers reported a clear response of the low-latitude ionosphere to the large-scale meteorological events in the stratosphere called Sudden Stratospheric Warming events ...” In response to the ITT, the VERA project [AD-3] was proposed to expand on the topic of the SSW influence on the ionosphere with special focus on the middle- and high-latitude region. VERA was selected as one of the Swarm+ Coupling projects and it was launched with a kick-off meeting on 11 June 2019. The project ran for approximately 16 months, as proposed, until 30 September 2020. Detailed descriptions of scientific tasks, project time line and management can be found in [AD-3].

Scientific tasks of the VERA project have been conducted based on the international collaboration among (1) German Research Center for Geosciences “GFZ” Potsdam, Germany, (2) Institute of Atmospheric Physics “CAS”, Prague, Czech Republic, and (3) University of New Brunswick “UNB”, New Brunswick, Canada. The team composition of each institution is as follows:

GFZ team composition:

- Yosuke Yamazaki, Dr. (Primary Coordinator)
- Claudia Stolle, Prof. Dr.
- Guram Kervalishvili, Dr.
- Tarique Adnan Siddiqui, Dr.*
- Bernhard Fluche, Dr. (Project Manager)

* now at IAP, Kühlungsborn German

CAS team composition:

- Jan Laštovička, Dr. (CAS Coordinator)
- Petra Koucka Knizova, Dr.
- Jaroslav Chum, Dr.
- Dalia Buresova, Dr.
- Daniel Kouba, Dr.
- Zbyšek Mošna, Dr.
- Michal Kozubek, Dr.
- Ilya Edemskiy, Dr.
- Jaroslav Urbar, Mgr.

UNB team composition:

- William Ward, Prof. Dr. (UNB Coordinator)
- David Themens, Dr. **
- Samuel Kristoffersen, Dr.

** now at University of Birmingham

GFZ's main responsibility in the VERA project is the management, Swarm data analysis, and theoretical modeling. CAS is in charge of identification/characterization of SSW events as well as ionospheric data analysis at middle latitudes. UNB mainly focuses on the analysis of high-latitude neutral and ionospheric data and empirical modeling of the high-latitude ionosphere.

1.3 Project Aim

The main aim of VERA project activity is to investigate the feasibility of vertical coupling studies based on Swarm capabilities. Swarm is ESA's satellite constellation mission (Friis-Christensen et al., 2006; Figure 1-1). Its high precision magnetometers and dedicated constellation for geospace research enable monitoring of the mid- and low-latitude interhemispheric field-aligned currents (IHFACs; Figure 1-2), which are fully explored in the VERA project. In addition to the Swarm data, 10 years of CHAMP (Reigber et al., 2002) magnetometer data are used to allow the opportunity to investigate more SSW events. These satellite observations are supported by ground-based ionospheric observations. Moreover, a recently-developed empirical model of the high-latitude ionosphere, E-CHAIM (Themens et al., 2017), and a physics-based models such as TIE-GCM (Richmond et al., 1992) are employed to help the interpretation of the data.

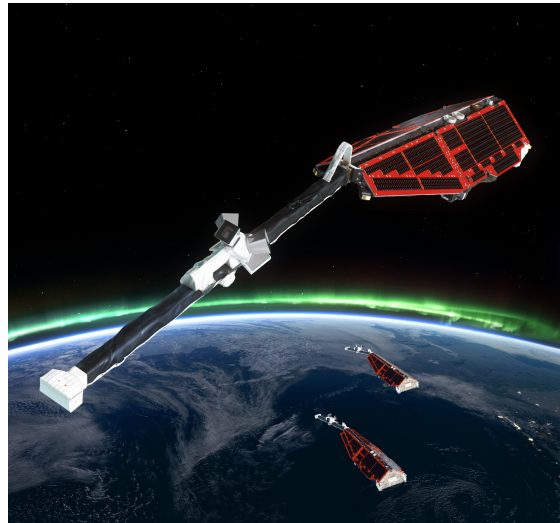


Figure 1-1. Artist view of Swarm satellite constellation (credits: ESA)

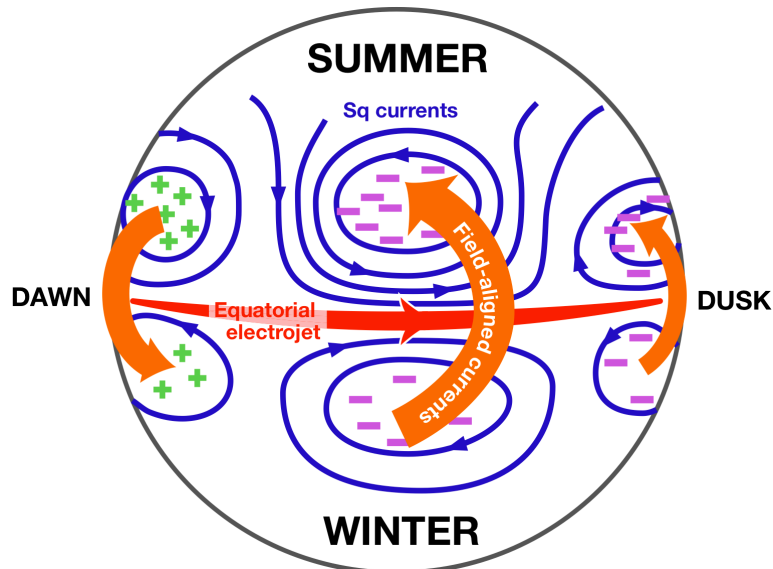


Figure 1-2. Schematic of interhemispheric field-aligned currents (IHFACs) during the Northern Hemisphere summer. From Fukushima (1994).

1.4 Main scientific Questions

The following are the main scientific questions that we intend to address in the VERA project:

- Q1.** What is the response of IHFACs to SSW events and what can we learn about hemispheric coupling?
- Q2.** What is the response of the high-latitude ionosphere to SSW events and what is the relative contribution compared to magnetospheric forcing?
- Q3.** What is the latitudinal extent of SSW effects on the ionosphere, e.g. are these effects similarly significant for the low-, mid- and high-latitude ionosphere?

1.5 Meetings

The following meetings have been held in connection with the VERA project activity:

- Kick-off meeting (KO) Online, 11 June 2019
- 1st Project Meeting (PM1) Potsdam, Germany, 7 October 2019
- 2nd Project Meeting (PM2) Prague, Czech Republic, 19 December 2019
- Mid Term Review (MTR) Potsdam, Germany, 18 March 2020
- 3rd Project Meeting (PM3) Online, 9 June 2020
- Final Presentation (FP) Online, 16 September 2020

1.6 Project-related Publications

Below is the list of publications related to the VERA project activity. The VERA project members are highlighted by bold type.

Lühr, H., **Kervalishvili, G.**, **Stolle, C.**, Rauberg, J., Michaelis, I. (2019), Average characteristics of low-latitude interhemispheric and F-region dynamo currents deduced from the Swarm satellite constellation, *JGR Space Physics*, 124, 10631–10644, <https://doi.org/10.1029/2019JA027419>.

Park, J., **Yamazaki, Y.**, Lühr, H. (2020), Latitude dependence of interhemispheric field-aligned currents (IHFACs) as observed by the Swarm constellation, *JGR Space Physics*, 125, e2019JA027694, <https://doi.org/10.1029/2019JA027694>.

Yamazaki, Y., Matthias, V., Miyoshi, Y., **Stolle, C.**, **Siddiqui, T.**, **Kervalishvili, G.**, **Laštovička J.**, **Kozubek M.**, **Ward W.**, **Themens D. R.**, **Kristoffersen S.**, **Alken P.** (2020), September 2019 Antarctic sudden stratospheric warming: quasi-6-day wave burst and ionospheric effects, *GRL*, 47, e2019GL086577, <https://doi.org/10.1029/2019GL086577>.

Miyoshi, Y., & **Yamazaki, Y.** (2020). Excitation mechanism of ionospheric 6 - day oscillation during the 2019 September sudden stratospheric warming event, *JGR Space Physics*, 125, e2020JA028283, <https://doi.org/10.1029/2020JA028283>.

Kozubek, M., **Laštovička, J.**, Krizan, P. (2020) Comparison of key SSW characteristics in the Southern Hemisphere and Northern Hemisphere, *Atmosphere* (accepted).

Yamazaki, Y., & Miyoshi, Y. (2020) Ionospheric tidal variability during the 2019 Southern Hemisphere sudden stratospheric warming: Evidence for tidal interactions with the quasi-6-day wave, *JGR Space Physics* (submitted).

Siddiqui, T. A., **Yamazaki, Y.**, **Stolle, C.**, Maute, A., **Laštovička, J.**, **Edemskiy, I. K.**, **Mošna, Z.** (2020) On the variability of total electron content over Europe during the 2009 and 2019 NH SSW events, *JGR Space Physics* (submitted), <https://doi.org/10.1002/essoar.10504461.1>.

1.7 Conference/Workshop Presentations

Below is the list of presentations related to the VERA project activity.

Yamazaki, Y. et al., (September 2019) VERA: Vertical Coupling in the Earth's Atmosphere at Mid and High Latitudes, *Swarm DQW*.

Siddiqui et al., (May 2020) TEC variability over Europe during the 2019 SSW, *EGU*.

Yamazaki, Y. et al., (May 2020) VERA: Vertical Atmospheric Coupling during the September 2019 Antarctic Sudden Stratospheric Warming, *EGU*.

Ward, W. et al., (February 2020), Coupling across the polar mesopause: The VERA project, *DASP*.

Ward, W. et al., (June 2020), Mesopause wind observations at 80N during the 2009, 2018 and 2019 SSW and comparisons with WACCM-X, *CEDAR*.

Mošna, Z. et al., (June 2020) Sudden Stratospheric Warming events effects observed in the ionosphere at middle latitudes during 2009, 2018 and 2018/2019, *CEDAR*.

Siddiqui, T. et al., (June 2020) Solar and lunar tidal variability during the 2018 and 2019 NH SSWs from WACCM-X simulations, *CEDAR*

Yamazaki, Y. & Miyoshi, Y. (June 2020) GAIA simulation results for 6-day ionospheric oscillation during the September 2019 SSW, *CEDAR*

1.8 Structure of This Document

The present document is organized as follows. Chapter 2 describes basic properties of the ionosphere-thermosphere system and its coupling to the lower atmosphere. SSW effects on the middle atmosphere, thermosphere, and ionosphere are discussed, and a list of the literature addressing the upper atmospheric response to SSWs is presented. Chapter 2 concludes with the justification for the VERA project science. Chapter 3 presents the data collected for the VERA project and describes how those data are obtained. A list of recent SSW events (2009-2019) is also presented therein. In Chapter 4, data analysis methods are described. Chapter 4 also introduces physics-based and empirical models used in the VERA project. In Chapter 5, the model results are compared to observations for validation. Main scientific results are presented in Chapter 6. The main scientific questions (see 1.4) are also addressed therein. Finally, Chapter 7 provides recommendations of topics and directions for future studies in light of the scientific results presented in Chapter 6.

Chapter 2

Scientific Requirement Consolidation

2 Scientific Requirement Consolidation

2.1 Scope and Outline

This chapter is to consolidate the preliminary scientific requirements for the VERA project. It first describes the ionosphere/thermosphere (IT) system and external sources of variability (2.2). In 2.3, sudden stratospheric warmings (SSWs) are identified as significant sources of ionospheric day-to-day variability during the Northern Hemisphere winter. Main characteristics of SSWs in the middle atmosphere are also described therein. 2.4 presents a list of the literature concerning the SSW influence on the IT system and 2.5 gives a summary of the current understanding of SSW-IT coupling and provides the justification for VERA project activity.

2.2 External Drivers of the Ionosphere/Thermosphere (IT) System

This section describes the basic features of the ionosphere and thermosphere, and their coupling processes, and introduces terminologies that are used in the rest of the document. It also describes sources of IT variability.

2.2.1 Ionospheric electrodynamics

The E region of the ionosphere is located at approximately 95-150 km altitude. The region is characterized by high perpendicular conductivities. The Pedersen and Hall conductivities peak around 120 and 105 km, respectively, on the order of 10^{-4} – 10^{-3} Sm^{-1} for typical dayside low-latitude conditions (e.g., Richmond, 2011). The associated current density can be expressed as follows (e.g., Richmond, 1995):

$$J_{\perp} = \sigma_P(B_{\perp} + U \times B) + \sigma_H \frac{B}{|B|} \times (E_{\perp} + U \times B) \quad \text{Eq. 2-1}$$

where σ_P is the Pedersen conductivity and σ_H is the Hall conductivity, E is a static electric field, and U is the neutral wind, and B is the Earth's main magnetic field. At E-region heights, the neutral wind speed is typically on the order of 10 – 10^2 m/s, resulting partly from direct solar heating of the dayside atmosphere by ultraviolet (UV) and extreme ultraviolet (EUV) solar radiation (Forbes, 1982; Hagan et al., 2001), and also partly from atmospheric waves (mainly upward-propagating tides; Forbes et al., 2008). The resulting currents are on the order of 10^{-5} – 10^{-6} A/m². Throughout the E- and F-region (>150 km), the parallel conductivity is many orders of magnitude greater than the perpendicular conductivities. Thus, the horizontal currents in the E region of the Northern and Southern Hemispheres are effectively shorted by field lines. The intensity of the parallel current can be calculated by integrating the divergence of the perpendicular currents (Eq. 2-1) along a magnetic field line from the bottom of the ionosphere to the height of interest:

$$J_{\parallel} = -|B| \int_{l_o}^l \frac{\nabla \cdot J}{|B|} dl' \quad \text{Eq. 2-2}$$

where dl' is an element of distance along the magnetic field line and l_o is some point where J_{\parallel} vanishes. The current intensity is typically on the order of 10^{-9} – 10^{-8} A/m², which is much smaller than the perpendicular currents. The magnetic perturbations due to the parallel current can be observed by low-Earth-orbit (LEO) satellites such as CHAMP and Swarm, which fly through the regions where the current flows (e.g., Park et al., 2011; Lühr et al., 2015). The Pedersen current (the first term in the right hand side of Eq. 2-1) and the Hall current (the second term in the right hand side of Eq. 2-1), together with the parallel current (Eq. 2-2), form a global-scale current circuit on the dayside ionosphere, which is commonly known as

the solar quiet (Sq) current system (Yamazaki and Maute, 2017). The Sq current system observed from ground and satellite altitudes are usually described in terms of "equivalent current system" on a spherical thin shell (usually set to be at 110 km), which is equivalent to the real ionospheric current system in that it produces the same magnetic perturbations with the real current system at the height of the observation. Figure 1-2 presents a schematic of the low- and middle-latitude ionospheric current system (after Fukushima, 1994). In addition to the horizontal Sq current system and interhemispheric field-aligned currents (IHFACs), the figure depicts an enhanced eastward current flow along the magnetic equator, which is commonly known as the equatorial electrojet (EEJ). The EEJ is essentially a Hall current (on the order of 10^{-6} A/m²) driven by the vertical electric field that is supported by the horizontal magnetic field over the magnetic equator. Due to the geometry restriction, the EEJ currents are confined within a narrow band latitude, about $\pm 3^\circ$ from the magnetic equator.

In the high-latitude region (above 60° magnetic latitude), the wind dynamo process (as described in Eq. 2-1) is not the primary driver of electric fields and currents. Instead, electric fields and currents arise mainly from magnetospheric sources. The magnetospheric convection electric field maps down to the high-latitude ionosphere along the equipotential magnetic field lines and drives electric currents. The high-latitude current system consists of horizontal vortices (commonly known as the DP2 current system) and region-1 (R1) and region-2 (R2) field-aligned currents, on the order of 10^{-7} – 10^{-6} A/m² (Figure 2-1). During geomagnetic storms and substorms, ionospheric conductivities are enhanced along the auroral oval due to energetic particle precipitation, which gives rise to a strong zonal current flow, known as the auroral electrojet (typically, 10^{-5} A/m²). Under quiet steady-state conditions, the middle- and low-latitude ionosphere is largely shielded from the high-latitude electric field (e.g., Wolf et al., 2007), but during geomagnetically active periods, the high-latitude electric field can extend into lower.

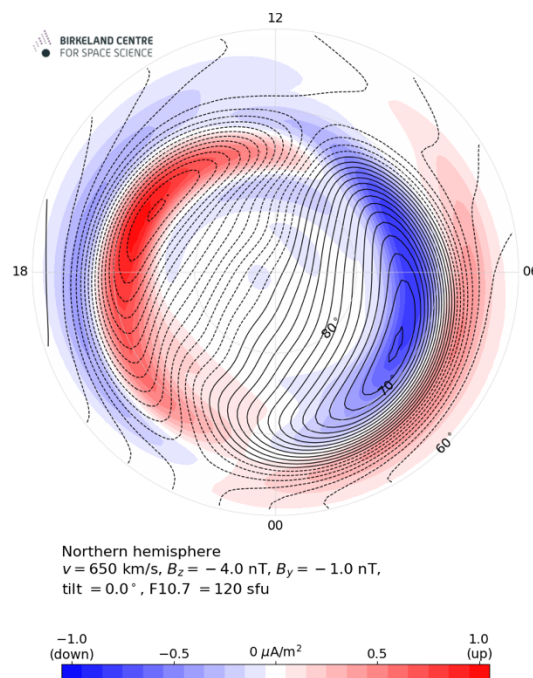


Figure 2-1. Polar view of the high-latitude ionospheric current system (contour) and field-aligned currents (colour) in the Northern Hemisphere derived from the empirical model AMPS (Laundal et al., 2018).

2.2.2 Ionosphere-thermosphere coupling

The ionosphere and thermosphere are strongly coupled with each other. At 300 km, the number density of atomic oxygen O (which is the dominant species of the thermosphere) is typically 10^{14} – 10^{15} m⁻³, while the number density of oxygen ion O⁺ (which is the dominant species of the F-region ionosphere) is 10^{11} – 10^{12} m⁻³. Thus, the thermosphere dominates the dynamical coupling between the ionosphere and thermosphere. In fact, the spatial and temporal variability of the neutral atmosphere is often observed to affect the ionosphere. For example, studies found that there are four longitudinal sectors where the daytime ionospheric plasma density is higher than other sectors (Immel et al., 2006; Scherliess et al., 2008). As later studies established, such a "wave-4" longitude pattern in the ionosphere can be explained by forcing from the eastward-propagating diurnal tidal wave with zonal wave number 3, also known as DE3 (Hagan et al., 2007; Wan et al., 2012). The zonal wind perturbation associated with DE3 has four longitudinal peaks in the dayside equatorial region at E-region heights (90–110 km), which leads to the regions of enhanced electric fields and currents. (The quantitative relationship between the driving wind and dynamo electric fields and currents can be found in Eq. 2-1) These dynamo electric fields are transmitted to the equatorial F-region along with equipotential magnetic field lines and redistribute the F-region plasmas that move with the E×B drift.

Another IT coupling mechanism is through the change in the neutral composition of the thermosphere. The main production mechanism of the F-region O⁺ is the photoionization of O, while the main loss mechanism of O⁺ is chemical processes where molecular nitrogen N₂ plays a catalytic role. Consequently, the production rate of O⁺ is proportional and reversely-proportional to the densities of O and N₂, respectively. Thus, the O⁺ density in the F region tends to vary with the [O]/[N₂] ratio (where the bracket signifies the number density). The semiannual variation of the ionospheric density is an example of the neutral composition influence on the ionosphere. In general, the F-region peak plasma density is higher during equinoxes than solstices. This is primarily due to the seasonal change in the [O]/[N₂] ratio at F-region heights (Rishbeth et al., 2000). The [O]/[N₂] ratio is lower during solstices than equinoxes due to the presence of the thermospheric wind from the summer to the winter hemisphere, sometimes referred to as "thermospheric spoon" (Fuller-Rowell, 1998). This meridional thermospheric circulation provides composition mixing (in other words, the downward transport and loss of O) to cause the reduction of the [O]/[N₂] ratio. During equinoxes, the summer-to-winter circulation of the thermosphere is largely absent, thus the [O]/[N₂] ratio remains relatively high.

In the polar region, the ion velocity can exceed 1,000 m/s due to the strong convection electric field from the magnetosphere. In such circumstances, the momentum of ionospheric plasmas is no longer negligible for neutral dynamics. Indeed, in the lower thermosphere at high latitudes, the horizontal wind pattern is often similar to that of the ion convection due to collisional interactions between plasmas and neutrals (Richmond and Lu, 2000).

2.2.3 External Sources of IT Variability

The weather of the IT system is driven mostly externally, unlike the terrestrial weather which is dominated by internally driven variability. There are three well-known external sources of IT variability, which in this document are referred to as "solar forcing", "magnetospheric forcing", and "lower atmospheric forcing". Solar forcing is mainly by energetic solar

radiation, such as extreme ultraviolet (EUV) and X-ray. They are the primary heating source of the thermosphere and ionization source of the ionosphere on the dayside. The Sun rotates at periods of 24-38 days depending on latitude. At 25° solar latitude, where sunspots usually appear, the rotation period is approximately 25 days. When viewed from the rotating Earth, the same sunspot structure appears approximately every 27 days. Since sunspots are magnetically active region where energetic solar radiation is relatively strong, solar forcing to the Earth's IT system has a period of 27 days and its harmonics (13.5 days, 9 days).

Magnetospheric forcing arises from the solar wind-magnetosphere interaction and subsequent magnetosphere-ionosphere interaction. The effect on the IT system is most severe during geomagnetic storms and substorms. The enhanced magnetospheric convection and energetic particle precipitation leads to an increase of electric fields and currents in the high-latitude ionosphere. The resulting Joule heating is the main energy input to the high-latitude thermosphere (Lu et al., 2016). The disturbance thermospheric winds driven in this process are not confined in the high latitude region but extends into lower latitudes, which alters the dynamo electric fields and currents at middle and low latitudes (e.g., Fejer et al., 2017). Also, under a rapidly changing magnetospheric configuration during geomagnetic storms and substorms, the magnetospheric shielding becomes ineffective. A consequence of this is the direct penetration of the high-latitude electric field into the lower latitudes (Huang et al., 2005; Kikuchi et al., 2008). Major geomagnetic storms, which occur irregularly during solar maximum, are often related to coronal mass ejections (CMEs), while moderate and minor storms during the declining phase of solar cycle are often associated with co-rotating interaction regions (CIRs) (Borovsky and Denton, 2006). The latter has a period of 27, 13.5, and 9 days due to the solar rotation, which contribute to multi-day variations of the IT system (e.g., Ram et al., 2010; Lei et al., 2011).

Lower atmospheric forcing is mainly by atmospheric waves that are generated in the lower and middle atmosphere and propagate vertically upward into the upper atmosphere (e.g., Laštovička, 2006; Liu, 2016). The waves that are known to have a significant influence on the IT system include migrating and non-migrating solar tides, lunar tides, traveling planetary waves (also known as Rossby normal modes), Kelvin waves, gravity waves. Some of these waves can propagate directly to E-region heights, where they generate the dynamo electric fields and currents (see Eq. 2-1). Although significant wave damping occurs in the lower thermosphere and above due to eddy and molecular dissipation, some wave signatures can be detected in the upper thermosphere (Oberheide et al., 2009; Forbes et al., 2013). Dissipation of upward-propagating waves in the lower thermosphere has a mixing effect on the thermosphere, which leads to a reduction of the [O]/[N₂] ratio and hence a decrease in the ionospheric plasma density (Yamazaki and Richmond, 2013; Yue and Wan, 2014). As the waves propagate in the lower and middle atmosphere, they interact with each other and generate secondary waves, which may also propagate into the upper atmosphere. Interactions among waves with different wave numbers and periods increase the variability of wave forcing to the IT system (Chang et al., 2011; Forbes et al., 2018).

The VERA project is concerned with upper atmospheric response to lower atmospheric forcing, especially during sudden stratospheric warmings (SSWs), which are described in the following section.

2.3 Sudden Stratospheric Warming (SSW)

This section describes the basic features of SSWs and highlights known effects of SSWs on the IT system. A more comprehensive review of the literature about the IT response to SSWs will be given in 2.4.

2.3.1 External Sources of IT Variability

SSWs are large-scale meteorological disturbances that usually take place in the Northern Hemisphere high-latitude region during winter times (Andrews et al., 1987; Labitzke & Van Loon, 1999). The first record of an SSW dates back to January 1952 when Richard Scherhag observed a rapid increase in the stratospheric temperature by more than 40° K in a few days in the radiosonde data.

The driving mechanism of SSWs is well understood through extensive observational and theoretical studies in the past. An SSW event is initiated by enhanced planetary-wave forcing from the troposphere to the stratosphere (Matsuno, 1971). Under quiet conditions, the winter polar stratosphere is approximately in geostrophic balance. That is, the cold pole (which provides a poleward pressure-gradient force) is surrounded by an eastward zonal mean flow (which provides an equatorward Coriolis force). Planetary-wave breaking in the stratosphere leads to a weakening of the polar vortex, which disrupts the geostrophic balance mentioned above. Consequently, the temperature and circulation pattern of the middle atmosphere are significantly altered during SSW events (Liu and Roble, 2002).

At present, there is no unambiguous standard definition for SSWs, and various detection criteria have been proposed and adopted in different studies. This issue was reviewed by Butler et al. (2015). It is, nonetheless, widely accepted that a "minor" SSW event occurs when the polar temperature rapidly increases in the stratosphere (e.g., by >25° K in a week or less according to the World Meteorological Organization, or WMO). The event is called "major" if the reversal of the zonal mean flow from eastward to westward occurs poleward of 60° latitude at 10 hPa (32 km) or below. The occurrence rate of a major SSW is approximately 0.6 event per year, while minor warmings occur almost every year. An SSW can be categorized as either "vortex-split" or "vortex-displaced" event, depending on the way polar vortex breakdown takes place (Charlton and Polvani, 2007). Vortex-split and vortex-displaced events are driven by a quasi-stationary planetary wave with zonal wave number 2 and 1, respectively. A major SSW rarely occurs in the Southern Hemisphere owing to the weak planetary wave activity. At the time of writing this document, the September 2002 event is the only major SSW observed in the Southern Hemisphere (e.g., Krüger et al., 2005). In this document, SSWs mean those in the Northern Hemisphere high-latitude region, unless otherwise stated.

2.3.2 SSW effects on the ionosphere

The circulation changes in the middle and lower atmosphere during SSWs affect the atmospheric waves that propagate to the upper atmosphere. The ionosphere can be disturbed during SSWs in response to altered lower atmospheric forcing. Both observations and numerical studies suggested that significant changes can occur in atmospheric tides in the lower thermosphere during SSWs (Stening et al., 1997; Hoffmann et al., 2007; Sridharan et al., 2009; Fuller-Rowell et al., 2011a; Pedatella et al., 2012; Paulino et al., 2012). Tidal wave forcing is now considered to be the primary source of large-scale ionospheric variability during SSWs. Tidal variability during SSWs can be caused by the change in propagation

conditions (Jin et al., 2012), the change in tidal sources (Goncharenko et al., 2012), the interaction with quasi-stationary planetary waves (Liu et al., 2010), and the change in resonance properties of the atmosphere (Forbes and Zhang, 2012).

A rapid development in the understanding of SSW effects on the ionosphere followed the occurrence of the January 2009 major SSW event, which was a particularly intense and long-lasting event (Manney et al., 2009). The event also took place under extreme solar minimum conditions (Solomon et al., 2010) when the ionospheric variability due to solar and magnetospheric forcing is small. Semidiurnal perturbations are observed in various ionospheric parameters mainly in the dayside low-latitude region, including the peak plasma density (NmF_2 ; e.g., Yue et al., 2010), total electron content (TEC; e.g., Goncharenko et al., 2010a), equatorial vertical plasma drift velocity (e.g., Chau et al., 2010), equatorial electrojet (Fejer et al., 2010). Later studies found that the observed semidiurnal ionospheric variations are not only due to the semidiurnal solar tide but also due to the semidiurnal lunar tide (Pedatella et al., 2014a; Lin et al., 2019). The enhancement of the semidiurnal lunar tide in the ionosphere has also been observed during many other SSW events (Fejer et al., 2011; Park et al., 2012; Yamazaki et al., 2012a; Siddiqui et al., 2015a). The timing and magnitude of lunar tidal enhancement during SSWs have been shown to be closely related to the timing and magnitude of polar vortex weakening (Zhang and Forbes, 2014; Chau et al., 2015; Siddiqui et al., 2015b). It is not understood whether solar tides also respond to SSWs in a similar way.

Studies that focused on middle and high latitudes are few. Some exceptions are the work by Yamazaki et al. (2012c) and Shpynev et al. (2015). Yamazaki et al. (2012c), using ground-based magnetic observations, described large changes in the pattern of geomagnetic daily variations at middle-latitude stations, Fredericksburg (48° geomagnetic latitude) and Port Stanley (-42° geomagnetic latitude), during the SSW events of January 2006 and January 2009. The results indicated an increase and decrease of middle-latitude ionospheric currents in the Southern and Northern Hemispheres, respectively. Such an asymmetric dynamo response is likely to involve the reconfiguration of the inter-hemispheric field-aligned currents (IHFACs). However, there is so far no study on the response of IHFACs to SSWs. Shpynev et al. (2015) used a Russian ionosonde network (5 stations) to examine SSW effects on the ionosphere at high latitudes. They showed that the ionospheric response depends on the location of the ionosonde station. However, due to the limited number of the stations involved, they were not able to determine the spatial pattern of the ionospheric changes associated with the SSWs. Also, the study showed great difficulties in separating the effects of SSWs from other sources, i.e., solar and magnetospheric forcing. Hibbins et al. (2019) observed tidal changes in the lower thermosphere at high latitudes during SSWs, which could potentially affect the high-latitude ionosphere, in a similar way as at low latitudes. However, no studies have examined the response of the high latitude ionosphere to tidal changes during SSWs.

2.3.3 SSW effects on the thermosphere

Compared with the studies on the SSW influence on the ionosphere, the studies that focused on the thermosphere during SSWs are much fewer. Conde and Nicolls (2010) showed a reduction of the thermospheric temperature by $\sim -50^\circ$ K at 240 km over Poker Flat, Alaska during the January 2009 SSW event. Liu et al. (2011a) reported thermospheric cooling of $\sim -50^\circ$ K during the same SSW event based on CHAMP and GRACE thermospheric mass

density data. However, Fuller-Rowell et al. (2011b) argued that the observed thermospheric temperature variations during the January 2009 SSW are likely due to magnetospheric forcing, rather than due to the SSW. Liu et al. (2013) conducted a numerical simulation using a whole atmospheric model GAIA and demonstrated that the model can reproduce thermospheric cooling observed by CHAMP and GRACE during the January 2009 SSW event but with a smaller magnitude of -12° K. Yamazaki et al. (2015) examined the response of the global-mean thermospheric density and temperature to 37 SSW events using satellite orbital drag data during 1967–2013 and found statistically significant thermospheric cooling of -7° K at 400 km. Since the satellite orbital drag data that Yamazaki et al. (2015) used are global means, the spatial structure (i.e., latitude, longitude, and height dependence) of the thermospheric response to SSWs is yet to be observationally established.

2.4 List of the Literature Concerning SSW Influence on the IT System

Previous studies investigated the response of the IT system to different SSWs using different parameters from different instruments at different locations and heights. A list below summarizes the studies that are concerned with the SSW influence on the ionosphere (Table 2-1) and thermosphere (Table 2-2). Modelling studies are also listed separately in Table 2-3. The only literature that are published in 2009 or later are included. Review articles (Chau et al., 2011; Pedatella et al., 2018) are not included.

2.4.1 Ionosphere

The table below (**Table 2-1**) lists studies concerned with the SSW influence on the ionosphere. It is noted that “SSW event(s)” indicates the winter period containing the SSWs that are investigated. For example, “2009” means the winter of 2008/2009, i.e., November 2008-February 2009. Therefore, the year does not necessarily match the year of SSW onset.

Authors (Year)	Main parameter	Location	SSW event(s)	Comment
Chau et al. (2009)	Vertical plasma drift velocity (ISR)	Jicamarca (Peru)	2008	Semidiurnal variation
Sridharan et al. (2009)	EEJ (ground-based magnetometer)	Trivandrum/Tirunelveli (India)	1999, 2002, 2004, 2006	CEJ
Vineeth et al. (2009)	EEJ (ground-based magnetometer)	Trivandrum/Tirunelveli	1998, 2004, 2005, 2006	CEJ, 16d variation
Anderson and Araujo-Pradere (2010)	Vertical plasma drift velocity (ground-based magnetometer)	Jicamarca & Davao (Philippines)	2003, 2004	
Chau et al. (2010)	TEC (ground-based GPS)	Arecibo	2008, 2009	Semidiurnal variation
Goncharenko et al. (2010a)	TEC (ground-based GPS)	Low latitude	2009	Semidiurnal variation
Goncharenko et al. (2010b)	TEC (ground-based GPS)	Low latitude	2009	Semidiurnal variation

Authors (Year)	Main parameter	Location	SSW event(s)	Comment
Fejer et al. (2010)	EEJ (ground-based magnetometer)	Equatorial region	2002, 2003, 2009	Lunar tide
Yue et al. (2010)	Electron density (COSMIC)	Global	2009	Semidiurnal variation
Pedatella and Forbes (2010)	TEC (IGS map)	Mid and low latitudes	2009	SW1
Fejer et al. (2011)	Vertical plasma drift velocity (JULIA)	Jicamarca	Multiple (2000-2010)	Lunar tide
Liu et al. (2011b)	TEC (ground-based GPS)	Southeast Asia	2009	Semidiurnal variation
Pancheva and Mukhtarov (2011)	Electron density (COSMIC)	Global	2008, 2009	Decrease in zonal mean and migrating diurnal tide
Rodrigues et al. (2011)	Vertical plasma drift velocity (C/NOFS)	Equatorial region	2009	Semidiurnal variation
Stening (2011)	EEJ (ground-based magnetometer)	Equatorial region	1960-2009	CEJ
Fejer et al. (2011)	Vertical plasma drift velocity (JULIA)	Jicamarca	Multiple (2000-2010)	Lunar tide
Liu et al. (2011b)	TEC (ground-based GPS)	Southeast Asia	2009	Semidiurnal variation
Pancheva and Mukhtarov (2011)	Electron density (COSMIC)	Global	2008, 2009	Decrease in zonal mean and migrating diurnal tide
Rodrigues et al. (2011)	Vertical plasma drift velocity (C/NOFS)	Equatorial region	2009	Semidiurnal variation
Stening (2011)	EEJ (ground-based magnetometer)	Equatorial region	1960-2009	CEJ
Park et al. (2012)	EEJ (CHAMP magnetometer)	Equatorial region	Multiple (2002-2009)	Lunar tide
Park and Lühr (2012)	F-region vertical current (CHAMP magnetometer)	Equatorial region	2002	Lunar tide
Sripathi and Bhattacharyya (2012)	TEC (ground-based GPS)	India	2006	13-14d variation
Yamazaki et al. (2012a)	EEJ (ground-based magnetometer)	Addis Abeba (Ethiopia)	Multiple (1958-2007)	Lunar tide
Yamazaki et al. (2012b)	Ionospheric currents (ground-based magnetometer)	Mid and low latitudes	2002, 2003	Lunar tide

Authors (Year)	Main parameter	Location	SSW event(s)	Comment
Yamazaki et al. (2012c)	Ionospheric currents (ground-based magnetometer)	Mid and low latitudes	2006, 2009	(2,3)-mode tide
Goncharenko et al. (2013a)	TEC (ground-based GPS)	Low latitude	2013	
Goncharenko et al. (2013b)	Ion temperature (ISR)	Millstone Hill (USA)	2010	Tides and planetary waves
CH Lin et al. (2013)	Electron density (FORMOSAT-3/COSMIC)	Mid and low latitudes	2009	
JT Lin et al. (2012)	Electron density (FORMOSAT-3/COSMIC)	Mid and low latitudes	2009	Decrease in zonal mean and migrating tides
Sathishkumar and Sridharan (2013)	EEJ (ground-based magnetometer)	Tirunelveli	2009	Solar vs lunar tides
Upadhayaya and Mahajan (2013)	foF2 (ionosonde)	Mid and low latitudes	2007, 2008, 2009	
Yamazaki (2013)	EEJ (ground-based magnetometer)	Addis Abeba	Multiple (1958-2007)	Lunar tide
Jonah et al. (2014)	TEC (ground-based GPS)	Brazil	2013	13-16d variation
Laskar et al. (2014)	TEC (ground-based GPS)	India	Multiple (2005-2013)	16d wave
Oyama et al. (2014)	Electron density (FORMOSAT-3/COSMIC)	Mid and low latitudes	2009	
Paes et al. (2014)	TEC (ground-based GPS)	Brazil	Multiple (2008-2011)	Semidiurnal variation
Patra et al. (2014)	Vertical plasma drift velocity (radar)	Gadanki (India)	2009	
Pedatella (2014)	Electron density (COSMIC)	Mid and low latitudes	Multiple	Lunar tide
Polyakova et al. (2014)	TEC (JPL map)	Russia	2009, 2013	Decrease in diurnal variation
Yamazaki (2014)	Ionospheric currents (ground-based magnetometer)	Mid and low latitudes	Multiple (1958-2007)	Lunar vs solar tides
de Paula et al. (2015)	S4 index (ground-based GPS)	São José dos Campos (Brazil)	2002, 2003, 2013	Decrease in scintillation intensity
Pedatella and Maute (2015)	hmF2 (COSMIC)	Mid and low latitudes	2009, 2013	Lunar tide
Shpynev et al. (2015)	foF2 (ionosonde)	Russia	2009, 2013	
Siddiqui et al. (2015a)	EEJ (ground-based magnetometer)	Huancayo	Multiple (1926-2009)	Lunar tide

Authors (Year)	Main parameter	Location	SSW event(s)	Comment
Siddiqui et al. (2015b)	EEJ (ground-based magnetometer)	Huancayo	Multiple (1998-2013)	Lunar tide
Bolaji et al. (2016)	Ionospheric currents (ground-based magnetometer)	Africa	2009	
Chen et al. (2016)	foF2 (ionosonde)	China	2013	16d wave
Gong et al. (2016)	Ion temperature (ISR)	Arecibo	2010	TW3 effect on midnight temperature maximum
Wu et al. (2016)	hmF2 (ISR)	Millstone Hill	2013	Comparison with TIE-GCM
de Jesus et al. (2017a)	TEC (ground-based GPS)	Brazil	2006	No influence on ionospheric irregularity
de Jesus et al. (2017b)	TEC (ground-based GPS)	Low latitude	2012	11-20d variation
de Jesus et al. (2017c)	TEC (ground-based GPS)	Brazil	2014	
Gupta and Upadhyaya (2017)	foF2	Mid and low latitudes	Multiple (2010-2016)	
Jose et al. (2017)	Ionogram	Trivandrum	2004, 2006	Modulation of ESF onset
Pal et al. (2017)	VLF/LF	Mid latitude	2009	
Siddiqui et al. (2017)	EEJ (ground-based magnetometer)	Equatorial region	2006, 2009	
Sridharan (2017)	TEC (IGS map)	15°N	2013	Increase in tides
Vieira et al. (2017)	TEC (ground-based GPS)	Brazil	2012	
Yadav et al. (2017)	TEC (ground-based GPS)	India	2009	
Goncharenko et al. (2018)	TEC (GNSS)	Mid and low latitudes	2013	Nighttime response discussed
Mo and Zhang (2018)	TEC (ground-based GPS)	Low latitude	2003, 2006, 2009	14-15d variation
Siddiqui et al. (2018a)	EEJ (ground-based magnetometer)	Huancayo	2003, 2006, 2009, 2013	Solar vs lunar tides
Siddiqui et al. (2018b)	EEJ (ground-based magnetometer)	Huancayo	Multiple (1958-2013)	QBO influence discussed
Yasyukevich (2018)	NmF2 (digisonde)	Norilsk (Russia)	Multiple (2006-2013)	
Lin et al. (2019)	TEC (GIS)	Mid and low latitudes	2009	Solar vs lunar tides
G. Liu et al. (2019)	TEC (ground-based GPS)	China	2018	
J. Liu et al. (2019)	TEC (ground-based GPS)	Low latitude	Multiple (2009-2018)	Lunar tide

Authors (Year)	Main parameter	Location	SSW event(s)	Comment
Nayak and Yigit (2019)	TEC (ground-based GPS)	~60°N	2009	Small-scale GW activity discussed
Owolabi et al. (2019)	EEJ (ground-based magnetometer)	Equatorial region	2006, 2009	
Yadav et al. (2019)	EEJ (ground-based magnetometer)	Tirunelveli	Multiple (2003-2013)	

2.4.2 Thermosphere

The table below (**Table 2-2**) lists studies concerned with the SSW influence on the thermosphere. It is noted that the only studies that consider the regions above 100 km are listed here. The studies that are concerned only with the mesosphere and lower thermosphere region are not included.

Authors (Year)	Main parameter	Location	SSW event(s)	Comment
Conde and Nicolls (2010)	Temperature (FPI)	Poker Flat (USA)	2009	Cooling
Funke et al. (2010)	Temperature (Envisat)	70-90°N	2009	Warming at 120-140 km
Kurihara et al. (2010)	Wind (NTMR)	Tromsø (Norway)	2009	Wind reversal at 100 km
Liu et al. (2011a)	Mass density (CHAMP & GRACE)	Mid and low latitudes	2009	Cooling
Forbes and Zhang (2012)	Temperature (SABER)	Mid and low latitudes	2009	Lunar tide
Gong et al. (2013)	Winds (ISR)	Arecibo	2010	Solar tides
Zhang and Forbes (2014)	Temperature (SABER)	Mid and low latitudes	Multiple (2002-2013)	Lunar tide
Wu and Nozawa (2015)	Ground-based winds	Mid and high latitudes	2010	Semidiurnal tides
Yamazaki et al. (2015)	Satellite orbital drag	Global	Multiple (1967-2013)	Statistics for cooling
Gong et al. (2018)	Winds (ISR)	Arecibo	2016	Quarterdiurnal tide

2.4.3 Modeling

The table below (**Table 2-3**) lists modeling studies concerned with the SSW influence on the ionosphere and thermosphere.

Authors (Year)	Main parameter	SSW event(s)	Findings
Liu et al. (2010)	TIME-GCM	Non-specific	PW-tide interaction drives ionospheric variability
Fuller-Rowell et al. (2010)	WAM	2009	Tidal changes in the thermosphere

Authors (Year)	Main parameter	SSW event(s)	Findings
Fuller-Rowell et al. (2011a)	WAM	2009	Enhancement occurs in TW3
Fuller-Rowell et al. (2011b)	WAM	2009	Thermospheric cooling is not supported
Wang et al. (2011)	WDAS	2009	Increase in TW3 is likely due to wave interactions among SW2, TW3, DW1
Bessarab et al. (2012)	GSM TIP	2009	Temperature variation leads to a decrease [O]/[N ₂] and electron density reduction
Fang et al. (2012)	WAM	2009	Migrating tides play a main role, but the ionospheric response can be longitudinally dependent
Jin et al. (2012)	GAIA	2009	SW2 drives ionospheric variability
Korenkov et al. (2012)	GSM TIP	2008	Temperature variation leads to a decrease [O]/[N ₂] and electron density reduction
Pedatella et al. (2012)	WACCM	Non-specific	Changes in SW2, M2, D0, SW1
Yigit and Medvedev (2012)	CMAT2 GCM	Non-specific	SSW affects upward propagation of GWs into the upper thermosphere
Liu et al. (2013)	GAIA	2009	Thermospheric cooling depends on LT
Pedatella and Liu (2013a)	WACCM	Non-specific	M2 response depends on the moon phase at the SSW onset
Sassi et al. (2013)	WACCM/NOGAPS-ALPHA	2009	Changes in DW1, SW2, UFKW, (1,1) and (2,1) Rossby modes at 100 km
Fang et al. (2014)	WAM/GIP	2009	Ionospheric response is greater during solar minimum than solar maximum
Liu et al. (2014)	GAIA	2009	Thermospheric cooling occurs at most latitudes
Maute et al. (2014)	TIME-GCM	2006	SW1 drives wave number 1 in the low latitude ionosphere
Pedatella et al. (2014a)	GAIA, HAMMONIA, WAM, WACCM-X	2009	Thermospheric response varies among different models
Pedatella et al. (2014b)	TIME-GCM	2009	M2 is important for low-latitude ionospheric response
Wang et al. (2014)	IDEA	2009	Model can predict ionospheric response 10 days in advance
Yigit et al. (2014)	CMAT2 GCM	Non-specific	GW drag increases in the high-latitude thermosphere above 150 km
Azeem et al. (2015)	IDA4D	2009	TEC response is modulated by SW1
Maute et al. (2015)	TIME-GCM	2013	Longitudinally dependent ionospheric response is due to winds and geomagnetic main field.

Authors (Year)	Main parameter	SSW event(s)	Findings
Miyoshi et al. (2015)	GAIA	Non-specific	GW drag causes changes in the meridional circulation
Pedatella and Maute (2015)	TIME-GCM	2009, 2013	M2 is important for mid- and low-latitude response of hmF2
Klimenko et al. (2015)	GSM TIP, TIME-GCM	2009	[O]/[N ₂] and thermospheric winds are important for ionospheric response
Pedatella et al. (2016a)	GAIA, WAM/GIP, WACCM-X/TIME-GCM	2009	Ionospheric response varies among different models
Pedatella et al. (2016b)	TIE-GCM/TIME-GCM	2009	Reduction of NmF2 is due to composition changes
Maute et al. (2016)	TIME-GCM	2013	Beating of SW2 and M2 is important for low-latitude ionospheric response
McDonald et al. (2018)	SAMI3/SD-WACCM-X	2018	Ionospheric response improves with new HA-NAVGEM forcing, compared to NOGAPS-ALPHA forcing

2.5 Conclusions

From Table 2.1–3, a few comments may be made regarding previous studies on the IT response to SSWs. Firstly, the January 2009 major SSW event is by far the most well investigated event, both observationally and theoretically. Secondly, most ionospheric studies are based on the electron density (including TEC and NmF2) or EEJ, and the studies involving other ionospheric parameters are few. Thirdly, studies mostly focused on the middle- and low-latitude regions, and avoided the high-latitude region where the interpretation of ionospheric variability is more complicated. Fourthly, many ionospheric studies examined tidal variations. Together with numerical work, the importance of the semidiurnal lunar tide for low-latitude ionospheric variability during SSWs is well established. It is noted that in some studies, the semimonthly oscillation of the lunar tide (14.8d) was interpreted as the effect of 16d planetary wave. Another important insight obtained through the combination of observations and modelling studies is the overall reduction of low-latitude ionospheric plasma density during SSWs and the contribution of [O]/[N₂] changes. Lastly, the knowledge on the thermospheric response to SSWs is limited due to difficulties in measurements as well as due to the high sensitivity of the thermosphere to other sources of variability.

In conclusion, future studies are encouraged to

- (a) investigate the high-latitude ionospheric response;
- (b) examine the ionospheric parameters other than electron density and EEJ;
- (c) investigate thermospheric response.

These conclusions, especially (a) and (b), justify the main objectives of the VERA project, and also support the choice of tasks and tools within VERA. The successful application of Swarm data for investigation of the upward propagation of atmospheric waves expands the scientific objectives of the Swarm mission towards atmosphere/magnetic field coupling. We are currently selecting SSW events, based on the inspection of stratospheric parameters and indices that describe the geomagnetic activity. The latter can potentially disturb the

ionosphere in a way that possible SSW effects will be difficult to separate. Based on this selection we will prepare and analyze the following data sets and models. Studying the effect of SSW on the IHFACs, we will apply Swarm and CHAMP observations, since these currents are only detectable by LEO satellites that carry high precision magnetometers. Both missions precessing slowly through all local times, provide ideal coverage for most of the SSW events. The data analyses will be supported by physics-based models of the upper atmosphere that take into account the effect of lower atmospheric forcing, e.g., TIE-GCM (Qian et al., 1992). Ionosonde data will be used to validate model results.

For a better description of the response of the polar ionosphere, we also make use of the E-CHAIM model (Themens et al., 2017), that has been found to well quantify regular seasonal effects or effects of moderate geomagnetic activity. The variations in the polar middle atmosphere are characterized through the atmospheric measurements at Eureka (Nunavut, Canada), and ionosonde data are used to decipher possible effects of SSW on the polar ionosphere. The following chapter presents the list of selected SSW effects including justification, and a detailed description of the data sets.

Chapter 3

Data Collection

3 Data Collection

3.1 Scope and Outline

This section describes the data collected for the VERA (Vertical Coupling in the Earth's Atmosphere at mid and high latitudes) project. Stratospheric data are first described and a list of recent sudden stratospheric warmings is generated based on those data. Ionospheric data are then described, including the total electron content (TEC) data from GNSS measurements; electron density profiles from ionosonde measurements in the regions of Europe and northern Canada; and electron density data from Swarm. The ionospheric data are supported by neutral atmosphere parameters measured in the mesosphere and lower thermosphere (MLT) at the Canadian northernmost station Eureka. All these data are used in analyzing upper atmospheric effects of sudden stratospheric warmings (SSWs) for all winters under study.

3.2 Stratospheric data

We use the ERA 5 reanalysis for identification of SSWs during period 2000–2019 because direct observations do not have sufficient spatial and geographical reliability especially in the stratosphere region (20–50 km). ERA5 is currently available for the period 1979 to present. It is being developed through the Copernicus Climate Change Service

(<https://climate.copernicus.eu>). ERA5 data is open access and free to download for all users (after simple registration), including commercial use through the C3S Climate Data Store at

- <https://cds.climate.copernicus.eu/cdsapp#!/dataset/reanalysis-era5-pressure-levels?tab=form>.

The data can be downloaded as NC or GRIB files. More details on ERA 5 can be found in C3S.

Data processing for ERA5 is carried out by ECMWF (<https://www.ecmwf.int>), using ECMWF's Earth System model IFS, cycle 41r2. The name ERA refers to 'ECMWF ReAnalysis', and ERA5 is the fifth major global reanalysis produced by ECMWF (after FGGE, ERA-15, ERA-40, ERA-Interim).

In ERA5 we can find the same parameters as in previous ERA-Interim. For the VERA project, we use mainly temperature and zonal or meridional wind speed. ERA5 is available in 37 pressure levels from 1000 hPa (surface) to 1 hPa (app.50 km) but for this project we use the data at levels from 50 hPa (20 km) to 1 hPa which covers the area in the stratosphere where SSWs take place.

The MERRA-2 reanalysis has also been used in some studies within the project. MERRA-2 is currently available for the period 1979 to present. It is developed at the NASA. MERRA-2 data is open access and free to download for all users (after simple registration) at

- https://cmr.earthdata.nasa.gov/search/concepts/C1276812931-GES_DISC.html.

The data can be downloaded as NC files. More details on MERRA-2 can be found in Gelaro et al. (2017).

MERRA-2 uses the Three-Dimensional Variational (3D VAR) assimilation process. The name MERRA refers to 'Modern-Era Retrospective analysis for Research and Applications', and MERRA-2 is the second major global reanalysis produced by NASA (after MERRA). MERRA-2 uses regular latitude–longitude grids from 1000 to 0.01 hPa ($1/2^\circ$ latitude \times $5/8^\circ$

longitude). In the VERA project, we mainly use temperature and zonal or meridional wind speed.

3.3 Sudden stratospheric warmings during 2000–2019

SSWs usually occur in winter (December-February). SSWs are essentially a Northern Hemisphere phenomenon. They are divided into ‘minor’ and ‘major’ SSWs, as well as into ‘split’ and ‘displacement’ types (e.g., Maycock and Hitchcock, 2015). A major SSW is accompanied by the reversal of zonal wind in the high latitude stratosphere, while a minor SSW involves no zonal wind reversal. An SSW is classified as split type if the polar stratospheric vortex is split into two vortices, while it is said to be displacement type if the vortex substantially moved its centre off the pole region.

We have examined ERA5 data for the period 2000–2019. For each winter, a plot is made for an overview of stratospheric dynamics, based on which we determine the occurrence of a major SSW and its start/peak/end times. Figure 3-1 gives an example of the plot for the winter of 2017–2018. We have detected 13 SSWs in the Northern Hemisphere during 2000–2019, which are listed in Table 3-1.

zonal wind reversal			wind at 30 hPa (m/s)	temp before (K)	polar temperature				type
start date	central date	end date			start date	max temp (K)	max date	end date	
18.01.2000	20.01.2000	22.01.2000	-0.8	214	14.01.2000	247	16.01.2000	25.01.2000	displaced
04.02.2001	11.02.2001	20.02.2001	-11.8	215	29.01.2001	240	08.02.2001	20.02.2001	split
24.12.2001	02.01.2002	05.01.2002	-4.4	212	23.12.2001	259	30.12.2001	04.01.2002	displaced
15.01.2003	18.01.2003	20.01.2003	-6.4	212	15.01.2003	250	17.01.2003	20.01.2003	split
04.01.2004	07.01.2004	15.01.2004	-12.0	223	02.01.2004	238	10.01.2004	13.01.2004	displaced
13.01.2006	21.01.2006	03.02.2006	-20.0	211	08.01.2006	263	22.01.2006	31.01.2006	displaced
21.02.2007	24.02.2007	01.03.2007	-18.0	206	20.02.2007	238	24.02.2007	01.03.2007	displaced
18.02.2008	22.02.2008	28.02.2008	-17.5	213	17.02.2008	260	23.02.2008	27.02.2008	displaced
19.01.2009	24.01.2009	07.02.2009	-15.0	215	19.01.2009	270	23.01.2009	07.02.2009	split
06.02.2010	09.02.2010	12.02.2010	-13.0	215	25.01.2010	240	01.02.2010	07.02.2010	split
04.01.2013	07.01.2013	20.01.2013	-19.0	208	04.01.2013	250	07.01.2013	22.01.2013	split
11.02.2018	16.02.2018	26.02.2018	-21.0	216	09.02.2018	243	17.02.2018	28.02.2018	split
30.12.2018	12.01.2019	29.01.2019	-15.0	210	18.12.2018	265	28.12.2018	29.01.2019	split

Table 3-1. List of major stratospheric warmings for 2000-2019.

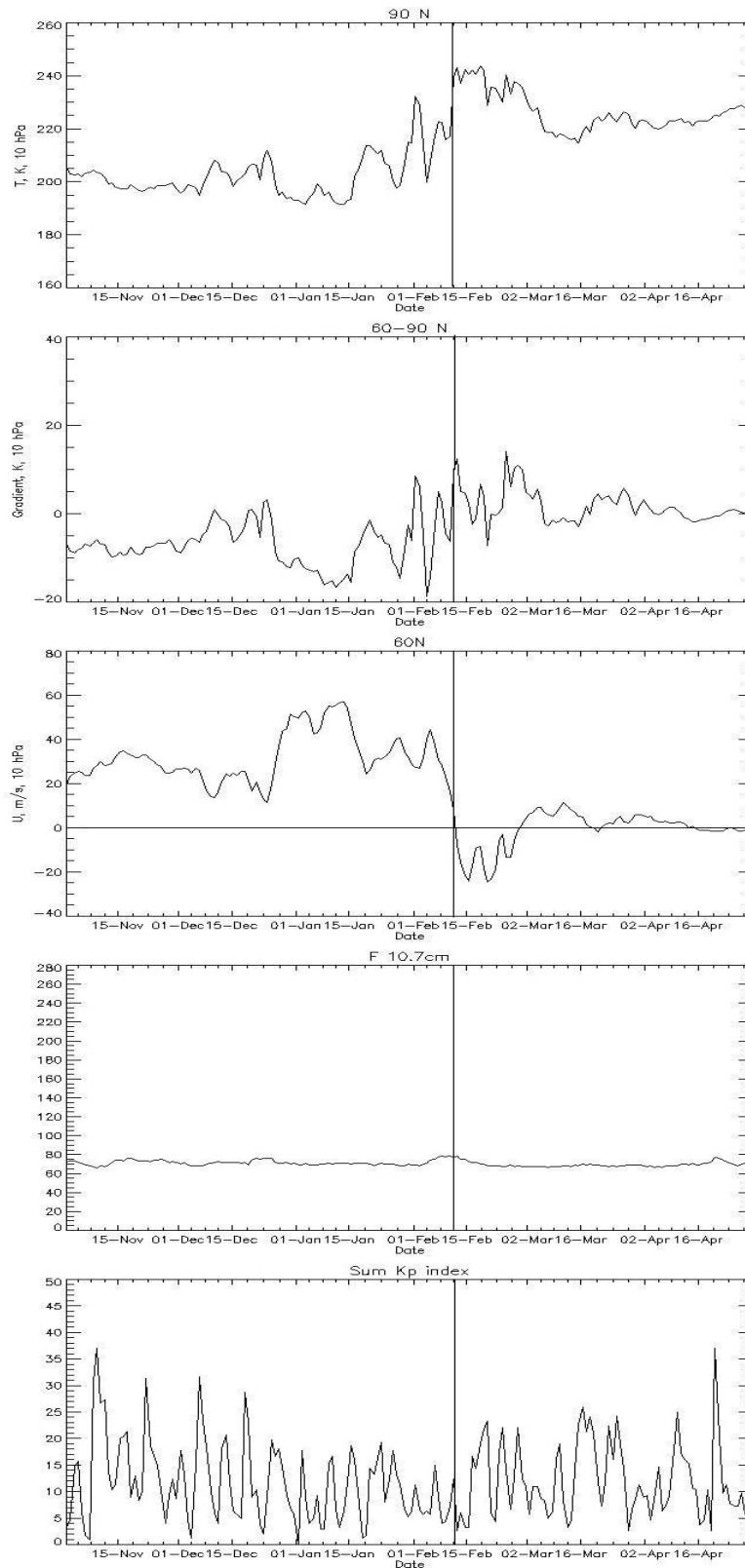


Figure 3-1. From top to bottom: Temperature at 90°N, temperature gradient between 60 and 90°N, zonal wind at 60°N (all at 10 hPa), F10.7 index and the daily sum Kp index for SSW 2018. Vertical line indicates the beginning of wind reversal.

3.4 European/global TEC data

Global navigation satellite systems, GNSS (GPS, GLONASS, Galileo, Beidou) are designed to provide precise coordinates with minimal dependence on ionosphere. Measuring temporal delay between transmission and reception of signal we can determine pseudoranges to the satellite and having pseudoranges to several (at least four) satellites to calculate the receiver position. Phase velocity of radiowave depends on medium reflection coefficient and therefore signal delays depending on it as well. Since the coefficient depends on signal's frequency, satellites transmit navigation signal at several (typically at two) frequencies making it possible to take into account ionospheric delay and obtain the precise coordinates. At the same time, reflection coefficient linearly depends on electron concentration. Using delay measurements at different frequencies we can solve a system of equations and obtain integral electron concentration along signal's propagation trajectory called slant total electron content (sTEC). This can then be re-calculated to the standard vertical electron content (vTEC or TEC). GNSS measurements are currently the most often used tool for observations of the ionosphere. Measurements are broadly available from the mid-1990s.

The most common format for GNSS measurements provision is the Receiver Independent Exchange (RINEX) format. Such files contain all the main parameters of the measured signals (carrier phase (L), Doppler shift (D) and strength (S) of the signal) and pseudoranges measured with C/A-code (C) and P-code (P). The header of each file contains technical information about the GNSS station including receiver and antenna types, coordinates of the antenna and a list of used software. Currently the newest RINEX version is 3.04, but the most widely used files are of version 2.11.

Total electron content I could be calculated from a combination of carrier phase values:

$$I_L = A(f_1, f_2)[(L_1 \lambda_1 - L_2 \lambda_2 + \text{const} + \sigma L)], \text{ where}$$

$$A(f_1, f_2) = \frac{1}{40.308} \frac{f_1^2 f_2^2}{f_1^2 - f_2^2}$$

The term L_i stands for a phase at f_i frequency, σL is a phase measurement error. TEC derived from phase measurements contains unknown constant due to initial phase ambiguity.

Code-measured pseudorange values P could be used for TEC calculation as well:

$$I_P = A(f_1, f_2)[(P_2 - P_1 + \sigma P)],$$

where P_i is pseudorange measured with f_i frequency and $A(f_1, f_2)$ is defined above. The same formulae are valid for combinations between measurements at all the available GNSS frequencies (L1, L2, L5, etc.)

Currently GNSS receivers are distributed globally and allow obtain TEC data all over the world. Using this data with different methods of interpolation several organizations provide global ionospheric maps (GIMs), namely: Center for Orbit Determination in Europe (CODE), European Space Agency (ESA), Jet Propulsion Laboratory (JPL), Universitat Politècnica de Catalunya (UPC), Wuhan University, the Chinese Academy of Sciences (CAS). International GNSS service (IGS) provides GIMs creating them as a combination of other maps (CODE, JPL, ESA, UPC). All the maps have spatial resolution is $2.5^\circ \times 5^\circ$ in latitude and longitude,

correspondingly. Typical temporal resolution is 2h but several organizations provide more frequent maps (1h for CODE, 30 min for CAS, 15 min for uqrg maps (UPC)).

All the maps are freely available in IONEX format for 1998–present at:

- <ftp://cddis.gsfc.nasa.gov/gps/products/ionex>

In dependence on a map type data is available two days (rapid maps) and from 2 to 10 days (standard maps) after the actual date. CODE provides one- and two-day prediction maps available at the actual day.

Royal Observatory of Belgium provides near real-time ionospheric maps with high temporal (15 min) and spatial resolution ($0.5^{\circ} \times 0.5^{\circ}$) (Bergeot et al., 2014). The maps are available with one-hour lag at:

- <ftp://gnss.oma.be/gnss/products/IONEX/>

DLR Neustrelitz provides near-real-time TEC maps for Europe with update each 15 min, global TEC maps and maps of 1 min ROTI in their IMPC (Ionospheric Monitoring and Prediction Center; <https://impc.dlr.de/products/>).

Rate of change of TEC index (ROTI) maps are product of TEC measurements (Cherniak et al., 2018). These maps depict TEC gradients in the Northern Hemisphere and are available at CDDIS server in IONEX format with temporal lag of one month for the period since 2010:

- <ftp://cddis.gsfc.nasa.gov/gps/products/ionex>.

3.5 European ionosonde data

The ionosondes make vertical ionospheric sounding using radio wave reflections from the ionosphere. Their product is the ionogram. The ionograms show time delay between the transmission of the sounding signal and echo reflected from the ionospheric layer which is proportional to reflection height (vertical axis) in dependence on the sounding frequency (horizontal axis). The inversion program NHPC runs in the Automatic Real Time Ionogram Scaler with True height algorithm (ARTIST) for real time application, for Digisonde ionogram post-analysis, and as a stand-alone program in PC for the true height inversion of traces obtained from digital or analog ionograms. The output is the electron density profile and derived parameters as critical frequencies (foF2, foE - correspond to maximum electron densities of ionospheric F2 and E layers), and their heights (hmF2, hE).

European stations have been using predominantly the digital ionosonde DPS4.5 (called digisonde) in the last decade, i.e. in the period of VERA investigations. Regular sounding has been done once per 15 minutes. Measurements are essentially continuous (except for small technical gaps). The ionospheric data were obtained using European digisondes located at stations Juliusruh (54.6oN, 13.4oW), Chilton (51.5oN, 1.3oW), Dourbes (50.1°N, 4.6°E), Pruhonice (49.98oN, 14.55°E), Ebro (40.8°N , 0.5°E), Athens (38.0°N, 23.5°E), and Rome (41.8oN, 12.5oE). Some stations provide automatic scaling data in quasi-real-time plus manually scaled data (more accurate) with some delay (up to several months), mainly Juliusruh, Pruhonice and Ebro, other stations provide regularly only automatic scaling data. European digisonde shave predominantly been measuring since the International Geophysical Year (1957/1958), so their measurements are available not only for the VERA project period but also for much longer period before the VERA interval.

The source data (ionograms and SAO text files) are publicly available in the GIRO database. The cornerstones of GIRO operations are the Digital Ionogram Data Base (DIDBase) and the expert-level platform-independent software client “SAO Explorer”. The Web portal access to them is <http://ulcar.uml.edu/DIDBase/>. SAO Explorer contains read/write access to the GIRO DIDBase over the Internet (jdbc:firebirdsql://129.63.134.212//ext/db/ib/didb) and to its IAP Prague mirror site for Europe and Asia (jdbc:firebirdsql://147.231.75.90//ext/db/ib/didb), which works substantially quicker than GIRO.

These data include ionospheric characteristics from automatic scaling and electron density height profiles. The manually scaled data are available on request from D. Kouba or Z. Mosna of IAP Prague (kouba@ufa.cas.cz, mosna@ufa.cas.cz). Data of station Roma are available also via eSWua (http://roma2.rm.ingv.it/en/facilities/data_bases/12/eswua). All these databases are public; they require only a simple registration.

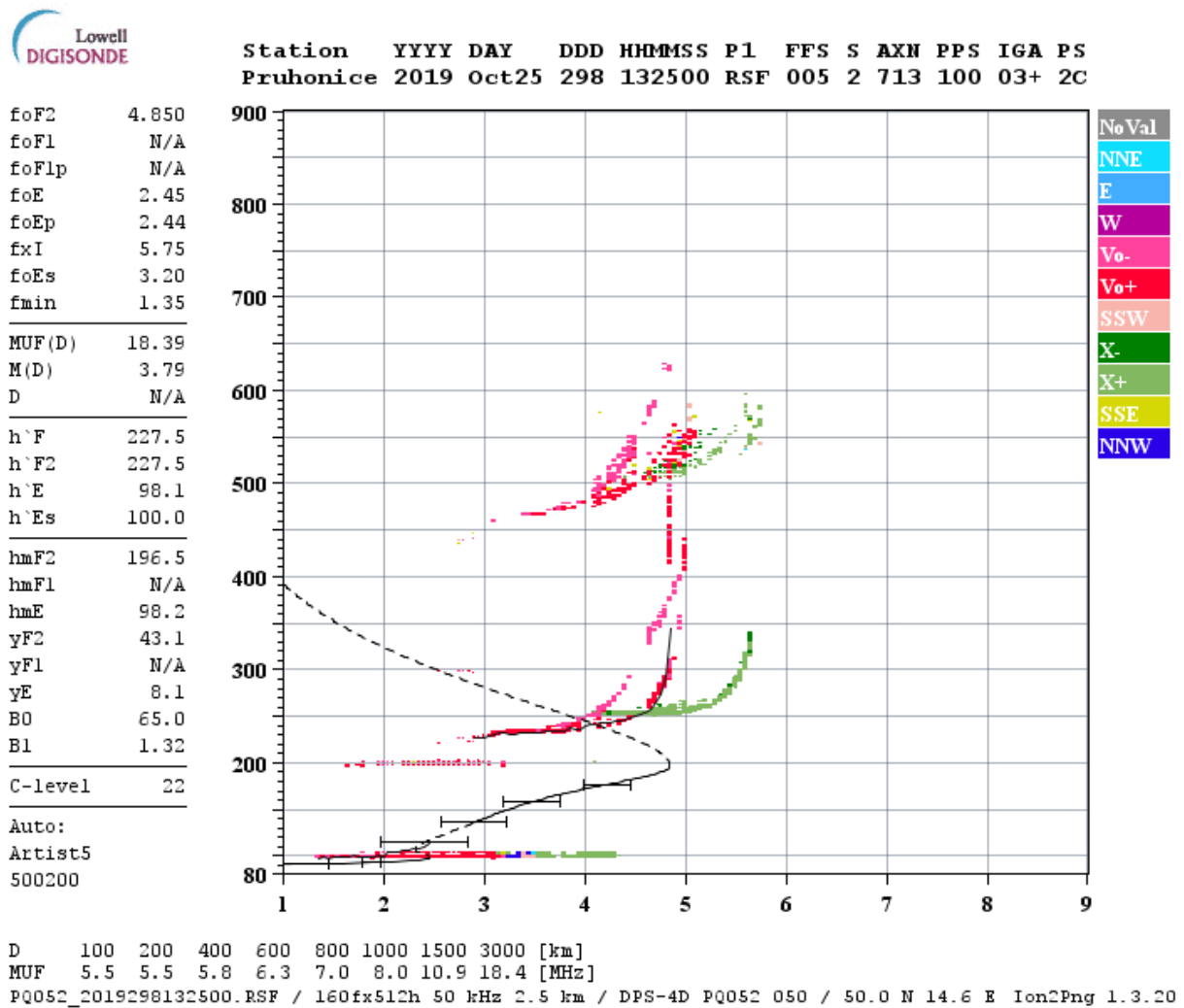


Figure 3-2. Ionogram from Pruhonice, 25 October 2019, 13:25 UT. Red – ordinary ray reflections; green – extraordinary ray reflections; black – electron density profile from automatic scaling.

3.6 Canadian ionospheric data

3.6.1 General information

CHAIN (Jayachandran et al., 2009) is a network of 25 GNSS receivers, nine of which are collocated with Canadian Advanced Digital Ionosondes (CADIs). The distribution of these instruments is illustrated in Figure 3-3.

The geographic coordinates for the stations pictured in Figure 3-3. can be found at

- <http://chain.physics.unb.ca/chain/pages/stations/>.

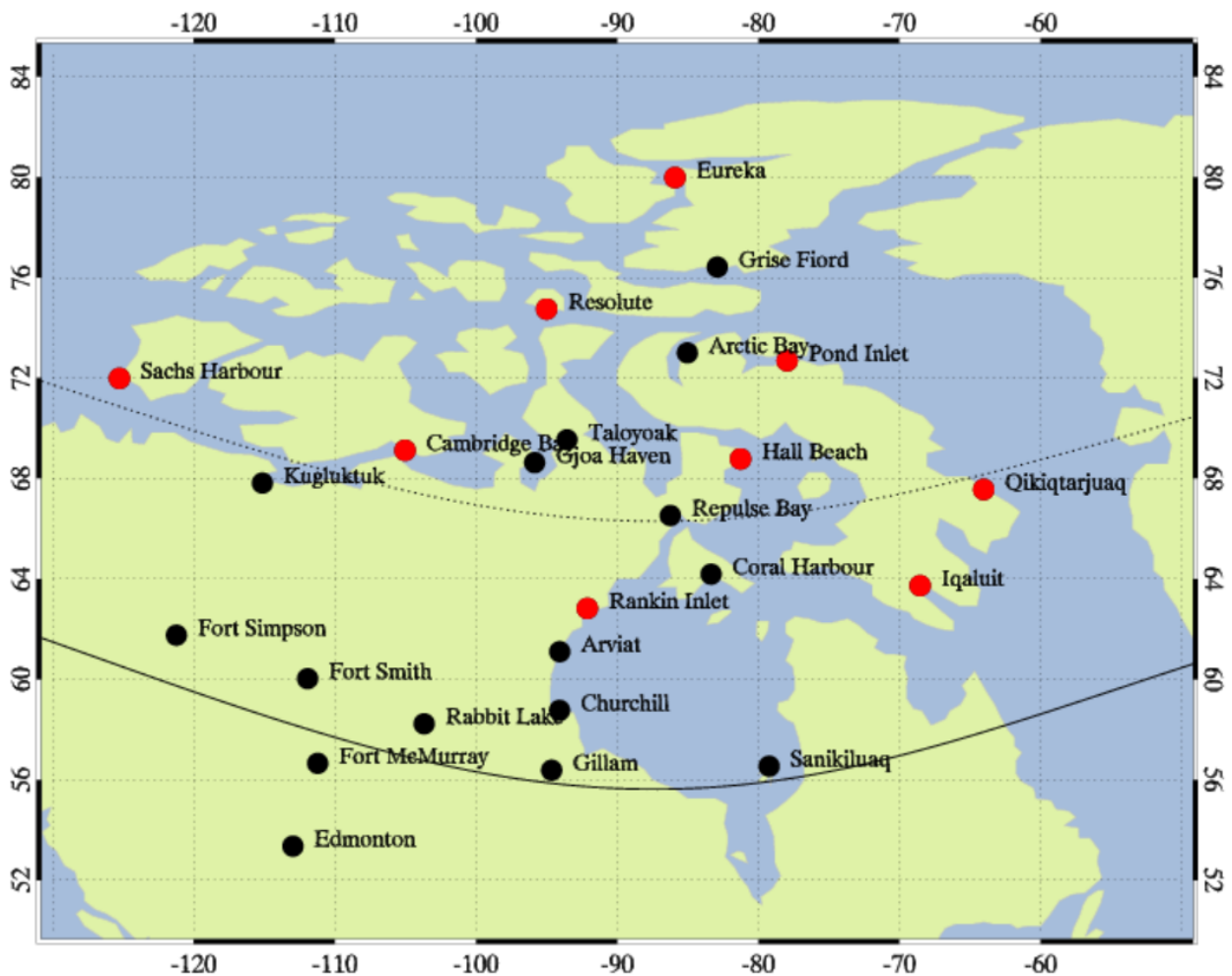


Figure 3-3. The geographic distribution of CHAIN stations within the Canadian Arctic. Stations with only a GNSS receiver are marked by black dots. Stations with both a GNSS receiver and a CADI system are marked with a red dot. Lines at 65° (dashed) and 75° (solid) geomagnetic latitude have been added to illustrate the geomagnetic location of the CHAIN stations.

The availability of these instruments since 2008 is provided in Figure 3-4 for the GNSS receivers and Figure 3-5 for the CADI ionosondes. Note that the information in these tables is separated into CHAIN and Expanded-CHAIN (ECHAIN), where ECHAIN represents an expansion and renewal of the network in 2014 that saw the addition of 15 GNSS receiver stations and, later, an additional three ionosondes.

All CHAIN data is openly available via FTP at

- <ftp://chain.physics.unb.ca/>.

An account is required for access; however, these accounts are automatically authorized without restriction. Accounts are merely used to limit bot activity on the CHAIN server and to inform users of anticipated outages or data issues. Information on the data formats and further instructions on how to access CHAIN data can be found here:

- http://chain.physics.unb.ca/chain/pages/data_download.

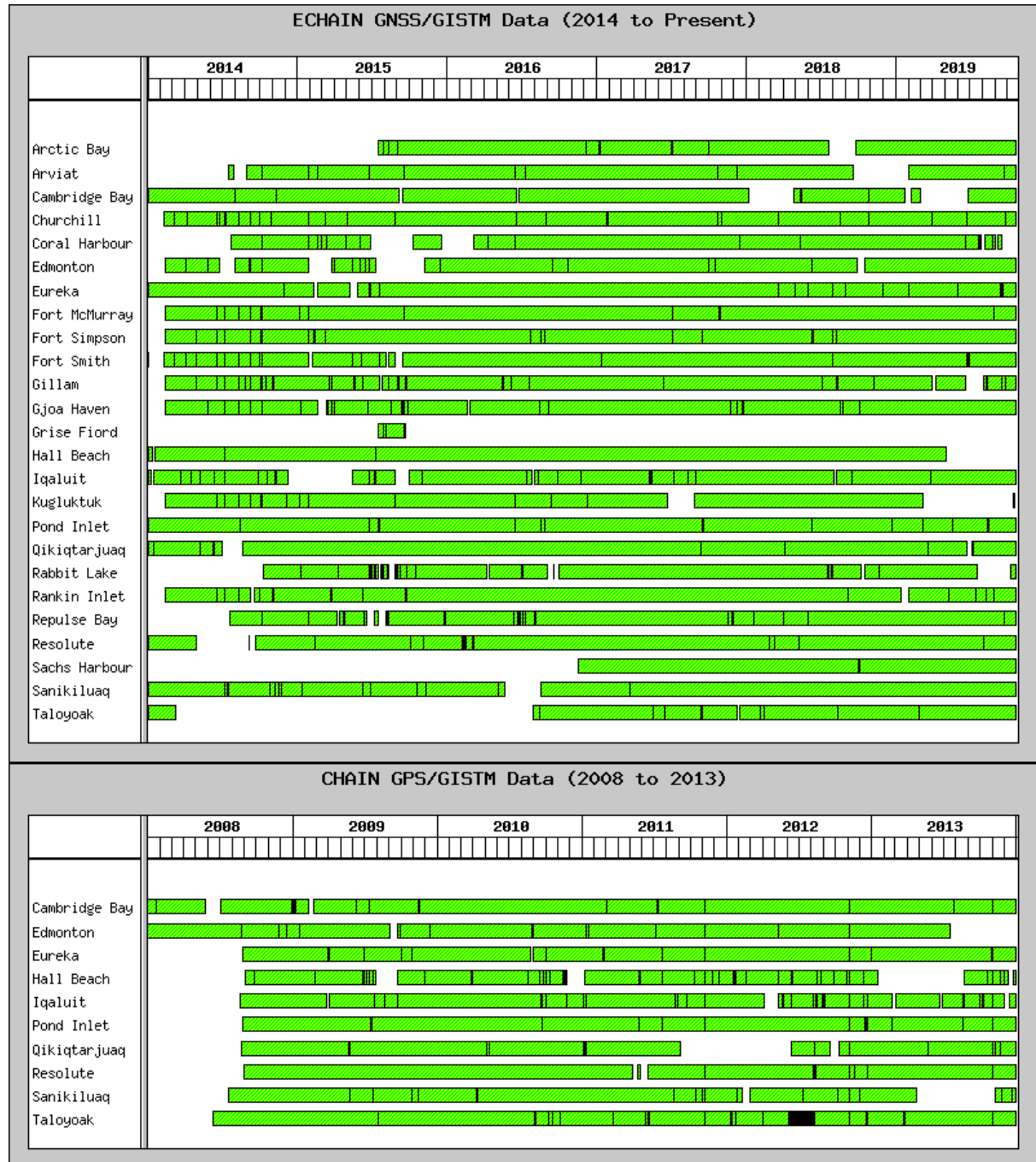


Figure 3-4. CHAIN GNSS receiver data availability. Continuous periods of operation are marked in green.

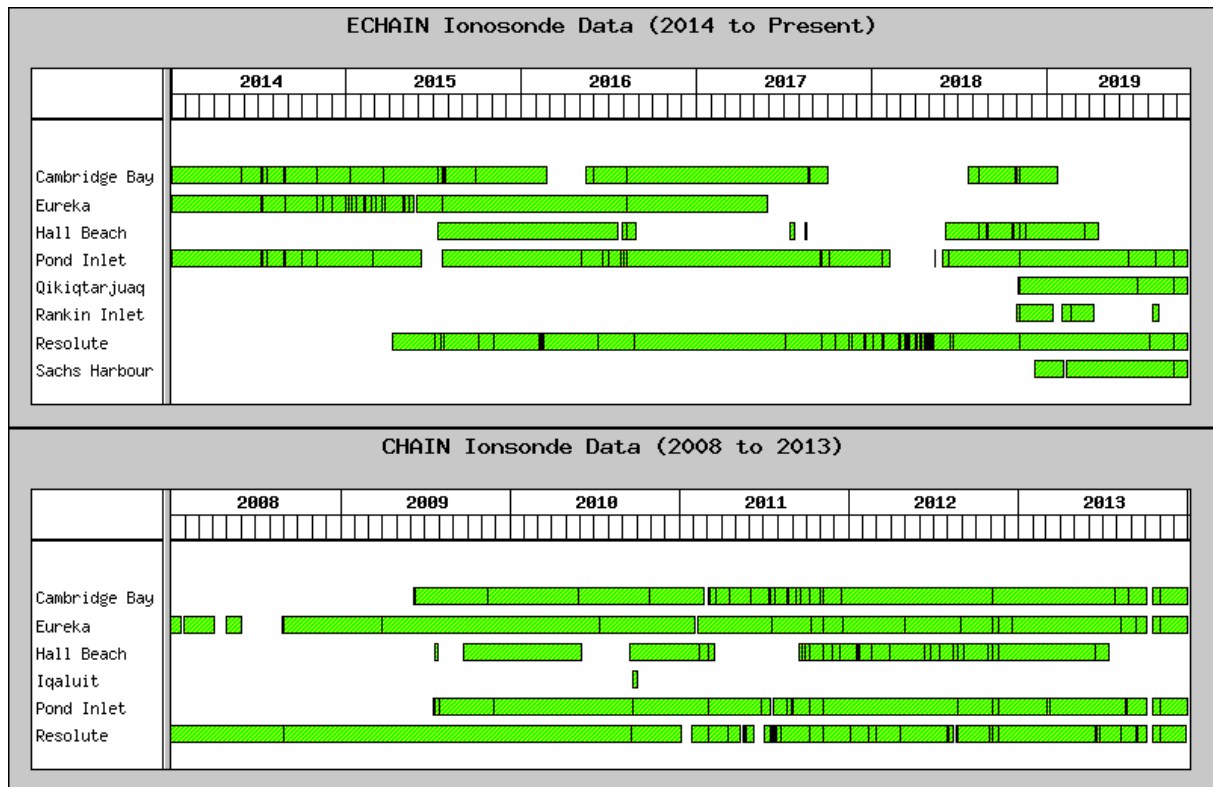


Figure 3-5. CHAIN CADI data availability. Continuous periods of operation are marked in green.

3.6.2 Ionosondes

Capability:

- The CADI ionosondes are capable of measuring ionospheric electron density profiles between ~90km and the F2-peak of the ionosphere. As part of this, the peak critical frequency of the ionosphere (foF2) and the peak height (hmF2) may be determined. As all of the data in this study is processed by hand, precisions of ~0.1MHz are achieved for foF2 and 10 km are achieved for hmF2. An example of foF2 and hmF2 accuracy as compared to Resolute Incoherent Scatter Radar (RISR) observations is provided in 2.4.4. Note that much of the spread in the error distributions of 2.4.4 are the result of the RISR measurement noise and a minor displacement between the location of the RISR and the CADI instruments.
- The CADI ionosondes can also provide information on sporadic-E occurrence and altitude, as well as ionospheric absorption, an indicator of D-Region behavior.

Processing:

- All CHAIN ionosonde data is processed by hand by Dr. David Themens. D. Themens is highly experienced in ionosonde data processing (scaling) and has scaled approximately 500,000 high latitude CADI ionograms and 1.5 million Digisonde ionograms).
- Inversion of CADI data is undertaken using manually scaled ionograms as input to the Polynomial Analysis (POLAN) inversion system of Titheridge (1988).

Limitations:

- CADI systems are limited by ionospheric absorption, such that periods of very low ionospheric electron density may not be observable with these systems. During the winter of the extreme solar minimum in 2009, this limitation results in an inability to measure ionospheric characteristics during most nighttime periods. CADI is incapable of providing peak electron density (N_{mF2}) when densities are below $\sim 4 \times 10^3$ (~ 1.8 MHz).
- Similarly, the enhancement of absorption during geomagnetic storms, solar energetic particle events, and solar flares also limits the utility of ionosonde systems, such that high latitude ionosondes may not be able of retrieving ionospheric parameters during these disturbances.

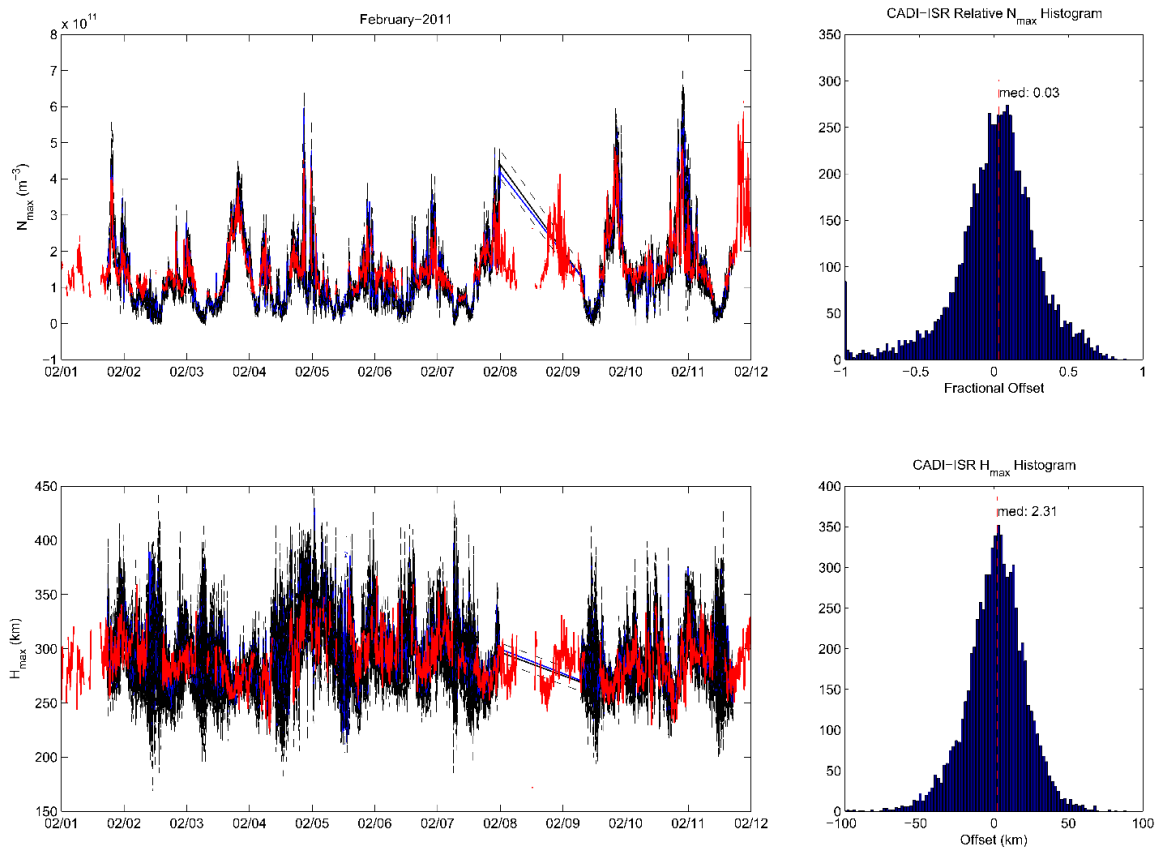


Figure 3-6. Example of ionosonde and Resolute Incoherent Scatter Radar (RISR-N) (top) ionospheric peak density (N_{mF2}) and (bottom) ionospheric peak height (h_{mF2}). RISR-N mean (black) and median (blue) curves for elevation angles greater than 60° are compared to Canadian Advanced Digital Ionosonde (CADI) (red) N_{mF2} and h_{mF2} measurements. Right panels show histograms of the ratio of RISR-N to CADI N_{mF2} (top) and h_{mF2} differences (bottom).

3.6.3 GNSS receivers

Capability:

- The CHAIN GNSS receivers measure the path integrated ionospheric electron density (TEC) along each receiver-satellite connection at one second cadence.

- The CHAIN GNSS receivers also sample raw signal amplitude and phase at 50Hz cadence to generate scintillation indices S_4 and σ_ϕ .
- These instruments are far less prone to temporary outages and provide reliable measurements during all but the very most disturbed ionospheric conditions.

Processing:

- GNSS receiver data is processed to derive total electron content using the methodology of Themens et al. (2013) with modified receiver bias estimation using the technique of Themens et al. (2015). The resulting TEC product is accurate to 1.5 TEC units (TECU) with a within-arc precision (relative TEC error) of 0.03 TECU.

3.7 Vernadsky Antarctic ionosonde

For the September 2019 Antarctic SSW, we make use of a new Software Defined Radio (SDR) ionosonde deployed in the Antarctic at the Ukrainian Antarctic Station (UAS), “Academic Vernadsky”, located at (65°14’44” S, 65°15’29” W). Full system details can be found in Zalizovski et al. (2018) (Russian). The ionograms from this ionosonde were manually processed by Dr. D.R. Themens at hourly cadence and were inverted for ionospheric parameters using POLAN.

3.8 Incoherent scatter radar

For this study, we also make use of the Poker Flat Incoherent Scatter Radar (PFISR), which was operating nearly continuously during both the 2009 and 2018-2019 SSW events. PFISR is an Alaskan deployment of the Advanced Modular Incoherent Scatter Radar (AMISR) class of phased array Incoherent Scatter Radars (ISRs) located at (65.13°N, 212.529°E) and operated by SRI International. The system transmits and receives at ~449 MHz with peak power of up to 2 MW. Full system details can be found in Valentic et al. (2013) and an image of the system is presented in Figure 3-7.

Incoherent Scatter Radars (ISRs) are high powered (generally Mega Watt) VHF/UHF radars that can be used to determine the ionospheric electron density, ion temperature, electron temperature, plasma drift, and, in some cases, even ion composition from altitudes within the D-Region of the ionosphere all the way into the topside (Evans, 1969). This is accomplished by impinging their high-powered radio signals on the ionosphere and making use of the very weak signals scattered back to the radar by ion acoustic waves within the ionospheric medium. The spectrum of this return signal is fit to a model spectrum to determine plasma parameters (Evans, 1969). Generally, ISRs are reliable instruments capable of providing unambiguous, absolute profiles of ionospheric parameters; however, to manage inversion errors in regions of low Signal-to-Noise (SNR), we have here employed an error filter that rejects any measurement with either electron density error larger than $1e11$ e/m³, temperature errors larger than 300 K, or plasma drift errors larger than 500 m/s. These thresholds are based on the recommendations of the instrument operator. Furthermore, measurements with exaggerated high confidence, typically associated with solid target contamination (e.g. satellites in the field of view) are also rejected.



Figure 3-7. Image of the PFISR array in Poker Flat, Alaska (Valentic et al., 2013).

3.9 Swarm data

Swarm is an ESA's Earth observation mission, which is designed for investigating the core dynamics, lithospheric magnetization, mantle conductivity, and magnetospheric and ionospheric current systems (Friis-Christensen et al., 2006). It involves three identical satellites (A, B and C) which were launched on 22 November 2013 into a near-polar orbit. The final constellation of the mission was achieved on 17 April 2014. Swarm A and C form the lower pair of satellites flying side-by-side (1.4° separation in longitude) at an altitude of 462 km (initial altitude) and at 87.35° inclination angle, whereas Swarm B is cruising at higher orbit of 511 km (initial altitude) and at 87.75° inclination angle. Each satellite is equipped with seven identical instruments:

- ASM – Absolute Scalar Magnetometer
- VFM – Vector Field Magnetometer
- STR – Star Tracker
- EFI – Electric Field Instrument
- GPSR – GPS Receiver
- LRR – Laser Retro-Reflector
- ACC – Accelerometer

More information on each instrument is available on the ESA's website at:

- <https://earth.esa.int/web/guest/missions/esa-co-missions/swarm/instruments-overview>.

The orbit information and instrument availability are provided for all Swarm satellites and can be found at:

- <https://earth.esa.int/web/guest/missions/esa-operational-co-missions/swarm/data-access/orbit-instrument-availability>

In the VERA project, we use the following parameters that are derived from Swarm measurements: electron density (Ne), total electron content (TEC), equatorial electrojet (EEJ), equatorial electric field (EEF), and field aligned current (FAC).

Swarm data (Level 1b and Level 2 products) are provided by ESA Earth Observation and are freely downloadable to all users via anonymous access via HTTP and ftp:

- <http://swarm-diss.eo.esa.int>
- <ftp://swarm-diss.eo.esa.int>

3.9.1 Electron density

The electron density Ne is derived from Langmuir Probes of EFI (Buchert et al., 2015). The data are archived at ESA as a Level 1b product EFIX_LP_1B (where “X” denotes the satellite; “A” for Swarm A, “B” for Swarm B and “C” for Swarm C) and are publicly available (e.g., via ftp) at:

- ftp://swarm-diss.eo.esa.int/Level1b/Latest_baselines/EFIX_LP/.

In the archive, daily data are saved in the CDF format (Figure 3-8). Each data file contains Ne data at 2 Hz rate, along with corresponding error estimates. The satellite time and location information are also included in each data file. Table 3-2 presents the full list of variables in the EFIX_LP_1B data product.

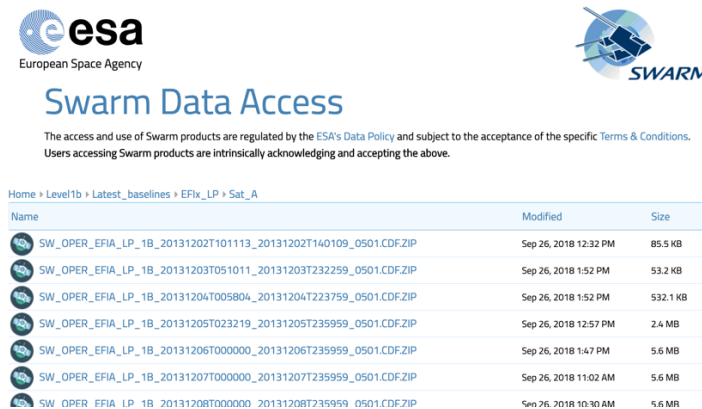


Figure 3-8. Screenshot of ESA Swarm data archive, listing EFIX_LP_1B data from Swarm A.

'Timestamp'	'Time stamp'	'_'
'SyncStatus'	'Synchronization status'	'_'
'Latitude'	'Position in ITRF - Latitude'	'deg'
'Longitude'	'Position in ITRF - Longitude'	'deg'
'Radius'	'Position in ITRF - Radius'	'm'
'U_orbit'	'Spacecraft velocity in the ITRF'	'm/s'
'Ne'	'Plasma density (electron)'	'cm-3'
'Ne_error'	'Error estimate of plasma density (Ne)'	'cm-3'
'Te'	'Plasma electron temperature'	'K'
'Te_error'	'Error estimate of plasma electron temperature (Te)'	'K'
'Vs'	'Spacecraft potential'	'V'
'Vs_error'	'Error estimate of spacecraft potential (U_pol)'	'V'
'Flags_LP'	'Flags indicating the source/method of LP measurements (ne, Te, Vs)'	'_'
'Flags_Ne'	'Flags characterizing the plasma density measurement'	'_'
'Flags_Te'	'Flags characterizing the electron temperature measurement'	'_'
'Flags_Vs'	'Flags characterizing the spacecraft potential measurement'	'_'

Table 3-2. The list of variables in the EFIX_LP_1B data product.

3.9.2 Total electron content

TEC values are derived using Swarm GPSR measurements. The data can be found in the ESA Earth Observation data archive, saved as a Swarm Level 2 product TECxTMS_2F:

- ftp://swarm-diss.eo.esa.int/Level2daily/Latest_baselines/TEC/TMS/.

A daily file contains vertical TEC data (labeled as “Absolute_VTEC”) at 1 Hz rate. Table 3-3 presents the full list of variables in the TECxTMS_2F data product.

Variable name	Description	Unit
Timestamp	Time stamps in Universal Time	cdf epoch
Latitude	Geographic latitude of the Swarm satellite	degree
Longitude	Geographic longitude of the Swarm satellite	degree
Radius	Distance of the Swarm satellite from the Earth’s center	m
GPS-Position	X-, Y-, Z-coordinates of the GNSS satellite used for STEC calculation	m
LEO-Position	X-, Y-, Z-coordinates of the Swarm satellite used for STEC calculation	m
PRN	Pseudo-Random Number (PRN) identifier of the GNSS satellite used for STEC calculation	no unit
L1	GNSS L1 carrier phase observation	m
L2	GNSS L2 carrier phase observation	m
P1	GNSS P1 carrier phase observation	m
P2	GNSS P2 carrier phase observation	m
S1	GNSS signal-to-noise ratio or raw signal strength on L1	no unit
S2	GNSS signal-to-noise ratio or raw signal strength on L2	no unit
Absolute-STECC	Absolute slant TEC	TECU
Absolute-VTECC	Absolute vertical TEC	TECU
Elevation-Angle	Elevation angle	degree
Relative-STECC	Relative slant TEC	TECU
Relative-STECC-RMS	Root mean square error of relative slant TEC	TECU
DCB	GNSS receiver differential code bias	TECU
DCB-Error	Error in the GNSS receiver differential code bias	TECU

Table 3-3. The list of variables in the TECxTMS_2F data product.

Full description of the Swarm TEC data, including the algorithm and data format, is available at:

- <https://earth.esa.int/web/guest/document-library/browse-document-library/-/article/swarm-level-2-tec-product-description>.

3.9.3 Equatorial electrojet/equatorial electric field

Latitudinal profiles of the height-integrated EEJ density at 110 km are derived using Swarm ASM measurements. The EEJ data are then used to estimate the zonal (eastward) electric field

at the magnetic equator. The algorithm is detailed in Alken et al. (2013a), and preliminary results are presented in Alken et al. (2015). Both EEJ profiles and EEF data can be found in Swarm Level 2 product EEF, which are accessible from the ESA Earth Observation data archive. An EEJ profile, covering $\pm 20^\circ$ Quasi-Dipole latitudes, is obtained for each orbit. Both EEJ and EEF data are available only during daytime. The description of the data format and data is available at:

- <ftp://swarm-diss.eo.esa.int/Advanced/EEF/>.

Table 3-4 presents the full list of variables in the EEFXTMS_2F data product.

Data	Description	Rate	Units	Comments
Timestamp	Timestamp of the EEF measurement (time of satellite crossing of magnetic equator)	1 per orbit	milliseconds elapsed since 00:00:00 January 1, 2000 UTC	CDF_EPOCH format
Longitude	Geographic longitude of the SWARM satellite crossing of the magnetic equator	1 per orbit	degrees	
Latitude	Geographic latitude of the SWARM satellite crossing of the magnetic equator	1 per orbit	degrees	
EEF	Equatorial eastward electric field estimate	1 per orbit	V/m	
EEJ	Height-integrated latitude profile of equatorial eastward current	1 per orbit	mA/m	Profile vector has length 81 (see section 5.1)
RelErr	Relative error between modelled and observed equatorial electrojet current	1 per orbit	N/A	see [AD-3]
Flags	Value describing the quality of the EEF estimate. Also contains identification information for SWARM satellite (A,B,C)	1 per orbit		See [AD-3]

Table 3-4. The list of variables in the EEFXTMS_2F data product.

3.9.4 Field-aligned current

There are two types of FAC products; namely, FAC-single and FAC-dual. Both are Level 2 product derived from Swarm VFM and can be downloaded from the ESA Earth Observation data archive. The difference of the two FAC products is that FAC-single is based on a traditional approach which uses magnetic measurements from a single satellite (e.g., Lühr et al., 1996) and is derived separately for Swarm A, B, and C; while FAC-dual is derived from the combined measurements by Swarm A and C (Ritter et al., 2013). The algorithm and data format for FAC-single can be found at

- <https://earth.esa.int/web/guest/document-library/browse-document-library/-/article/swarm-level-2-fac-single-product-description>.

The algorithm and data format for FAC-dual can be found at

- <https://earth.esa.int/web/guest/document-library/browse-document-library/-/article/swarm-level-2-fac-dual-product-description>.

FAC-single and FAC-dual are available only where the absolute value of magnetic inclination angle is greater than 30°. Also, FAC-dual is not calculated near the poles (above 86° latitude).

Variable name	Description	Unit
Timestamp	Time stamps in Universal Time	cdf epoch
Latitude	Geographic latitude of the Swarm satellite	degree
Longitude	Geographic longitude of the Swarm satellite	degree
Radius	Distance of the Swarm satellite from the Earth's center	m
IRC	Ionospheric radial current (vertically upward)	$\mu\text{A}/\text{m}^2$
IRC-Error	Error in ionospheric radial current	$\mu\text{A}/\text{m}^2$
FAC	Ionospheric field-aligned current	$\mu\text{A}/\text{m}^2$
FAC-Error	Error in ionospheric field-aligned current	$\mu\text{A}/\text{m}^2$
Flags	Flags characterizing the L2 FAC-single product quality	no unit
Flags F	Flags about the magnetic field intensity measurement (zero is nominal), passed through from the L1b data	no unit
Flags B	Flags about the magnetic field vector measurement (zero is nominal), passed through from the L1b data	no unit
Flags q	Flags about the attitude information (zero is nominal), passed through from the L1b data	no unit

Table 3-5. The list of variables in the FACxTMS_2F and FAC_TMS_2F data product.

Inter-hemispheric field-aligned currents (IHFACs) are a part of FACs that flow from one hemisphere to the other hemisphere. IHFACs, which are used in the VERA project, are derived by calculating the symmetric part of FAC (either FAC-single or FAC-dual) about the magnetic equator.

3.10 CHAMP data

CHAMP (Challenging Minisatellite Payload) is a German satellite operated during July 2000–September 2010 (Reigber et al., 2002). Mission details, including instrument information, can be found in the GFZ website at:

- <https://www.gfz-potsdam.de/en/section/geomagnetism/infrastructure/champ/>

CHAMP carried a similar set of scientific instruments as Swarm satellites. Thus, the CHAMP data can be used in the VERA project for investigating sudden stratospheric warming events that occurred during 2000–2010, prior to the Swarm mission.

3.10.1 Electron density

The electron density N_e is derived from Planar Langmuir Probe measurements. See the report by McNamara et al. (2007) for the N_e retrieval procedures, as well as validation of CHAMP

Ne based on a comparison with Jicamarca digisonde data. The data can be downloaded through an ftp client:

- <ftp://isdctftp.gfz-potsdam.de/champ/ME/Level2/PLPT/>

Daily files can be found under yearly directories (See Figure 3-9), and each file contains electron density and electron temperature with a 15s sampling interval, along with the time and location information. The header contains the information about the data format.

Index of /champ/ME/Level2/PLPT/2002/

 [parent directory]








Name	Size	Date Modified
 CH-ME-2-PLPT+2002-02-19_1.zip	159 kB	2/15/18, 1:00:00 AM
 CH-ME-2-PLPT+2002-02-20_1.zip	159 kB	2/15/18, 1:00:00 AM
 CH-ME-2-PLPT+2002-02-21_1.zip	158 kB	2/15/18, 1:00:00 AM
 CH-ME-2-PLPT+2002-02-22_1.zip	159 kB	2/15/18, 1:00:00 AM
 CH-ME-2-PLPT+2002-02-23_1.zip	159 kB	2/15/18, 1:00:00 AM
 CH-ME-2-PLPT+2002-02-24_1.zip	159 kB	2/15/18, 1:00:00 AM
 CH-ME-2-PLPT+2002-02-25_1.zip	159 kB	2/15/18, 1:00:00 AM

Figure 3-9. Screenshot of CHAMP Ne data archive for the year 2002.

3.10.2 Equatorial electrojet/equatorial electric field

The equatorial electrojet EEJ intensity can be derived from scalar magnetic field measurements by Overhauser magnetometer (e.g., Lühr et al., 2004), and from the EEJ, the equatorial zonal electric field EEF can be estimated (e.g., Alken et al., 2013b). P. Alken agreed that we can use these EEJ data within VERA. Currently, there is no publicly available CHAMP EEJ/EEF data. Availability of the CHAMP EEJ data to ESA within VERA will require further agreement with P. Alken.

3.11 Canadian MLT data from Eureka

Eureka (80.2°N and 273.8°E; geomagnetic coordinates are 87.7°N and 87.17°W as of 2015) is the northernmost Canadian station (see also Figure 3-3). Nighttime measurements of the instrument ERWIN at Eureka are used in the VERA project (in winter nighttime at Eureka means 24 hours).

The ERWIN measures winds in the mesosphere and lower thermosphere (MLT) via Doppler shifts in three nightglow emissions:

- Atomic oxygen green line (557.7 nm) at a height of ~97km
- Molecular oxygen (860 nm) at a height of ~94 km
- Hydroxyl (843 nm) at a height of ~87 km

The available data is meridional, zonal, and vertical winds, and the line-of-sight winds for the north, east, south, and west directions at an angle of 38.7 degrees to the horizon (see Figure 3-9 for viewing geometry). Additionally, the airglow irradiances and visibilities for the five viewing directions are available.

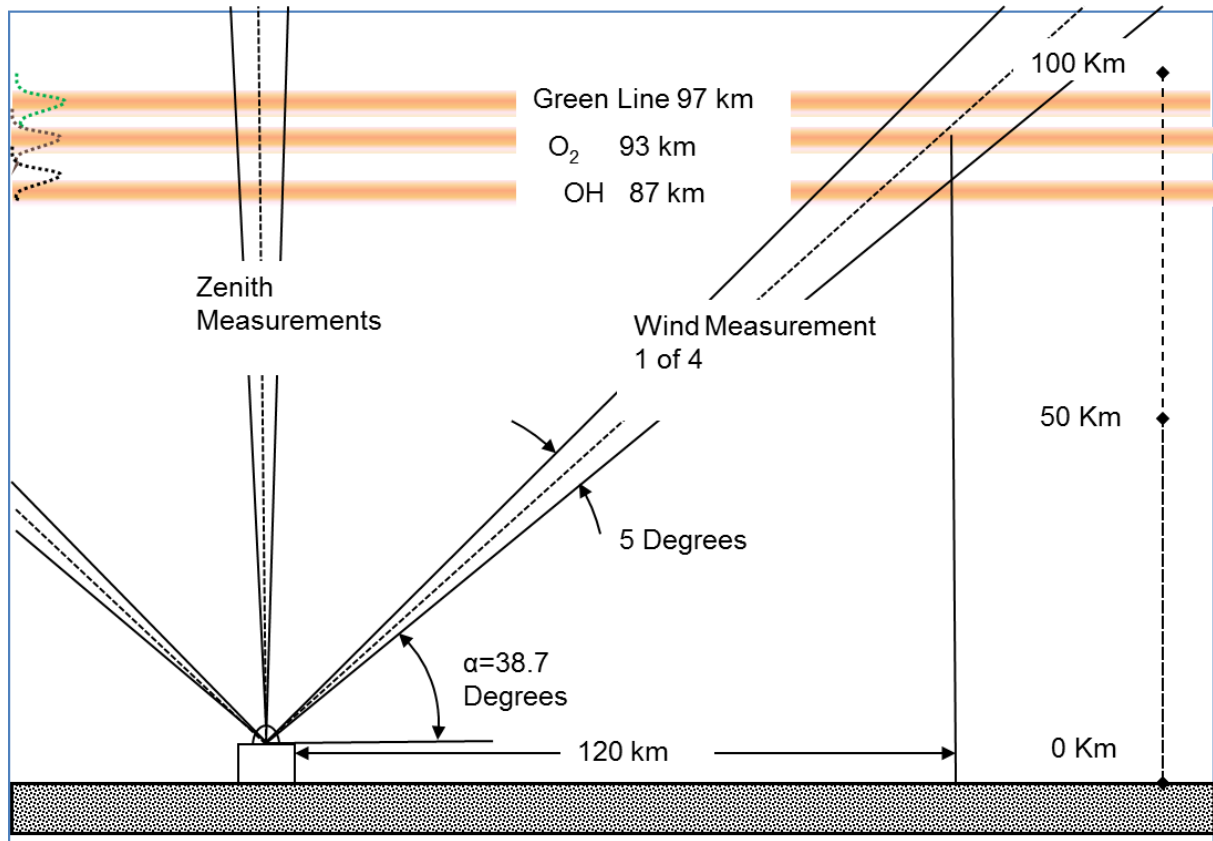


Figure 3-10. Schema of ERWIN measurements.

Standard errors for each line-of-sight wind (north, east, south, west, and vertical) are available, but given in radians. The conversion to m/s is:

$$\sigma_v = \frac{\sigma_\phi c \lambda}{2\pi \Delta}$$

where σ_ϕ is the given standard uncertainty, c is the speed of light, λ is the emission wavelength (see above for values) and Δ is the ERWIN optical path difference (11 cm).

At Eureka there is also red line wind data from a Fabry-Perot interferometer operated by Qian Wu with NCAR. It has wind observations every ~20 minutes.

The ERWIN data are available in text files, at:

- <http://webdata.candac.ca/gocanada/downloads/downloads.php?type=ERWIN>.

The FPI data are available at:

- <http://www.candac.ca/candacweb/content/eureka-fabry-perot-fp-yeu>.

These are freely available, without need for a password or account. The number of days the data are available for each season (= winter) is shown in Figure 3-10. Note: the 2011/2012 season is unavailable as the ERWIN was not operational that season.

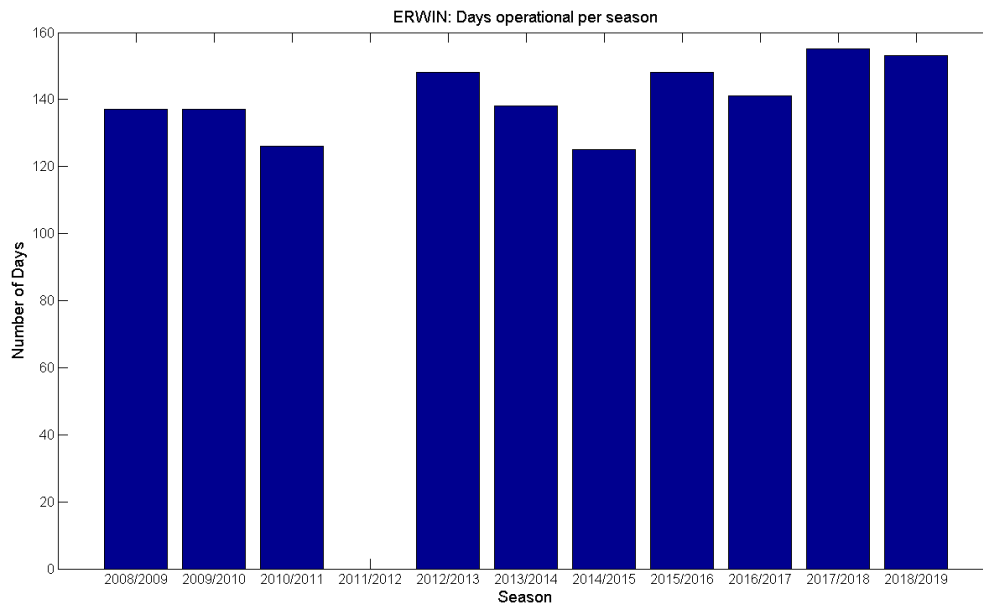


Figure 3-11. Number of days with available ERWIN data in each winter.

3.11.1 Aura satellite data

Geopotential height measurements from the Microwave Limb Sounder (MLS) on the Aura satellite (Schwartz et al., 2008; Waters et al., 2006) are used. Version 4.2 data (DOI:10.5067/Aura/MLS/DATA2008) are available from the Goddard Earth Sciences Data and Information Services Center (Acker and Leptoukh, 2007). Briefly, the Aura/MLS measurements cover the latitude range of $\pm 82^\circ$ and the pressure levels from 261 hPa (~ 9 km) to 0.001 hPa (~ 96 km). The local time coverage is limited as the Aura satellite is in a Sun-synchronous orbit. We use the data from both ascending and descending parts of the orbit, which correspond to ~ 14 LT and ~ 02 LT, respectively.

3.12 Conclusions

This chapter contains information on the basic data to be used in the VERA project and on methods of their measurements. These data are the atmospheric reanalysis ERA5 for determination of SSWs, additional middle atmosphere data from the MERRA-2 reanalysis and Aura satellite for further characterization of SSWs, ground-based observations of the TEC and its rate of change for Europe, Canada and globally, ionospheric parameters from ionosonde measurements in Europe, Canada and with possibility of global extension, Swarm and CHAMP satellite data (electron density, total electron content, equatorial electrojet/equatorial electric field, field-aligned currents), and mesospheric and lower thermospheric neutral atmosphere observations from the northernmost Canadian station Eureka.

The analyses of observational data will be supported by numerical calculations with models E-CHAIM (Empirical Canadian High Arctic Ionospheric Model), TIE-GCM (Thermosphere-Ionosphere-Electrodynamics General Circulation Model) and WACCM-X (Whole Atmospheric Climate Community Model – Extended), which will be described in Chapter 4.

Chapter 4

Models and Data Analysis Methods

4 Models and Data Analysis Methods

4.1 Scope and Outline

The purpose of this chapter is two-fold. One is to introduce physics-based and empirical models that are used in the VERA (Vertical Coupling in the Earth's Atmosphere at mid and high latitudes) project. The other is to describe the methods of data analysis that are used in the VERA project. The model descriptions are given in section 2, while the methods of data analysis are detailed in Section 3. Section 4 gives a summary and addresses the topics within the VERA project for which the introduced models and data analyses techniques are applied.

4.2 Models

This section provides basic information of the models that are used in the VERA project. Models are categorized into two, that is, “physics-based” (or “theoretical”) and “empirical”. The former refers to the models that are based on mathematical equations derived from established laws of physics. The latter refers to the models that are based on fitting of empirical formula to observations.

4.2.1 Physics-based models

4.2.1.1 TIE-GCM

Thermosphere-Ionosphere-Electrodynamics General Circulation Model (TIE-GCM) is a first-principles model of the coupled thermosphere-ionosphere system (Richmond et al., 1992; Qian et al., 2014, and references therein), developed at National Center for Atmospheric Research (NCAR), Boulder CO. The model solves the continuity, momentum, and energy equations on a three-dimensional spatial grid as a function of time. For the VERA project, we use version 2.0.

The model source code is publicly available at:

- <https://www.hao.ucar.edu/modeling/tgcm/>

Also, the model user's guide can be found at:

- <https://www.hao.ucar.edu/modeling/tgcm/tiegcmd2.0/userguide/html/>

The description of the TIE-GCM is given at:

- https://www.hao.ucar.edu/modeling/tgcm/doc/description/model_description.pdf

Since the basic information of the TIE-GCM can be found in the links above, the model is described only briefly herein. The TIE-GCM uses constant pressure surfaces $Z = \ln(P_0/P)$ as the vertical coordinate, where P is pressure and P_0 is a reference pressure of 5×10^{-7} hPa. The lower boundary of the model is $Z=-7$, which corresponds to ~ 97 km altitude. The upper boundary is $Z=7$, which is $\sim 400-700$ km altitude depending on solar flux conditions. The horizontal resolution of the model is $2.5^\circ \times 2.5^\circ$ in geographic longitude and latitude, and the vertical resolution is 4 grid points per vertical scale height. This is sufficient for resolving large-scale waves such as atmospheric tides and planetary waves. For electrodynamics calculations (i.e., electric fields and currents), the model uses the Magnetic Apex coordinate system (Richmond, 1995) based on a realistic geomagnetic field configuration.

Model inputs are summarized in the table below:

Input name	Note
Year	The input is required for the model to specify the geomagnetic main field.
Date (Month/Day)	The input is required for the model to specify the solar zenith angle at each grid point.
Solar flux	The solar flux input is used specify the solar spectrum. The user can provide the daily $F_{10.7}$ index. For a given $F_{10.7}$, the TIE-GCM estimates the solar spectrum based on the EUVAC model (Richards et al., 1994).
Hemispheric power (HP) & cross polar cap potential (CPCP)	HP (in units of GW) and CPCP (in kV) inputs are used to specify the auroral energy flux and high-latitude ion convection pattern. Instead of specifying the HP and CPCP values, the user can provide the 3-hourly K_p index. The model then estimates HP and CPCP based on these empirical formulae: $HP = 16.82 \cdot \exp(0.32 \cdot K_p) - 4.86 \dots \text{ for } K_p \leq 7$ $HP = 153.13 + 73.435 \cdot (K_p - 7) \dots \text{ for } K_p > 7$ $CPCP = 15 + 15 \cdot K_p + 0.8 \cdot K_p^2$ Alternatively, the user can also provide 1-min solar wind parameters, with which the model estimates HP and CPCP.
Lower boundary tides	Tidal perturbations in neutral winds, geopotential height, and temperature at the lower boundary (~97 km) can be specified. In the standard setup, the lower-boundary tides are given by the migrating and nonmigrating solar diurnal and semidiurnal tides from the Global Scale Wave Model (GSWM; Hagan and Forbes, 2002 & 2003). Alternatively, the user can also take tidal perturbations from other models (such as WACCM-X) or satellite observations if available.

Model outputs are summarized in the table below:

Output name	Long name	Units
TN	Neutral temperature	deg K
UN	Neutral zonal wind (positive eastward)	cm/s
VN	Neutral meridional wind (positive northward)	cm/s
O2	Molecular oxygen	mmer
O1	Atomic oxygen	mmer
N4S	$N(^4S)$	mmer
NO	Nitric oxide	mmer
HE	Helium	mmer
AR	Argon	mmer
OP	O^+ ion	mmer
N2D	$N(^2D)$	mmer
TI	Ion temperature	deg K
TE	Electron temperature	deg K
NE	Electron density	cm ⁻³
O2P	O_2^+ ion	cm ⁻³
OMEGA	Vertical motion	s ⁻¹
Z	Geopotential height	cm
POTEN	Electric potential	volts
CO2 COOL	CO ₂ cooling	erg/g/s
NO COOL	NO cooling	erg/g/s
DEN	Total density	g/cm ³
HEATING	Total heating	erg/g/s
HMF2	hmF2 height of the F2 layer	km
NMF2	nmF2 peak density of the F2 layer	1/cm ³
FOF2	foF2 critical frequency of the F2 layer	MHz
JE13D	Eastward current density (3D)	A/m ²
JE23D	Downward current density (3D)	A/m ²

JQR	Upward current density (2D)	A/m ²
KQLAM	Height-integrated current density (positive northward)	A/m
KQPHI	Height-integrated current density (positive eastward)	A/m
LAMDA HAL	Hall ion drag coefficient	1/s
LAMDA PED	Pedersen ion drag coefficient	1/s
MU M	Molecular viscosity coefficient	g/cm/s
QJoule	Joule heating	erg/g/s
SCHT	Pressure scale height	km
SIGMA HAL	Hall conductivity	S/m
SIGMA PED	Pedersen conductivity	S/m
TEC	Total electron content	1/cm ²
UI ExB	Zonal ion drift (ExB)	cm/s
VI ExB	Meridional ion drift (ExB)	cm/s
WI ExB	Vertical ion drift (ExB)	cm/s
WN	Neutral vertical wind (plus up)	cm/s
O N2	O/N ₂ ratio	none
QJoule INTEG	Height-integrated Joule heating	erg/cm ² /s
BX	BX/BMAG normalized eastward component of magnetic field	[none]
BY	BY/BMAG normalized northward component of magnetic field	[none]
BZ	BZ/BMAG normalized upward component of magnetic field	[none]
BMAG	Magnetic field magnitude	Gauss
EX	Zonal component of electric field	V/m
EY	Meridional component of electric field	V/m
EZ	Vertical component of electric field	V/m
ED1	Magnetic eastward component of electric field	V/m
ED2	Magnetic downward (equatorward) component of electric field	V/m
PHIM2D	2D electric potential on magnetic grid	V
N2	Molecular Nitrogen	mmr
ZGMID	Geometric height at midpoints	cm
CUSP	Cusp low energy electron flux	erg/cm ² /s
DRIZZLE	Drizzle low energy electron flux	erg/cm ² /s
ALFA	Aurora characteristic energy	keV
NFLUX	Aurora number flux	#/cm ² /s
EFLUX	Aurora energy flux	erg/cm ² /s

The user can choose the parameters to be output. For the VERA project we mainly use TN, UN, VN and Z from the thermosphere, and NE, HMF2, NMF2, TEC, WI_ExB from the ionosphere.

4.2.1.2 WACCM-X

The Whole Atmosphere Community Climate Model with thermosphere and ionosphere extension (WACCM-X) is a comprehensive numerical model ranging from the surface of the Earth to the upper thermosphere. WACCM-X is a configuration of the NCAR Community Earth System Model (CESM; Hurrell et al., 2013) that extends the atmospheric component into the thermosphere, with a model top boundary between 500 and 700 km depending on the solar and geomagnetic activity. The current release code of CESM is publicly available and can be downloaded from:

- http://www.cesm.ucar.edu/models/cesm2/release_download.html.

Physical processes represented in WACCM-X build upon those in regular WACCM, which has a model top at ~130 km, and in turn is built upon the Community Atmosphere Model (CAM), which goes up to ~40 km. WACCM-X is currently based on CAM-4 physics, as

released in CESM 1.0, and employs a conventional latitude - longitude grid with horizontal resolution of $1.9^\circ \times 2.5^\circ$ (latitude x longitude). The newly released WACCM-X version includes a fully coupled ionosphere, including electric field effects and ion transport in order to self-consistently simulate the coupled atmosphere-ionosphere system (Liu et al., 2018). As a CESM component, WACCM-X is also capable of being run in a configuration where the atmosphere is coupled to active or prescribed ocean, sea ice, and land components, enabling studies of thermospheric and ionospheric weather and climate (e.g., Liu et al., 2018).

The interactive chemistry package of WACCM-X is derived from the Model for Ozone and Related Chemical Tracers (MOZART) (Kinnison et al., 2007) that comprises of 87 photolysis and photoionization reactions and 202 gas phase and heterogeneous reactions. In the development of WACCM-X, two metastable O^+ states, $O^+(2D)$ and $O^+(2P)$, were added to the chemistry package, which already includes 5 ions (O^+ , O_2^+ , NO^+ , N^+ , and N_2^+), electrons, and 74 neutral species (Liu et al., 2018).

Being a coupled model, WACCM-X enables more realistic simulation of upper atmospheric variability due to lower atmospheric forcing and better understanding and quantification of space weather and space climate as compared to TIE-GCM. To study the lower atmospheric forcing impacts on the thermosphere and ionosphere for particular time intervals, WACCM-X has an option to constrain the tropospheric and stratospheric dynamics using meteorological reanalysis datasets. This WACCM-X configuration is called as the “specified dynamics” or more commonly as SD-WACCM-X. In this configuration, temperature, zonal, and meridional winds up to ~ 50 km and surface pressure are relaxed toward the NASA Modern Era Retrospective Analysis for Research and Applications (MERRA; Rienecker et al., 2011).

For the VERA project, we produce hourly outputs of temperature (T), zonal wind (U), meridional wind (V), geopotential height (Z), electron density (e), vertical $E \times B$ drift (WI) from the WACCM-X runs for the specified time intervals.

4.2.1.3 TIE-GCM/WACCM-X

For the inclusion of lower atmospheric forcing into the TIE-GCM model we force its lower boundary ($Z = -7$; approximately at 97 km altitude) with the WACCM-X model outputs. We use the hourly outputs of geopotential height, temperature, and winds (e.g., Maute et al., 2017) from WACCM-X at ~ 97 km altitude to incorporate the lower atmospheric forcing conditions that are representative of any particular time period. With this method, the temporally varying zonal mean, planetary waves, migrating and non-migrating tides propagating from below are included at the TIE-GCM lower boundary.

In the default TIE-GCM lower boundary (LB) background, the neutral temperature is set to latitudinally invariant values of 181 K, the geopotential height to $z = 96.37$ km, and the horizontal winds to zero. Jones et al., 2014 found that the default TIE-GCM LB background fails to capture significant latitudinal and seasonal variations in the thermosphere-ionosphere system as compared to the case when the neutral temperature and wind climatology from Mass Spectrometer Incoherent Scatter Radar Extended (MSISE00) (Picone et al., 2002) and the horizontal wind model (HWM07) (Drob et al., 2008) were included in the TIE-GCM LB. With the use of WACCM-X outputs at the TIE-GCM LB, the variability of lower atmospheric forced planetary waves and tides for a particular time interval is incorporated. The TIE-GCM model is then run as described in **4.2.1.1**.

The TIE-GCM run that we have employed in this work uses the setup in which the magnetospheric forcing in the model has been switched off. This effectively means that ionospheric variability resulting only due to lower atmospheric forcing is produced from the TIE-GCM model. The setup that disables magnetospheric forcing is easier to implement in a standalone model such as TIE-GCM rather than in a coupled model such as WACCM-X. For these reasons, we are using the WACCM-X outputs to force the TIE-GCM model.

4.2.2 Empirical model

4.2.2.1 E-CHAIM

E-CHAIM is an empirical, climatological model intended as an alternative to the use of the International Reference Ionosphere (IRI) model at high latitudes (Themens et al., 2017; 2018; 2019). To this end, the model represents ionospheric electron density in the region above 50°N geomagnetic latitude. The model is composed of several sub-models, each representing a key feature in the ionospheric electron density profile. Like the IRI, NmF2 and hmF2 are chosen as the anchor point of the profile, with all other components representing characteristics with respect to the F2 peak density and height. Each of these sub-models feature a spherical cap harmonic expansion in the new Altitude-Adjusted Corrected Geomagnetic (AACGM) coordinates of Shepherd (2014), calculated at 350km altitude, for the representation of the horizontal structure of the modelled parameter. The order and degree of this expansion is determined experimentally, based on the amount, distribution, and quality of available data. The seasonal variability is modelled by a Fourier expansion and solar cycle variability is modelled via a function of solar F10.7 cm flux and IG ionospheric index. Furthermore, E-CHAIM's topside and bottomside models use Auroral Electrojet (AE) index to model storm-time ionospheric behaviour and the NmF2 model includes a storm parameterization driven by AE, Dst, and ap geomagnetic indices. The model is presented in Themens et al. (2017).

The E-CHAIM source code in Matlab, C, and IDL is openly available at:

- <https://e-chaim.chain-project.net>.

E-CHAIM requires the use of an account. These accounts are automatically authorized without any restriction. Interested parties may also use the web interface without the need for an account.

4.3 Data Analysis Technique

4.3.1 Ionosphere data analysis

Ionosondes are special radars measuring electron densities (height profile of electron densities) from the lower ionosphere up to the height of its electron density maximum by sounding through radio impulses of various frequencies. The ionospheric sounders used in Europe are predominantly digital ionosondes (digisondes) DPS-4 or DPS-4.5, while those used in Canada are Canadian Advanced Digital Ionosondes (CADIs). The main product of a sounding is an ionogram, which is used to derive the electron density profile of the ionosphere. The DPS Digisondes use automatic evaluation by the ARTIST automatic “scaling” software (e.g., Galkin et al., 2008), which is sufficiently accurate for operational use but for scientific investigations, particularly in the case of ionospheric disturbances and

perturbations, the results of ARTIST have to be manually verified. The CADI ionograms used in the VERA project are interpreted manually by D.R. Themens and inverted into electron density profiles using the Polynomial Analysis software tool (Titheridge, 1988). Figure 3.2 shows an ionogram and the related critical frequency profile from Pruhonice station in central Czechia.

DPS Digisondes and CADIs also measure ionospheric plasma drifts. If there are enough reflection points, it is possible to simultaneously measure drifts separately in different ionospheric layers, such as the F, E and sporadic-E layers (Grant et al., 1995). For this work, we have included newly developed quality control measures in addition to the standard automatic built-in evaluation of drifts - skymap point selection method (Kouba et al., 2008). The method consists of a three-step selection of skymap points and application of the standard on the corrected skymaps: (i) robust height range selection, (ii) setting limits on the Doppler frequency shift, and (iii) setting limits on the echo arrival angle. This selection method guarantees a better quality of obtained drift velocities.

Ionosonde data allow for the analysis of planetary wave-like activity, usually by applying a wavelet transform of some form. For example, in the past such analyses studied the characteristic duration of planetary wave events in foF2 over Europe (Laštovička et al., 2003), while others have specified vertical coupling between the stratosphere and ionospheric sporadic-E layer in the planetary wave period range (Mosna and Koucka Knizova, 2012).

4.3.2 Wave analysis of Eureka data

The Eureka data consists of the E-Region Wind Interferometer (ERWIN-II) providing neutral winds and airglow brightness at 87 to 97 km; the Spectral Airglow Temperature Imager (SATI) providing neutral atmosphere temperatures and airglow brightness at 87 to 94 km; and a Fabry-Perot interferometer which provides neutral winds at approximately 250 km. The bulk of this wave analysis will be done using the ERWIN-II wind data. The viewing geometry, and operational methodology is described in Chapter 3, and in Kristoffersen et al. (2013).

The waves are identified using an S-transform, and a Lomb-Scargle periodogram, with the frequency determined from the Lomb-Scargle periodogram. It is assumed that the waves follow the form of

$$A \cos(kx + ly - \omega t + \phi),$$

where A is the amplitude, k is the zonal wave number, l is the meridional wave number, x is the zonal position, y is the meridional position, ω is the angular frequency of the wave, t is time, and ϕ is the phase of the wave. The amplitude, and phase of the waves are then determined using a least-mean squares fit to four line of sight (LOS) wind observations. The relative phase offsets (and nominal layer heights) are used to determine the zonal and meridional wavelengths, given the viewing geometry. This approach can be used to identify and characterize tides, planetary waves, and gravity waves.

In addition to this wave characterization, the gravity wave activity can be determined through the variance of the wind observations. Gravity waves will result in an increase in the variability of the observed winds. To isolate the gravity wave variance, a 4-hour running mean is subtracted from the meridonal and zonal wind observations. This running mean

removes the longer scale waves (e.g. planetary waves) from the observations, with the remaining variability due to gravity waves. Thus, the daily variance of the winds (with running mean subtracted) provides an estimate for the gravity wave activity for that day.

4.3.3 Wave analysis of satellite and model data

4.3.3.1 Zonal wavenumber analysis

In contrast to data from a ground station, satellite and model data include the information about spatial variations as well as temporal variations of the atmosphere/ionosphere. Such data enable to simultaneously determine the frequency and zonal/meridional structures of the variations. A global-scale wave can be expressed as:

$$A \cos \left[2\pi \left(\frac{t}{T} + s\lambda - \phi \right) \right]$$

where A is the amplitude of the wave, t is the universal time (in days), T is the period of the wave (in days), s is the zonal wave number of the wave, λ is the longitude (in degrees), and ϕ is the phase of the wave. For tidal waves, $T = 1$ for diurnal tides, $T = 1/2$ for semidiurnal tides, $T = 1/3$ for terdiurnal tides, and so on. For traveling planetary waves, typically $T = 2-20$. Westward- and eastward-propagating waves correspond to $s > 0$ and $s < 0$, respectively, and stationary waves correspond to $s = 0$. For a given combination of (T, s) , the amplitude and phase of the wave can be determined by least-squares fitting the formula above to the data collected at a certain latitude.

The table below summarizes the tidal and planetary waves that are commonly observed in the atmosphere/ionosphere:

Period T (in days)	Zonal wave number s	Known as	Features	Examples
1	1	Migrating solar diurnal tide, or DW1	Atmospheric tide; the most dominant tidal mode throughout the atmosphere	McLandress et al. (1996), Wu et al. (2008), Gan et al. (2014)
0.5	2	Migrating solar semidiurnal tide, or SW2	Atmospheric tide; the second most dominant tidal mode	Zhang et al. (2006), Chang et al. (2013)
1	-3	Eastward-propagating solar diurnal tide with wave number 3, or DE3	Atmospheric tide; the primary cause of the ionospheric “wave-4” longitudinal structure	Forbes et al. (2003), Immel et al. (2006)
~2	3	2-day wave, or quasi-2-day wave (Q2DW)	Traveling planetary wave; mixed Rossby-gravity mode	Moudden and Forbes (2014), Chang et al. (2011)
~6	1	5-day wave, 6.5-day wave, or quasi-6-day wave (Q6DW)	Traveling planetary wave; First symmetric Rossby normal mode	Pancheva et al. (2018), Gu et al. (2014a)
~10	1	10-day wave, or quasi-10-day wave (Q10DW)	Traveling planetary wave; First asymmetric Rossby normal mode	Forbes et al. (2015), Yamazaki and Matthias (2019)

~16	1	16-day wave, or quasi-16-day wave (Q16DW)	Traveling planetary wave; Second symmetric Rossby normal mode	McDonald et al. (2011), Forbes and Leveroni (1991)
~3	-1	Ultra-fast Kelvin wave (UFKW)	Equatorial Kelvin mode	Forbes et al. (2009), Gu et al. (2014b)

In the ionosphere, the amplitude and phase strongly depend on local solar time. For this reason, Swarm ionospheric products (e.g., electron density and total electron content) need to be analyzed separately for ascending and descending parts of the orbit. In the middle atmosphere, on the other hand, the local-time dependence of a wave can be ignored.

Since Swarm slowly precesses in local solar time, it is difficult to resolve short-time variability of solar tides (e.g., DW1, SW2, and DE3). Model data and ground-based ionospheric measurements are more suitable for studying the response of solar tides to sudden stratospheric warmings (SSWs).

For traveling planetary waves, we use the time window that is 3 times the wave period. Traveling planetary waves are usually observed as bursts of wave activity, which typically last 3-4 wave cycles (Laštovička et al., 2003). We limit the wave analysis for the period range $T = 3-10$ d. For $T = 10$ d, the analysis time window is 30 d, within which the local solar time of Swarm changes by ~ 2.5 h. Thus, for longer period waves, it becomes more difficult to ignore the change of the local solar time within the analysis time window.

4.3.3.2 Lunar tidal analysis for Swarm and CHAMP data

Atmospheric lunar tides are global-scale oscillations of the atmosphere with periods of harmonics of a lunar day. Among various modes with different periods and zonal wavenumbers, by far largest is the migrating semidiurnal mode, known as M2. As detailed in Chapter 2, M2 is known to play an important role for low-latitude ionospheric variability during SSWs. In the VERA project, we also pay special attention to M2 effects on the low-latitude ionosphere.

Swarm (also CHAMP) completes a 12h lunar-time sampling approximately every 13.3d. In other words, M2 has an apparent period of 13.3d in Swarm (or CHAMP) ionospheric data collected at a fixed latitude and local time. We use the technique of Park et al. (2012) to Swarm and CHAMP equatorial electrojet (EEJ) data. Briefly, the EEJ data are first normalized using the following formula:

$$EEJ' = \frac{EEJ}{\sqrt{\frac{F_{10.7}}{200} \left| \cos \left\{ \frac{\pi}{12} (LT - 12) \right\} \right|}}$$

where EEJ' is the normalized EEJ intensity, $\overline{F_{10.7}}$ is the 81-day average of daily $F_{10.7}$ index, LT is the local solar time. The purpose of this normalization is (1) to mitigate daily variations due to diurnally-varying ionospheric conductivities and (2) to mitigate the effects of solar activity cycle (~ 11 years) and solar rotation (~ 27 days). Next, the wavelet analysis of Torrence and Compo (1998) is applied to the EEJ' data to evaluate the 13-day modulation of the EEJ and thus the M2 modulation of the EEJ. We also apply the lunar tidal analysis to the Swarm inter-hemispheric field-aligned current (IHFAC) data, but without the normalization.

4.4 Conclusions

This chapter describes the models, including both physics-based and empirical, that are used in the VERA project. The model configurations are selected to be optimal for investigating SSW effects on the high-latitude ionosphere. For instance, using TIE-GCM/WACCM-X simulations without magnetospheric forcing, one can evaluate the effect of upward-propagating waves on the high-latitude ionosphere. At the same time, the E-CHAIM can empirically predict magnetospheric forcing influences on the high-latitude ionosphere. These model results can help us interpret observations. This document also describes the methods of data analysis employed in the VERA project. Wave analysis techniques can reveal which type of atmospheric waves plays a role in vertical atmospheric coupling during SSWs.

Chapter 5

Model Validation and Comparison with Observations

5 Model Validation and Comparison with Observations

5.1 Scope and Outline

This document describes the validation of the models as well as the validity of the model results compared to observations from models used for the VERA project. A significant component of the VERA study is the comparison of observations with an empirical model (E-CHAIM, Themens et al., 2017, 2018, 2019) and sophisticated first-principles models (TIE-GCM, Qian et al., 2014, and WACCM-X, Liu et al., 2018) and the use of these models to explore the causal relationship associated with observed coupling. Since the lower atmosphere of WACCM-X is driven by reanalysis data, the upward propagating disturbances, which affect the upper atmosphere and ionosphere are expected to be reasonably well simulated on the larger temporal and spatial scales.

In this document, the model validation is undertaken through comparisons between model simulations of conditions during the 2009 SSW as well as two other warmings which took place in early 2018 and 2019. The 2009 SSW is the strongest one to have taken place in the last two decades and observations of the atmosphere and ionosphere and the observed coupling between the two have motivated much of the research on this topic over the past decade. The peak of the stratospheric temperature enhancement associated with this warming took place on 25 January 2009. Associated with this warming was a cooling in the mesosphere, a warming of the polar thermosphere and modifications of semi-diurnal tidal signatures throughout the atmosphere and ionosphere. The SSWs in 2018 and 2019 were less robust.

This document is organized as follows. The first section (5.2) following this introduction, deals with the validation of WACCM-X and the TIE-GCM. The WACCM-X simulation of the 2009 SSW is summarized and the approach to using it to define the lower boundary of the TIE-GCM is summarized. The TIE-GCM and WACCM-X semi-diurnal tides, $E \times B$ drift and total electron content are compared to each other and observations for the same event reported in the literature. Results for runs for the 2018 and 2019 warmings are also presented and the modelled TEC. The section closes with a comparison between WACCM-X results in the polar mesopause region and observations with the E-Region Wind Interferometer. This comparison provides an indication of the extent to which the larger scale variations and smaller scale variability of the real atmosphere is simulated by the models.

The next section (5.3) describes the validation of WACCM-X and E-CHAIM with respect to observations during the 2009 warming period. Comparisons are made between the simulations with WACCM-X, E-CHAIM and ionospheric electron density observations from ionosondes, GNSS, and Incoherent Scatter Radar. A short concluding section completes this chapter.

5.2 Validation of the TIE-GCM and WACCM-X

5.2.1 Simulating the 2009 SSW with SD-WACCM-X

The 2009 SSW event has been simulated using the “Specified Dynamics (SD)” setup of the Whole Atmosphere Community Climate Model extended Version (WACCM-X). In this setup, the winds and temperatures are constrained at each model time step from 0-50 km

toward the National Aeronautics and Space Administration (NASA) Modern-Era Retrospective Analysis for Research and Applications (MERRA) meteorological fields (Kunz et al., 2011). Between 50-60 km altitude, the constraint on the model is linearly relaxed to zero and above 60 km the model is free-running. This configuration of WACCM-X has been used to investigate the dynamical variability during SSWs (e.g., Pedatella et al., 2014a).

Figure 5-1 presents the zonal mean temperature averaged between 70 and 80°N during January-February 2009 from Aura Microwave Limb Sounder (MLS) observations (Figure 5-1a) and from SD-WACCMX simulations (Figure 5-1b). The stratopause starts to descend from its usual levels between 0.1–1 hPa to below 10 hPa after day 15. After the peak warming around day 25, the stratopause vanishes and then reappears again around day 35 at a much higher altitude. SD-WACCMX reproduces this elevated stratopause event along with the mesospheric cooling that occurs simultaneously with the warming of the stratosphere.

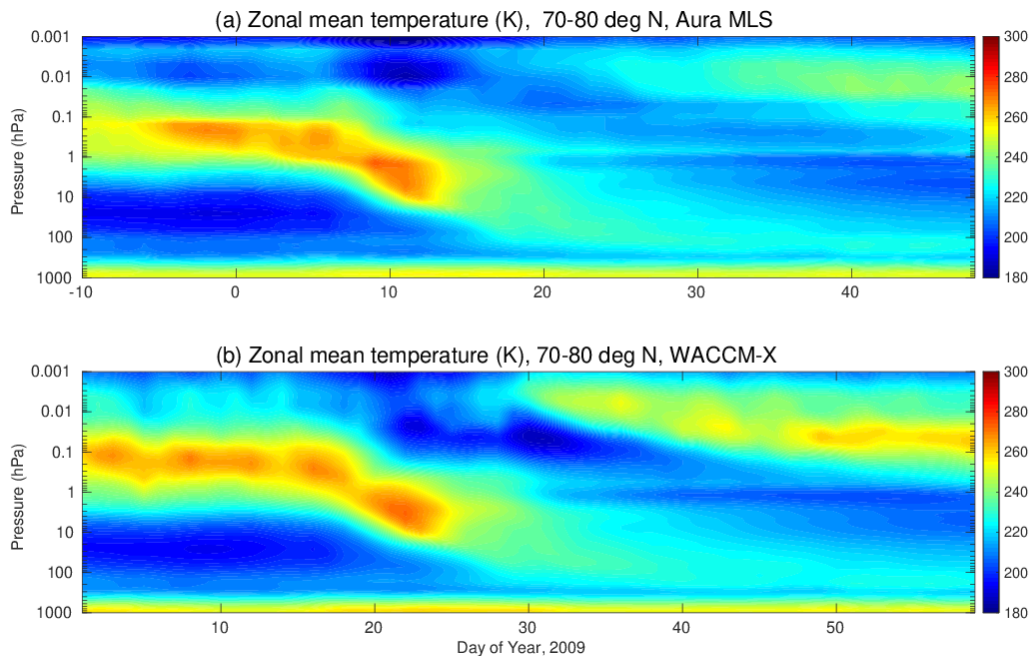


Figure 5-1. Zonal mean temperature (K) averaged between 70 and 80°N as a function of time and pressure are presented for (a) Aura MLS, (b) WACCM-X.

Figure 5-2 presents the zonal mean zonal wind at 60°N between January and February, 2009. The main features of the SSW have been well reproduced with the descent of the zonal mean westward wind from mesospheric to stratospheric altitudes around day 20. The reversal of the wind continues to lower altitudes and reaches up to 100 hPa around day 50.

5.2.2 Using WACCM-X outputs as input to the TIE-GCM lower boundary

In our simulation of the 2009 SSW using WACCM-X, the ionosphere-magnetosphere coupling is present. To switch off this coupling and investigate only the impact of lower atmospheric forcing on the thermosphere-ionosphere region, we utilize the Thermosphere Ionosphere Electrodynamics General Circulation Model (TIE-GCM) model. Unlike the

coupled WACCM-X model, the TIE-GCM is a standalone model, which makes it easier to implement modified runs without destabilizing the model in comparison with WACCM-X. The lower atmospheric forcing is incorporated into the TIE-GCM lower boundary by using the hourly WACCM-X outputs of geopotential height, meridional wind, zonal wind and temperature at 97 km altitude.

By using this simulation method of forcing the TIE-GCM lower boundary with WACCM-X outputs we are able to make some control runs in which we can completely turn off the magnetospheric forcing in TIE-GCM and investigate only the impact of lower atmospheric forcing on the thermosphere-ionosphere system.

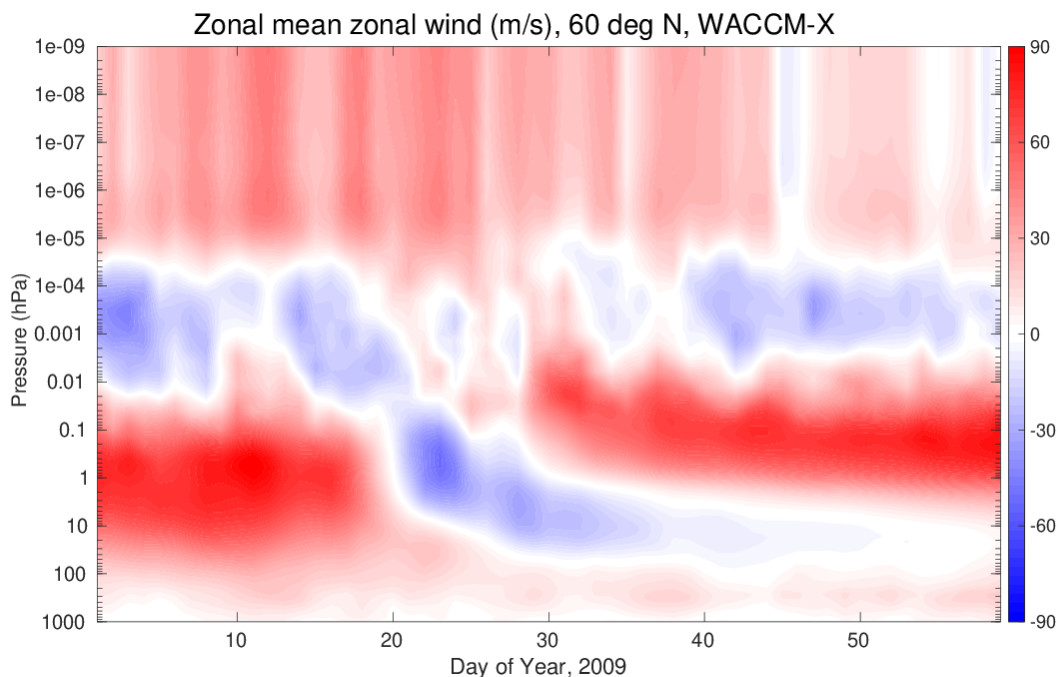


Figure 5-2. Zonal mean zonal wind (m/s) at 60°N as a function of time and pressure are presented from the WACCM-X simulation.

5.2.2.1 Semidiurnal tides from WACCM-X and TIE-GCM simulations

Figures 5-3a and 5-3b present the amplitudes of migrating solar semidiurnal tide (SW2) and migrating semidiurnal lunar tide (M2), respectively, at 110 km altitude during the 2009 SSW obtained from WACCM-X simulation. Figures 5-4a and 5-4b present the same but from the TIE-GCM simulation.

On comparing the tidal variability in both the simulations, we find that the variability of SW2 and M2, individually, look similar in both the simulations. The amplification of SW2 happens before and after the peak day of SSW (shown in bold white line) while the M2 enhancement happens around the peak SSW day.

The SW2 variability in Figure 5-3a and Figure 5-4a shows relative weakening in amplitude in the Southern Hemisphere around the peak day of SSW. This SW2 weakening has also been

found in different whole atmosphere models from the results of Pedatella et al. (2014a) in case of the 2009 SSW event.

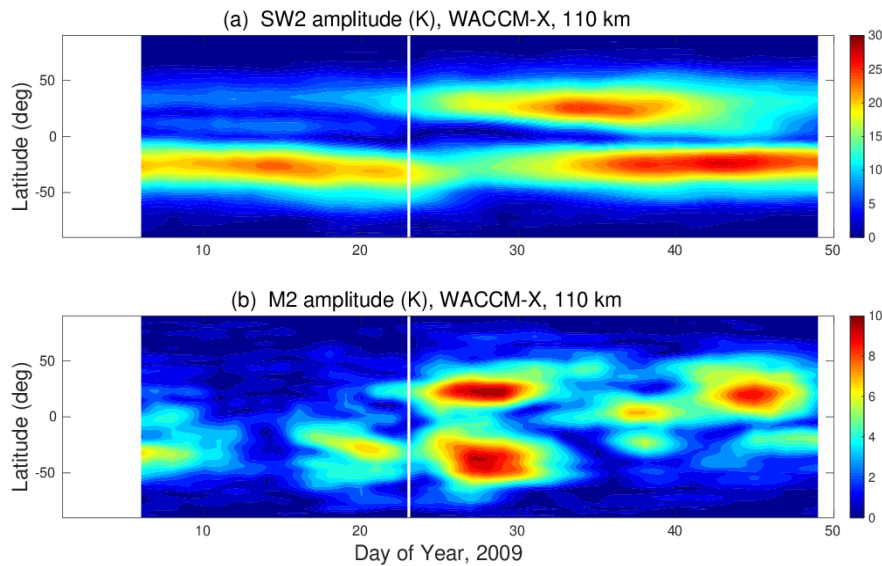


Figure 5-3. The top panel (a) presents the SW2 amplitude in neutral temperature at 110 km and the bottom panel (b) presents the M2 amplitude in neutral temperature at the same altitude from the WACCM-X simulation.

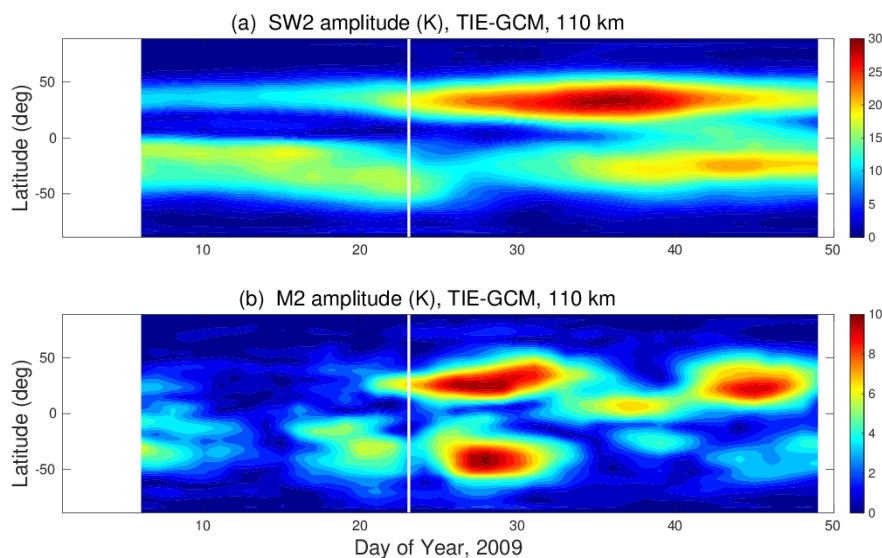


Figure 5-4. The top panel (a) presents the SW2 amplitude in neutral temperature at 110 km and the bottom panel (b) presents the M2 amplitude in neutral temperature at the same altitude from the TIE-GCM simulation.

Figure 5-5 and Figure 5-6 present the SW2 and M2 tidal amplitudes in zonal wind at 120 km altitude from WACCM-X and TIE-GCM simulations, respectively. The M2 variability in both the simulations (Figures 5-5b and 5-6b) during the 2009 SSW event look similar with the M2 amplitudes differing only slightly. The M2 enhancement around days 25 and 30 is clearly captured in both the simulations.

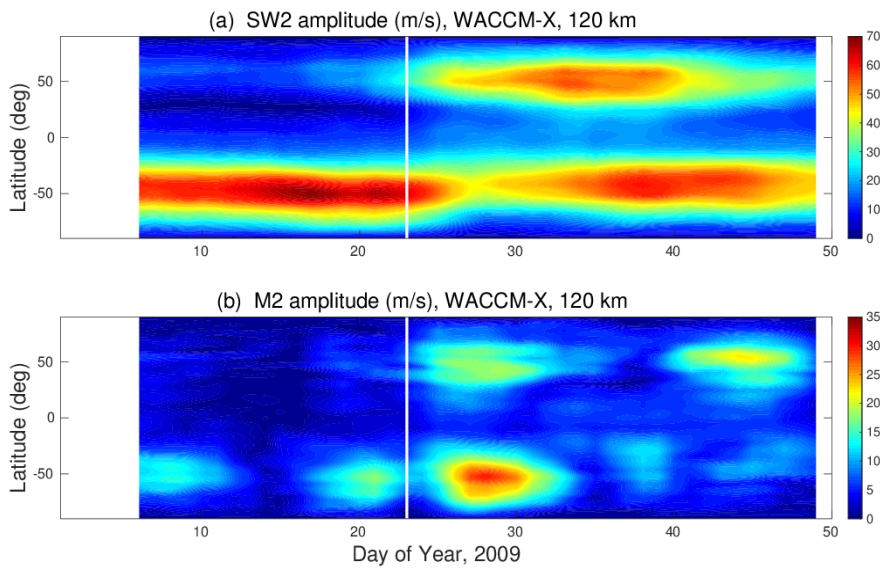


Figure 5-5. The top panel (a) presents the SW2 amplitude in zonal wind at 120 km and the bottom panel (b) presents the M2 amplitude in zonal wind at the same altitude from the WACCM-X simulation.

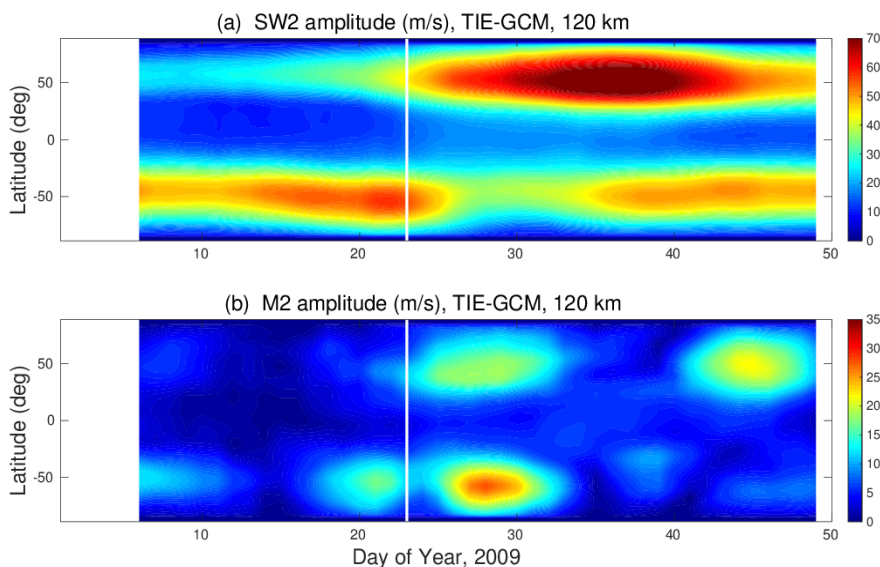


Figure 5-6. The top panel (a) presents the SW2 amplitude in zonal wind at 120 km and the bottom panel (b) presents the M2 amplitude in zonal wind at the same altitude from the TIE-GCM simulation.

In case of the SW2 variability, the SW2 enhancement before and after the peak SSW date (following the definition of polar vortex weakening by Zhang and Forbes (2014) and denoted here by white line) is captured in both the simulations. The weakening of SW2 is also seen in both the simulations, albeit a bit prolonged in the TIE-GCM simulation. From the two simulations, the SW2 amplitude is found to be stronger in the TIE-GCM simulation as compared to those from WACCM-X and this is likely to be due to the damping of tides in WACCM-X (Liu et al., 2018).

5.2.2.2 Vertical $E \times B$ drifts from WACCM-X and TIE-GCM simulations

Figure 5-7 shows the changes in the vertical $E \times B$ drifts at $75^\circ W$, $12^\circ S$ for WACCM-X and TIE-GCM simulations for the first 60 days of 2009. The changes in $E \times B$ drifts have been calculated by removing the hourly means over the entire 60 days period for each local time.

This particular location has been chosen to compare the simulations with the observational $E \times B$ drifts obtained from the Incoherent Scatter Radar at the Jicamarca Radio Observatory during the 2009 SSW. These two plots can be compared to the observations from the results shown in Pedatella et al., 2014b (see their Figure 3c). Here again we find that the variability of $E \times B$ drifts is produced similarly in both the simulations.

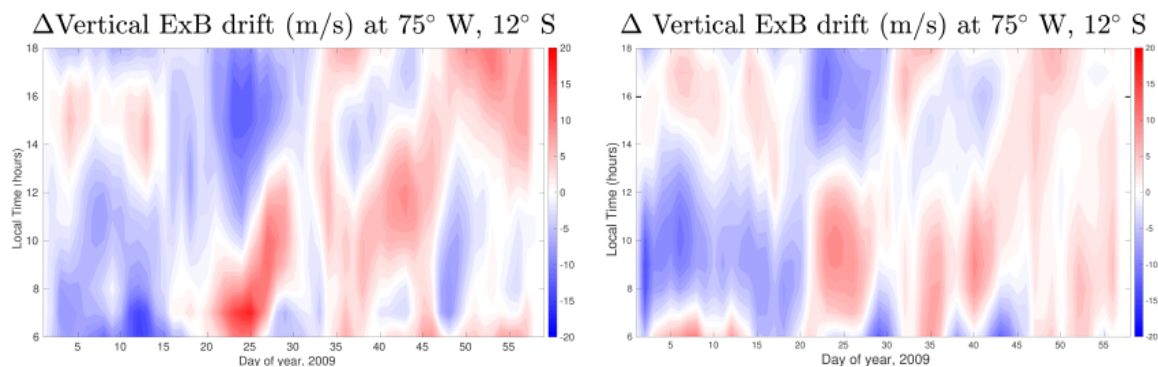


Figure 5-7. Changes in the vertical $E \times B$ drifts at $75^\circ W$, $12^\circ S$ for (left) WACCM-X and (right) TIE-GCM simulations.

5.2.2.3 TEC from TIE-GCM simulations and GPS observations

Figure 5-8 presents the Total Electron Content (TEC) at $75^\circ W$ and 18 LT from the TIE-GCM simulation and GPS observations. The plot of TEC from GPS observations has been adapted from Pedatella et al., (2014b). The black dashed line denotes the peak SSW day.

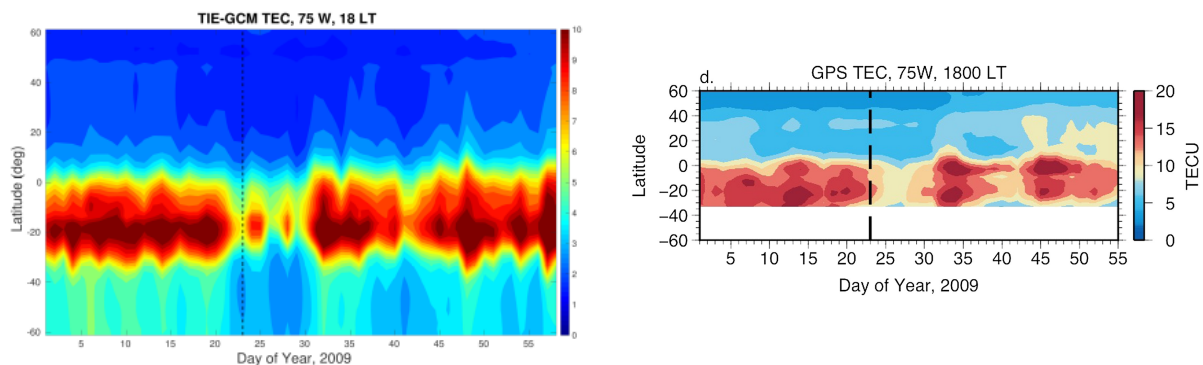


Figure 5-8. Total Electron Content (TEC) in TECU at $75^\circ W$ for (left) TIE-GCM and (right) GPS observations, adapted from Pedatella et al. (2014b).

From the simulation results, we find that the TEC variability is generally well reproduced and is consistent in comparison with the observation. The weakening of TEC is well reproduced in the TIE-GCM simulation around the peak day of SSW around the low- and mid-latitudes. The enhancement of TEC before and after the peak SSW day also seems to agree with the observations.

As a brief summary, we have validated the TIE-GCM simulation, which is forced at its lower boundary with the WACCM-X hourly outputs, with observations and other similar modeling.

5.2.3 Simulating the 2018 and 2019 NH major SSWs using WACCM-X

The 2018 and 2019 SSWs have been simulated using WACCM-X. Figure 5-9 shows the zonal mean temperature and zonal mean zonal wind over the polar region for the first two months of 2018. In the top panel of Figure 5-9, the zonal mean temperature averaged between 70 and 80°N is presented. The descent of the stratopause, denoting the SSW conditions, can be observed between days 40 and 50. The bottom panel of Figure 5-9 shows the zonal mean zonal wind at 60°N. The reversal of the zonal mean zonal wind from eastward to westward direction around 10 hPa can be observed again between days 40 and 50 during the occurrence of the SSW.

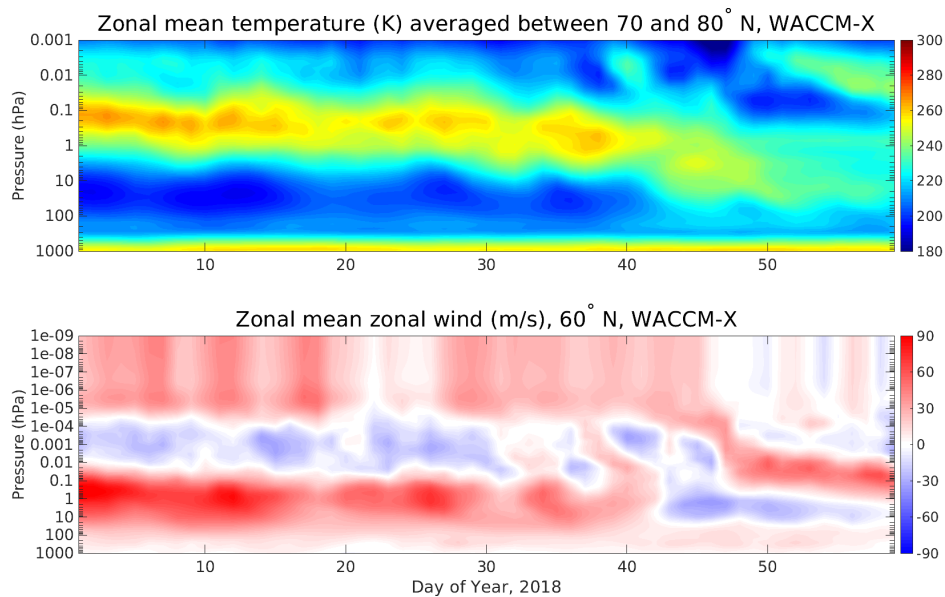


Figure 5-9. Zonal mean temperature (K) averaged between 70 and 80°N as a function of time and pressure are presented in the top panel (a) while in the bottom panel (b), zonal mean zonal wind at 60°N is presented from the WACCM-X simulation for the 2018 SSW.

The top panel in Figure 5-10 shows the zonal mean temperature averaged between 70 and 80°N and the bottom panel shows the zonal mean zonal wind at 60°N between December 2018 and January 2019. The occurrence of SSW started around day -10 as can be seen with the descent of stratopause in Figure 5-10a. The SSW conditions persisted till day 15. The reversal of zonal mean zonal wind around 10 hPa from eastward to westward can also be seen between days -10 and 15.

5.2.4 WACCM-X vs GPS observations of TEC for 2018 and 2019 SSWs

Figure 5-11 shows the average TEC over Europe as a function of day of year and Universal Time (UT) from WACCM-X simulations and GPS observations for the first two months of 2018.

The left side of Figure 5-11 shows the TEC over Europe from WACCM-X. The white line in this plot shows the day of the peak SSW day. The right side of Figure 5-11 shows the TEC

over Europe from GPS observations. There is a good consistency between the modeling and observation results. The TEC enhancement around day 45 as seen in the GPS data is well reproduced in WACCM-X but the magnitude of TEC from WACCM-X is approximately half of that seen from GPS data. This is expected as the top boundary of WACCM-X only extends up to ~ 750 km.

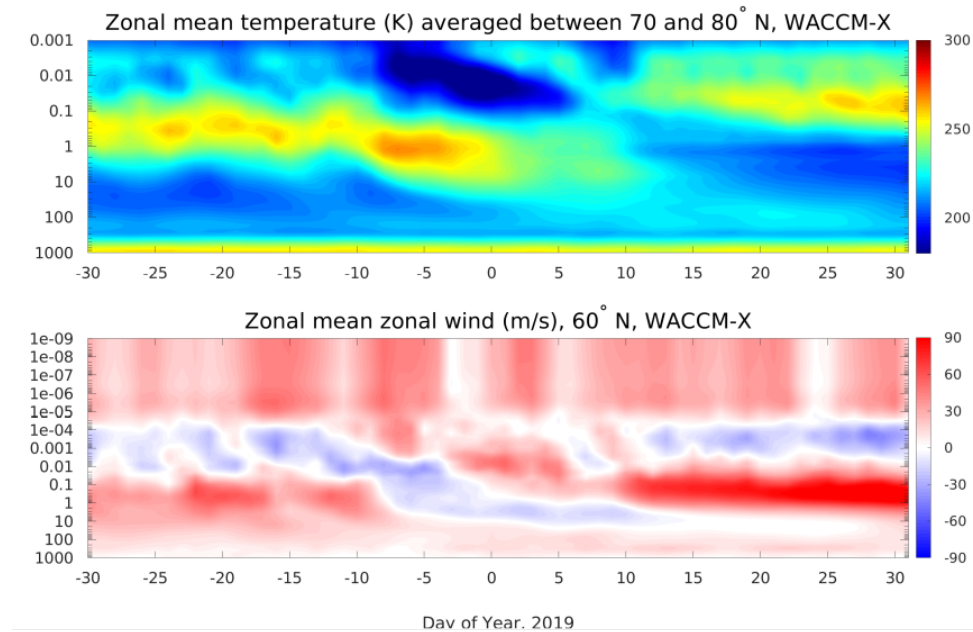


Figure 5-10. Same as Figure 5-9 but for 2019 SSW.

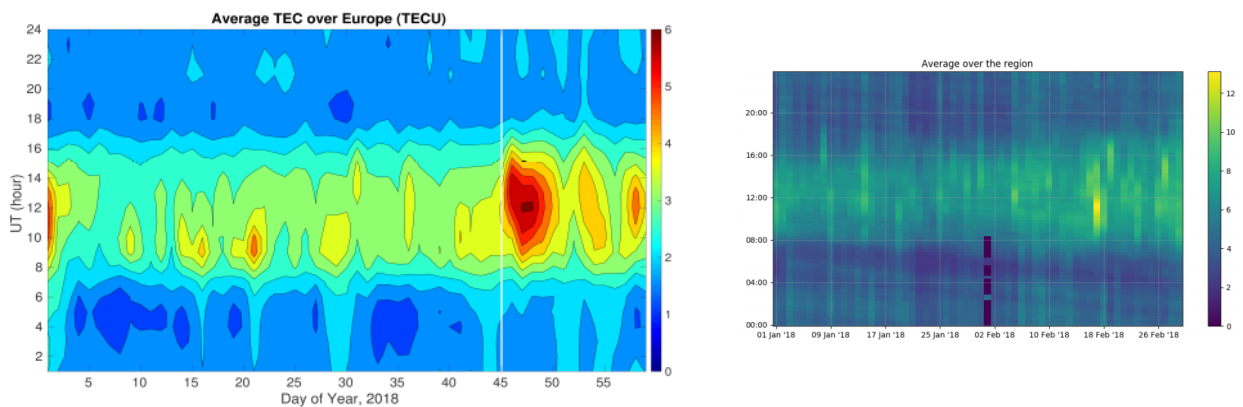


Figure 5-11. Average TEC over Europe from (left) WACCM-X and (right) GPS observations for 2018 SSW.

Figure 5-12 shows the average TEC over Europe as a function of day of year and Universal Time (UT) from WACCM-X simulations and GPS observations between December 2018 and January 2019. We observe again that there is an enhancement in the TEC around the peak SSW day towards the end of December. This enhancement seen in the TEC over Europe from GPS observations have been well reproduced in WACCM-X but with a lesser magnitude.

From our results, we find that WACCM-X is capable of reproducing the variability in the ionosphere associated with the SSWs.

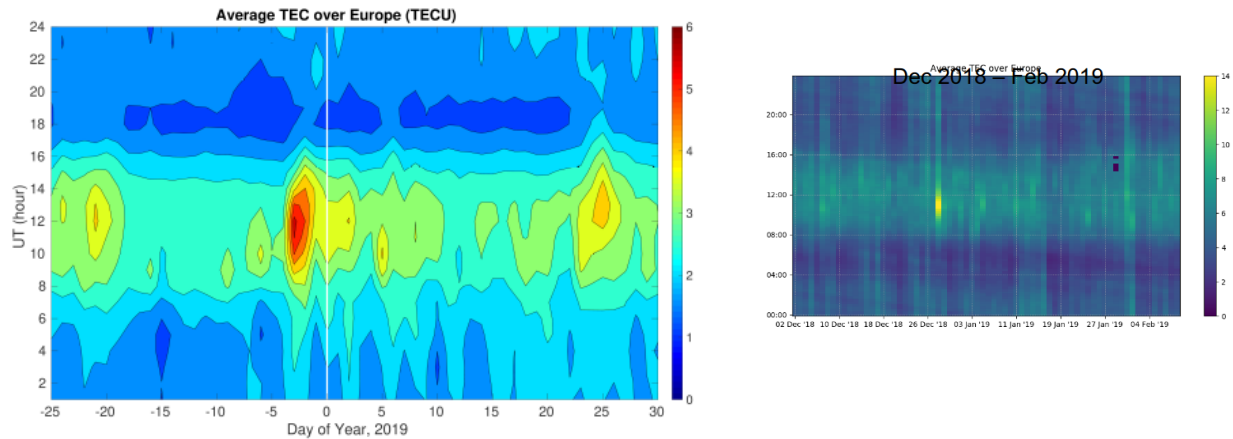


Figure 5-12. Same as Figure 5-11 but for 2019 SSW.

5.2.5 WACCM-X vs Eureka data for 2009 SSW

The E-Region Wind Interferometer is described in the previous chapter of this report. It provides observations of winds at the mesopause region at Eureka, Nu (80°N, 85°W) in the Canadian High Arctic on a ~5-minute cadence. Comparisons of these observations with WACCM-X winds at this latitude for the warming period provide an indication of the degree to which the modelled dynamical conditions at the mesopause match observations. Two aspects of the comparison are of interest. The first is whether the longer-term variations (days to weeks) in the model winds match those observed. The second is whether shorter-term variability matches the observations. As gravity waves play a significant role in the coupling, this comparison is important. However, it must be noted that some of the gravity wave variability in the model is associated with the gravity wave parameterization and will not manifest at the smallest temporal and spatial scales.

Figure 5-13 shows time series (brown line) of ERWIN observations of the meridional and zonal winds at ~97, 93 and 87 km at Eureka, Nu, at the Polar Environment Atmospheric Research Laboratory. Also plotted are the WACCM-X winds at the same heights and locations. Figure 2 14 shows daily averaged plots for the same time-period. This pair of plots provides an indication of the nature of the short term and long-term variability from these two sources.

Figure 5-14 indicates that the general trend and magnitude of the longer-term averaged winds with ERWIN and WACCM-X match reasonably well at all heights. This is especially evident in the zonal winds where the change in wind direction during the warming period is present in both data sets. This agreement is less evident in the meridional winds in this figure but on average the winds from both sources are similar.

Where the winds do not match is in the short term and medium-term variability. In general, the WACCM-X winds vary considerably more than the ERWIN winds. This difference is striking in the daily average plots (Figure 5-14). In Figure 5-13 where the short-term variations are included, it is evident that ERWIN exhibits more short-term variability, although it is of a smaller amplitude than that in WACCM-X and there is more high

frequency variability. The lack of high frequency variability in the WACCM-X data set would be expected because of the model resolution and gravity wave parameterization.

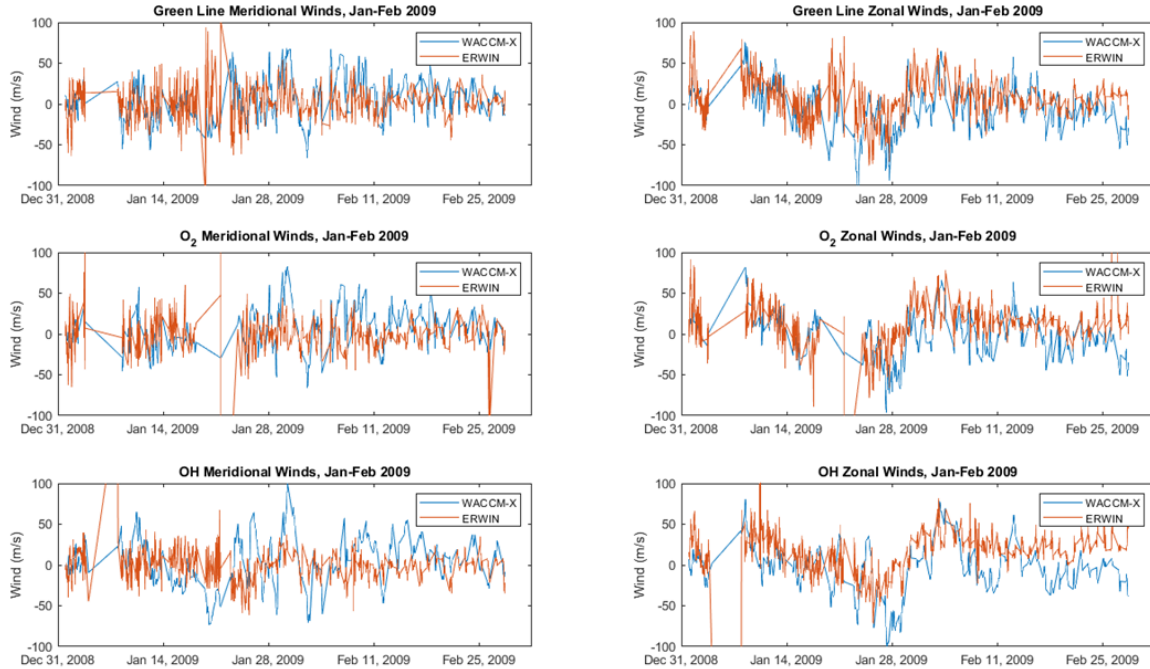


Figure 5-13. Time series of hourly averaged ERWIN observations of zonal (left panels) and meridional wind (right panels) observations at three different heights (top to bottom: ~97 km – green line, ~93 km – O₂ and ~87 km –OH) and from WACCM-X at the same location and heights. Straight line segments correspond to times when ERWIN was not taking observations.

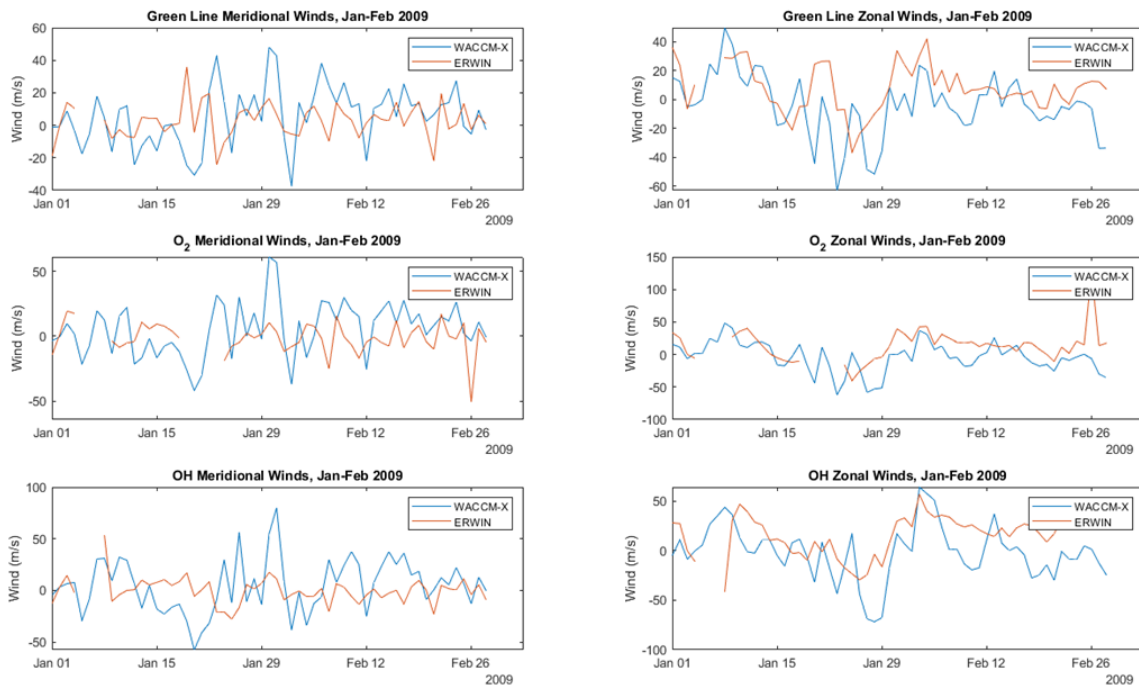


Figure 5-14. Same as Figure 5-13 but for daily averaged winds.

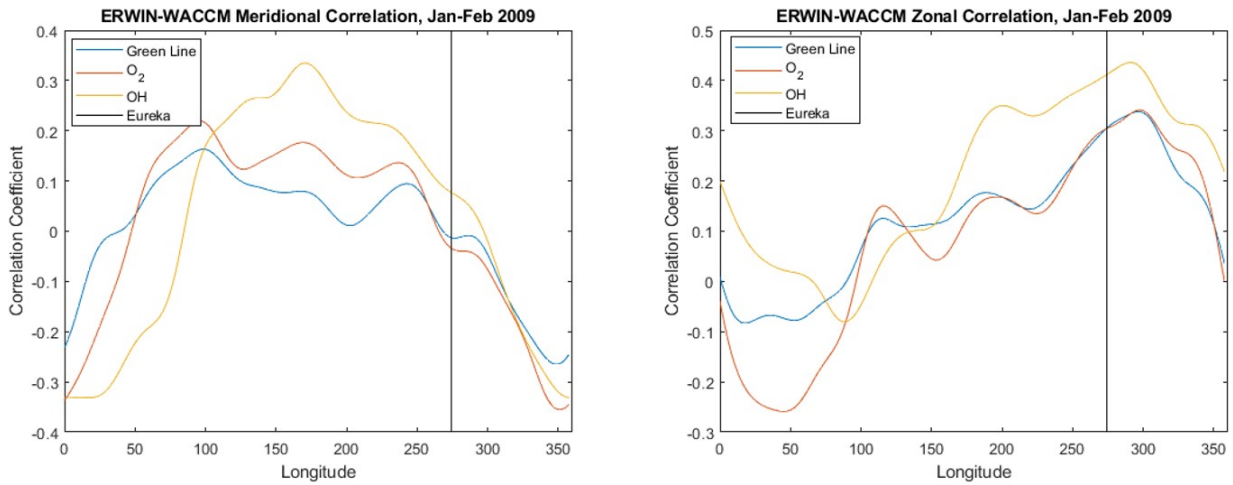


Figure 5-15. Correlation plots between ERWIN winds and WACCM-X wind observations at various longitudes for the same January-February 2009 time period shown in Figure 5-13 and Figure 5-14. The longitude from which the WACCM time series originates for the correlation is indicated on the abscissa and the correlation coefficient on the ordinate. The vertical line indicates the longitude where ERWIN is located.

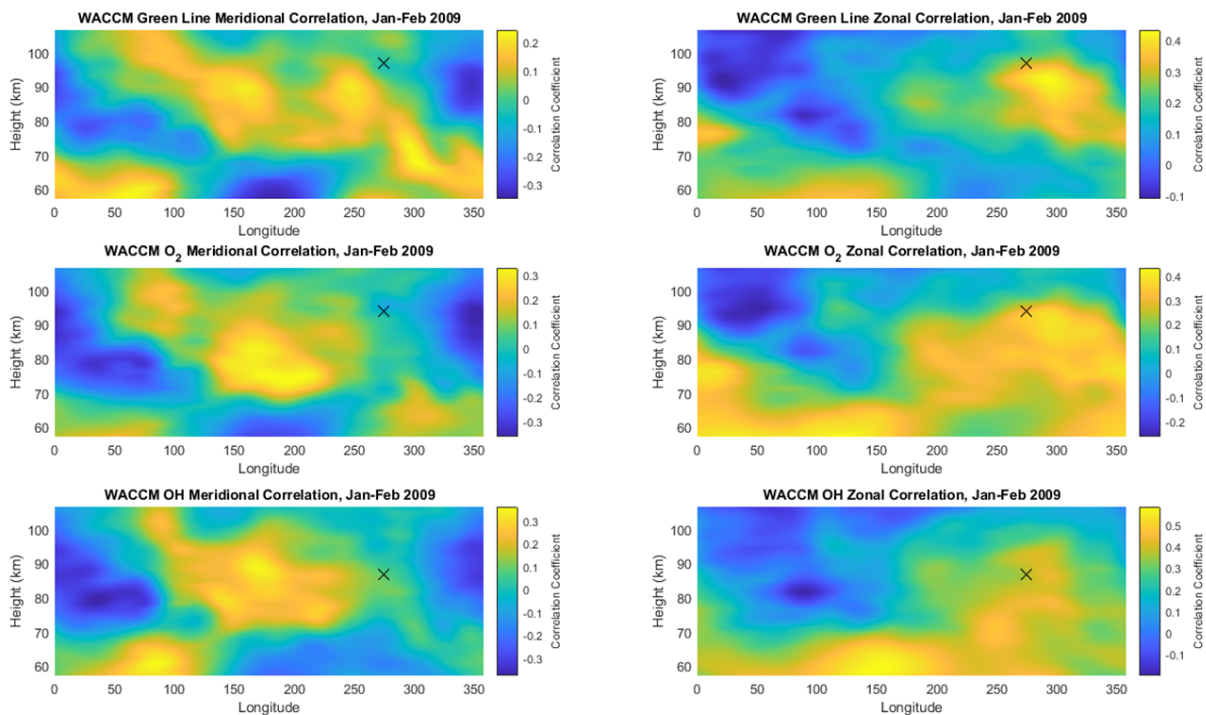


Figure 5-16. Latitude/height false colour plots of the correlation between WACCM-X winds at all longitudes and heights between 60 and 110 km. The x in each panel indicates the location of the ERWIN wind observations at the nominal height of each airglow layer.

Correlations between the two-time series are shown in Figure 5-15. To ensure that there is not a longitudinal phase difference between the two data sets, correlations between ERWIN and WACCM-X winds at all longitudes on the 80° N latitude circle were calculated and plotted in this figure. The best correlations occur at a longitude close to that of Eureka for the zonal wind, but the meridional winds do not match well.

To ensure that the differences between the two data sets are not related to height mismatches, this correlation was undertaken for heights between 60 and 110 km. The results are presented in Figure 5-16. As with the correlations shown in Figure 5-15, the best correlation for the zonal wind time series occurs close to the longitude and height of the Eureka time series. For the meridional winds, the best correlation occurs at a longitude about 100 degrees west of Eureka and close to 10 km below the height of the observations.

Somewhat puzzling is the appearance of the Wave 1 signature in these figures. This suggests the presence of a stationary feature in the WACCM-X observations. The nature of this feature had not been identified at the time this chapter was written. Should the reason for this pattern be determined prior to the writing of the final report, further discussion of this feature will be included in the report.

5.3 E-CHAIM, TIE-GCM and Data Comparisons

In this section we present and discuss the impacts of SSWs on ionospheric electron density using ionosonde, GNSS, and Incoherent Scatter Radar in comparison to E-CHAIM and TIE-GCM. To this end we focus on, the 2009. The form of this warming has been discussed in 5.2 of this chapter and in the previous chapter.

During the 2009 event, CHAIN had two ionosondes operational: one in Resolute (74.75°N, 265.00°E) and one in Eureka (79.99°N, 274.10°E). Both ionosondes reside well within the polar cap. Beginning with Resolute, in Figure 5-17 we present a time series of the peak ionospheric critical frequency (foF2) from the Resolute ionosonde, along with the corresponding modeled values from E-CHAIM and a run of the TIE-GCM that was driven by WACCM-generated lower-atmospheric forcing and without geomagnetic forcing.

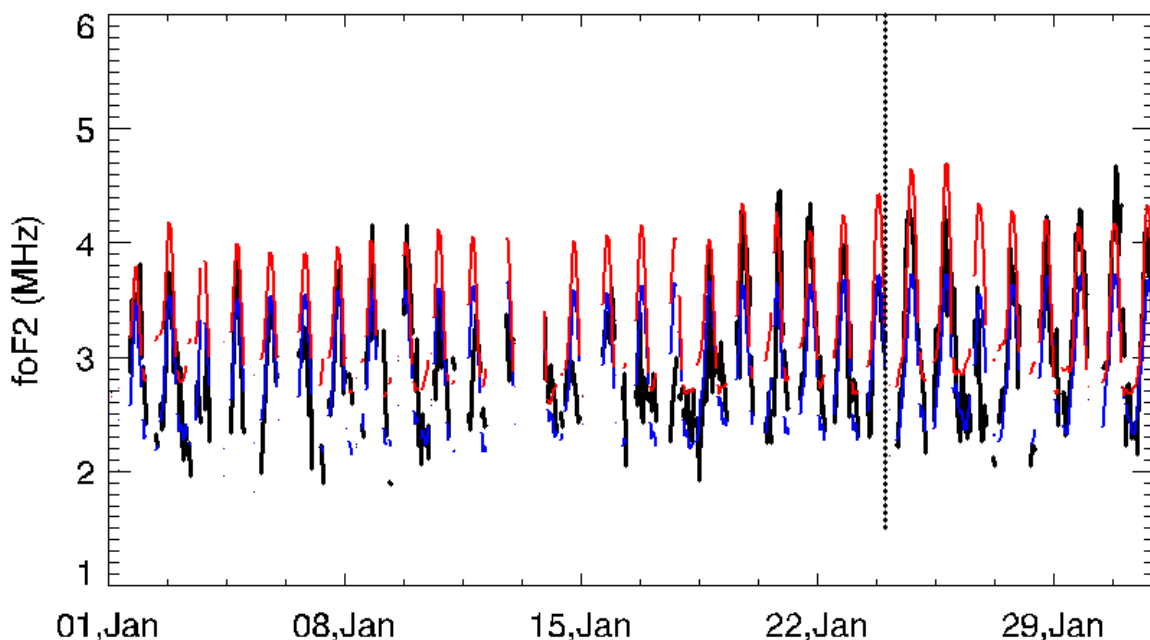


Figure 5-17. Ionosonde-measured (black), TIE-GCM-modeled (red), and E-CHAIM-modeled (blue) foF2 for the month of January, 2009. The dashed vertical line corresponds to January 24, 2009, at 00UTC. Note that model data is only plotted for periods with corresponding measured values.

During the SSW period, with the stratospheric zonal wind reversal marked by the dashed line, there is a substantial depletion in daytime foF2 (and therefore peak electron density) coincident with the zonal wind reversal. Also, prior to the zonal wind reversal, there is an appreciable increase in daytime electron density, beginning roughly on January 20th. Interestingly, the TIE-GCM model run predicts an increase in foF2 to occur following the zonal wind reversal, which is not consistent with the observations. Given the lack of significant geomagnetic activity prior to the 26th, this would suggest either that the observed enhancement prior to the reversal, and the depletion thereafter, are the result of something other than lower atmospheric forcing or that this forcing is incorrect in the model. Given that there are no substantial changes in solar activity, solar energetic particle activity, or solar X-ray activity, the latter option is far more likely. We direct the reader to the section documenting the validation of the WACCM lower atmospheric forcing against Eureka mesospheric wind observations for further details on the performance of this forcing.

Looking at Eureka in Figure 5-18, we note a much more substantial increase in foF2 that marks the highest observed densities of the entire month. Furthermore, the depletion in electron density on the day of the reversal, and just prior, is strongly pronounced in the Eureka data.

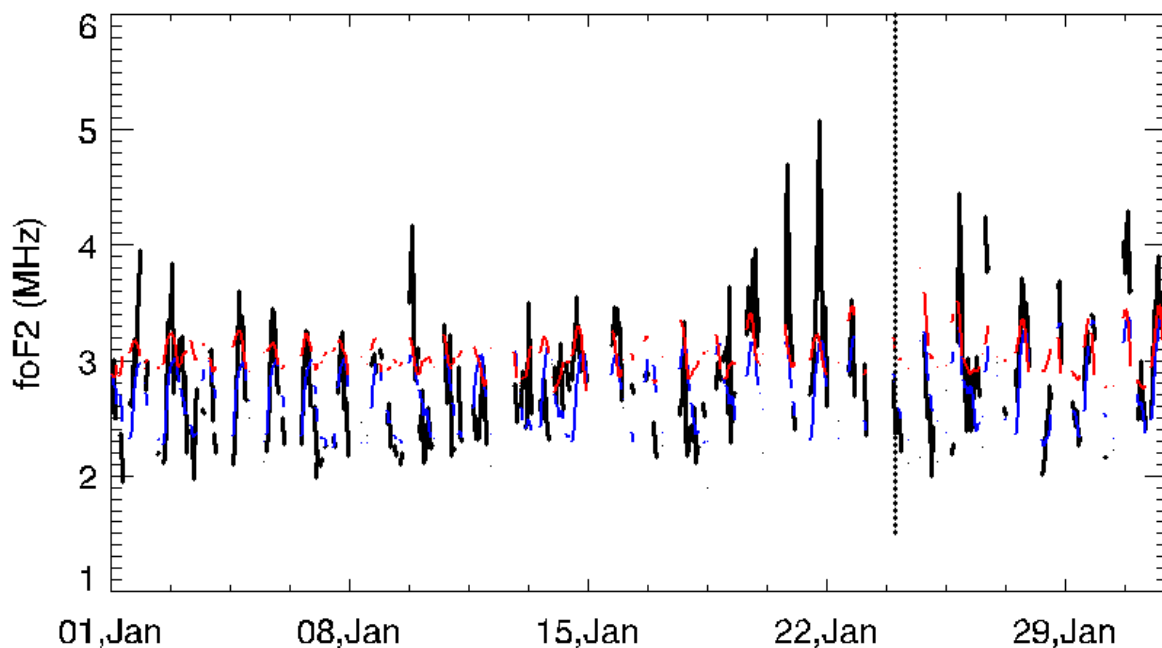


Figure 5-18. Same as Figure 5-17 but for Eureka.

Here we again note that the TIE-GCM run does not reproduce either the enhancement or depletion in electron density, nor does E-CHAIM. Unfortunately, ionosondes are limited by an observational bias during events of interest, where they are incapable of measuring densities when those densities are below the lower observational threshold of the instrument, controlled by D-region absorption. To ensure that these anomalies, particularly the density minimum, are not significantly affected by artefacts of this observational bias, we present the vertically integrated electron density at Eureka, measured by a GNSS receiver collocated with the Eureka ionosonde, in Figure 5-19.

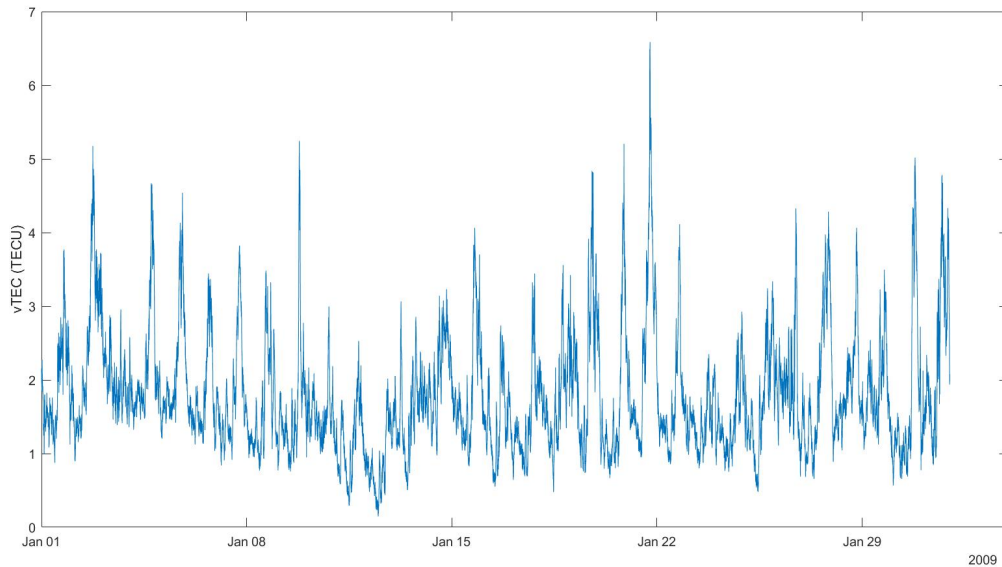


Figure 5-19. Average vertical Total Electron Content (vTEC) at Eureka for the month of January, 2009.

We note from this figure that there is, in fact, an anomalous enhancement in electron density beginning on the 20th that peaks at the highest TEC observed over the entire month. Correspondingly, we also note a substantial depletion of electron density during the zonal wind reversal that corresponds to the lowest observed daytime TEC of the month, outside those low values caused by geomagnetic disturbances.

One can also look at the peak height of the F-region (hmF2); for example, in Figure 5-20 we present the hmF2 for the same period as Figure 5-17.

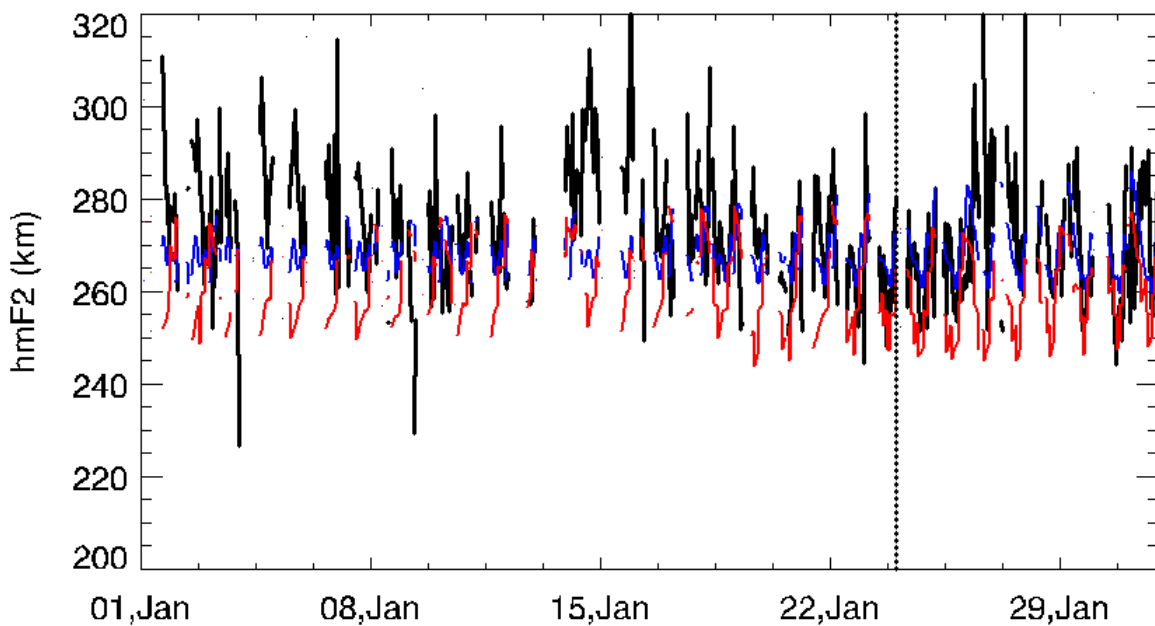


Figure 5-20. Same as 5-17 but for hmF2 at Resolute.

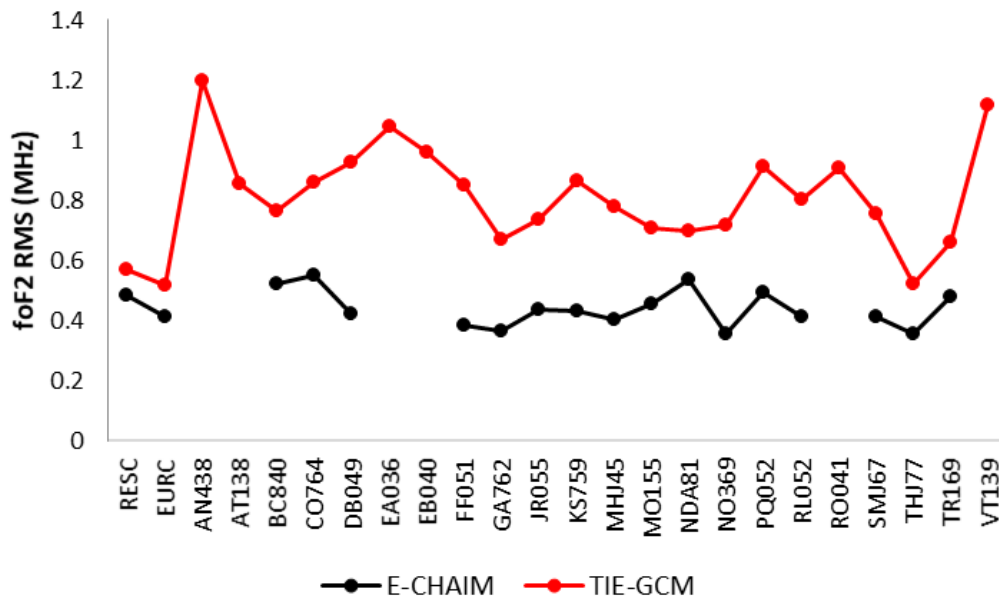


Figure 5-21. Overall RMS error in foF2 for E-CHAIM (black) and the TIE-GCM (red) for the period of January 2009 for a number of Northern Hemisphere ionosondes. Locations without an E-CHAIM value correspond to stations that are located below E-CHAIM's lower boundary at 50oN geomagnetic latitude.

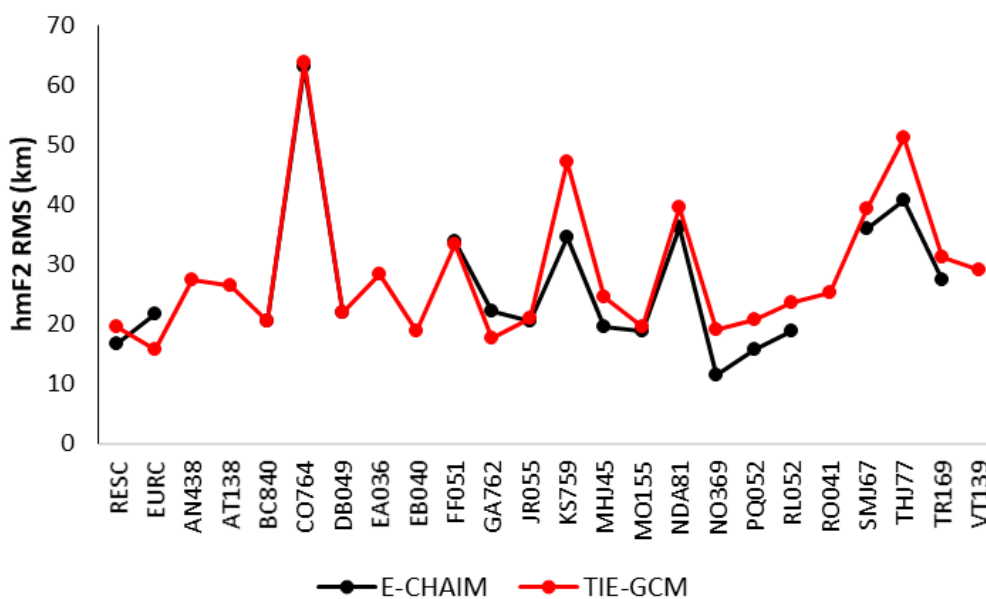


Figure 5-22. Same as Figure 5-21 but for hmF2.

In terms of hmF2, the results are far more complicated, as hmF2 appears highly sensitive to geomagnetic activity, where enhanced geomagnetic activity causes an increase in hmF2. Based on this geomagnetic complexity, it is unlikely that this study will be able to reliably infer SSW impacts on hmF2. This is further complicated by E-CHAIM's lack of geomagnetic forcing for its hmF2 model; thus, E-CHAIM cannot be used to isolate the geomagnetically-driven behavior of hmF2.

To provide some context on the degree of accuracy in which one may interpret model out, we present overall RMS errors of each model in reproducing foF2 and hmF2 from a number of ionosondes for the entire month of January, 2009, in Figure 5-21 and Figure 5-22, respectively.

5.4 Poker Flat Incoherent Scatter Radar Validations of TIE-GCM

The errors in TIE-GCM electron density, presented in 5.3, suggest that there are significant consequent issues that require a more comprehensive dataset to investigate. To this end, we here make use of Poker Flat Incoherent Scatter Radar (PFISR) observations made, nearly-continuously, during the 2009 SSW event. In Figure 5-23 we present that electron density during the 2009 SSW period from PFISR and the TIE-GCM run with geomagnetic forcing. From this figure, a number of deficiencies can be identified, namely substantial systematic overestimation of night time F-region electron density, significantly overestimated occurrence and magnitude of particle precipitation in the night time E-Region, and underestimation of daytime electron density in the F-Region, particularly in the near-peak topside. These concerns are highlighted more clearly in Figure 5-24, where differences between PFISR and TIE-GCM electron densities are presented. Note that positive values in that figure imply overestimation by the model and negatives imply underestimation by the model.

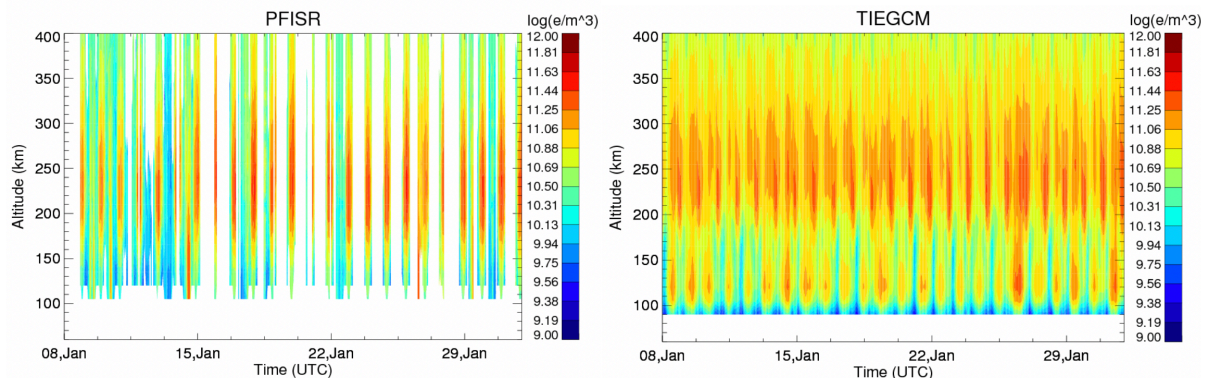


Figure 5-23. Vertical electron density profiles from PFISR (left) and corresponding profiles from TIE-GCM (right) with geomagnetic forcing during the 2009 SSW.

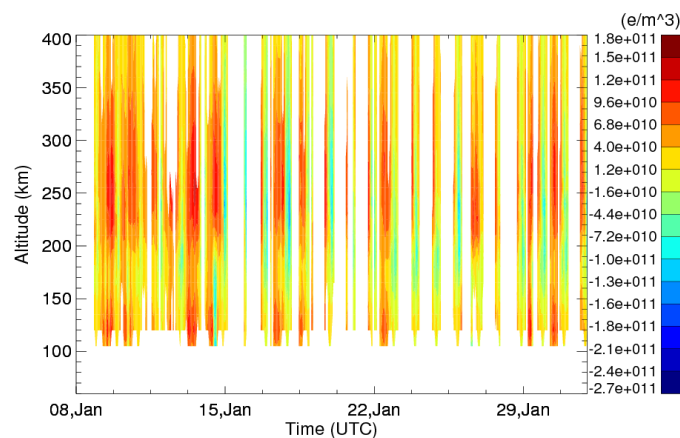


Figure 5-24. Differences between PFISR-measured and TIE-GCM-modelled electron density during the 2009 SSW event.

The overestimation and overprediction of auroral particle precipitation highlights a significant source of error in the TIE-GCM's particle precipitation model, consistent with previous comparisons to Defense Meteorological Satellite Program (DMSP) SSUSI inversions of auroral particle energy flux and suggesting that a more sophisticated driver, such as the Assimilative Mapping of Ionospheric Electrodynamics (AMIE) system, could provide measurable improvement to these simulations (Lu et al., 2016).

To provide a more complete picture of these modelling issues at high latitudes, we can also look at the model- and PFISR-derived electron and ion temperatures in Figure 5-25 and Figure 5-26, respectively.

Clearly, from Figure 5-25 the electron temperatures from the TIE-GCM significantly overestimate those from PFISR observations, reaching as high as 2000K greater than the PFISR electron temperatures at 400km altitudes during the daytime. Furthermore, the TIE-GCM does not reproduce the electron temperature enhancements in the E-Region during particle precipitation events. With regard to the ion temperatures, the TIE-GCM does not reproduce the ion temperature enhancement seen in the PFISR observations at altitudes between 120km and 200km appears to overestimate ion temperatures in the lower topside and at night. This is somewhat surprising given the model's tendency to significantly overestimate the occurrence and intensity of particle precipitation, likely resulting in greater electrical conductivities and precipitation-induced heating within the model.

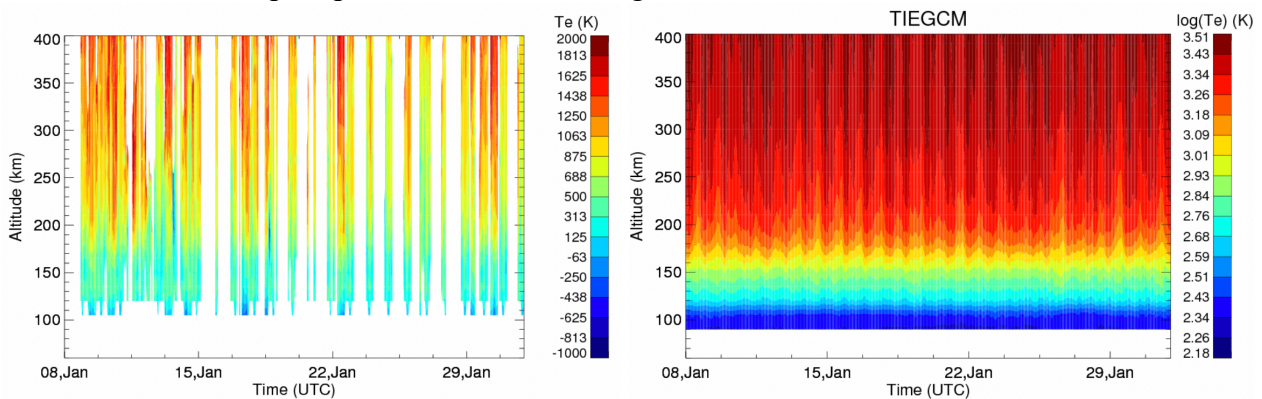


Figure 5-25. Vertical electron temperature profiles from PFISR (left) and corresponding profiles from TIE-GCM (right) with geomagnetic forcing during the 2009 SSW.

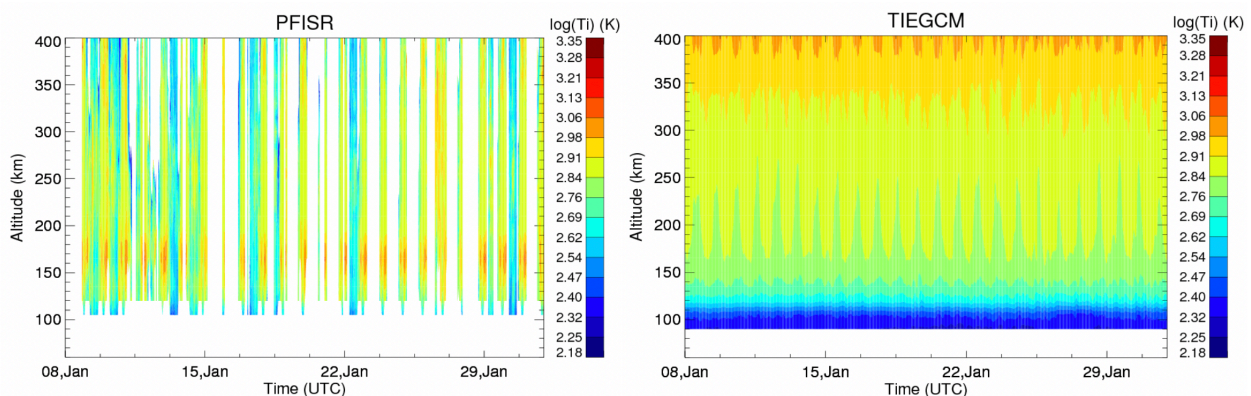


Figure 5-26. Vertical ion temperature profiles from PFISR (left) and corresponding profiles from TIE-GCM (right) with geomagnetic forcing during the 2009 SSW.

The severe overestimation of electron and ion temperatures should be what is causing exaggerated diffusion within the TIE-GCM, somewhat explaining the tendency for the model to exhibit scale heights in electron density much larger than those seen in the PFISR observations. The smoothed time evolution of electron density in the F-Region from day to day, culminating in a severe overestimation of night time electron density by the model, remains a mystery; however, it may be tied to issues in TIE-GCM eddy diffusion.

5.5 Conclusions

The validation of the WACCM-X, TIE-GCM and E-CHAIM models in the context of the VERA project are presented in this Chapter. The appropriateness of using the WACCM-X dynamics to drive the lower boundary of the TIE-GCM was validated through comparisons between the models at altitudes significantly higher than the lower boundary. These indicated that the upward propagating dynamical features observed in WACCM-X also appeared in the TIE-GCM run. This lends confidence to the use of the TIE-GCM with this lower boundary forcing to allow influences from the lower atmosphere to be separated from downward influences from the magnetosphere. Comparisons with observations of the semi-diurnal tide, $E \times B$ drift and total electron content, also were favourable further supporting the use of these models for investigating ionospheric coupling from above and below. Comparisons of the WACCM-X wind fields in the polar mesopause region indicated that the monthly variations in the mean winds were modelled reasonably well but the variability on time scales of several days and shorter was not modelled well.

The TIE-GCM/E-CHAIM comparisons with observations were less conclusive. This is in part because of the complexity of the causal relationships and the sensitivity of the observables to geomagnetic activity. Nevertheless, the TIE-GCM without geomagnetic forcing (so that only influences from below were important) did not produce time series which matched the observations well. Overall, the RMS error in foF2 associated with the TIE-GCM was greater than that associated with E-CHAIM. Observed variations in the foF2 during the warming period were not present in the TIE-GCM or E-CHAIM simulations though they do suggest the possibility of some dynamical influences from below. This needs to be investigated further.

Swarm could act as an excellent candidate to further examine the spatial behaviour of physics-based model performance, particularly once Swarm's in situ plasma temperature reliability is consolidated in the near future. Swarm Langmuir Probe data can be used to determine whether the observed plasma density issues are far-reaching and can diagnose these behaviours, to some extent, with the use of its plasma temperature measurements, as we have done here for a single location. This is particularly relevant with the recent release of version 0301 of the Swarm thermal ion imager data.

Further work will be undertaken on these comparisons. The SSW of 2018 and 2019 are being studied. Conclusions from these additional events will be incorporated into this study should they provide further insights into the nature of upward influences on the ionosphere.

Chapter 6

Final Findings and Results of Impact Assessment

6 Final Findings and Results of Impact Assessment

6.1 Scope and Outline

This document describes the results of data analyses conducted in the VERA project. Each section (6.2–6.6) presents an SSW event and describes effects of the SSW on the ionosphere as well as on the neutral atmosphere in the mesosphere and lower thermosphere (MLT) region. 6.2 focuses on the January 2009 SSW, which is the only event from the pre-Swarm period. The January 2009 SSW has been extensively studied in previous studies (see Chapter 2) and serves here as the base case to compare with the other SSWs. 6.3 examines the “minor” warming in January 2015, while 6.4 and 6.5 concentrate on the “major” SSWs in February 2018 and January 2019, respectively. 6.6 discusses the impact of the Antarctic SSW event in September 2019. The September 2019 SSW is a rare example of a southern hemisphere (SH) SSW. In 6.7, the main scientific questions of the VERA project are addressed in light of the results presented in 6.2–6.6.

6.2 January 2009 SSW

6.2.1 Description of SSW

The January 2009 is one of the strongest SSWs in meteorological records. The middle atmosphere dynamics during the January 2009 SSW was described in detail by Manney et al. (2009) and Harada et al. (2010). Ionospheric effects of the SSW have also been extensively studied as summarized in Chapter 2. In the VERA project, the January 2009 SSW represents the base case for comparisons with other SSWs.

Figure 6-1 shows the zonal wind at 60°N and polar temperature at 10 hPa during the January 2009 SSW. The SSW began on 19 January with the start of a strong increase of polar temperature (at about 60K in a week), and a strong zonal wind reversal starts on 24 January. The maximum temperature occurred on 23-24 January when temperature at 10 hPa reached 270K, whereas the pronounced maximum of easterly wind occurred on 28 January. The SSW ended in late February–early March. The zonal wind returned to being westerly on 22 February.

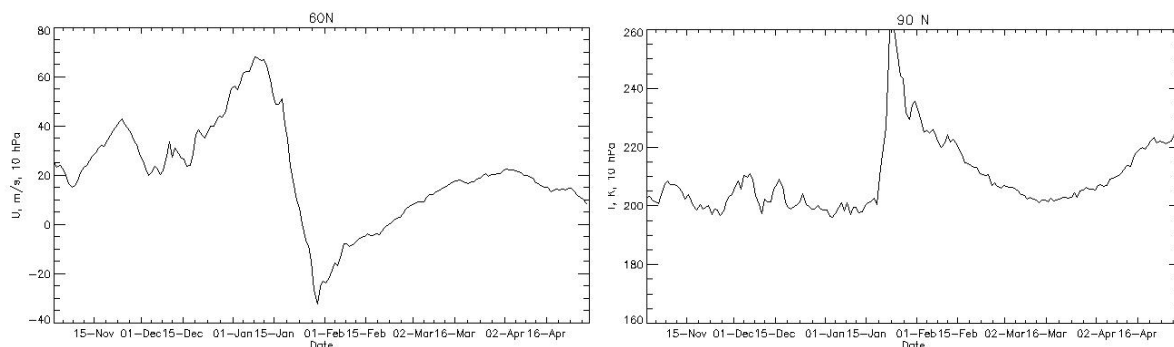


Figure 6-1. Zonal mean zonal wind at 60°N (left) and temperature at 90°N (right) at 10 hPa during November 2008–April 2009 derived from ERA5.

6.2.2 High-latitude MLT region

During the January 2009 SSW, the neutral atmosphere response at MLT heights above Eureka conformed to the accepted life cycle of major warmings. Zonal wind and meridional wind reversals were observed during the peak of the SSW seen in all three emission layers (see Figure 6-2).

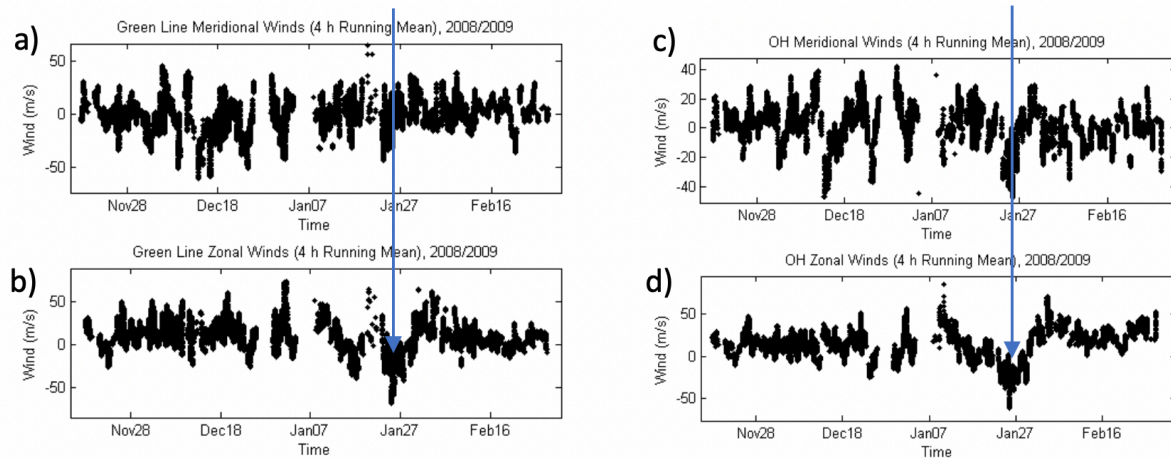


Figure 6-2. 4-hour running mean of the (a) green line meridional, (b) green line zonal, (c) OH meridional, and (d) OH zonal winds during the 2008/2009 season. The arrows highlight the wind reversal during the SSW.

In addition to the standard response described above, a decrease in the observed wind variances was observed during the SSW (see Figure 6-3), flanked by an increase in the variances at the beginning and end of the SSW. This could indicate that there is decrease in gravity wave activity during the SSW, with a burst of activity at the beginning and end of the SSW event. It is possible that this burst of activity corresponds to the period when the zonal wind profile crosses the zero-wind line and the gravity wave filtering is minimal. This requires further analysis to confirm.

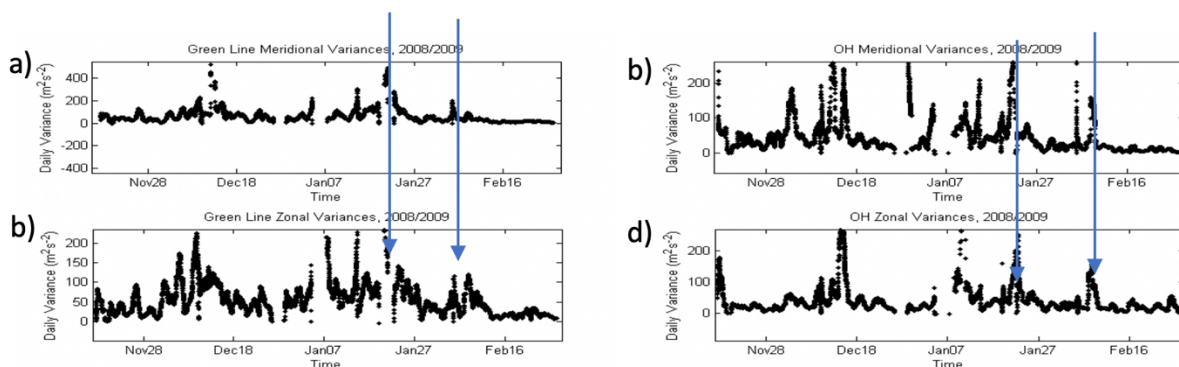


Figure 6-3. Running daily variance of the (a) green line meridional wind, (b) green line zonal wind, (c) OH meridional wind, and (d) OH zonal wind during the 2008/2009 season. The arrows denote the increase in variances observed at the beginning and end of the SSW.

Consideration of the spectral features of the winds is also revealing. The S-transform (similar to a wavelet transform) provides a measure of the spectral features as a function of both time

and frequency. The S-transform (see Figure 6-4) of the green line zonal winds, shows that there is a burst of wave activity with a period of ~ 3 days slightly before the start of the SSW. A 10-day oscillation is present during the warming.

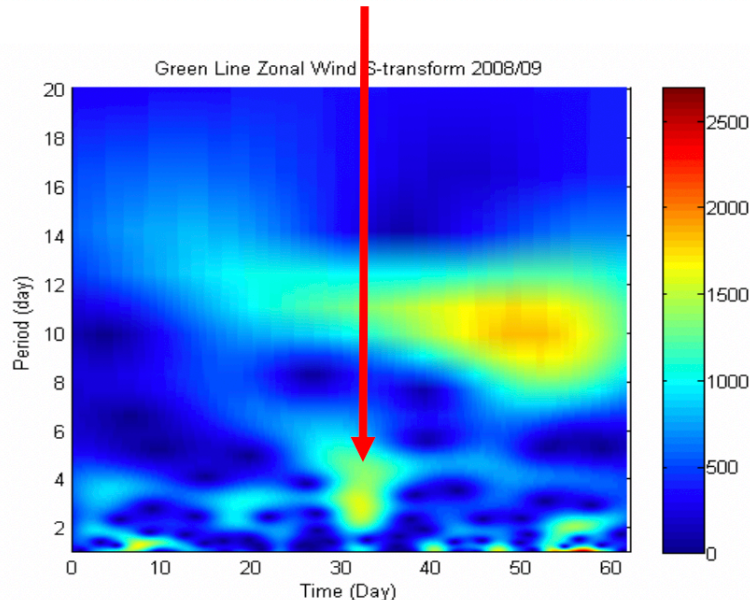


Figure 6-4. S-transform of the green line zonal wind from December 1, 2008 to January 31, 2009. The red arrow highlights the position of the 3 cpd wave event.

6.2.3 High-latitude ionosphere

In Chapter 5, we examined the validity of TIE-GCM model runs in modeling the effects of SSWs on the high latitude ionosphere. In that analysis, we, unfortunately, came to the conclusion that those TIE-GCM simulations were not sufficiently accurate to be useful in model/data comparisons. That is not to say, however, that there are no suspected SSW effects on the high latitude ionosphere. In Figures 5-18 and 5-19 of Chapter 5, we note substantial enhancements in foF2 and TEC at Eureka ahead of the SSW, followed by anomalously depleted foF2 and TEC during the day of the SSW wind reversal. These enhancements and depletions respectively represent the periods of greatest and lowest plasma density for daytime periods over the entire month surrounding the SSW event and, as such, we consider the origin of these anomalies being tied to the SSW as highly probable. Unfortunately, these anomalies were not present in the model runs, with or without geomagnetic forcing. As a result, we are limited in the depth of diagnostics we can conduct regarding their origin and nature.

To further examine this event a little bit further, we present the wavelet transform for the v TEC time series at Eureka (time series available in Chapter 5, Figure 5-19) in Figure 6-5. In Figure 6-5 we see a significant enhancement in the diurnal and semi-diurnal variability of v TEC at Eureka ahead of the SSW; however, we also note a substantial decay in the semi-diurnal mode as the SSW reversal begins. Unfortunately, because the TIE-GCM only provides electron density up to 700km, there is no analogue for v TEC within the model runs. As an alternative to this diagnostic, we have examined the wavelet transform for the modeled and measured NmF2 at Eureka in Figure 6-6.

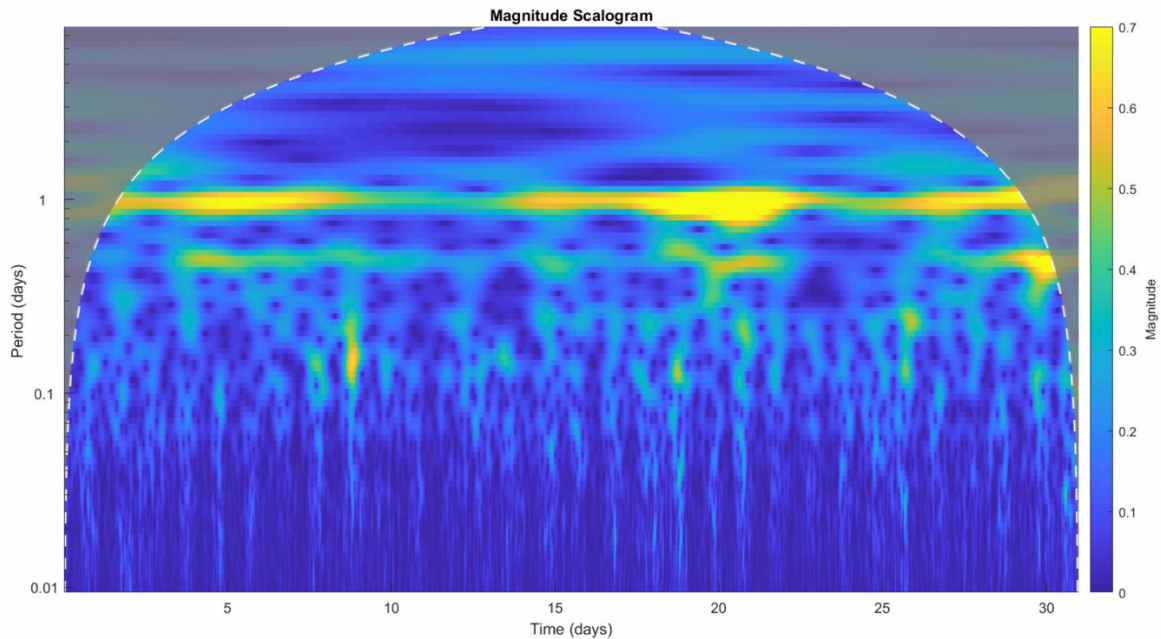


Figure 6-5. Wavelet transform of the vTEC at Eureka during and around the 2009 SSW event. Note that the x-axis corresponds to days since 01 January, 2009.

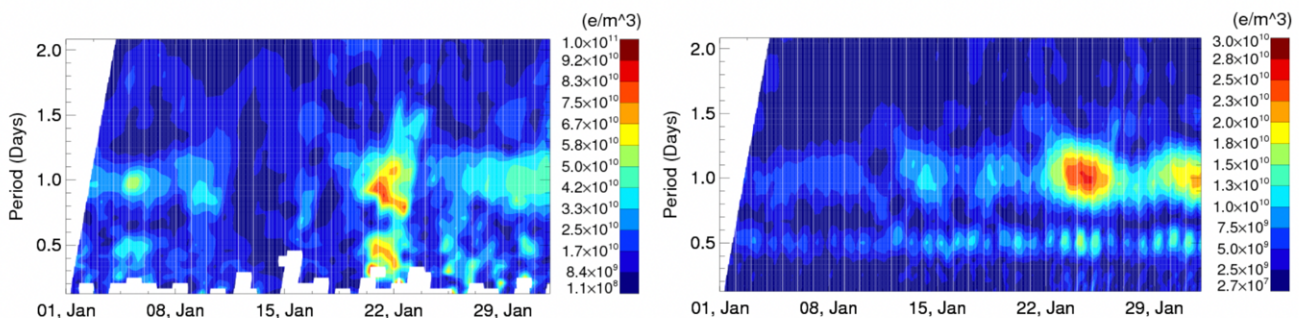


Figure 6-6. Wavelet transform of the NmF2 at Eureka from the CADI ionosonde (left) and from the TIE-GCM model run without geomagnetic forcing (right) during the period of the 2009 SSW.

Both the NmF2 observations and the TIE-GCM model run exhibit the same enhancement in the diurnal and semi-diurnal modes ahead of the SSW wind reversal. While the amplitude in the TIE-GCM run was substantially weaker than that of the observations and the model appears to have issues in capturing the seasonal variation at Eureka, it nonetheless has generated similar morphology in its spectrum at daily and within-day time scales. As the TIE-GCM run does not include geomagnetic activity and is purely driven by the WACCM winds at its lower boundary, it is very likely that these enhancements are related to the SSW event. Further exploration is necessary in order to identify the mechanism behind this enhancement.

6.2.4 Mid-latitude ionosphere

Ionospheric response in mid-latitudes over Europe is represented here by the response of the ionosphere above Pruhonice (central Czechia) station as measured by a digisonde (described in 3.5) and by the behavior of TEC (described in 3.4). Other European digisondes (situated at Juliusruh in the northernmost Germany, Dourbes in Belgium, Ebro-Roquetes in the

northeastern Spain, Rome in Italy and Athens in Greece) exhibit patterns of ionospheric response consistent with that described based on the Pruhonice digisonde measurements.

Figure 6-7 shows the evolution of electron density profilograms at Pruhonice. No significant changes in electron density before the maximum of SSW occurred. Only during the SSW maximum on 24 January, was an enhancement and maximum of electron density (yellow and orange color) and of related critical frequency foF2 (the highest radio wave frequency vertically reflected from the ionosphere) observed. The geomagnetic activity on 24 January and a few days prior was extremely calm ($K_p = 0-1$), so the enhanced electron density cannot be attributed to geomagnetic activity. After this maximum, the electron density and foF2 returned to regular seasonal behavior with the electron density slowly increasing with time due to the ascending noontime solar zenith angle. Some other electron density enhancements, such as that on 26 January and the night of 26/27, are caused by minor enhancements of geomagnetic activity, which are capable of causing significant ionospheric effects under very low solar activity conditions (as was the case in 2009 (Burešová et al., 2014)). The enhancement of electron density on 24 January was not accompanied by a change in the height of electron density maximum, hmF2. Of note is that during this SSW, the ionospheric F1 layer has often been observed, which is unusual for winter. In contrast to foF2, the average TEC over Europe, Figure 6-8 showed no pronounced effects in relation to this SSW and its maximum on 24 January contrary to foF2.

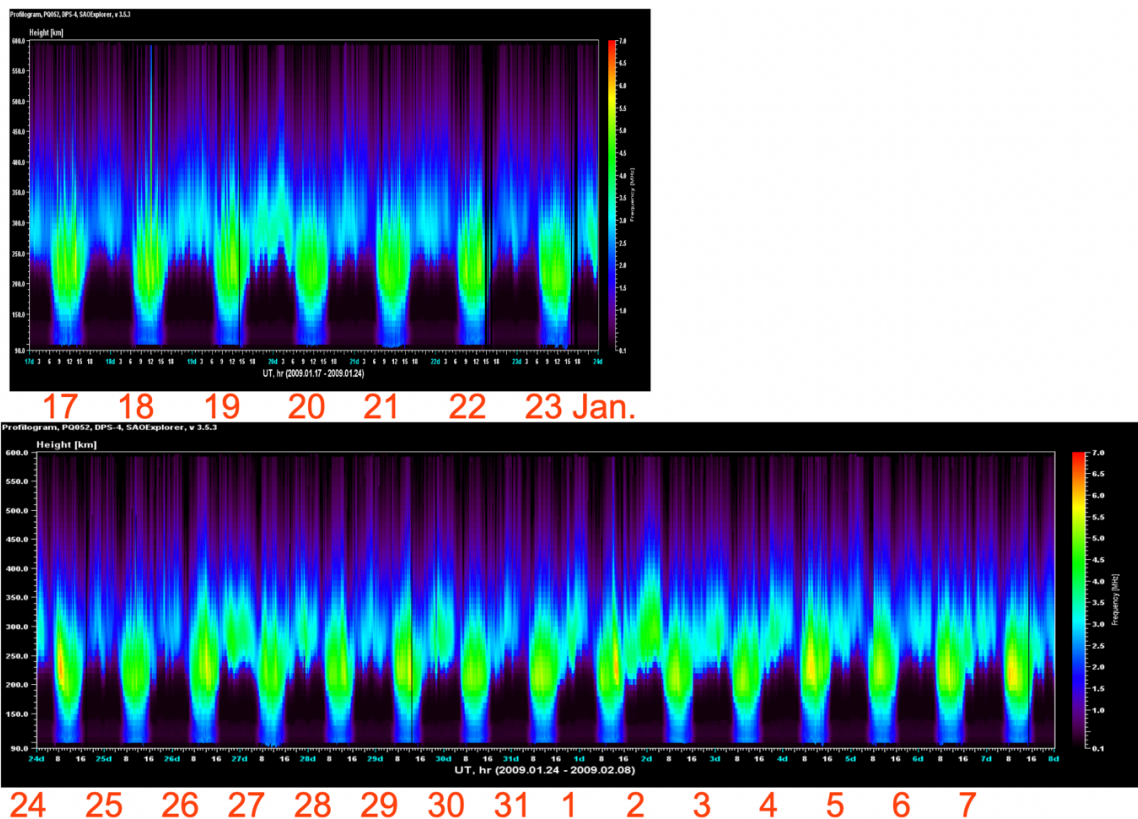


Figure 6-7. Evolution of electron density profilograms (height profiles) at Pruhonice. Top panel rising branch up to the maximum of SSW (19-23 January 2009) with two quiet days before (17-18 January 2009), bottom panel part of the period of wind reversal (24 January–7 February 2009).

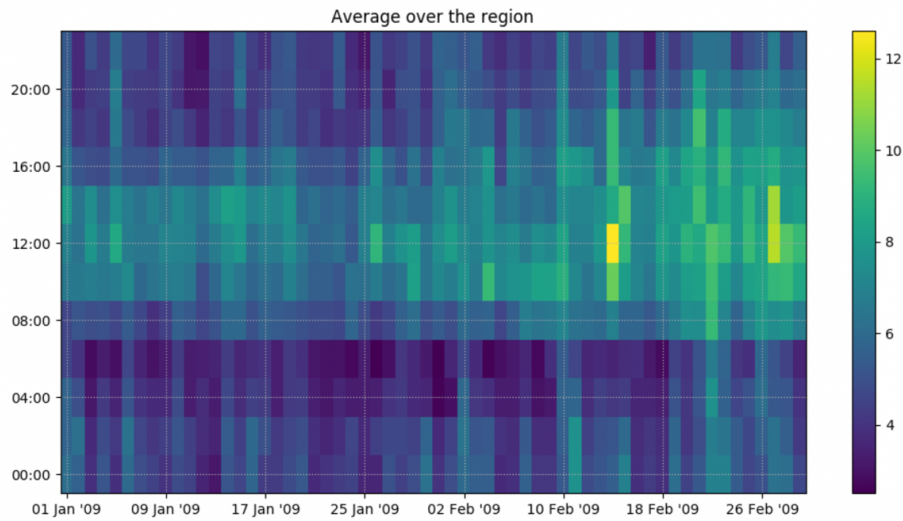


Figure 6-8. Temporal evolution of the observed average TEC over mid-latitude Europe (35-62N, 15W-25E), January-February 2009.

6.2.5 Low-latitude ionosphere

Previous studies have established that the response of the low-latitude ionosphere to the January 2009 SSW is dominated by effects of enhanced solar and lunar semidiurnal tides (e.g., Pedatella et al., 2014b). Here we present the EEJ data from CHAMP to confirm findings by earlier work.

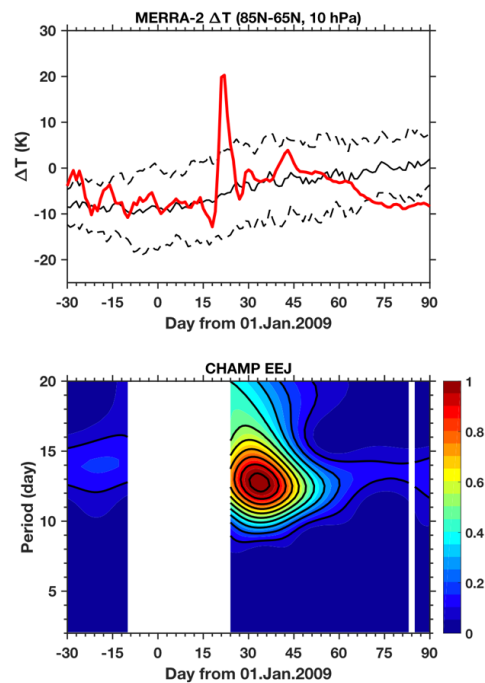


Figure 6-9. (Top) Meridional gradient in the high-latitude stratospheric temperature at 10 hPa during December 2008–March 2009 as derived from MERRA-2. The red line shows the data for 2008–2009 while the black line indicates the climatological seasonal cycle with standard deviation. A sudden reversal in the meridional temperature gradient in January 2009 indicates the occurrence of SSW. (Bottom) Wavelet power of the EEJ intensity derived from CHAMP magnetic field measurements. The power is normalized to the maximum value.

In general, it is difficult to resolve solar semidiurnal variations in satellite data collected in a near Sun-synchronous orbit as is the case for CHAMP and Swarm. The problem is their slow precession in local solar time. For instance, CHAMP precesses in local solar time at the rate of ~ 5.4 min per day, and thus it takes approximately 130 days for CHAMP to cover 12 hours local solar time. In other words, the solar semidiurnal tide has a period of ~ 130 days in CHAMP data. On the other hand, CHAMP (also Swarm) covers 12 hours local lunar time in approximately 13 days (e.g., Forbes et al., 2013). Thus, it is possible to infer the response of lunar semidiurnal tide (M2) to SSWs from the modulation of ~ 13 -day variations in CHAMP and Swarm data.

Figure 6-9 shows enhanced ~ 13 -day variations in the EEJ as derived from CHAMP magnetic field measurements during the January 2009 SSW. The results are consistent with the previous study by Park et al. (2012). The large ~ 13 -day variation during the SSW can be interpreted as a result of enhanced M2 tidal variability in the EEJ.

6.3 January 2015 SSW

6.3.1 Description of SSW

The January 2015 SSW is a “minor” warming, for which the reversal of the zonal mean flow (from eastward to westward) does not take place. Nevertheless, Manney et al. (2015) noted unexpectedly large disturbances in the middle atmosphere during this event. He and Chau (2019) reported large enhancements of the M2 tide in the mesosphere and lower thermosphere during the SSWs of January 2009, 2013 and 2015, using ground-based radar data for 2009–2016. In this section, we demonstrate that the minor warming of January 2015 also had a significant impact on the ionosphere through enhanced M2 tidal forcing.

Figure 6-10 shows the zonal wind at 60°N and polar temperature at 10 hPa during the SSW in January 2015. A rapid increase of about 30K per week can be seen in the polar temperature at the beginning of January. During this period, there is no zonal wind reversal at 10 hPa, and hence this is considered a minor warming. The maximum of the SSW occurred on 8-9 January when the temperature at 10 hPa reached 240K. This SSW was followed by several smaller minor SSWs during the month of February.

Figure 6-11 presents the amplitude of the M2 tide in temperature at 110 km for the SSWs in January 2009, January 2015, February 2018, and January 2019, as derived from TIMED/SABER data. It can be seen that the January 2009 SSW is followed by a large M2 tide with the maximum amplitude exceeding 25K at low latitudes. An M2 enhancement is also seen during the January 2015 SSW, with a maximum amplitude of ~ 20 K. Relative to the January 2009 and 2015 events, the M2 response is unclear during the SSWs in February 2018 and January 2019.

We have also examined the M2 tide for the other winters of the Swarm operation period (2014, 2016, and 2017) using TIMED/SABER data and found that the M2 tide was largest in January 2015. In what follows, we examine M2 tidal variability in Swarm data during the January 2015 SSW, focusing on the low-latitude region where the ionospheric response to M2 is most pronounced.

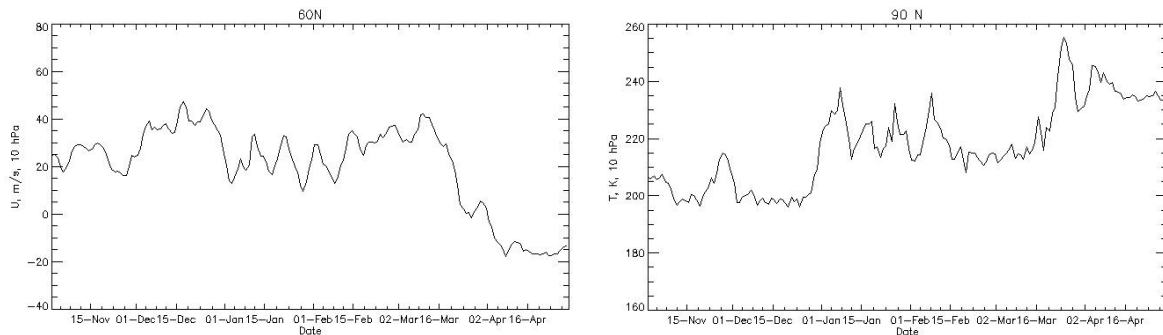


Figure 6-10. Zonal mean zonal wind at 60°N (left) and temperature at 90°N (right) at 10 hPa during November 2014–April 2015 derived from ERA5.

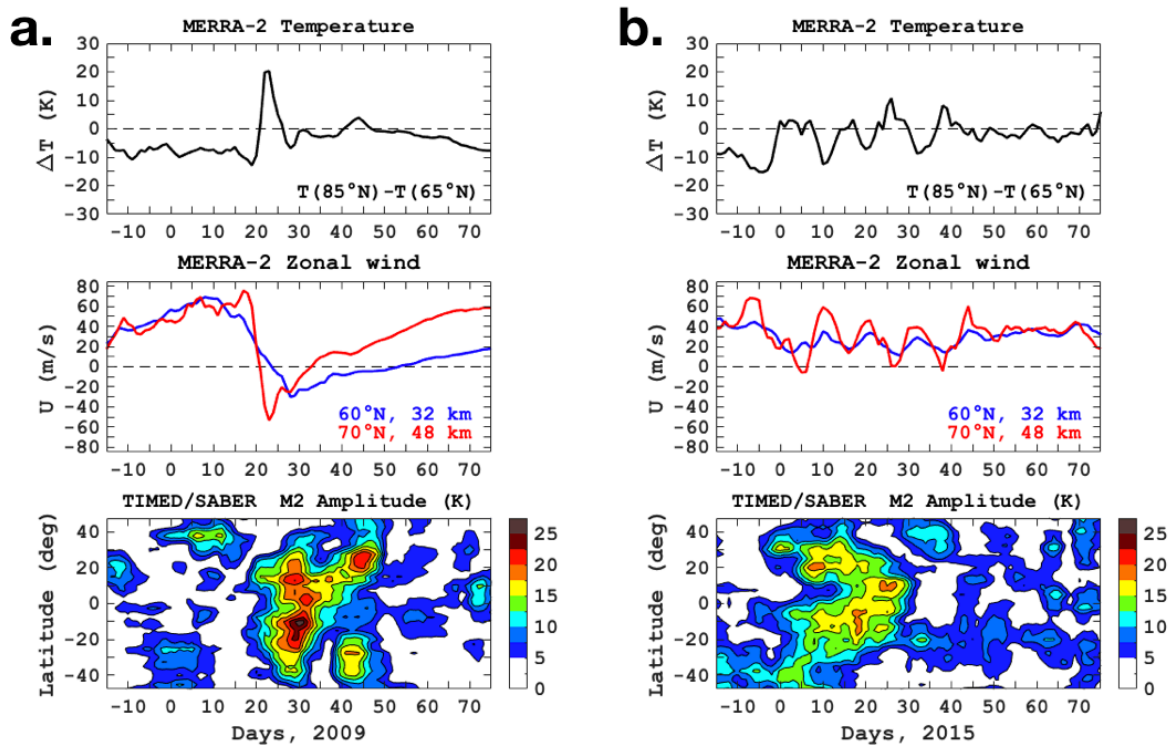


Figure 6-11. Amplitude of the lunar semidiurnal (M2) tide for the boreal winters of 2009 (a), 2015 (b), 2018 (c), and 2019 (d). In each of (a)–(d), the top panel shows the meridional gradient in the high-latitude stratospheric temperature at 10 hPa as derived from MERRA-2. The middle panel shows the zonal mean zonal wind at 60°N at 10 hPa (blue) and 70°N at 1 hPa (red) as derived from MERRA-2. The bottom panel shows the M2 amplitude at 110 km obtained from TIMED/SABER data.

6.3.2 Low-latitude response

Swarm observations reveal enhanced M2 tidal wave activity in the ionosphere during the January 2015 SSW. In Figure 6-12, enhanced ~ 13 -day variations are seen in the EEJ derived from both Swarm A (bottom right) and Swarm B (bottom left). The peak spectral power is weaker than that during the January 2009 SSW (cf. Figure 6-9). It is interesting that an enhanced ~ 13 -day variation is also seen in the inter-hemispheric field-aligned current (IHFAC) intensity at 20–30° magnetic latitude. The results suggest that M2 tidal forcing during the SSW led to modulations of IHFAC as well as EEJ.

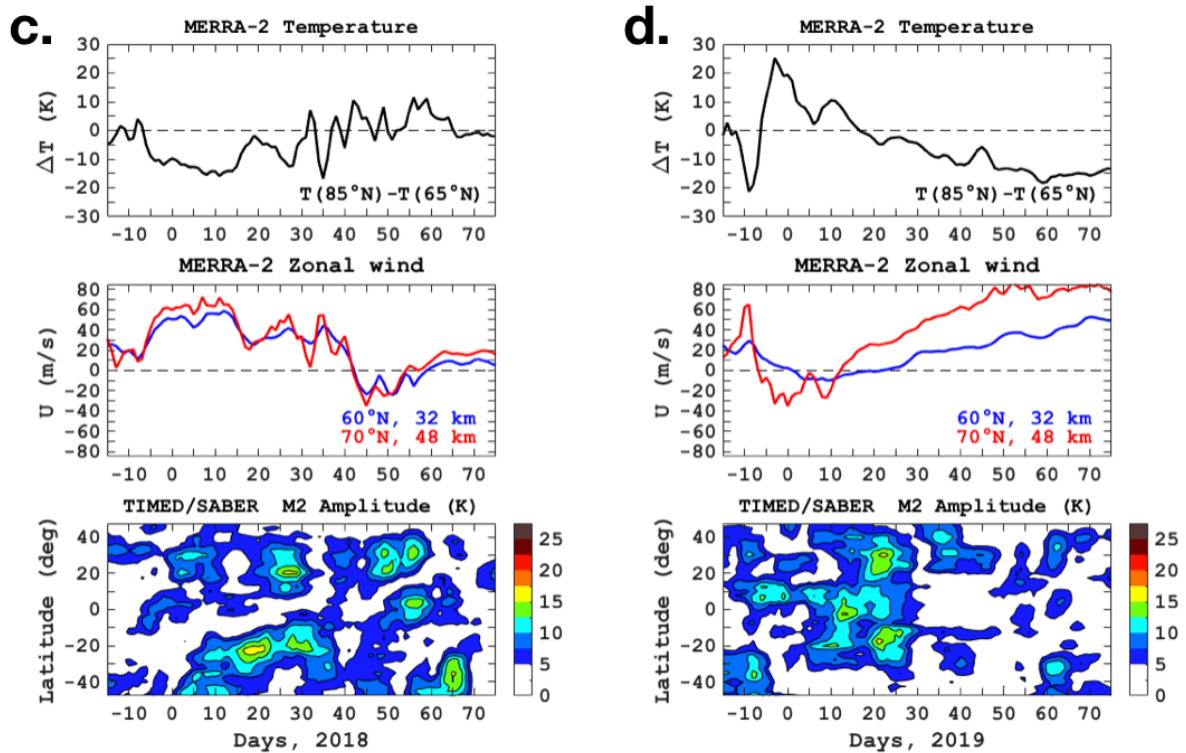


Figure 6-11. Continued.

M2 tidal variations are also seen in the Swarm electron density data. Figure 6-13 shows that the amplitude of the M2 variation in the electron density is as large as 40% of the background at 20° magnetic latitude on the dayside during the 2015 January SSW. Similar results are obtained from the electron density data from the dayside orbit of Swarm A (not shown here).

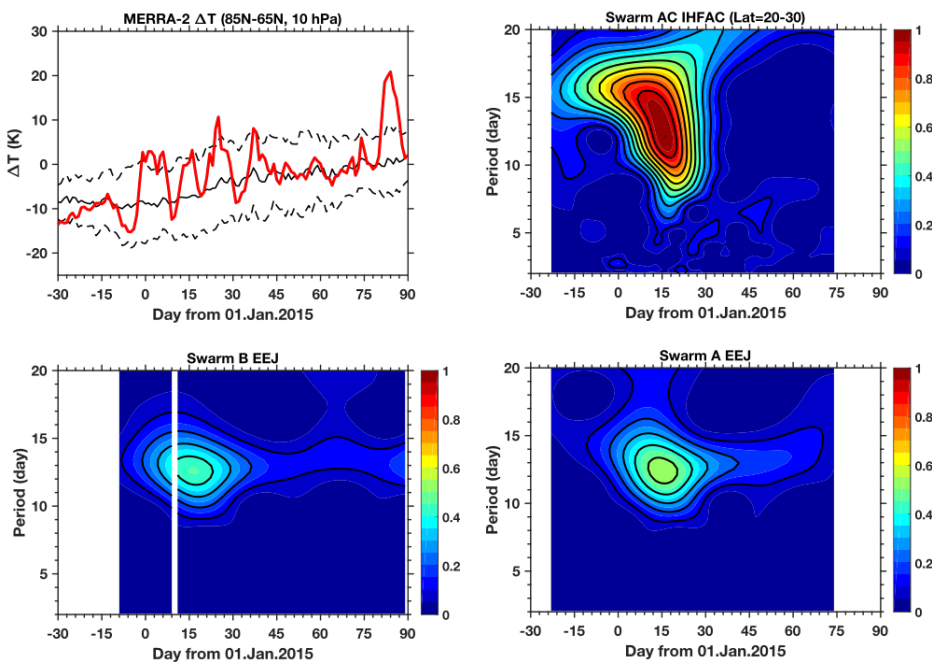


Figure 6-12. (Top-left) Meridional gradient in the high-latitude stratospheric temperature at 10 hPa during December 2014–March 2015 as derived from MERRA-2. (Top-right) Wavelet power of IHFAC intensity at 20–30° magnetic latitude, as derived from the Swarm dual-FAC product. The power is normalized to the maximum value. (Bottom-left) Wavelet power of the EEJ intensity derived from Swarm B magnetic field measurements. The power is normalized to the maximum value of EEJ wavelet power during the January 2009 SSW (see Figure 2.5.1). (Bottom-right) Same as the bottom-left panel except for the EEJ from Swarm A.

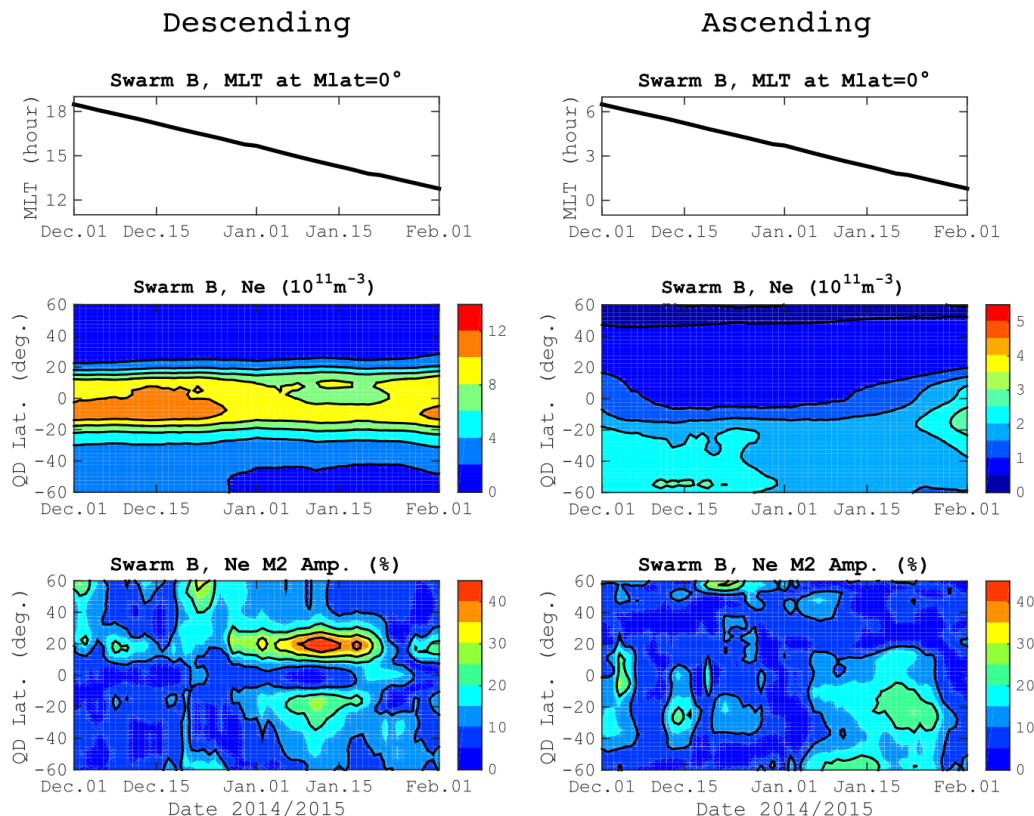


Figure 6-13. (Top) Magnetic local time of the equator crossing of Swarm B. (Middle) Zonal and 21-day mean of the electron density observed by Swarm B. (Bottom) Relative amplitude of the 13.3-day variation, which corresponds to the period of M2. The left panels are based on the data from the descending parts of the orbit, while the right panels are from the ascending parts of the orbit.

6.4 February 2018 SSW

6.4.1 Description of SSW

The February 2018 SSW took place after a 4-year hiatus in major warmings after the January 2013 (Rao et al., 2018; Karpechko et al., 2018). Figure 6-14 shows the zonal mean zonal wind at 60°N and polar temperature at 10 hPa during this event. The SSW started on 4 February with an increase of polar temperature (of about 40K in a week) and the zonal wind reversal started on 11 February. The multi-peak maximum in temperature occurred during the 13-18 February period when the temperature at 10 hPa reached 245K. The double-peak amplitude maxima of the reversed zonal wind were on the 15th and 20th of February. In terms of temperature response, this SSW ended on 4-5 March, whereas zonal wind returned to

westerly on 3 March. This major SSW is not as strong as the 2009 SSW and the temperature increase is comparable to that of the minor SSW in 2015.

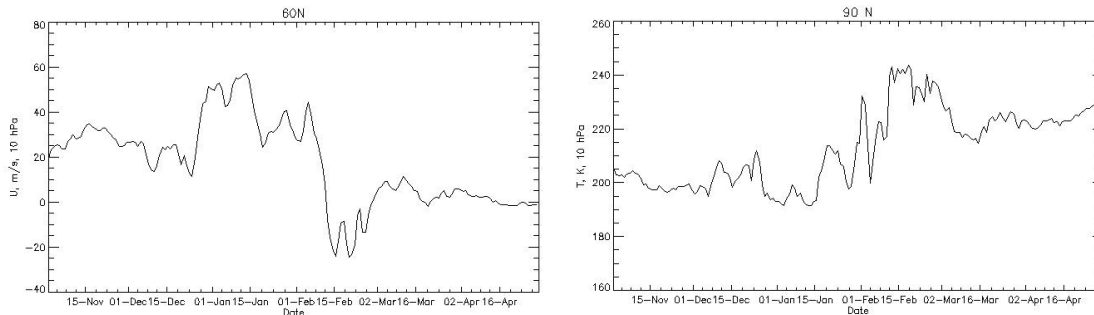


Figure 6-14. Zonal mean zonal wind at 60°N (left) and temperature at 90°N (right) at 10 hPa during November 2017–April 2018 derived from ERA5.

6.4.2 High-latitude MLT region

During the 2018 SSW, the neutral atmosphere response was also typical, but not as strong as that observed during the 2009 SSW. There was an observable zonal wind reversal during the peak of the SSW (see Figure 6-15). Additionally, a decrease in the observed wind variances was observed during the SSW (see Figure 6-16), bracketed by increases in the variances at the beginning and end of the SSW. As with the 2008/2009 season, this could indicate that there is decrease in gravity wave activity during the SSW, with a burst of activity at the beginning and end of the SSW event. Because this warming occurred in February when there were significant periods of twilight each day, wave diagnosis was difficult during the period of this warming.

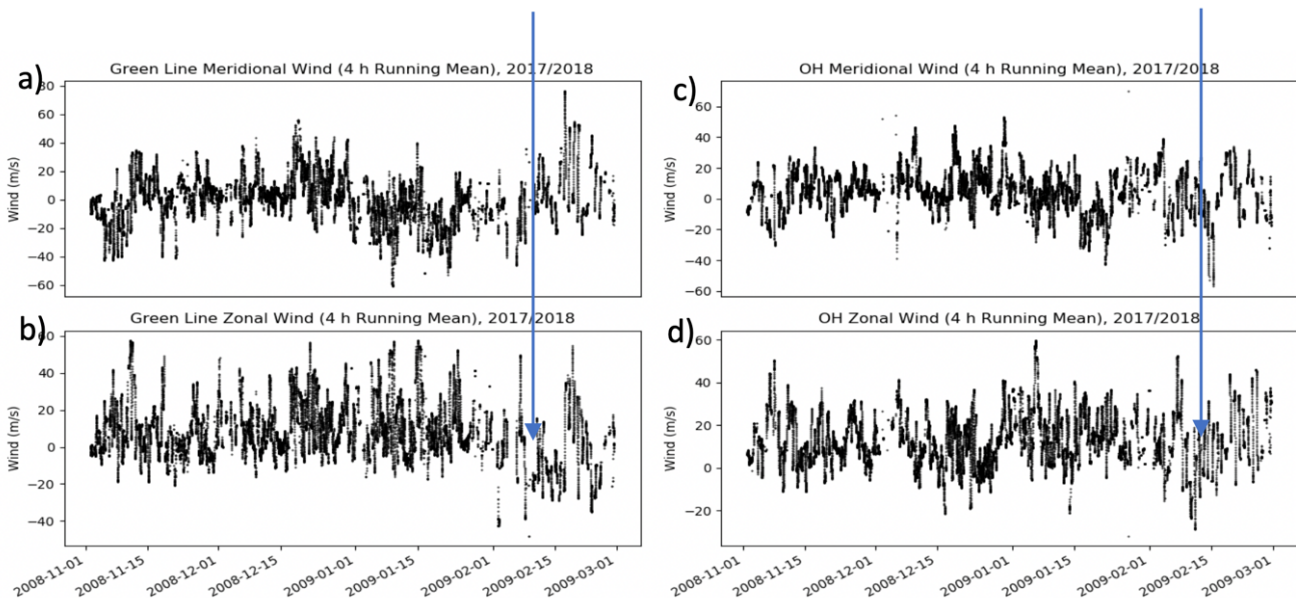


Figure 6-15. 4-hour running mean of the (a) green line meridional, (b) green line zonal, (c) OH meridional, and (d) OH zonal winds during the 2017/2018 season. The arrows highlight the zonal wind reversal during the SSW.

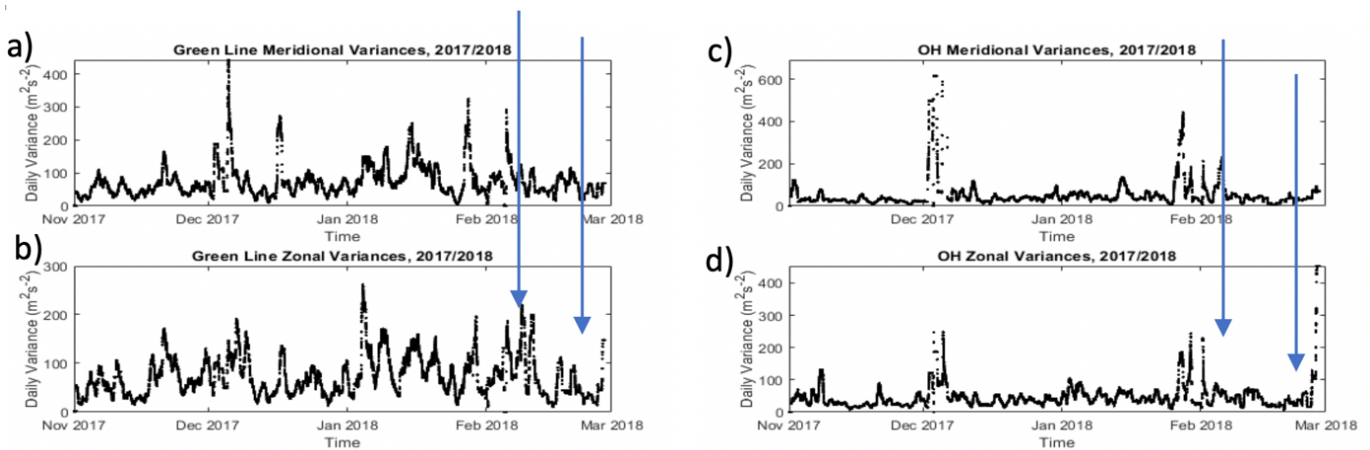


Figure 6-16. Running daily variance of the (a) green line meridional wind, (b) green line zonal wind, (c) OH meridional wind, and (d) OH zonal wind during the 2017/2018 season. The arrows denote the increase in variances observed at the beginning and end of the SSW.

6.4.3 Mid-latitude ionosphere

The temporal evolution of electron density profilograms is shown for Pruhonice in Figure 6-17. Relative to other days during this period, an increase and maximum in NmF2 (foF2), increases in electron density in general, and a slight increase of hmF2 occurred on 17 February, the day of SSW maximum, in daytime as well as in early night. This electron density enhancement is the main ionospheric feature of this SSW event. The geomagnetic activity on 17 February was not calm, it reached $K_p = 3+$ in the morning before the electron density enhancement but on 18, 19 and 23 February it was higher (up to $K_p = 5$) without any significant effect in foF2.

Temporal evolution of the observed and simulated average TEC over mid-latitude Europe ($35\text{--}62^\circ\text{N}$, $15^\circ\text{W}\text{--}25^\circ\text{E}$) are presented in Chapter 5 (Figure 5-11). The maximum TEC over the whole interval was observed on 17 February, the day of the warming maximum, in coincidence with foF2 data. No other comparable enhancement of TEC was observed during this SSW event, which supports attributing the maximum TEC and foF2 over Europe on 17 February 2018, the day of the SSW maximum, to a non-geomagnetic origin. Model simulations clearly confirm the maximum of TEC on 17 February, as well.

Figure 6-18 shows daily TEC maps over Europe for 11-19 February 2018. They show that TEC was enhanced on 17 February everywhere in Europe compared with other days, particularly at lower middle latitudes, and that it was not solely a local or sub-regional enhancement. It should also be mentioned that NH maps of ROTI (not shown here) indicate that pattern for January 17 is not a calm one, but on January 18 and 19 (magnetically more perturbed days) ROTI maps indicate that a more disturbed pattern of the ionosphere at high latitudes occurred.

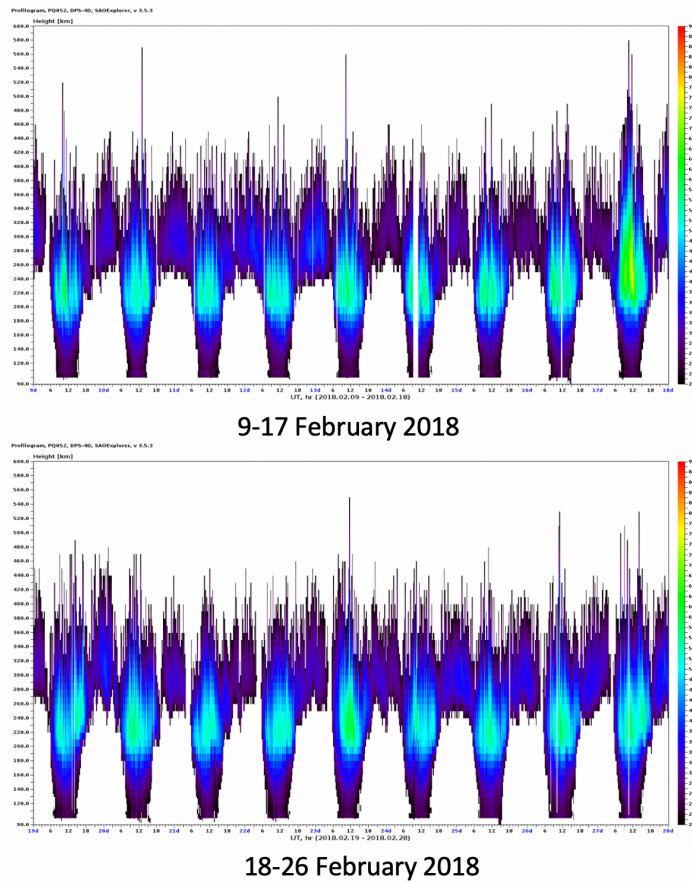


Figure 6-17. Temporal evolution of electron density profilograms for Pruhonice during SSW of February 2018. Top panel 9-17 February, bottom panel 18-26 February.

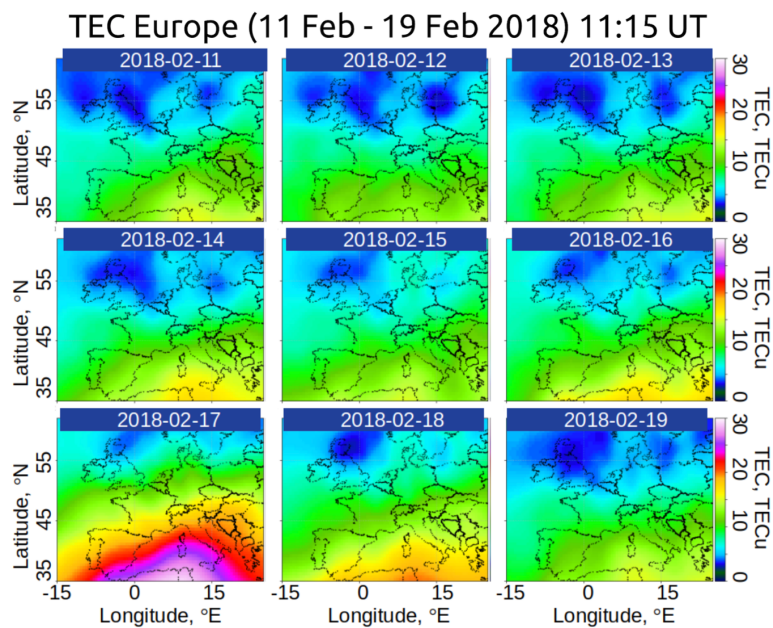


Figure 6-18. Daily TEC maps over Europe at 11:15 UT for 11-19 February 2018.

6.4.4 Low-latitude ionosphere

Figure 6-19 shows enhanced ~ 13 -day variations in the Swarm EEJ (bottom left and right) and IHFAC (top right) during the February 2018 SSW. The results are similar to those during the January 2015 SSW (Figure 6-12) but the spectral power of the ~ 13 -day variation is lower for the February 2018 SSW. It is thus speculated that the low-latitude ionosphere was affected by enhanced M2 wave during the February 2018 SSW but the wave forcing was weaker than that of the January 2015 SSW.

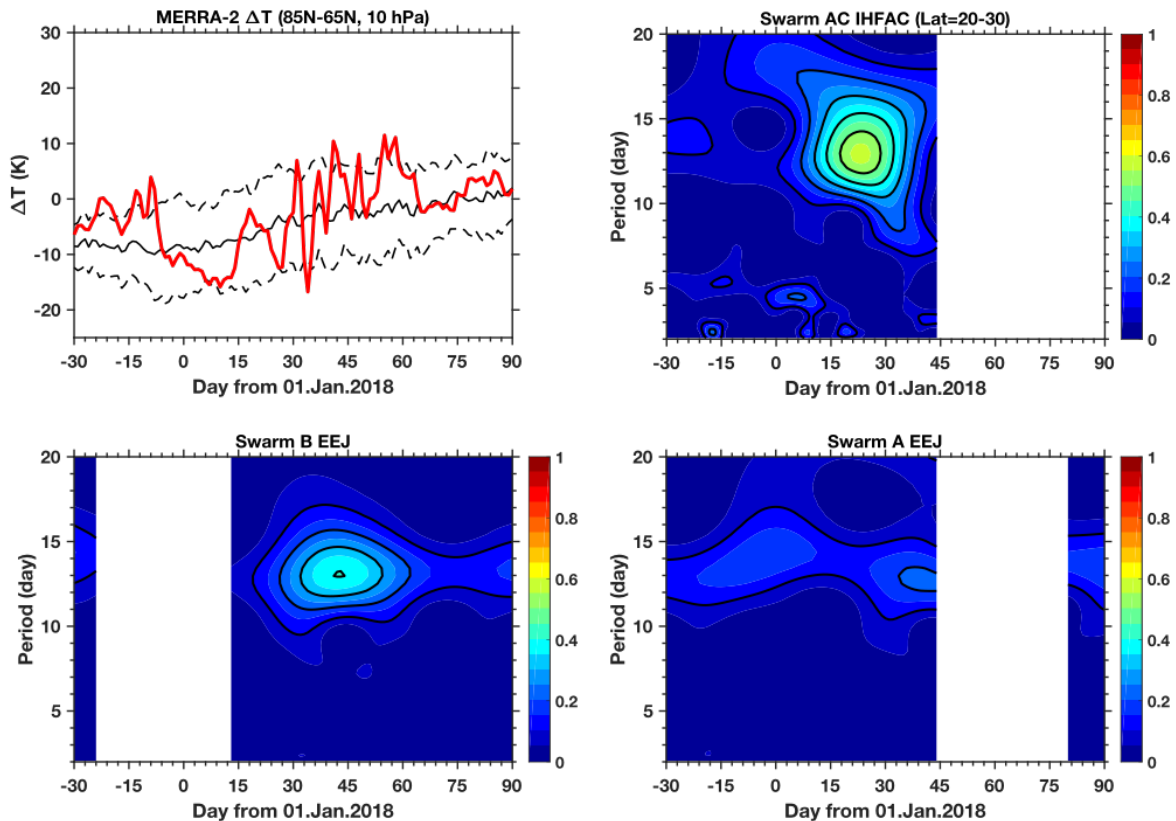


Figure 6-19. Same variables as Figure 6-12 but for December 2017–March 2018.

6.5 January 2019 SSW

6.5.1 Description of SSW

The January 2019 SSW is the most recent major warming event (Oberheide et al., 2020). Figure 6-20 shows the zonal mean zonal wind at 60°N and polar temperature at 10 hPa during the boreal winter of 2018/2019. The SSW started on 22 December with an increase of polar temperature (more than 60K in a week) and also a zonal wind reversal, which took place later on 2 January 2020. The maximum of the SSW occurred on 28 December when temperature at 10 hPa reached 265K, and the warming finished around 3 February. The maximum zonal wind reversal was on 10 January and wind returned to westerlies around 20 January. The temperature increase is comparable to the major SSW of 2009 but the zonal wind reversal is much weaker and shorter than in 2009.

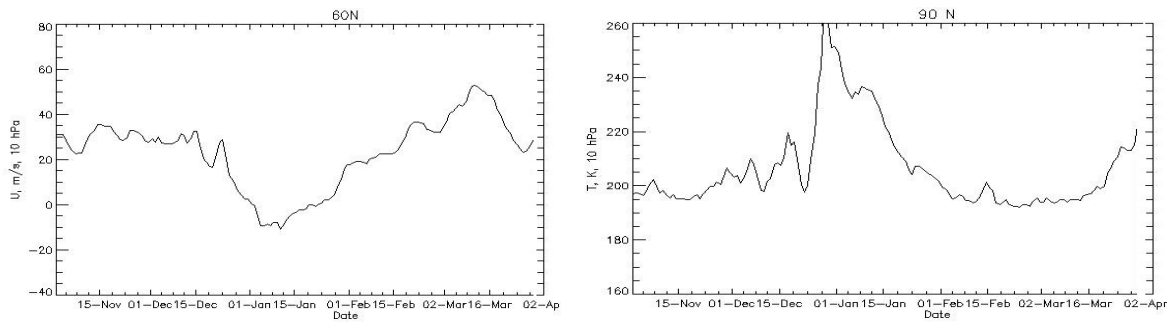


Figure 6-20. Zonal mean zonal wind at 60°N (left) and temperature at 90°N (right) at 10 hPa during November 2018–April 2019 derived from ERA5.

6.5.2 High-latitude MLT region

During the 2019 SSW, the neutral atmosphere response was not typical, and differs from that observed during the 2009 and 2018 SSWs. This season, there was no observable zonal wind reversal during the peak of the SSW, but there were two weaker pre-warming wind reversals (see Figure 6-21). However, as with these earlier warmings, a decrease in the observed wind variances was observed during the SSW (see Figure 6-22), abutted by increases in the variances at the beginning and end of the SSW. Again, this could indicate that there is decrease in gravity wave activity during the SSW, with a burst of activity at the beginning and end of the SSW event.

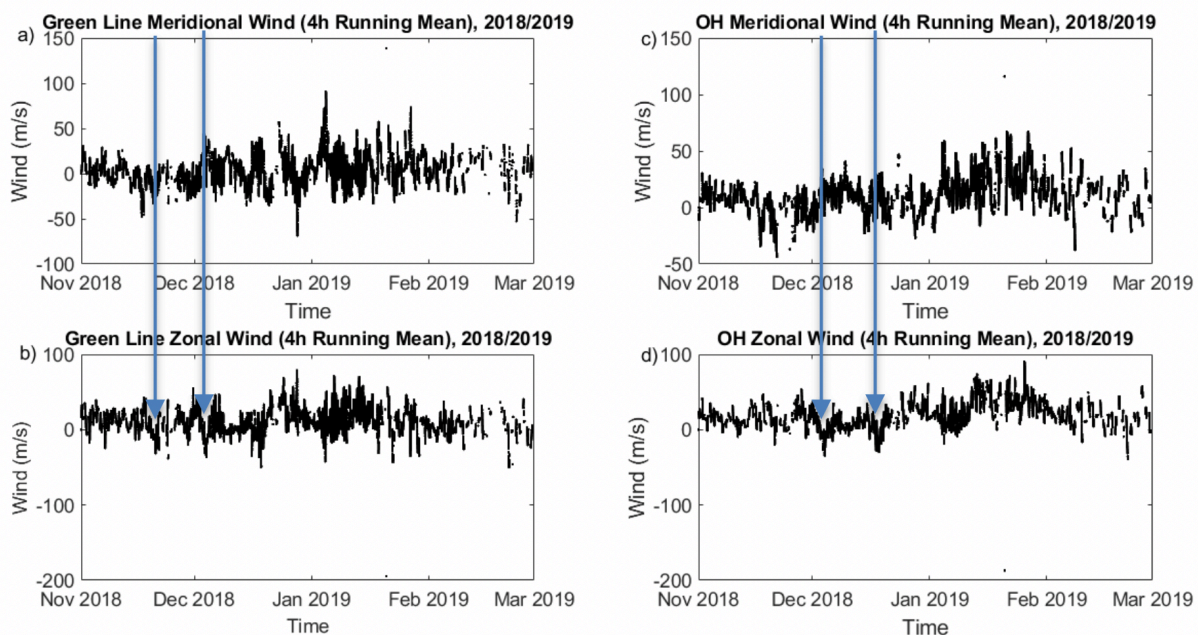


Figure 6-21. 4-hour running mean of the (a) green line meridional, (b) green line zonal, (c) OH meridional and (d) OH zonal winds during the 2018/2019 season. The arrows highlight the weak zonal wind reversal that occurred before the SSW.

The spectral information, provided in the S-transform shown in Figure 6-22, indicates that there is an increase in approximately 3-day wave activity slightly before the start of the SSW. This is consistent with what was observed during the 2009 SSW event. However, this feature was not observed during the 2018 SSW event.

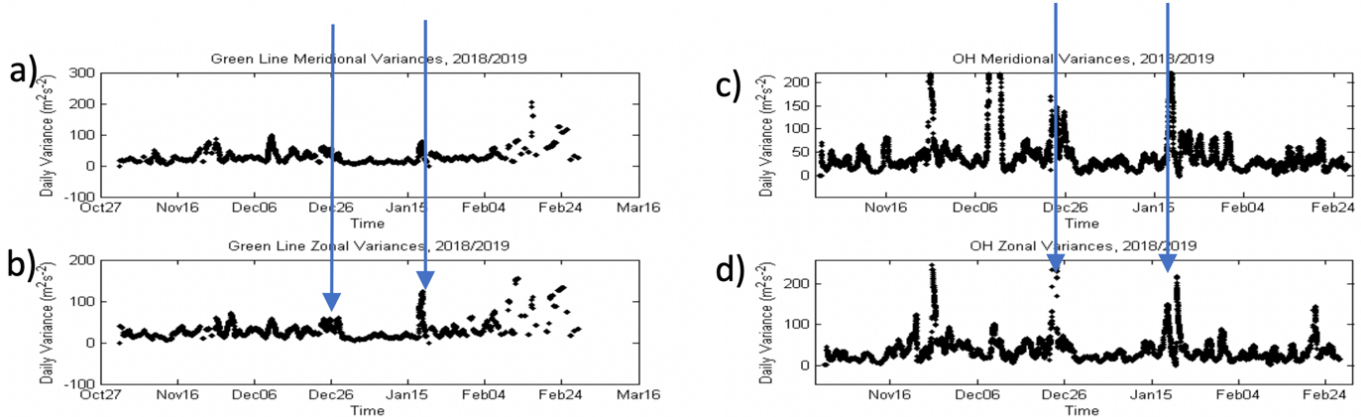


Figure 6-22. Running daily variance of the (a) green line meridional wind, (b) green line zonal wind, (c) OH meridional wind, and (d) OH zonal wind during the 2018/2019 season. The arrows denote the increase in variances observed at the beginning and end of the SSW.

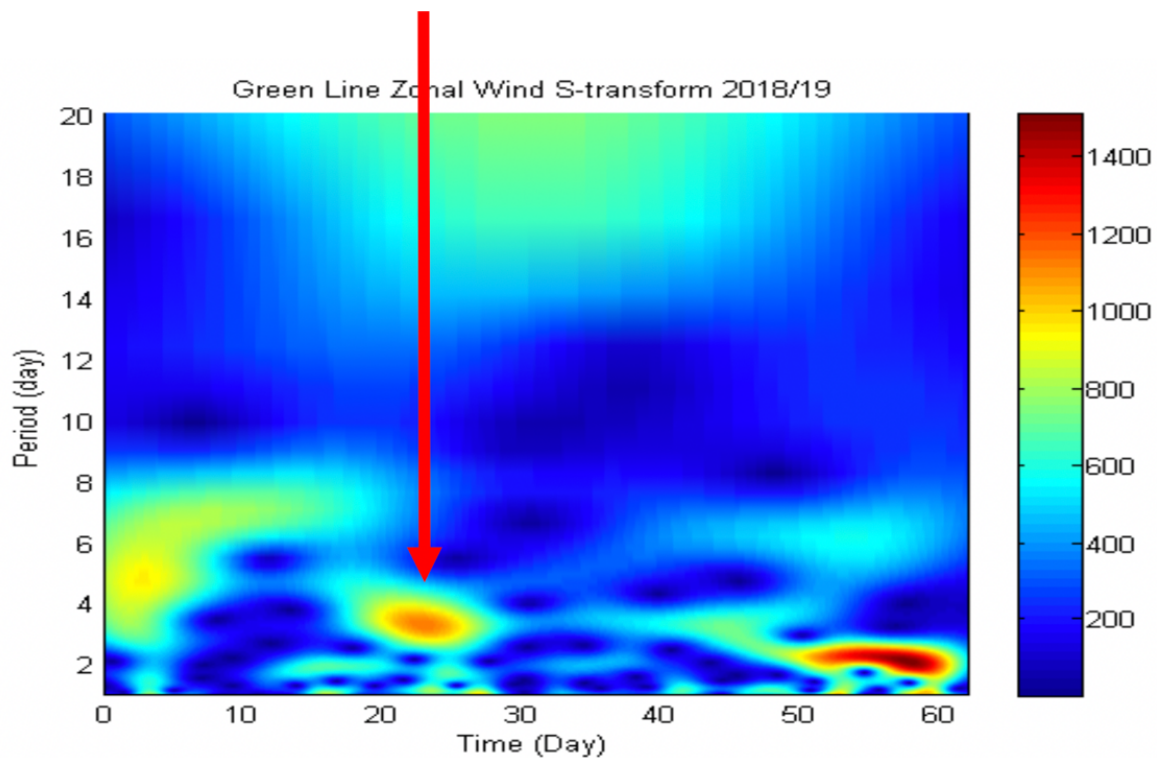


Figure 6-23. S-transform of the green line zonal wind from December 1, 2018, to January 31, 2019. The red arrow highlights the position of the 3 cpd wave event.

An interesting feature appears to show a cascade of energy from lower frequency (~6-day period) activity to higher frequency (~3-day period) activity starting in mid-December 2018 (before the SSW event) through to early January 2019 (see Figure 6-24). A similar cascade in frequency was seen in the sporadic-E signatures seen in the ionosonde data from several Canadian Arctic stations. This feature needs to be studied further to determine the linkages between the neutral wind observations and the sporadic-E signatures.

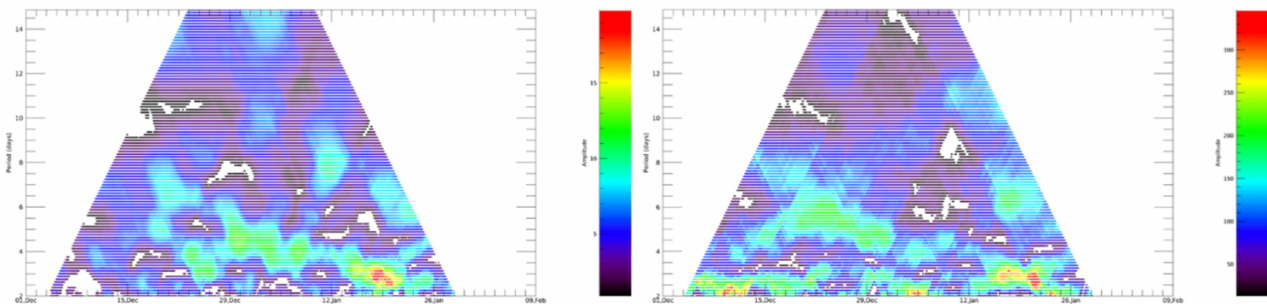


Figure 6-24. Periodogram showing the cascade of wave activity from ~6-day period to ~3-day period during December 2018 and January 2019 for a) OH meridional wind, and b) Es power.

6.5.3 High-latitude ionosphere

As was the case with the 2009 SSW, inferring ionospheric responses from the model simulations was very challenging. The 2019 SSW appears to have been further complicated by the occurrence of a moderate geomagnetic storm coincident with the SSW period. In Figure 6-25, we present the daily averaged foF2 for the period between December 2018 to January 2019 at the Chilton ionosonde.

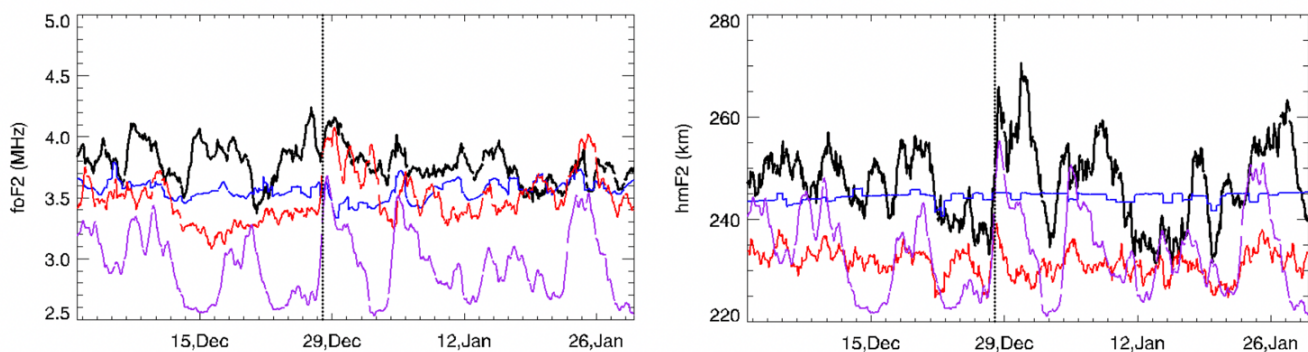


Figure 6-25. Daily smoothed foF2 (left) and hmF2 (right) timeseries from the Chilton ionosonde (black) and for the corresponding E-CHAIM (blue) and TIE-GCM (red) model runs. Note that the TIE-GCM run here was that without geomagnetic forcing; furthermore, we have included Kp index smoothed over the same sampling window and scaled to arbitrary units for reference. The dotted vertical line marks December 28th, at 00:00 UTC.

We note from Figure 6-25 that the period where the TIE-GCM predicts the greatest SSW response is very well aligned with the commencement of a geomagnetic storm. For hmF2, it is clear that geomagnetic activity directly drives ionospheric lifting and, as such, the impacts of the SSW on hmF2 cannot be reliably assessed here. Examining foF2, however, we note that the expected response to this storm, from E-CHAIM, is a negative ionospheric response, where foF2 decreases as a result of the geomagnetic storm. This effect acts against the enhancement feature seen in the TIE-GCM simulations. Looking more closely at the diurnal variations in foF2, we can get a much better picture of what these ionospheric responses look like. In Figure 6-26, we present the foF2 timeseries from the ionosonde and both models after removing the mean diurnal trend.

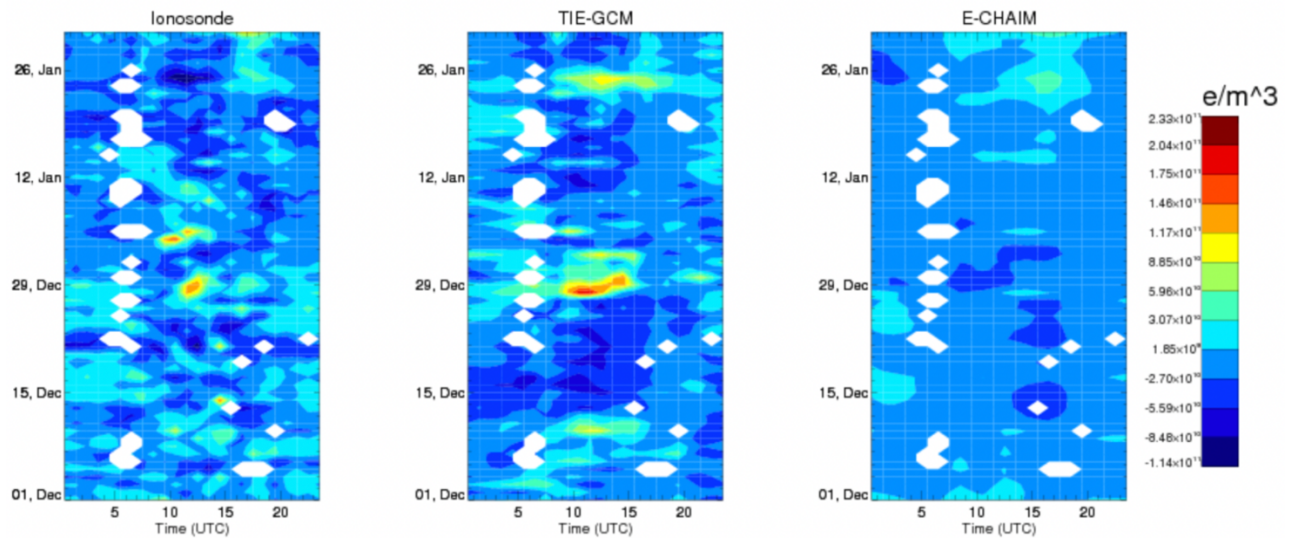


Figure 6-26. foF2 from the Chilton ionosonde, the TIE-GCM without geomagnetic forcing, and the E-CHAIM model, after having removed the mean diurnal trend, calculated over the entire 2-month period.

During the SSW period, we note an anomalous increase in foF2 at the ionosonde during daylight periods with similar behavior in the TIE-GCM run. E-CHAIM, which should only reflect expected geomagnetic impacts on these observations, exhibits a depletion in foF2 during this period, associated with the enhanced geomagnetic activity, that bisects the TIE-GCM enhancement period. One may interpret that the negative ionospheric response acted against the enhancement due to the SSW causing the bisected ionospheric response observed by the ionosonde.

High latitude responses are, however, far more complicated as the regions sensitivity to geomagnetic activity is far more complex than at mid latitudes and the magnitude of the SSW effect on the ionosphere appears to be substantially weaker in the TIE-GCM model simulations. Because of this, attempts to quantify the ionospheric response during this 2018-2019 SSW were discontinued at the preliminary stage. Nevertheless, in Figure 6-27 we present timeseries for foF2 and hmF2 at the Resolute Bay, Canada, ionosonde. In this figure, we have opted not to smooth the data, as was done in Figure 6-25, as the high latitude ionosonde succumbed to absorption-related data gaps regularly over the period.

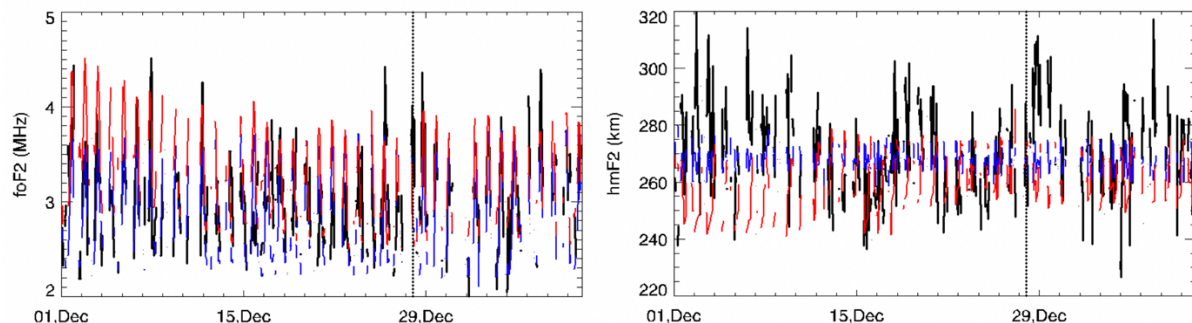


Figure 6-27. foF2 (left) and hmF2 (right) timeseries from the Resolute Bay ionosonde (black) and for the corresponding E-CHAIM (blue) and TIE-GCM (red) model runs. Note that the TIE-GCM run here was that without geomagnetic forcing. The dotted vertical line marks December 28th, at 00:00 UTC.

We note from Figure 6-27, that there is only a subtle model response to the SSW on December 28th, in stark contrast to the European mid-latitude stations. Similar to the 2009 SSW period, however, in the ionosonde foF2 we note a significant enhancement in daytime foF2 ahead of the SSW reversal. The hmF2 behavior, unfortunately, is so heavily dominated by geomagnetic activity during this period that no assessment is possible with respect to real data, despite the appearance of a strong, one-day enhancement in hmF2 in the TIE-GCM simulation.

6.5.4 Mid-latitude ionosphere

Figure 6-28 shows that the highest foF2 is observed on 28 December (third day from the left), the day of the maximum warming. It is accompanied by a slight increase of hmF2. However, on this day a minor-to-moderate geomagnetic storm ($K_p = 4$) occurred, so the effect is a mixture of both peak of SSW and storm. On the other hand, a stronger storm of 5 January ($K_p = 5$) produced a significantly lower enhancement of electron density (foF2).

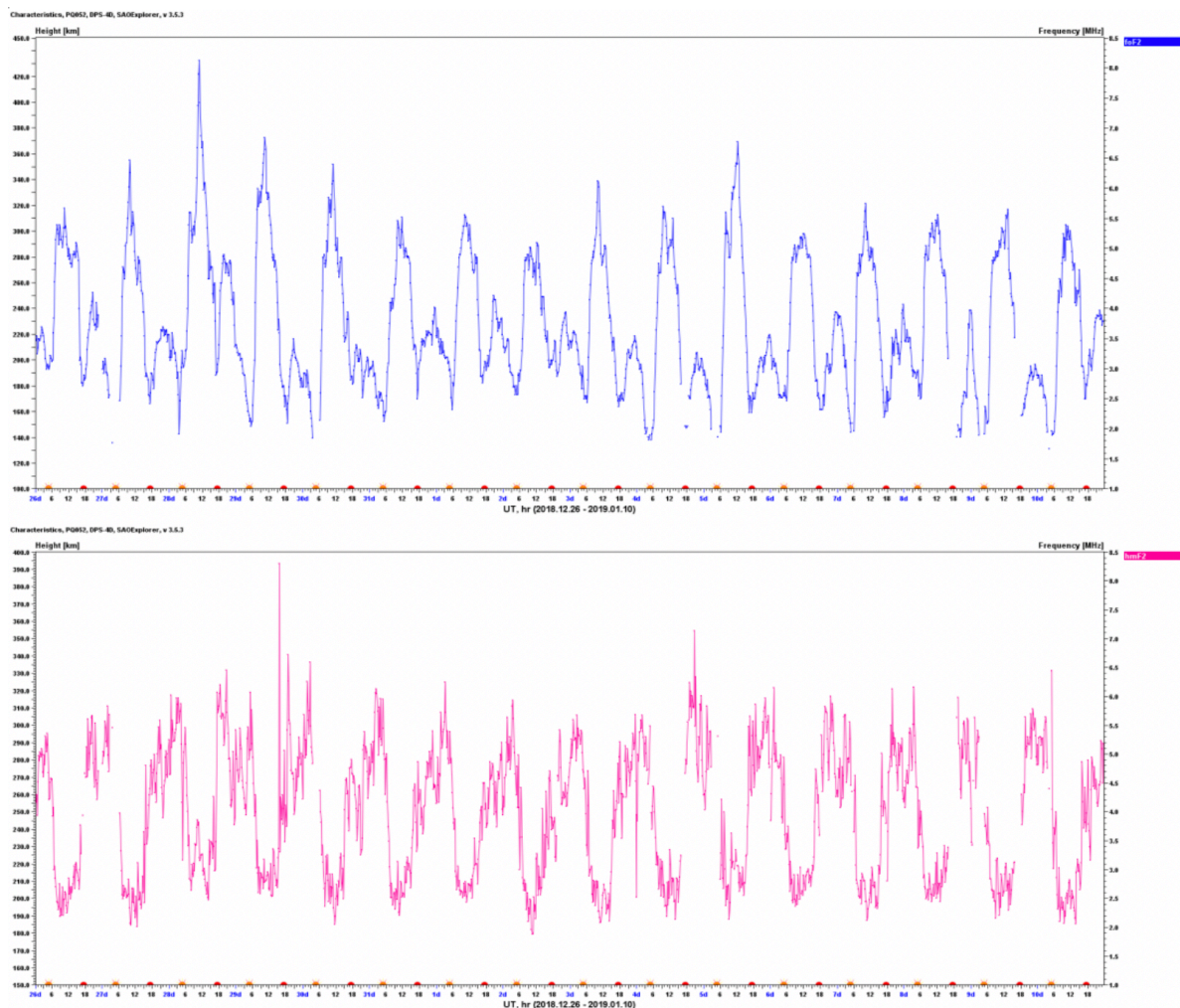


Figure 6-28. Temporal evolution of foF2 (top panel) and hmF2 (bottom panel) at Pruhonice, 26 December 2018 – 10 January 2019.

As for TEC, the only substantial enhancement of the average TEC over Europe was observed on 28 December, again the day of the warming maximum (see Figure 5-12 in Chapter 5). Figure 6-29 compares TEC over Europe for a quiet day, a day when geomagnetic storm occurred, and a day of maximum warming and maximum TEC. Compared to the quiet day, TEC is moderately enhanced everywhere, particularly at higher latitudes. On the day of maximum warming the enhancement of TEC is much larger than the other two cases and it occurs particularly at lower latitudes as in the case of the SSW of February 2018.

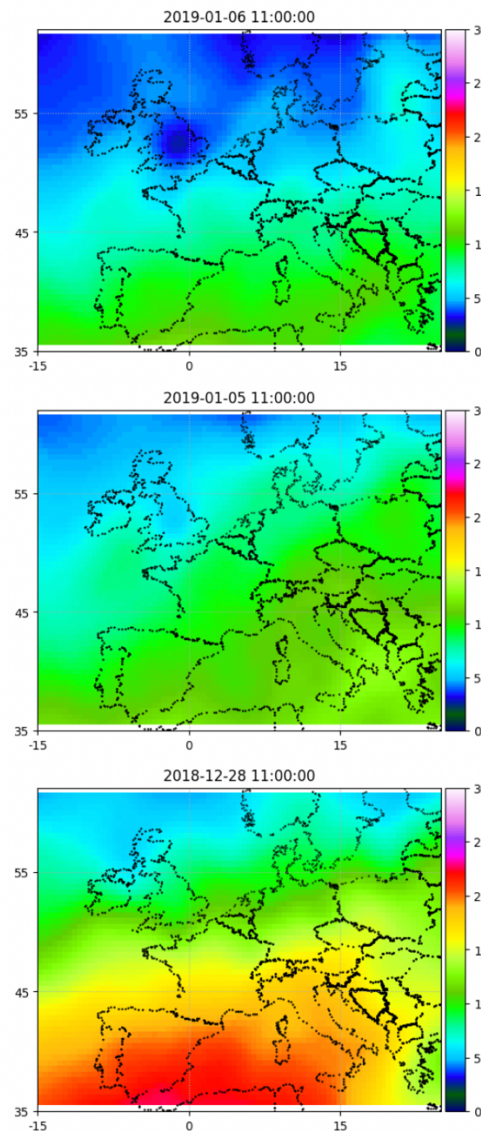


Figure 6-29. Maps of TEC for Europe at 11 UT. Top panel – quiet day; middle panel – day of magnetic storm (5 January, $K_p = 5$); bottom panel – day of maximum warming (28 December).

6.5.5 Low-latitude ionosphere

Figure 6-30 displays the variability of Swarm EEJ (bottom left and right) and IHFAC (top right) during the January 2019 SSW in a similar format as Figures 6-12 and 6-19. Unlike the

January 2015 and February 2018 SSWs, no evidence is found for enhanced ~13-day variations. The results suggest that the M2 tide did not play as important a role for ionospheric variability during the January 2019 SSW.

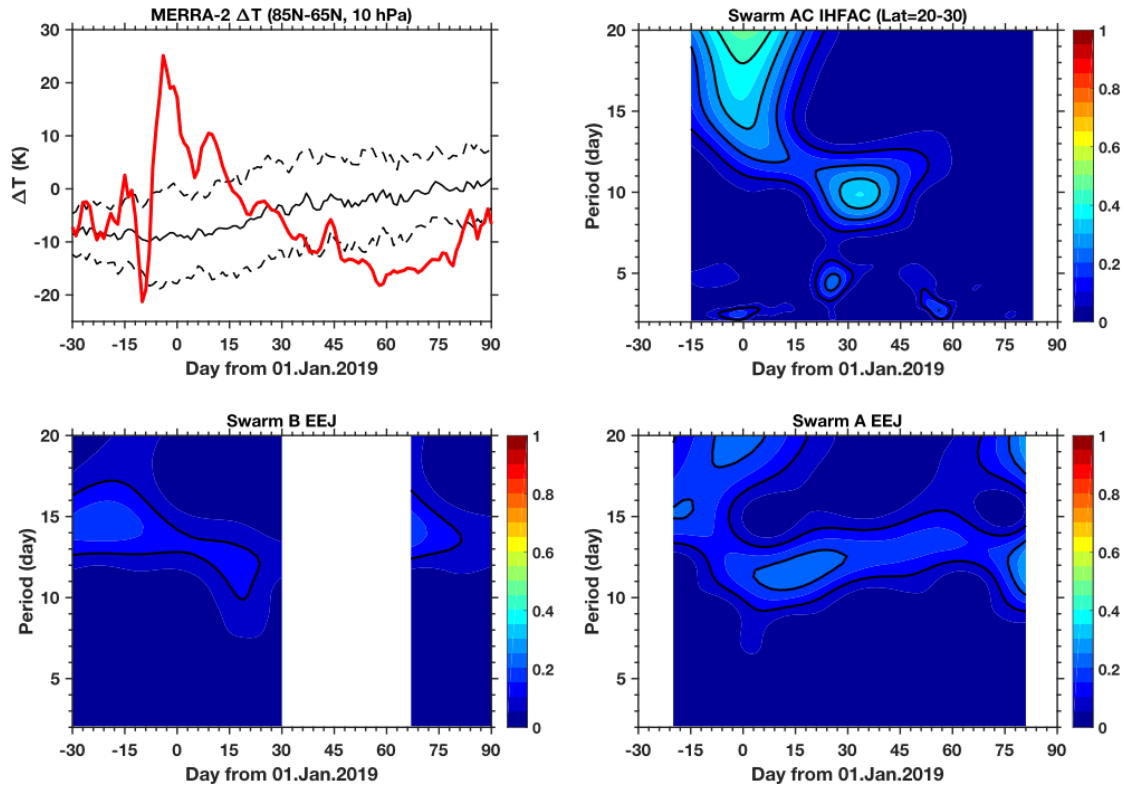


Figure 6-30. Same variables as Figure 6-12 but for December 2018–March 2019.

6.6 September 2019 SSW

6.6.1 Description of SSW

A rare SSW event occurred in the southern hemisphere (SH) in September 2019 (Yamazaki et al., 2020). Figure 6-31 shows the zonal mean zonal wind at 60°S and Antarctic polar temperature at 10 hPa during the September 2019 SSW.

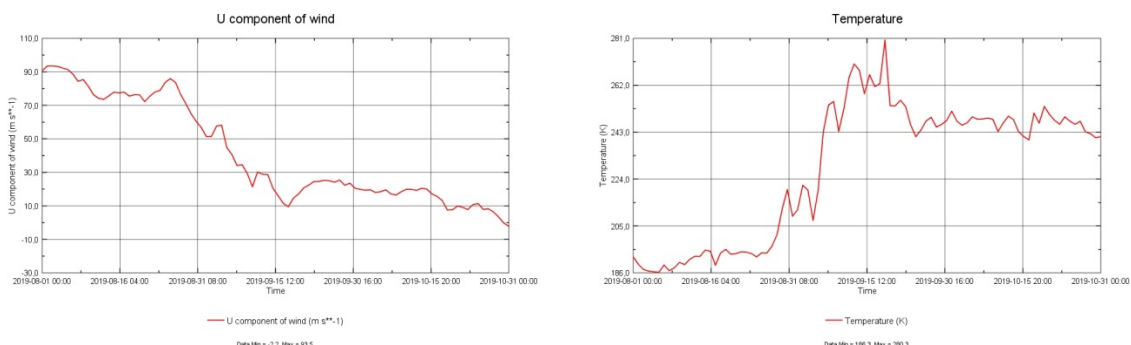


Figure 6-31. Zonal mean zonal wind at 60°S (left) and temperature at 90°S (right) at 10 hPa during June 2019–October 2019 derived from ERA5.

The SSW started on 6 September with an increase of polar temperature (by about 65K in a week). The zonal wind reversal did not occur at 10 hPa. Thus, the event is classified as a minor warming. The maximum of the SSW occurred on 18-20 September when temperature at 10 hPa reached 280K. This SSW is one of the strongest SSW in the SH and the temperature increase is stronger than that of the September 2002 SSW, which is the only major warming identified in the SH (Krüger et al., 2005).

6.6.2 MLT region

Figure 6-32 illustrates the enhancement of the quasi-6-day wave (Q6DW) during the September 2019 SSW. The top panel shows the stratospheric polar temperature at 10 hPa, similar to Figure 6.1.1 but derived from the MERRA-2 reanalysis. The bottom panel displays the amplitude of the westward-propagating wave with zonal wavenumber (ZW) 1 at a height of 96 km at 50°S, as derived from Aura/MLS GPH measurements. Following the temperature enhancement in early September, enhanced wave activity is seen at a period of 5–6 days.

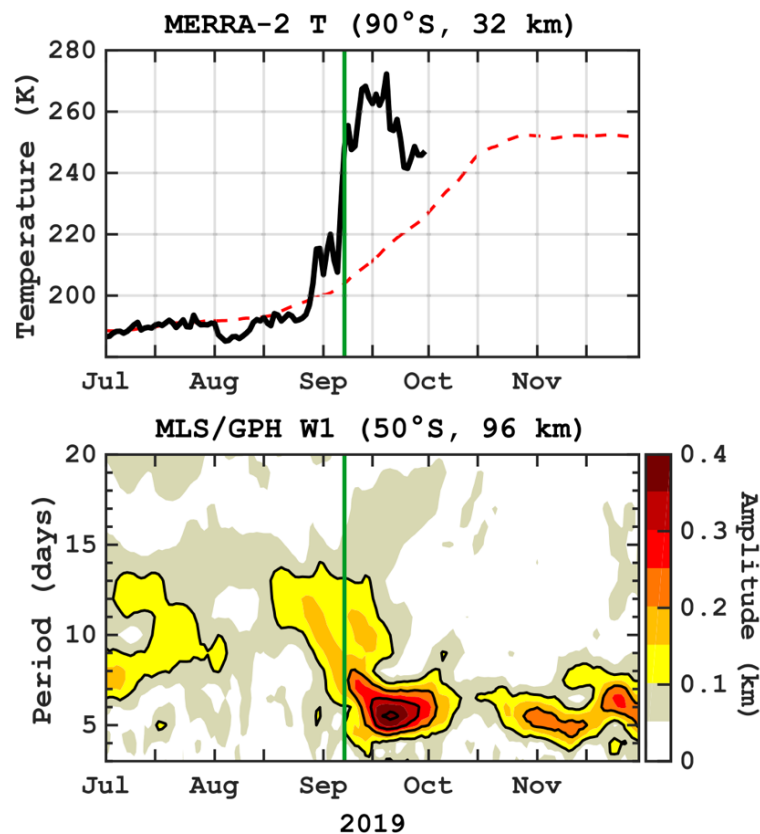


Figure 6-32. (Top) Air temperature at 90°S at 10 hPa during July–November 2019 as derived from MERRA-2. The red dashed line indicates the climatological seasonal cycle. (Bottom) Amplitude of the westward-propagating wave with zonal wavenumber 1 in geopotential height at 50°S at 0.001 hPa as derived from Aura/MLS data.

Figure 6-33 shows the height and latitude structures of the Q6DW in GPH during 10-30 September 2019. At altitudes above 50 km, the amplitude pattern is largely symmetric about the equator with peaks around $\pm 45^\circ$ latitudes. The amplitude structure is consistent with that of the (1,1) Rossby normal mode predicted in linear wave theory (e.g., Forbes, 1995).

Based on Aura/MLS measurements, Yamazaki (2018) reported occasional bursts of Q6DW activity in the MLT region, with the GPH amplitude up to 300 m. The amplitude of the Q6DW observed in September 2019 exceeds 400 m, which is largest ever observed by Aura/MLS since November 2004. Thus, the Q6DW observed following the September 2019 SSW is “exceptional” due to its large amplitude. More studies are required to clarify the causal link between the SSW and large Q6DW.

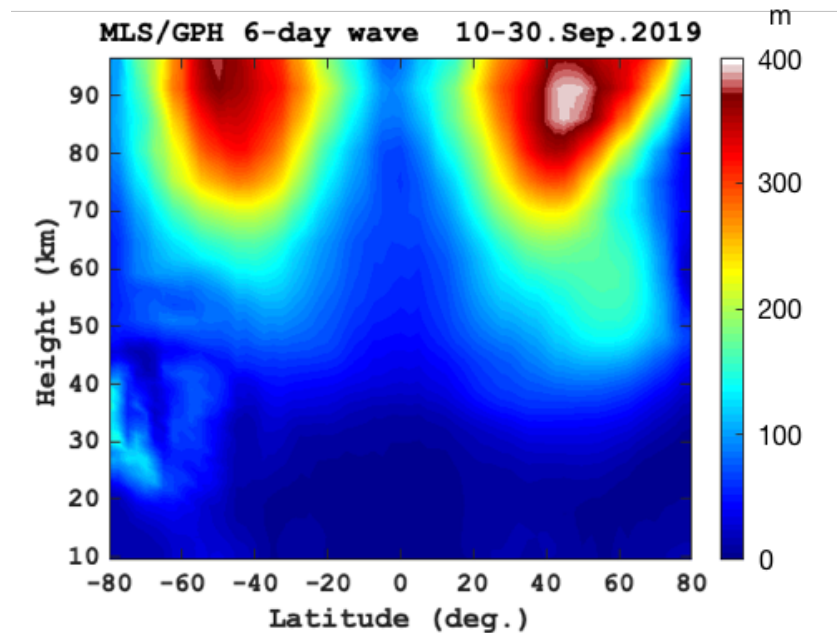


Figure 6-33. Amplitude of the Q6DW (westward propagating wave with zonal wavenumber 1 and period of 6.0 days) in geopotential height during 10–30 September 2019.

6.6.3 High-latitude ionosphere

For the 2019 September SSW, we have gathered two months of manually processed data from the Ukrainian Vernadsky Antarctic station. To first get an impression of the effect of SSW-induced changes on the D-Region ionosphere, we here examine the behavior of the minimum observable frequency f_{min} from the Vernadsky ionosonde in Figure 6-34.

During the SSW we note a substantial and consistent increase in f_{min} both during daytime and at night that persists for several days. While modeling is necessary to infer the cause, previous work suggests that increases in ionospheric absorption during SSWs can be attributed to an increase in planetary wave activity and modulation of NO abundance in the D-Region (Kazimirovsky et al., 2003; Pancheva et al., 1991; Kawahira, 1985). In terms of the F-Region ionosphere, we present a time series of foF2 for the same period as Figure 6-34 in Figure 6-35.

Similar to the other SSW events we have examined at high latitudes, there again appears to be an enhancement in foF2 ahead of the SSW wind reversal at 1 hPa; however, geomagnetic activity is substantially more problematic for this event than the previous SSWs. From the time series of Figure 6-35 we apply a wavelet transform to examine the behavior of the dominant wave modes in the foF2 time series. This wavelet transform is presented in Figure 6-36. From this wavelet transform we note the dominance of diurnal variability modulated

mostly by geomagnetic activity; however, of particular note is the decay of the semi-diurnal mode ahead of and during the SSW period, beginning roughly on the 25th of August and extending until approximately September 7th. It is unlikely that this behavior can be attributed to geomagnetic storms, as such storms tend to modulate the diurnal model and hourly time scales rather than scales between 8 and 16 hours. Simulations are necessary in order to further examine the nature of this semi-diurnal mode decay.

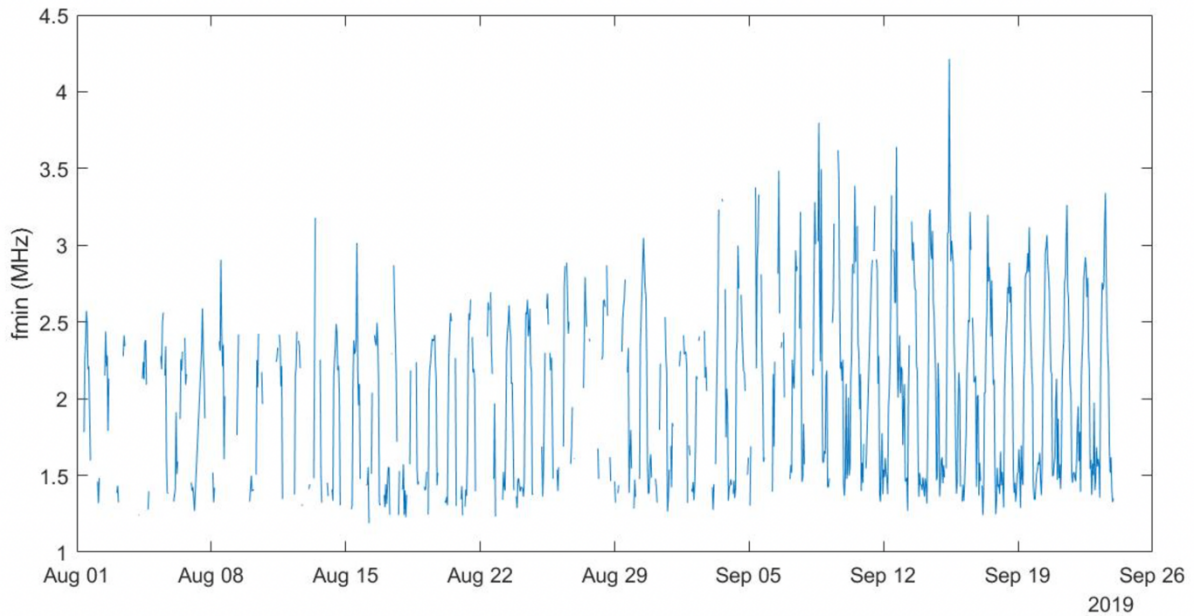


Figure 6-34. Time series of f_{min} from the Vernadsky during the 2019 September SSW.

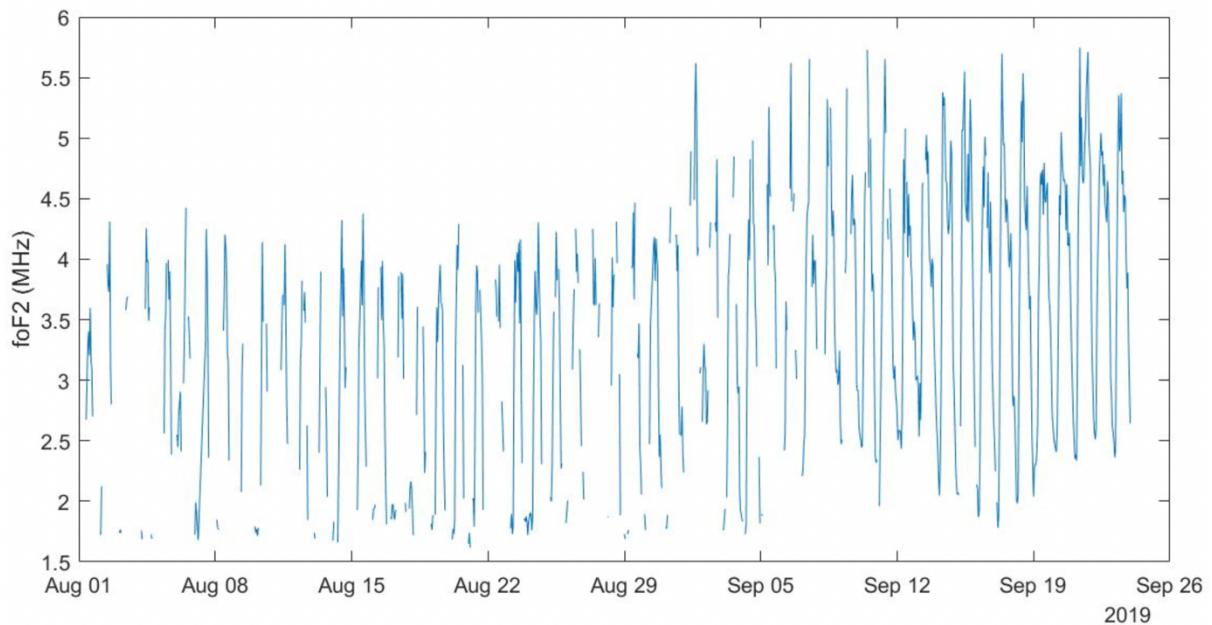


Figure 6-35. Time series of f_oF_2 from the Vernadsky during the 2019 September SSW.

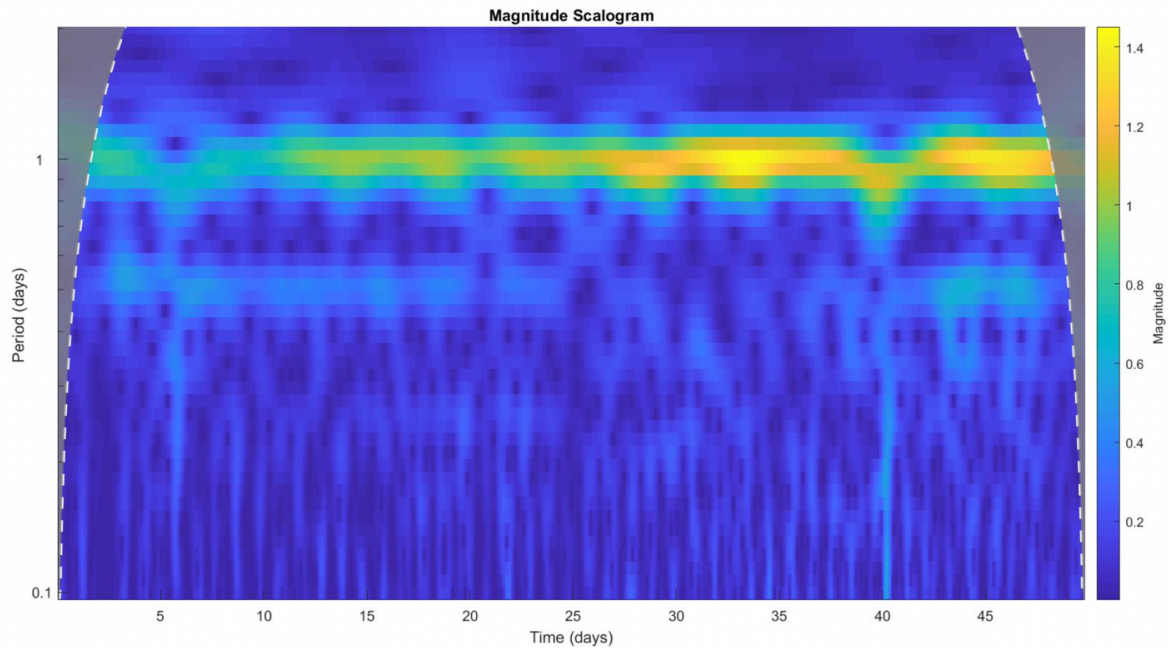


Figure 6-36. Wavelet transform of the observed foF2 at the Vernadski ionosonde. The x-axis is days since the 1st of August, 2019, and amplitudes are in MHz.

6.6.4 Low-latitude ionosphere

Figure 6-37 displays the EEJ intensity during 5 September–5 October 2019 as observed by Swarm B. During this time, the Swarm B satellite was flying in the noontime sector (around 12–13 LT), where EEJ magnetic signatures are largest due to high ionospheric conductivities. The left panel of Figure 6.4.1 reveals ~6-day variations in the EEJ intensity at all longitudes. In the right panel, variations of the EEJ with periods of 4.5–7.5 days are extracted using a bandpass filter. It is seen that the ~6-day variations have a ZW-1 structure with a westward phase propagation, which agree with previously-reported features of the Q6DW effect on the EEJ (Yamazaki et al., 2018).

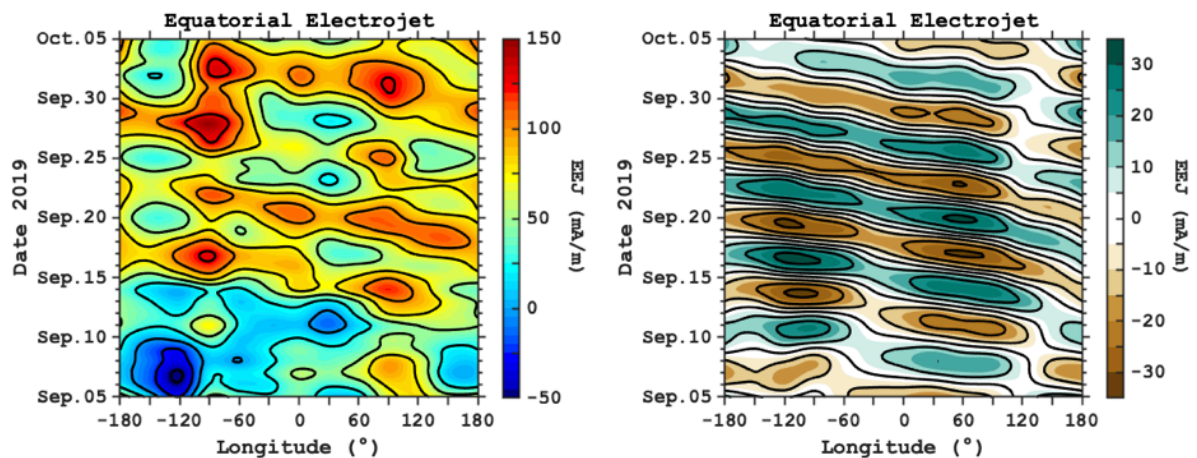


Figure 6-37. EEJ intensity observed by Swarm B during 5 September–5 October 2019. In the right panel, ~6-day variations are extracted using a bandpass filter for periods 4.5–7.5 days.

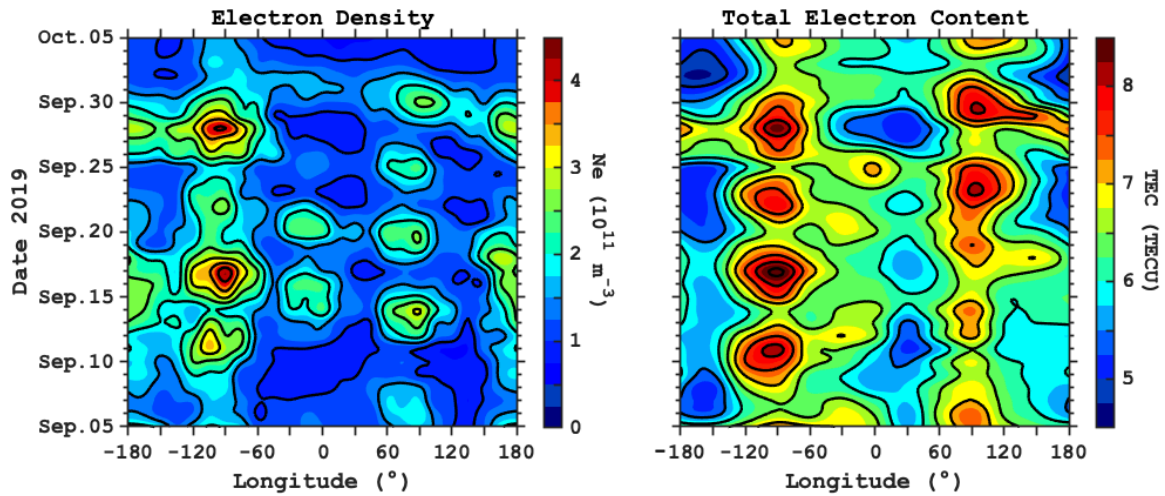


Figure 6-38. Electron density (left) and total electron content (right) observed by Swarm B during 5 September–5 October 2019.

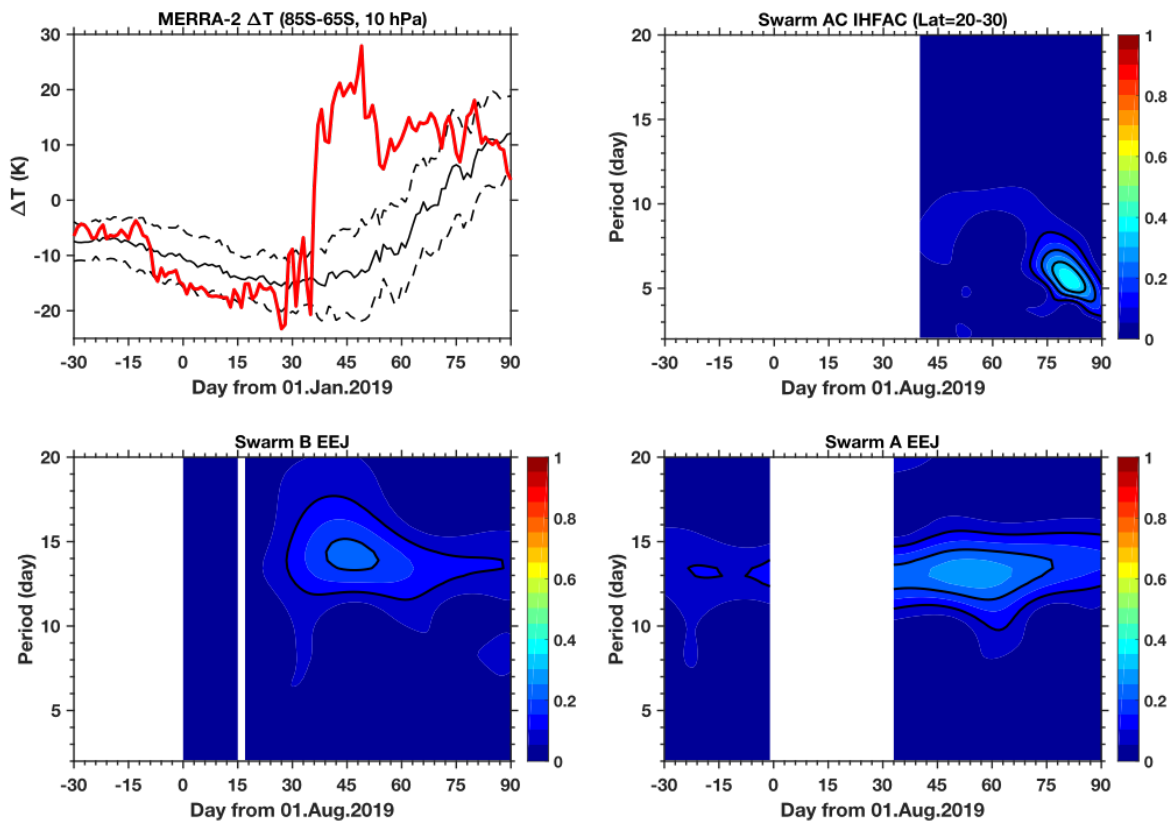


Figure 6-39. Same variables as Figure 6-12 but for July–October 2019.

Figure 6-38 shows that ~6-day variations are also present in plasma densities in the low-latitude region. The ~6-day variations are more prominent at some longitudes than others. The density variability is consistent with that of the EEJ. That is, both the electron density and TEC tend to be larger when the EEJ is stronger. This correlation can be understood as the

dynamo electric field control of the behavior of both EEJ and F-region plasma density (Stolle et al., 2008). The ~6-day variations in Swarm ionospheric parameters are considered to be linked to the unusually strong Q6DW observed in the middle atmosphere during September 2019. More studies are necessary to determine the mechanism by which the Q6DW drives ~6-day ionospheric variations.

As seen in Figures 6-39, the zonal mean EEJ shows ~13-day variability during the SSW, which may be associated with forcing by the M2 tide. Meanwhile, no ~13-day variation is seen in the IHFAC.

6.7 Impact Assessment and Conclusions

6.7.1 Re-statement of VERA scientific questions

The following are the three main scientific questions that are stated in [AD-2]:

- Q1.** What is the response of IHFACs to SSW events and what can we learn about hemispheric coupling?
- Q2.** What is the response of the high-latitude ionosphere to SSW events and what is the relative contribution compared to magnetospheric forcing?
- Q3.** What is the latitudinal extent of SSW effects on the ionosphere, e.g. are these effects similarly significant for the low-, mid- and high-latitude ionosphere?

Below we address these questions in light of the results presented in this Chapter.

6.7.2 Answers to the VERA scientific questions

For **Q1**: We found that the zonal mean IHFAC shows enhanced ~13-day variations during the January 2015 and February 2018 SSWs. Similar variations are also found in the zonal mean EEJ at the same time. These ~13-day variations are considered to be due to forcing by the semidiurnal M2 lunar tide that is known to enhance during SSWs (Zhang and Forbes, 2014). Interestingly, M2 tidal variations are not detected in the IHFAC or EEJ during the January 2019 SSW, which is the strongest SSW in our data since the launch of Swarm in November 2013. The results suggest the possibility that the IHFAC intensity is a useful parameter to monitor the influence of lower atmospheric forcing in the dynamo region like the EEJ intensity.

For **Q2**: The response of the high-latitude ionosphere remains unclear. Model simulations that eliminate magnetospheric forcing do not predict large ionospheric response at high latitudes. The predicted high-latitude ionospheric variability is much smaller than that observed, which is apparently dominated by effects of magnetospheric forcing (especially hmF2). The model does not reproduce the observations well, even when magnetospheric forcing is included. Thus, it is not clear whether the model results obtained without magnetospheric forcing can be trusted.

For **Q3**: Previous studies have established that an SSW can significantly affect the low-latitude ionosphere (see Chapter 2). This has been confirmed with Swarm measurements for recent SSW events. Ionospheric effects of SSWs have also been analyzed for European middle latitudes. The most pronounced ionospheric effect is substantial enhancement in the electron density and foF2 on the day of maximum of stratospheric warming. Its origin has not

yet been understood. In two out of three events (i.e., February 2018 and January 2019 SSWs) the foF2 enhancement is accompanied by a substantial increase of TEC, particularly at European lower latitudes. These results suggest that SSW effects on the ionosphere may be extended into middle latitudes, rather than being confined to low latitudes. Meanwhile, SSW effects on the high-latitude ionosphere seem small, although more study is needed to determine these effects definitively.

6.7.3 Conclusions

In this chapter, we have presented the results of data analyses for the SSWs in January 2009, January 2015, February 2018, January 2019, and September 2019. Based on these results, main scientific questions of the VERA project have been addressed. Progress has been made in identifying SSW effects on the interhemispheric coupling of the ionosphere (Q1) as well as the latitudinal extent of SSW effects on the ionosphere (Q3). However, quantifying SSW effects on the high-latitude ionosphere (Q2) is still a challenge due to overwhelmingly strong effects by magnetospheric forcing, as well as the tenuous performance of the numerical models. More work is needed for better modeling of the high-latitude ionosphere. Progress has also been made in addressing the impact of Antarctic SSWs on the ionosphere owing to the fortunate occurrence of the September 2019 event, which happened to take place during the VERA project.

Chapter 7

Scientific Roadmap

7 Scientific Roadmap

7.1 Scope and Outline

This chapter provides recommendations of topics that can potentially transfer the scientific outcomes of the VERA project into future research activities. 7.2 covers research topics aimed at addressing the scientific questions that emerged through the work of the VERA project. 7.3 highlights the topics that have not been considered in the VERA project but relevant to Swarm+ Coupling [AD-1] in the broader context of SSW effects on the upper atmosphere.

7.2 Recommendations: Follow-on research activities

7.2.1 Numerical modelling of the high-latitude ionosphere

As discussed in Chapter 6, SSW effects on the high-latitude ionosphere remain to be quantified. The models used in the VERA project (i.e., WACCM-X and TIE-GCM) were not able to reproduce high-latitude ionospheric variability during SSWs, which made it difficult to interpret high-latitude data by separating variability due to magnetospheric forcing from those associated with SSW. Improvement of the model is required for a better description of the high-latitude ionosphere. In what follows, we discuss areas of potential improvement for physics-based and empirical models.

In physics-based models, eddy diffusion is a challenging source of error that remains unsolved (Wu et al., 2017). Previous studies have shown that even drag estimates from a single satellite could sufficiently constrain this eddy diffusion to substantially improve model performance (Pilinski and Crowley, 2015) and may be an avenue for future model improvement that could assist in the identification of high latitude SSW effects on the ionosphere.

Specific to high latitudes, both WACCM-X and TIE-GCM use the Roble and Ridley (1987) precipitation scheme, whose characteristic particle precipitation energy does not vary with geomagnetic activity. This is despite Zhang and Paxton (2008) demonstrating that this characteristic energy can vary from 1 keV to 3 keV between Kp 0 and 9. Regardless, both schemes are highly spatially smooth and are driven by a 3-hour Kp index which lacks temporal resolution. Furthermore, the high latitude convection scheme used here, the Heelis model, is similarly driven by Kp and lacks both the temporal and spatial resolution to properly resolve structures, highly important to the overall Joule heating. These issues could affect both the evolution of the ionospheric state and the specification of high latitude mesospheric winds, which are strongly forced by ion drag and Joule heating on timescales that could explain some of the observed WACCM discrepancies with respect to Eureka observations.

These high latitude-specific challenges could be addressed to some extent by migrating to the use of OVATION Prime (Newell et al., 2014) for particle precipitation (similar to what is done with GITM) and a more spatially resolved convection model. Even the simple migration to a better temporally resolved Kp index, perhaps through the use of new products generated at GFZ Potsdam, could provide some improvement. The AMIE assimilative convection system (e.g., Lu, 2017) could similarly improve performance; however, care must be taken in

its application to separate any SSW effects that may manifest in the data assimilated into AMIE.

Regarding empirical models, Themens et al., (2020) demonstrated that existing storm parameterizations in this class of model have begun to push the limits of prescriptive empirical modeling approaches. The simple fact that the high latitude ionosphere exhibits strong forcing at sub-monthly timescales from not only geomagnetic but also atmospheric forcing sources forces the question of whether climatology is at all representative at high latitudes. As E-CHAIM already uses Auroral Electrojet (AE) index and Dst (1-hour resolution), improvement cannot be achieved simply by increasing the resolution of the driving indices. One may attempt to use advanced non-linear techniques to improve the performance of empirical models during geomagnetic disturbances, but the dominance of diurnal and seasonal timescales on the overall variability budget of the high latitude ionosphere will forever make it challenging to extract appreciable forecasting skill without using spectral techniques. Furthermore, the nonlinear interactions between atmospheric and geomagnetic forcing creates a situation whereby correct capturing of geomagnetic forcing cannot be achieved without subsuming some amount of atmospheric forcing into that geomagnetic component, removing the main utility of empirical models in this type of study, namely in that empirical models are independent of atmospheric forcing.

7.2.2 Mechanism for the ionospheric response to SSW at middle and high latitudes

As demonstrated in Chapter 6, Pruhonice ionosonde data, as well as regional-mean TEC, suggest enhancement of the electron density on the day of SSW maximum. The duration of the electron density enhancement is only a day or less. This is different from ionospheric effects of SSW at low latitudes, which have been reported to last for days to weeks. At low latitudes, the ionospheric response to SSW is mainly caused by forcing by solar and lunar semidiurnal tides. The mechanism for the short-lived response at mid latitudes is yet to be identified. As shown in Chapter 5, the TIE-GCM/WACCM-X reproduces TEC enhancement over the Europe during the 2018 and 2019 SSW. We are currently investigating the mechanism for the ionospheric response to SSW at mid latitudes using these simulation results.

We noted evidence of correlations between the meridional wind and sporadic-E on time scales from 3 to 6 days at high latitudes during the 2018/2019 warming. At middle latitudes, the wind-shear mechanism (Whitehead, 1961) dominates the formation of sporadic-E layers, and the sporadic-E occurrence is strongly influenced by neutral wind variability in the lower thermosphere (Arras et al., 2009). However, the role of neutral wind variability for sporadic-E at high latitudes is not established, and more studies are needed.

7.2.3 Changes in gravity wave activity

Mesospheric wind measurements at Eureka reveal a reduction in the wind variance during SSWs. The results may reflect changes in gravity wave (GW) activity during SSWs. Changes in the wind field in the middle atmosphere will result in times when changes in GW filtering will result in enhancements in the propagation of GWs into the thermosphere. As with tides, their dissipation will affect the thermospheric winds (both short term variability and large-

scale induced flows) and constituent profiles in the thermosphere and the character of the ionosphere (Yiğit and Medvedev, 2016).

Global models such as WACCM-X are not capable of resolving GWs. Thus, changes in GWs in the middle atmosphere during SSWs could not be addressed in the VERA project. GW-resolving global models (e.g., Liu et al., 2014; Miyoshi et al., 2018) would be useful for studying this aspect in the future. Effects of GW changes on the ionosphere during SSWs are also to be investigated.

7.2.4 Antarctic SSW

A rare SSW occurred in the SH in September 2019. The investigation of this event was not initially planned in the VERA project, but it has made an excellent case to highlight the difference between ionospheric responses to NH and SH SSWs. Swarm observations have revealed that ionospheric parameters underwent prominent 6-day variations at low latitudes during the September 2019 SSW. It is considered that the 6-day ionospheric variations are associated with the large quasi-6-day wave (Q6DW), which was observed in the middle atmosphere at the same time. ~13-day variations are also found in Swarm data at low latitudes, indicating M2 tidal activity, but the variations are not as large as those during the NH SSWs of January 2009, 2015 and February 2018. Full details of Swarm ionospheric observations during the September 2019 Antarctic SSW can be found in Yamazaki et al. (2020).

The follow-up work, Miyoshi and Yamazaki (2020), examined the link between the Q6DW and 6-day ionospheric variations during the September 2019 SSW on the basis of numerical simulations with GAIA (Ground-to-topside model of Atmosphere and Ionosphere for Aeronomy) (Jin et al., 2011). The results revealed that the 6-day ionospheric variations observed by Swarm are not caused directly by the Q6DW but caused indirectly through the non-linear interaction between the Q6DW and tides.

The remaining questions regarding the SH SSW in September 2019 include (1) the mechanism for the Q6DW enhancement during this SSW, (2) the response of the mid- and high-latitude ionosphere to the SSW, and (3) the response of the thermosphere to the SSW.

7.3 Recommendations: Broader context

7.3.1 SSW effects on small-scale ionospheric structures

High-precision and high-cadence (2 Hz) plasma density measurements from Swarm satellites can resolve not only large-scale structures such as the equatorial ionization anomaly (EIA) but also smaller structures associated with phenomena such as equatorial plasma bubbles (EPBs) (Xiong et al., 2016; Wan et al., 2018), medium-scale traveling ionospheric disturbances (MSTIDs) (Park et al., 2015; Kil et al., 2017), and polar cap patches (e.g., Goodwin et al., 2015). Those phenomena might be influenced by lower atmospheric forcing (and thus SSWs). Both model studies and observations confirm propagation of GWs well into the ionosphere (Vadas and Liu, 2009; Lastovicka, 2006; Yigit et al., 2016), which can be a source of MSTIDs.

Small-scale ionospheric variability may also result from changes in large-scale ionospheric structures. For instance, the longitudinal and seasonal dependence of EPBs is dominated by

the equatorial $E \times B$ vertical plasma drift velocity at the sunset time (Stolle et al., 2008; Xiong et al., 2010), which is strongly controlled by large-scale wave forcing from below (Liu et al., 2020).

Possible SSW effects on small-scale ionospheric structures have been discussed (De Paula et al., 2015; Yu et al., 2020), but the results available so far are not conclusive. Swarm plasma density data are not fully explored in this context. Swarm magnetic data are also available for investigating small-scale ionospheric structures (e.g., Park et al., 2013; Rodríguez-Zuluaga et al., 2019). With 50 Hz magnetic data from Swarm, one can study phenomena with the horizontal scale of less than 10 km (Yin et al., 2019), which cannot be fully resolved by 2 Hz plasma density data. More analyses of Swarm plasma density and magnetic data are recommended for future studies on the response of small-scale ionospheric structures to SSWs together with meteorological observations of the low and middle atmosphere during SSW events.

7.3.2 Ionospheric response to other meteorological phenomena

Although the VERA project has focused on SSW effects on the ionosphere, there are other meteorological processes on various spatial and temporal scales that can potentially drive upper atmospheric variability. For instance, extreme weather phenomena such as storm, tornado and tropical cyclones are known to produce ionospheric perturbations (Nishioka et al., 2013; Chou et al., 2017; Koucká Knížová et al., 2020). On longer time scales, the Madden-Julian Oscillation (MJO) (Zhang, 2005) dominates variability of 30-90 days in the equatorial troposphere. The MJO has an impact on the upward propagation of tides and equatorial Kelvin waves into the upper atmosphere (Gasperini et al., 2020; Kumari et al., 2020), and thus may affect ionospheric variability. The quasi biennial oscillation (QBO) (Baldwin et al., 2001) in the equatorial stratosphere and mesosphere has a period of ~28 months and influences the upward propagation of tides (e.g., Xu et al., 2009), which may drive an ionospheric variation at the same period (e.g., Tang et al., 2014; Yamazaki et al., 2017). Similarly, the El Niño-Southern Oscillation (ENSO) (Wan and Picaut, 2004) with a period of 2-7 years is considered to affect upward wave propagation and thus the ionosphere (e.g., Pedatella and Forbes, 2009; Pedatella and Liu, 2013b). Ionospheric effects of those meteorological phenomena have not been studied as extensively as the ionospheric response to SSW. Dedicated studies based on Swarm ionospheric data are recommended. Long-term ionospheric measurements by Swarm in combination with related satellites providing ionospheric data, such as CHAMP, GRACE, and GRACE-FO (see current ESA DISC Swarm study TIRO) would be useful for separating the variability associated with QBO and ENSO from the well-known 11-year solar-cycle variability.

7.3.3 Upper limit of geomagnetic activity for SSW-ionosphere coupling studies

The ionosphere is strongly controlled by geomagnetic activity. Thus, geomagnetically quiet conditions are preferred when studying relatively small SSW effects on the ionosphere. The question arises as to how quiet is quiet enough for confidently distinguishing ionospheric perturbations associated with SSW and magnetospheric forcing. To answer this question, one needs to know the typical magnitude of ionospheric perturbations during SSWs. At the same time, one also needs to know the typical magnitude of ionospheric perturbations at different

levels of geomagnetic activity. The latter could be evaluated with Swarm plasma density measurements by sorting the data for different Kp or Hp values. (The Hp index is high-cadence version of Kp index; Matzka et al., 2019.) Not only the present value of Kp/Hp but also Kp/Hp values of preceding hours need to be taken into account due to the effect of accumulated geomagnetic activity on the ionosphere (e.g., Araujo-Pradere et al., 2002). The analysis needs to be conducted separately for different latitudes, seasons and solar activity conditions. Thus, long-term data of Swarm and related missions (see 7.3.2) are required. Similar analysis can also be conducted using ground-based ionosondes, they provide very good estimation of the electron density up to the peak height of F2 layer for relatively high number of stationary points for extended periods.

7.3.4 Neutral vs plasma density response to SSW

Simultaneous measurements of thermospheric and ionospheric parameters can provide useful information about the upper atmospheric response to SSWs. The plasma density response can arise from changes in both electric field and neutral composition. During SSWs, winds associated with atmospheric waves from the lower atmosphere drive electric field perturbations at E-region heights. These electric fields are transmitted along equipotential magnetic field lines to the F region where the $E \times B$ drift dominates the plasma transport. As a result, the F-region plasmas distribution can be altered in response to wave forcing from the lower atmosphere (e.g., Chau et al., 2010; Goncharenko et al., 2010). It is also known that wave forcing can affect the neutral composition of the upper atmosphere. This is because most upward-propagating waves from the lower atmosphere dissipate in the lower thermosphere and the dissipation of waves has a mixing effect on the atmospheric composition (Yamazaki and Richmond, 2013; Yue and Wang, 2014). Enhanced tidal forcing during SSWs is predicted to reduce the ratio of the atomic oxygen O to molecular nitrogen N₂ (the so-called [O]/[N₂] ratio) of the entire thermosphere, which reduces the plasma density at mid and low latitudes (Pedatella et al., 2016b).

Oberheide et al. (2020) reported a reduction in the [O]/[N₂] ratio during the January 2019 SSW and attributed it to the mixing effect caused by enhanced tidal forcing. The tidal mixing effect may also be detected in the thermospheric mass density derived, for example, from an accelerometer. The loss of O in the upper thermosphere due to wave mixing is expected to cause a reduction in the mass density at those altitudes. Indeed, Liu et al. (2011) reported mass density reductions of up to 45% based on accelerometer data from CHAMP (~325 km) and GRACE (~475 km) during the January 2009 SSW. Fuller-Rowell et al. (2011b), however, argued that the decrease in the thermospheric mass density during the SSW can be attributed, in large part, to changes in geomagnetic activity. Later, Yamazaki et al. (2015) using satellite orbital decay data during 1967–2013 showed that the global-mean thermospheric mass density reduction during SSW is 3–7%. Unfortunately, Swarm accelerometer suffered from disturbances of various causes (Siemes et al., 2016) and detecting mass density perturbations of 3–7% appears to be difficult.

As a recommendation for future studies on the SSW effects on the plasma density, especially those intending to separate the contributions of the electric field and neutral composition, it is desired to involve thermospheric mass density measurements with precision better than a few % and/or measurements of the [O]/[N₂] ratio with similar precision, along with plasma density measurements.

7.3.5 Optimum stratospheric parameters for SSW-ionosphere coupling studies

The onset and magnitude of an SSW is conventionally determined based on the temperature and zonal mean zonal wind velocity at 10 hPa at 60°N (Butler et al., 2015). The zonal wind at 10 hPa is used to judge whether the SSW is "major" or "minor". It is known, however, that the distinction between major and minor warming is not necessarily relevant to the SSW impact on the middle and upper atmosphere. For instance, the minor warming in January 2015 caused strong disturbances in the middle atmosphere that are similar to those during major warmings (Manney et al., 2015). In the VERA project, we found that lunar tidal perturbations in interhemispheric field-aligned currents (IHFACs) and equatorial electrojet (EEJ) intensity observed by Swarm were more pronounced during the 2015 minor SSW than during the 2019 major SSW. A search of a stratospheric parameter that better predicts the SSW impact on the middle and upper atmosphere is recommended.

Zhang and Forbes (2014) used the zonal mean zonal wind at 1 hPa at 70°N to evaluate SSW effects on the semidiurnal lunar tide (M2) in the neutral temperature at an altitude of 110 km. They showed that the peak amplitude and onset time of the M2 enhancement during 2003–2018 are correlated with those of the weakening of the zonal mean zonal wind (1 hPa, 70°N), which they call the polar vortex weakening (PVW). Siddiqui et al. (2015b) found that there is good correspondence between the PVW and M2 tidal variability in the EEJ intensity during 1997–2013. In the VERA project, however, we found that the M2 tidal enhancement in the neutral temperature at 110 km, as well as those in IHFACs and EEJ, was weaker during the 2019 major SSW than during the 2015 minor SSW despite the stronger PVW (Chapter 6, Figure 6-11). The results suggest that the PVW is not a perfect parameter for predicting SSW effects on the ionosphere, and therefore a search for a better proxy should be continued.

Apart from the zonal mean zonal wind, temperature parameters are also used for characterization of SSWs, such as the polar temperature and the meridional gradient of the zonal mean temperature at 10 hPa. It may be possible to create a more robust proxy for SSW effects on the ionosphere by combining various wind and temperature parameters, rather than using a parameter at a single height and latitude.

7.3.6 Acquisition of more comprehensive and global data

Finally, it is important to collect more upper atmospheric data for a better understanding of the response of the ionosphere and thermosphere to SSWs. Both ground-based measurements and in-situ satellite measurements give limited information about the global response. One approach to this issue is to use a whole atmosphere model that is partially constrained with meteorological data and use upper atmospheric data to validate the model. In the VERA project we took this approach as has been done in many other studies (e.g., Jin et al., 2012; Pedatella et al., 2014b). Another approach is data assimilation. In this case, upper atmospheric data are combined with a model to estimate the optimal state of the upper atmosphere. For plasma density data, which are relatively abundant, some data assimilation products already exist (e.g., Schunk et al., 2004; Lin et al., 2017) and have been used to investigate ionospheric response to SSWs (e.g., Lin et al., 2019). Data assimilation products also exist for thermospheric mass density (e.g., Matsuo et al., 2012; Sutton, 2018) but more data inputs will be necessary to achieve the accuracy required for the detection of a few % perturbations that are expected from observations during SSWs (Yamazaki et al., 2015). More ionospheric and

thermospheric data are anticipated from NASA's latest satellite mission Ionospheric Connection Explorer (ICON) (Immel et al., 2017). Also, Daedalus (Sarris et al., 2020), a candidate for ESA Earth Explore Mission, is expected to add a substantial amount of ionospheric and thermospheric data if the mission succeeds. Coordinated international observational campaigns focusing on SSWs would also enhance the amount of upper atmospheric data useful for vertical coupling studies. These would also provide global information on short term variability such as that associated with GWs and determine the extent to which the variability peaks at the beginning and end of warmings reported on in this study are a global phenomenon which needs to be incorporated as part of our understanding of the ionospheric and thermospheric response to SSWs.

Applicable Documents

- [AD-1] ESA AO/1-9514/18/NL/IA, Invitation to Tender for Swarm+ Coupling: High-Low Atmosphere Interactions, 19/09/2018.
- [AD-2] ESA-EOPSM-SWRM-SOW-3403, Statement of Work for Swarm+ Coupling: High-Low Atmosphere Interactions, Issue 1, Revision 0, 12/09/2018.
- [AD-3] Proposal for Swarm+ Coupling: High-Low Atmosphere Interactions, VERA: VERTICAL coupling in Earth's Atmosphere at mid and high latitudes, 19/11/2018.

References

- Acker, J. G., & Leptoukh, G. (2007). Online analysis enhances use of NASA Earth science data. *Eos, Transactions American Geophysical Union*, 88(2), 14–17, <https://doi.org/10.1029/2007EO020003>.
- Araujo-Pradere, E. A., Fuller-Rowell, T. J., & Codrescu, M. V. (2002) STORM: An empirical storm-time ionospheric correction model: 1. Model description. *Radio Science*, 37(5), 1-12, <https://doi.org/10.1029/2001RS002467>.
- Arras, C., Jacobi, C., & Wickert, J. (2009). Semidiurnal tidal signature in sporadic E occurrence rates derived from GPS radio occultation measurements at higher midlatitudes. *Annales geophysicae* Vol. 27, No. 6, pp. 2555-2563, <https://doi.org/10.5194/angeo-27-2555-2009>.
- Alken, P., Maus, S., Vigneron, P., Sirol, O., & Hulot, G. (2013a). Swarm SCARF equatorial electric field inversion chain. *Earth Plan. Space*, 65(11), 11, <https://doi.org/10.5047/eps.2013.09.008>.
- Alken, P., Chulliat, A., Maus, S. (2013b). Longitudinal and seasonal structure of the ionospheric equatorial electric field. *J. Geophys. Res. Space Phys.*, 118(3), 1298-1305, <https://doi.org/10.1029/2012JA018314>.
- Alken, P., Maus, S., Chulliat, A., Vigneron, P., Sirol, O., & Hulot, G. (2015). Swarm equatorial electric field chain: first results. *Geophys. Res. Lett.*, 42(3), 673-680, <https://doi.org/10.1002/2014GL062658>.
- Anderson, D., & Araujo-Pradere, E. A. (2010). Sudden stratospheric warming event signatures in daytime ExB drift velocities in the Peruvian and Philippine longitude sectors for January 2003 and 2004. *Journal of Geophysical Research: Space Physics*, 115(A8), <https://doi.org/10.1029/2010JA015337>.
- Andrews, D. G., Leovy, C. B., & Holton, J. R. (1987). *Middle atmosphere dynamics* (Vol. 40). Academic press.
- Azeem, I., Crowley, G., & Honniball, C. (2015). Global ionospheric response to the 2009 sudden stratospheric warming event using Ionospheric Data Assimilation Four - Dimensional (IDA4D) algorithm. *Journal of Geophysical Research: Space Physics*, 120(5), 4009-4019, <https://doi.org/10.1002/2015JA020993>.

- Baldwin, M. P., Gray, L. J., Dunkerton, T. J., Hamilton, K., Haynes, P. H., Randel, W. J., Holton, J. R., Alexander, M. J., Hirota, I., Horinouchi, T., Jones, D. B. A., Kinnersley, J. S., Marquardt, C., & Sato, K. (2001). The quasi-biennial oscillation. *Reviews of Geophysics*, 39(2), 179-229, <https://doi.org/10.1029/1999RG000073>.
- Bergeot N., Chevalier J.-M., Bruyninx C., Pottiaux E., Aerts W., Baire Q., Legrand J., P. Defraigne, W. Huang (2014). Near real-time ionospheric monitoring over Europe at the Royal Observatory of Belgium using GNSS data. *J. Space Weather Space Clim.*, <https://doi.org/10.1051/swsc/2014028>.
- Bessarab, F. S., Korenkov, Y. N., Klimenko, M. V., Klimenko, V. V., Karpov, I. V., Ratovsky, K. G., & Chernigovskaya, M. A. (2012). Modeling the effect of sudden stratospheric warming within the thermosphere–ionosphere system. *Journal of Atmospheric and Solar-Terrestrial Physics*, 90, 77-85, <https://doi.org/10.1016/j.jastp.2012.09.005>.
- Bolaji, O. S., et al. (2016), Solar quiet current response in the African sector due to a 2009 sudden stratospheric warming event, *J. Geophys. Res. Space Physics*, 121, 8055– 8065, doi:10.1002/2016JA022857, <https://doi.org/10.1002/2016JA022857>.
- Borovsky, J. E., & Denton, M. H. (2006). Differences between CME-driven storms and CIR-driven storms. *Journal of Geophysical Research: Space Physics*, 111(A7), <https://doi.org/10.1029/2005JA011447>.
- Burešová, D., Laštovička, J., Hejda, P., Bochníček, J. (2014). Ionospheric disturbances under low solar activity conditions. *Adv. Space Res.*, 54, 185-196, <http://dx.doi.org/10.1016/j.asr.2014.04.007>.
- Buchert, S., Zangerl, F., Sust, M., André, M., Eriksson, A., Wahlund, J. E., Opgenoorth, H. (2015). SWARM observations of equatorial electron densities and topside GPS track losses. *Geophys. Res. Lett.*, 42(7), 2088-2092, <https://doi.org/10.1002/2015GL063121>.
- Butler, A. H., Seidel, D. J., Hardiman, S. C., Butchart, N., Birner, T., & Match, A. (2015). Defining sudden stratospheric warmings. *Bulletin of the American Meteorological Society*, 96(11), 1913-1928, <https://doi.org/10.1175/BAMS-D-13-00173.1>.
- Chang, L. C., Palo, S. E., & Liu, H. L. (2011). Short-term variability in the migrating diurnal tide caused by interactions with the quasi 2 day wave. *Journal of Geophysical Research: Atmospheres*, 116(D12), <https://doi.org/10.1029/2010JD014996>.
- Chang, L. C., Liu, J. Y., & Palo, S. E. (2011). Propagating planetary wave coupling in SABER MLT temperatures and GPS TEC during the 2005/2006 austral summer. *Journal of Geophysical Research: Space Physics*, 116(A10), <https://doi.org/10.1029/2011JA016687>.
- Chang, L. C., Lin, C. H., Liu, J. Y., Balan, N., Yue, J., & Lin, J. T. (2013). Seasonal and local time variation of ionospheric migrating tides in 2007–2011 FORMOSAT - 3/COSMIC and TIE - GCM total electron content. *Journal of Geophysical Research: Space Physics*, 118(5), 2545-2564, <https://doi.org/10.1002/jgra.50268>.
- Charlton, A. J., & Polvani, L. M. (2007). A new look at stratospheric sudden warmings. Part I: Climatology and modeling benchmarks. *Journal of Climate*, 20(3), 449-469.

- Chau, J. L., B. G. Fejer, and L. P. Goncharenko (2009), Quiet variability of equatorial ExB drifts during a sudden stratospheric warming event, *Geophys. Res. Lett.*, 36, L05101, <https://doi.org/10.1029/2008GL036785>.
- Chau, J. L., N. A. Aponte, E. Cabassa, M. P. Sulzer, L. P. Goncharenko, and S. A. González (2010), Quiet time ionospheric variability over Arecibo during sudden stratospheric warming events, *J. Geophys. Res.*, 115, A00G06, <https://doi.org/10.1029/2010JA015378>.
- Chau, J. L., Goncharenko, L. P., Fejer, B. G., & Liu, H. L. (2012). Equatorial and low latitude ionospheric effects during sudden stratospheric warming events. *Space Science Reviews*, 168(1-4), 385-417, <https://doi.org/10.1007/s11214-011-9797-5>.
- Chen, G., Wu, C., Zhang, S., Ning, B., Huang, X., Zhong, D., Qi, H., Wang, J., and Huang, L. (2016), Midlatitude ionospheric responses to the 2013 SSW under high solar activity, *J. Geophys. Res. Space Physics*, 121, 790–803, <https://doi.org/10.1002/2015JA021980>.
- Cherniak, I., Krankowski, A., Zakharenkova, I. (2018), *GPS Solut.*, 22, 69, <https://doi.org/10.1007/s10291-018-0730-1>.
- Chou, M. Y., Lin, C. C., Yue, J., Tsai, H. F., Sun, Y. Y., Liu, J. Y., & Chen, C. H. (2017). Concentric traveling ionosphere disturbances triggered by Super Typhoon Meranti (2016). *Geophysical Research Letters*, 44(3), 1219-1226, <https://doi.org/10.1002/2016GL072205>.
- Conde, M. G., and M. J. Nicolls (2010), Thermospheric temperatures above Poker Flat, Alaska, during the stratospheric warming event of January and February 2009, *J. Geophys. Res.*, 115, D00N05, <https://doi.org/10.1029/2010JD014280>.
- Copernicus Climate Change Service (C3S): ERA-5: Fifth generation of ECMWF atmospheric reanalyses of the global climate. Copernicus Climate Change Service Climate Data Store (CDS).
- de Jesus, R., Batista, I. S., Fagundes, P. R., Venkatesh, K., & de Abreu, A. J. (2017a). Ionospheric response to the 2006 sudden stratospheric warming event over the equatorial and low latitudes in the Brazilian sector using GPS observations. *Journal of Atmospheric and Solar-Terrestrial Physics*, 154, 92-103, <https://doi.org/10.1016/j.jastp.2016.12.005>.
- de Jesus, R., Batista, I. S., de Abreu, A. J., Fagundes, P. R., Venkatesh, K., & Denardini, C. M. (2017b). Observed effects in the equatorial and low-latitude ionosphere in the South American and African sectors during the 2012 minor sudden stratospheric warming. *Journal of Atmospheric and Solar-Terrestrial Physics*, 157, 78-89, <https://doi.org/10.1016/j.jastp.2017.04.003>.
- de Jesus, R., Batista, I. S., Jonah, O. F., Abreu, A. J., Fagundes, P. R., Venkatesh, K., & Denardini, C. M. (2017c). An investigation of the ionospheric disturbances due to the 2014 sudden stratospheric warming events over Brazilian sector. *Journal of Geophysical Research: Space Physics*, 122, 11,698–11,715. <https://doi.org/10.1002/2017JA024560>.
- de Paula, E. R., O. F. Jonah, A. O. Moraes, E. A. Kherani, B. G. Fejer, M. A. Abdu, M. T. A. H. Muella, I. S. Batista, S. L. G. Dutra, and R. R. Paes (2015), Low-latitude scintillation weakening during sudden stratospheric warming events, *J. Geophys. Res. Space Physics*, 120, 2212–2221, <https://doi.org/10.1002/2014JA020731>.

Drob, D. P., Emmert, J. T., Crowley, G., Picone, J. M., Shepherd, G. G., Skinner, W., Hays, P., Niecejewski, R. J., Larsen, M., She, C. Y., Meriwether, J. W., Hernandez, G., Jarvis, M. J., Sipler, D. P., Tepley, C. A., O'Brien, M. S., Bowman, J. R., Wu, Q., Murayama, Y., Kawamura, S., Reid, I. M., and Vincent, R. A. (2008), An empirical model of the Earth's horizontal wind fields: HWM07, *J. Geophys. Res.*, 113, A12304, <https://doi.org/10.1029/2008JA013668>.

Evans, J. (1969), Theory and practice of ionosphere study by Thomson scatter radar, *Proc. IEEE*, 57(4), 496–530.

Fang, T.-W., T. Fuller-Rowell, R. Akmaev, F. Wu, H. Wang, and D. Anderson (2012), Longitudinal variation of ionospheric vertical drifts during the 2009 sudden stratospheric warming, *J. Geophys. Res.*, 117, A03324, <https://doi.org/10.1029/2011JA017348>.

Fang, T. W., Fuller - Rowell, T., Wang, H., Akmaev, R., & Wu, F. (2014). Ionospheric response to sudden stratospheric warming events at low and high solar activity. *Journal of Geophysical Research: Space Physics*, 119(9), 7858-7869, <https://doi.org/10.1002/2014JA020142>.

Fejer, B. G., M. E. Olson, J. L. Chau, C. Stolle, H. Lühr, L. P. Goncharenko, K. Yumoto, and T. Nagatsuma (2010), Lunar-dependent equatorial ionospheric electrodynamic effects during sudden stratospheric warmings, *J. Geophys. Res.*, 115, A00G03, <https://doi.org/10.1029/2010JA015273>.

Fejer, B. G., B. D. Tracy, M. E. Olson, and J. L. Chau (2011), Enhanced lunar semidiurnal equatorial vertical plasma drifts during sudden stratospheric warmings, *Geophys. Res. Lett.*, 38, L21104, <https://doi.org/10.1029/2011GL049788>.

Fejer, B. G., Blanc, M., & Richmond, A. D. (2017). Post-storm middle and low-latitude ionospheric electric fields effects. *Space Science Reviews*, 206(1-4), 407-429, <https://doi.org/10.1007/s11214-016-0320-x>.

Forbes, J. M. (1982). Atmospheric tides: 1. Model description and results for the solar diurnal component. *Journal of Geophysical Research: Space Physics*, 87(A7), 5222-5240.

Forbes, J. M., & Leveroni, S. (1992). Quasi 16-day oscillation in the ionosphere. *Geophysical Research Letters*, 19(10), 981-984, <https://doi.org/10.1029/92GL00399>.

Forbes, J. M., Zhang, X., Talaat, E. R., & Ward, W. (2003). Nonmigrating diurnal tides in the thermosphere. *Journal of Geophysical Research: Space Physics*, 108(A1), <https://doi.org/10.1029/2002JA009262>.

Forbes, J. M., Zhang, X., Palo, S., Russell, J., Mertens, C. J., & Mlynczak, M. (2008). Tidal variability in the ionospheric dynamo region. *Journal of Geophysical Research: Space Physics*, 113(A2), <https://doi.org/10.1029/2007JA012737>.

Forbes, J. M., Zhang, X., Palo, S. E., Russell, J., Mertens, C. J., & Mlynczak, M. (2009). Kelvin waves in stratosphere, mesosphere and lower thermosphere temperatures as observed by TIMED/SABER during 2002–2006. *Earth, planets and space*, 61(4), 447-453, <https://doi.org/10.1186/BF03353161>.

- Forbes, J. M., & Zhang, X. (2012). Lunar tide amplification during the January 2009 stratosphere warming event: Observations and theory. *Journal of Geophysical Research: Space Physics*, 117(A12), <https://doi.org/10.1029/2012JA017963>.
- Forbes, J. M., Zhang, X., Bruinsma, S., & Oberheide, J. (2013). Lunar semidiurnal tide in the thermosphere under solar minimum conditions. *Journal of Geophysical Research: Space Physics*, 118(4), 1788-1801, <https://doi.org/10.1029/2012JA017962>.
- Forbes, J. M., & Zhang, X. (2015). Quasi-10-day wave in the atmosphere. *Journal of Geophysical Research: Atmospheres*, 120(21), 11-079, <https://doi.org/10.1002/2015JD023327>.
- Forbes, J. M., Zhang, X., Maute, A., & Hagan, M. E. (2018). Zonally symmetric oscillations of the thermosphere at planetary wave periods. *Journal of Geophysical Research: Space Physics*, 123(5), 4110-4128, <https://doi.org/10.1002/2018JA025258>.
- Friis-Christensen, E., Lühr, H., Hulot, G. (2006). Swarm: A constellation to study the Earth's magnetic field. *Earth Plan. Space*, 58(4), 351-358, <https://doi.org/10.1186/BF03351933>.
- Fukushima, N. (1994). Some topics and historical episodes in geomagnetism and aeronomy. *Journal of Geophysical Research: Space Physics*, 99(A10), 19113-19142, <https://doi.org/10.1029/94JA00102>.
- Fuller-Rowell, T. J. (1998). The "thermospheric spoon": A mechanism for the semiannual density variation. *Journal of Geophysical Research: Space Physics*, 103(A3), 3951-3956, <https://doi.org/10.1029/97JA03335>.
- Fuller-Rowell, T., F. Wu, R. Akmaev, T.-W. Fang, and E. Araujo-Pradere (2010), A whole atmosphere model simulation of the impact of a sudden stratospheric warming on thermosphere dynamics and electrodynamics, *J. Geophys. Res.*, 115, A00G08, <https://doi.org/10.1029/2010JA015524>.
- Fuller-Rowell, T., H. Wang, R. Akmaev, F. Wu, T.-W. Fang, M. Iredell, and A. Richmond (2011), Forecasting the dynamic and electrodynamic response to the January 2009 sudden stratospheric warming, *Geophys. Res. Lett.*, 38, L13102, <https://doi.org/10.1029/2011GL047732>.
- Fuller-Rowell, T., R. Akmaev, F. Wu, M. Fedrizzi, R. A. Viereck, and H. Wang (2011), Did the January 2009 sudden stratospheric warming cool or warm the thermosphere?, *Geophys. Res. Lett.*, 38, L18104, <https://doi.org/10.1029/2011GL048985>.
- Funke, B., M. López-Puertas, D. Bermejo-Pantaleón, M. García-Comas, G. P. Stiller, T. von Clarmann, M. Kiefer, and A. Linden (2010), Evidence for dynamical coupling from the lower atmosphere to the thermosphere during a major stratospheric warming, *Geophys. Res. Lett.*, 37, L13803, <https://doi.org/10.1029/2010GL043619>.
- Galkin, I. A., Khmyrov, G. M., Kozlov, A. V., Reinisch, B. W., Huang, X., & Paznukhov, V. V. (2008). The ARTIST 5, Radio Sounding and Plasma Physics, AIP Proceedings # 974, <https://doi.org/10.1063/1.2885024>.

Gan, Q., J. Du, W. E. Ward, S. R. Beagley, V. I. Fomichev, S. D. Zhang, The Climatology of the Diurnal Tides from eCMAM30 (1979-2010) and its Comparison with SABER (2014), *Earth, Planets and Space*, 66:103, <https://doi.org/10.1186/1880-5981-66-103>.

Gasperini, F., Liu, H., & McInerney, J. (2020). Preliminary Evidence of Madden-Julian Oscillation Effects on Ultra-Fast Tropical Waves in the Thermosphere. *Journal of Geophysical Research: Space Physics*, e2019JA027649, <https://doi.org/10.1029/2019JA027649>.

Gelaro, R.W., McCarty, M.J., Suárez, R., Todling, A., Molod, L., Takacs, C.A., Randles, A., Darmenov, M.G., Bosilovich, R., Reichle, K., et al.: The modern-era retrospective analysis for research and applications, Version 2 (MERRA-2), (2017) *J. Clim.*, 30, 5419–5454, <https://doi.org/10.1175/JCLI-D-16-0684.1>.

Goncharenko, L. P., A. J. Coster, J. L. Chau, and C. E. Valladares (2010a), Impact of sudden stratospheric warmings on equatorial ionization anomaly, *J. Geophys. Res.*, 115, A00G07, <https://doi.org/10.1029/2010JA015400>.

Goncharenko, L. P., Chau, J. L., Liu, H. L., Coster, A. J. (2010b). Unexpected connections between the stratosphere and ionosphere. *Geophysical Research Letters*, 37, L10101, <https://doi.org/10.1029/2010GL043125>.

Goncharenko, L. P., Coster, A. J., Plumb, R. A., & Domeisen, D. I. (2012). The potential role of stratospheric ozone in the stratosphere-ionosphere coupling during stratospheric warmings. *Geophysical Research Letters*, 39(8), <https://doi.org/10.1029/2012GL051261>.

Goncharenko, L., J. L. Chau, P. Condor, A. Coster, and L. Benkevitch (2013a), Ionospheric effects of sudden stratospheric warming during moderate-to-high solar activity: Case study of January 2013, *Geophys. Res. Lett.*, 40, 4982–4986, <https://doi.org/10.1002/grl.50980>.

Goncharenko, L. P., V. W. Hsu, C. G. M. Brum, S.-R. Zhang, and J. T. Fentzke (2013b), Wave signatures in the midlatitude ionosphere during a sudden stratospheric warming of January 2010, *J. Geophys. Res. Space Physics*, 118, 472–487, <https://doi.org/10.1029/2012JA018251>.

Goncharenko, L. P., Coster, A. J., Zhang, S. R., Erickson, P. J., Benkevitch, L., Aponte, N., & Hernández - Espiet, A. (2018). Deep ionospheric hole created by sudden stratospheric warming in the nighttime ionosphere. *Journal of Geophysical Research: Space Physics*, 123(9), 7621-7633, <https://doi.org/10.1029/2018JA025541>.

Gong, Y., Q. Zhou, and S. Zhang (2013), Atmospheric tides in the low-latitude E and F regions and their responses to a sudden stratospheric warming event in January 2010, *J. Geophys. Res. Space Physics*, 118, 7913–7927, <https://doi.org/10.1002/2013JA019248>.

Gong, Y., Zhou, Q., Zhang, S., Aponte, N., and Sulzer, M. (2016), An incoherent scatter radar study of the midnight temperature maximum that occurred at Arecibo during a sudden stratospheric warming event in January 2010, *J. Geophys. Res. Space Physics*, 121, 5571–5578, <https://doi.org/10.1002/2016JA022439>.

Gong, Y., Ma, Z., Lv, X., Zhang, S., Zhou, Q., Aponte, N., & Sulzer, M. (2018). A study on the quarterdiurnal tide in the thermosphere at Arecibo during the February 2016 sudden

stratospheric warming event. *Geophysical Research Letters*, 45, 13,142– 13,149.

<https://doi.org/10.1029/2018GL080422>.

Goodwin, L. V., Iserhienrhien, B., Miles, D. M., Patra, S., van der Meeren, C., Buchert, S. C., Burchill, J. K., Clausen, L. B. N., Knudsen, D. J., McWilliams, K. A., & Moen, J. (2015). Swarm in situ observations of F region polar cap patches created by cusp precipitation. *Geophysical Research Letters*, 42(4), 996-1003, <https://doi.org/10.1002/2014GL062610>.

Grant, I. F., J. W. MacDougall, J. M. Ruohoniemi, W. A. Bristow, G. J. Sofko, J. A. Koehler, D. Danskin, and D. Andre (1995). Comparison of plasma flow velocities determined by the ionosonde Doppler drift technique, SuperDARN radars, and patch motion, *Radio Sci.*, 30, 1537-1599, <https://doi.org/10.1029/95RS00831>.

Gu, S. Y., Liu, H. L., Li, T., Dou, X., Wu, Q., & Russell III, J. M. (2014a). Observation of the neutral - ion coupling through 6 day planetary wave. *Journal of Geophysical Research: Space Physics*, 119(12), 10-376, <https://doi.org/10.1002/2014JA020530>.

Gu, S. Y., Dou, X., Lei, J., Li, T., Luan, X., Wan, W., & Russell III, J. M. (2014b). Ionospheric response to the ultrafast Kelvin wave in the MLT region. *Journal of Geophysical Research: Space Physics*, 119(2), 1369-1380, <https://doi.org/10.1002/2013JA019086>.

Gupta, S., and Upadhayaya, A. K. (2017), Morphology of ionospheric F2 region variability associated with sudden stratospheric warmings, *J. Geophys. Res. Space Physics*, 122, 7798–7826, <https://doi.org/10.1002/2017JA024059>.

Hagan, M. E., Roble, R. G., & Hackney, J. (2001). Migrating thermospheric tides. *Journal of Geophysical Research: Space Physics*, 106(A7), 12739-12752, <https://doi.org/10.1029/2000JA000344>.

Hagan, M. E., A. Maute, R. G. Roble, A. D. Richmond, T. J. Immel, and S. L. England (2007), Connections between deep tropical clouds and the Earth's ionosphere, *Geophys. Res. Lett.*, 34, L20109, <https://doi.org/10.1029/2007GL030142>.

Harada, Y., Goto, A., Hasegawa, H., Fujikawa, N., Naoe, H., & Hirooka, T. (2010). A major stratospheric sudden warming event in January 2009. *Journal of the Atmospheric Sciences*, 67(6), 2052-2069, <https://doi.org/10.1175/2009JAS3320.1>.

He, M., & Chau, J. L. (2019). Mesospheric semidiurnal tides and near-12 h waves through jointly analyzing observations of five specular meteor radars from three longitudinal sectors at boreal midlatitudes. *Atmospheric Chemistry & Physics*, 19(9), <https://doi.org/10.5194/acp-19-5993-2019>.

Hoffmann, P., Singer, W., Keuer, D., Hocking, W. K., Kunze, M., & Murayama, Y. (2007). Latitudinal and longitudinal variability of mesospheric winds and temperatures during stratospheric warming events. *Journal of Atmospheric and Solar-Terrestrial Physics*, 69(17-18), 2355-2366, <https://doi.org/10.1016/j.jastp.2007.06.010>.

Huang, C. S., Foster, J. C., & Kelley, M. C. (2005). Long-duration penetration of the interplanetary electric field to the low-latitude ionosphere during the main phase of magnetic storms. *Journal of Geophysical Research: Space Physics*, 110(A11), <https://doi.org/10.1029/2005JA011202>.

Hurrell, J.W., M.M. Holland, P.R. Gent, S. Ghan, J.E. Kay, P.J. Kushner, J. Lamarque, W.G. Large, D. Lawrence, K. Lindsay, W.H. Lipscomb, M.C. Long, N. Mahowald, D.R. Marsh, R.B. Neale, P. Rasch, S. Vavrus, M. Vertenstein, D. Bader, W.D. Collins, J.J. Hack, J. Kiehl, and S. Marshall (2013), The Community Earth System Model: A Framework for Collaborative Research. *Bull. Amer. Meteor. Soc.*, 94, 1339–1360, <https://doi.org/10.1175/BAMS-D-12-00121.1>.

Immel, T. J., Sagawa, E., England, S. L., Henderson, S. B., Hagan, M. E., Mende, S. B., ... & Paxton, L. J. (2006). Control of equatorial ionospheric morphology by atmospheric tides. *Geophysical Research Letters*, 33(15), <https://doi.org/10.1029/2006GL026161>.

Immel, T. J., England, S. L., Mende, S. B., Heelis, R. A., Englert, C. R., Edelstein, J., Frey, H. U., Korpela, E. J., Ttaylor, E. R., Craig, W. W., Harris, S. E., Bestter, M., Bust, G. S., Crowley, G., Forbes, J. M., Gérard, J.-C., Harlander, J. M., Huba, J. D., Hubert, B., Kamalabadi, F., Makela, J. J., Maute, A. I., Meier, R. R., Raftery, C., Rochus, P., Siegmund, O. H. W., Stephan, A. W., Swenson, G. R., Frey, S., Hysell, D. L., Saito, A., Rider, K. A., & Sirk, M. M., (2018). The Ionospheric Connection Explorer mission: mission goals and design. *Space Science Reviews*, 214(1), 13, <https://doi.org/10.1007/s11214-017-0449-2>.

Jayachandran, P. T., R. B. Langley, J. W. MacDougall, S. C. Mushini, D. Pokhotelov, A. M. Hamza, I. R. Mann, D. K. Milling, Z. C. Kale, R. Chadwick, T. Kelly, D. W. Danskin, and C. S. Carrano (2009), The Canadian high arctic ionospheric network (CHAIN), *Radio Sci.*, 44, RS0A03, <https://doi.org/10.1029/2008RS004046>.

Jin, H., Miyoshi, Y., Fujiwara, H., Shinagawa, H., Terada, K., Terada, N., Ishii, M., Otsuka, Y., & Saito, A. (2011). Vertical connection from the tropospheric activities to the ionospheric longitudinal structure simulated by a new Earth's whole atmosphere-ionosphere coupled model. *Journal of Geophysical Research: Space Physics*, 116(A1), <https://doi.org/10.1029/2010JA015925>.

Jin, H., Y. Miyoshi, D. Pancheva, P. Mukhtarov, H. Fujiwara, and H. Shinagawa (2012), Response of migrating tides to the stratospheric sudden warming in 2009 and their effects on the ionosphere studied by a whole atmosphere-ionosphere model GAIA with COSMIC and TIMED/SABER observations, *J. Geophys. Res.*, 117, A10323, <https://doi.org/10.1029/2012JA017650>.

Jones, M., Forbes, J. M., Hagan, M. E., and Maute, A. (2014), Impacts of vertically propagating tides on the mean state of the ionosphere - thermosphere system, *J. Geophys. Res. Space Physics*, 119, 2197- 2213, <https://doi.org/10.1002/2013JA019744>.

Jonah, O. F., Paula, E. R., Kherani, E. A., Dutra, S. L. G., and Paes, R. R. (2014), Atmospheric and ionospheric response to sudden stratospheric warming of January 2013, *J. Geophys. Res. Space Physics*, 119, 4973–4980, <https://doi.org/10.1002/2013JA019491>.

Jose, L., Vineeth, C., & Pant, T. K. (2017). Impact of Stratospheric Sudden Warming on the Occurrence of the Equatorial Spread-F. *Journal of Geophysical Research: Space Physics*, 122(12), 12-544, <https://doi.org/10.1002/2017JA024652>.

Karpechko, A. Y., Charlton-Perez, A., Balmaseda, M., Tyrrell, N., & Vitart, F. (2018). Predicting sudden stratospheric warming 2018 and its climate impacts with a multimodel

ensemble. *Geophysical Research Letters*, 45(24), 13-538,
<https://doi.org/10.1029/2018GL081091>.

Kawahira, K. (1985), The D region winter anomaly at high and middle latitudes induced by planetary waves, *Radio Sci.*, 20(4), 795– 802, <https://doi.org/10.1029/RS020i004p00795>.

Kazimirovsky E, Herraiz M, De La Morena B A. Effects on the Ionosphere Due to Phenomena Occurring Below it. *Surv Geophys*, 2003, 24: 139–184,
<https://doi.org/10.1023/A:1023206426746>.

Kikuchi, T., Hashimoto, K. K., & Nozaki, K. (2008). Penetration of magnetospheric electric fields to the equator during a geomagnetic storm. *Journal of Geophysical Research: Space Physics*, 113(A6), <https://doi.org/10.1029/2009JA014562>.

Kil, H., & Paxton, L. J. (2017). Global distribution of nighttime medium-scale traveling ionospheric disturbances seen by Swarm satellites. *Geophysical Research Letters*, 44(18), 9176-9182, <https://doi.org/10.1002/2017GL074750>.

Kinnison, D. E., Brasseur, G. P., Walters, S., Garcia, R. R., Marsh, D. R., Sassi, F., Harvey, V. L., Randall, C. E., Emmons, L., Lamarque, J. F., Hess, P., Orlando, J. J., Tie, X. X., Randel, W., Pan, L. L., Gettelman, A., Granier, C., Diehl, T., Niemeier, U. and Simmons, A. J. (2007), Sensitivity of chemical tracers to meteorological parameters in the MOZART - 3 chemical transport model, *J. Geophys. Res.*, 112, D20302,
<https://doi.org/10.1029/2006JD007879>.

Klimenko, M. V., Klimenko, V. V., Bessarab, F. S., Korenkov, Y. N., Liu, H., Goncharenko, L. P., and Tolstikov, M. V. (2015), Study of the thermospheric and ionospheric response to the 2009 sudden stratospheric warming using TIME - GCM and GSM TIP models: First results, *J. Geophys. Res. Space Physics*, 120, 7873–7888,
<https://doi.org/10.1002/2014JA020861>.

Korenkov, Y. N., et al. (2012), The global thermospheric and ionospheric response to the 2008 minor sudden stratospheric warming event, *J. Geophys. Res.*, 117, A10309,
<https://doi.org/10.1029/2012JA018018>.

Kouba, D., Boska, J., Galkin, I.A., Santolik, O., & Sauli, P. (2008). Ionospheric drift measurements: Skymap point selection. *Radio Sci.*, 43 (1), RS1S90,
<https://doi.org/10.1029/2007RS003633>.

Koucká Knížová, P., Podolská, K., Potužníková, K., Kouba, D., Mošna, Z., Boška, J., & Kozubek, M. (2020). Evidence of vertical coupling: meteorological storm Fabienne on 23 September 2018 and its related effects observed up to the ionosphere. *Annales Geophysicae*, Vol. 38, No. 1, pp. 73-93, <https://doi.org/10.5194/angeo-38-73-2020>.

Kristoffersen, S. K., Ward, W. E., Brown, S., & Drummond, J. R. (2013). Calibration and validation of the advanced E-Region Wind Interferometer. *Atmospheric Measurement Techniques*, 6(7), 1761-1776, <https://doi.org/10.5194/amt-6-1761-2013>.

Krüger, K., Naujokat, B., & Labitzke, K. (2005). The unusual midwinter warming in the Southern Hemisphere stratosphere 2002: A comparison to Northern Hemisphere phenomena. *Journal of the atmospheric sciences*, 62(3), 603-613, <https://doi.org/10.1175/JAS-3316.1>.

- Kumari, K., Oberheide, J., & Lu, X. (2020). The Tidal Response in the Mesosphere/Lower Thermosphere to the Madden-Julian Oscillation Observed by SABER. *Geophysical Research Letters*, e2020GL089172, <https://doi.org/10.1029/2020GL089172>.
- Kunz, A., Pan, L. L., Konopka, P., Kinnison, D. E., & Tilmes, S. (2011). Chemical and dynamical discontinuity at the extratropical tropopause based on START08 and WACCM analyses. *Journal of Geophysical Research*, 116, D24302, <https://doi.org/10.1029/2011JD016686>.
- Kurihara, J., Y. Ogawa, S. Oyama, S. Nozawa, M. Tsutsumi, C. M. Hall, Y. Tomikawa, and R. Fujii (2010), Links between a stratospheric sudden warming and thermal structures and dynamics in the high - latitude mesosphere, lower thermosphere, and ionosphere, *Geophys. Res. Lett.*, 37, L13806, <https://doi.org/10.1029/2010GL043643>.
- Labitzke, K. G., & Van Loon, H. (1999). *The stratosphere: phenomena, history, and relevance*. Springer Science & Business Media.
- Laskar, F. I., Pallamraju, D., & Veenadhari, B. (2014). Vertical coupling of atmospheres: dependence on strength of sudden stratospheric warming and solar activity. *Earth, Planets and Space*, 66(1), 94, <https://doi.org/10.1186/1880-5981-66-94>.
- Laštovička, J., Križan, P., Sauli, P., & Novotná, D. (2003). Persistence of the planetary wave type oscillations in foF2 over Europe, *Annales Geophysicae*, Vol. 21, No. 7, pp. 1543-1552, <https://doi.org/10.4401/ag-3098>.
- Laštovička, J. (2006). Forcing of the ionosphere by waves from below. *Journal of Atmospheric and Solar-Terrestrial Physics*, 68(3-5), 479-497, <https://doi.org/10.1016/j.jastp.2005.01.018>.
- Laundal, K. M., Finlay, C. C., Olsen, N., & Reistad, J. P. (2018). Solar wind and seasonal influence on ionospheric currents from Swarm and CHAMP measurements. *Journal of Geophysical Research: Space Physics*, 123(5), 4402-4429, <https://doi.org/10.1029/2018JA025387>.
- Lei, J., Thayer, J. P., Forbes, J. M., Sutton, E. K., & Nerem, R. S. (2008). Rotating solar coronal holes and periodic modulation of the upper atmosphere. *Geophysical Research Letters*, 35(10), <https://doi.org/10.1029/2008GL033875>.
- Lin, C. H., J. T. Lin, L. C. Chang, J. Y. Liu, C. H. Chen, W. H. Chen, H. H. Huang, and C. H. Liu (2012), Observations of global ionospheric responses to the 2009 stratospheric sudden warming event by FORMOSAT-3/COSMIC, *J. Geophys. Res.*, 117, A06323, <https://doi.org/10.1029/2011JA017230>.
- Lin, C. H., Lin, J. T., Chang, L. C., Chen, W. H., Chen, C. H., & Liu, J. Y. (2013). Stratospheric sudden warming effects on the ionospheric migrating tides during 2008–2010 observed by FORMOSAT-3/COSMIC. *Journal of Atmospheric and Solar-Terrestrial Physics*, 103, 66-75, <https://doi.org/10.1016/j.jastp.2013.03.026>.
- Lin, C. Y., Matsuo, T., Liu, J. Y., Lin, C. H., Huba, J. D., Tsai, H. F., & Chen, C. Y. (2017). Data assimilation of ground-based GPS and radio occultation total electron content for global ionospheric specification. *Journal of Geophysical Research: Space Physics*, 122(10), 10-876, <https://doi.org/10.1002/2017JA024185>.

Lin, J. T., C. H. Lin, L. C. Chang, H. H. Huang, J. Y. Liu, A. B. Chen, C. H. Chen, and C. H. Liu (2012), Observational evidence of ionospheric migrating tide modification during the 2009 stratospheric sudden warming, *Geophys. Res. Lett.*, 39, L02101, <https://doi.org/10.1029/2011GL050248>.

Lin, J. T., Lin, C. H., Lin, C. Y., Pedatella, N. M., Rajesh, P. K., Matsuo, T., & Liu, J. Y. (2019). Revisiting the modulations of ionospheric solar and lunar migrating tides during the 2009 stratospheric sudden warming by using global ionosphere specification. *Space Weather*, 17, 767–777, <https://doi.org/10.1029/2019SW002184>.

Liu, H., E. Doornbos, M. Yamamoto, and S. Tulasi Ram (2011a), Strong thermospheric cooling during the 2009 major stratosphere warming, *Geophys. Res. Lett.*, 38, L12102, <https://doi.org/10.1029/2011GL047898>.

Liu, H., Yamamoto, M., Tulasi Ram, S., Tsugawa, T., Otsuka, Y., Stolle, C., & Nagatsuma, T. (2011b). Equatorial electrodynamics and neutral background in the Asian sector during the 2009 stratospheric sudden warming. *Journal of Geophysical Research: Space Physics*, 116(A8), <https://doi.org/10.1029/2011JA016607>.

Liu, H., H. Jin, Y. Miyoshi, H. Fujiwara, and H. Shinagawa (2013), Upper atmosphere response to stratosphere sudden warming: Local time and height dependence simulated by GAIA model, *Geophys. Res. Lett.*, 40, 635–640, <https://doi.org/10.1002/grl.50146>.

Liu, H., Miyoshi, Y., Miyahara, S., Jin, H., Fujiwara, H., & Shinagawa, H. (2014). Thermal and dynamical changes of the zonal mean state of the thermosphere during the 2009 SSW: GAIA simulations. *Journal of Geophysical Research: Space Physics*, 119(8), 6784-6791, <https://doi.org/10.1002/2014JA020222>.

Liu, H. L., & Roble, R. G. (2002). A study of a self-generated stratospheric sudden warming and its mesospheric-lower thermospheric impacts using the coupled TIME-GCM/CCM3. *Journal of Geophysical Research: Atmospheres*, 107(D23), ACL-15, <https://doi.org/10.1029/2001JD001533>.

Liu, H. L., Wang, W., Richmond, A. D., & Roble, R. G. (2010). Ionospheric variability due to planetary waves and tides for solar minimum conditions. *Journal of Geophysical Research: Space Physics*, 115(A6), <https://doi.org/10.1029/2009JA015188>.

Liu, H. L., McInerney, J. M., Santos, S., Lauritzen, P. H., Taylor, M. A., & Pedatella, N. M. (2014). Gravity waves simulated by high-resolution whole atmosphere community climate model. *Geophysical Research Letters*, 41(24), 9106-9112, <https://doi.org/10.1002/2014GL062468>.

Liu, H. L. (2016). Variability and predictability of the space environment as related to lower atmosphere forcing. *Space Weather*, 14(9), 634-658, <https://doi.org/10.1002/2016SW001450>.

Liu, H. L., Bardeen, C. G., Foster, B. T., Lauritzen, P., Liu, J., Lu, G., ... Wang, W. (2018). Development and validation of the Whole Atmosphere Community Climate Model with thermosphere and ionosphere extension (WACCM - X 2.0). *Journal of Advances in Modeling Earth Systems*, 10, 381– 402, <https://doi.org/10.1002/2017MS001232>.

- Liu, H. L. (2020). Day-to-Day Variability of Prereversal Enhancement in the Vertical Ion Drift in Response to Large-Scale Forcing From the Lower Atmosphere. *Space Weather*, 18(4), e2019SW002334, <https://doi.org/10.1029/2019SW002334>.
- Lu, G. (2017). Large scale high-latitude ionospheric electrodynamic fields and currents. *Space Science Reviews*, 206(1-4), 431-450, <https://doi.org/10.1007/s11214-016-0269-9>.
- Lu, G., A. D. Richmond, H. Lühr, and L. Paxton (2016), High-latitude energy input and its impact on the thermosphere, *J. Geophys. Res. Space Physics*, 121, 7108–7124, <https://doi.org/10.1002/2015JA022294>.
- Liu, G., Huang, W., Shen, H., Aa, E., Li, M., Liu, S., & Luo, B. (2019). Ionospheric Response to the 2018 Sudden Stratospheric Warming Event at Middle- and Low-Latitude Stations Over China Sector. *Space Weather*, 17(8), 1230-1240, <https://doi.org/10.1029/2019SW002160>.
- Liu, J., Zhang, D. H., Hao, Y. Q., & Xiao, Z. (2019) The Comparison of Lunar Tidal Characteristics in the Low-Latitudinal Ionosphere Between East Asian and American Sectors During Stratospheric Sudden Warming Events: 2009–2018. *Journal of Geophysical Research: Space Physics*, <https://doi.org/10.1029/2019JA026722>.
- Lühr, H., Warnecke, J. F., & Rother, M. K. (1996). An algorithm for estimating field-aligned currents from single spacecraft magnetic field measurements: a diagnostic tool applied to Freja satellite data. *IEEE transactions on geoscience and remote sensing*, 34(6), 1369-1376, doi:10.1109/36.544560.
- Lühr, H., Maus, S., & Rother, M. (2004). Noontime equatorial electrojet: Its spatial features as determined by the CHAMP satellite. *J. Geophys. Res. Space Phys.*, 109(A1), <https://doi.org/10.1029/2002JA009656>.
- Lühr, H., Kervalishvili, G., Michaelis, I., Rauberg, J., Ritter, P., Park, J., & Brauer, P. (2015). The interhemispheric and F region dynamo currents revisited with the Swarm constellation. *Geophysical Research Letters*, 42(9), 3069-3075, <https://doi.org/10.1002/2015GL063662>.
- Manney, G. L., Schwartz, M. J., Krüger, K., Santee, M. L., Pawson, S., Lee, J. N., ... & Livesey, N. J. (2009). Aura Microwave Limb Sounder observations of dynamics and transport during the record - breaking 2009 Arctic stratospheric major warming. *Geophysical Research Letters*, 36(12), <https://doi.org/10.1029/2009GL038586>.
- Manney, G. L., Lawrence, Z. D., Santee, M. L., Read, W. G., Livesey, N. J., Lambert, A., ... & Schwartz, M. J. (2015). A minor sudden stratospheric warming with a major impact: Transport and polar processing in the 2014/2015 Arctic winter. *Geophysical Research Letters*, 42(18), 7808-7816, <https://doi.org/10.1002/2015GL065864>.
- Matsuno, T. (1971). A dynamical model of the stratospheric sudden warming. *Journal of the Atmospheric Sciences*, 28(8), 1479-1494, [https://doi.org/10.1175/1520-0469\(1971\)028<1479:ADMOTS>2.0.CO;2](https://doi.org/10.1175/1520-0469(1971)028<1479:ADMOTS>2.0.CO;2).
- Matsuo, T., Lee, I. T., & Anderson, J. L. (2013). Thermospheric mass density specification using an ensemble Kalman filter. *Journal of Geophysical Research: Space Physics*, 118(3), 1339-1350, <https://doi.org/10.1002/jgra.50162>.

- Matzka, J., Stolle, C., Kervalishvili, G., Rauberg, J., & Yamazaki, Y. (2019) The Hp geomagnetic index test dataset 2003, 2004, 2005 and 2017. GFZ Data Services. <https://doi.org/10.5880/GFZ.2.3.2019.002>.
- Maute, A., Hagan, M. E., Richmond, A. D., & Roble, R. G. (2014). TIME-GCM study of the ionospheric equatorial vertical drift changes during the 2006 stratospheric sudden warming. *Journal of Geophysical Research: Space Physics*, 119(2), 1287-1305, <https://doi.org/10.1002/2013JA019490>.
- Maute, A., Hagan, M. E., Yudin, V., Liu, H. L., & Yizengaw, E. (2015). Causes of the longitudinal differences in the equatorial vertical $E \times B$ drift during the 2013 SSW period as simulated by the TIME-GCM. *Journal of Geophysical Research: Space Physics*, 120(6), 5117-5136, <https://doi.org/10.1002/2015JA021126>.
- Maute, A., Fejer, B. G., Forbes, J. M., Zhang, X., & Yudin, V. (2016). Equatorial vertical drift modulation by the lunar and solar semidiurnal tides during the 2013 sudden stratospheric warming. *Journal of Geophysical Research: Space Physics*, 121(2), 1658-1668, <https://doi.org/10.1002/2015JA022056>.
- Maute, A. (2017), Thermosphere-Ionosphere-Electrodynamics General Circulation Model for the Ionospheric Connection Explorer: TIEGCM-ICON. *Space Sci Rev* 212, 523–551, <https://doi.org/10.1007/s11214-017-0330-3>.
- Maycock, A. C., P. Hitchcock, P. (2015), Do split and displacement sudden stratospheric warmings have different annular mode signatures? *Geophys. Res. Lett.*, 42, 10,943–10,951, <https://doi.org/10.1002/2015GL066754>.
- McDonald, A. J., Hibbins, R. E., & Jarvis, M. J. (2011). Properties of the quasi 16 day wave derived from EOS MLS observations. *Journal of Geophysical Research: Atmospheres*, 116(D6), <https://doi.org/10.1029/2010JD014719>.
- McDonald, S. E., Sassi, F., Tate, J., McCormack, J., Kuhl, D. D., Drob, D. P., & Mannucci, A. J. (2018). Impact of non-migrating tides on the low latitude ionosphere during a sudden stratospheric warming event in January 2010. *Journal of Atmospheric and Solar-Terrestrial Physics*, 171, 188-200, <https://doi.org/10.1016/j.jastp.2017.09.012>.
- McLandress, C., Shepherd, G. G., & Solheim, B. H. (1996). Satellite observations of thermospheric tides: Results from the Wind Imaging Interferometer on UARS. *Journal of Geophysical Research: Atmospheres*, 101(D2), 4093-4114, <https://doi.org/10.1029/95JD03359>.
- McNamara, L. F., Cooke, D. L., Valladares, C. E., Reinisch, B. W. (2007). Comparison of CHAMP and Digisonde plasma frequencies at Jicamarca, Peru. *Radio Sci.*, 42(2), <https://doi.org/10.1029/2006RS003491>.
- Miyoshi, Y., Fujiwara, H., Jin, H., & Shinagawa, H. (2015). Impacts of sudden stratospheric warming on general circulation of the thermosphere. *Journal of Geophysical Research: Space Physics*, 120(12), 10-897, <https://doi.org/10.1002/2015JA021894>.
- Miyoshi, Y., Jin, H., Fujiwara, H., & Shinagawa, H. (2018). Numerical study of traveling ionospheric disturbances generated by an upward propagating gravity wave. *Journal of*

Geophysical Research: Space Physics, 123(3), 2141-2155,
<https://doi.org/10.1002/2017JA025110>

Miyoshi, Y., & Yamazaki, Y. (2020). Excitation mechanism of ionospheric 6 - day oscillation during the 2019 September sudden stratospheric warming event. *Journal of Geophysical Research: Space Physics*, e2020JA028283,
<https://doi.org/10.1029/2020JA028283>.

Moudden, Y., & Forbes, J. M. (2014). Quasi-two-day wave structure, interannual variability, and tidal interactions during the 2002-2011 decade. *Journal of Geophysical Research: Atmospheres*, 119(5), 2241-2260, <https://doi.org/10.1002/2013JD020563>.

Mosna, Z., & Koucka Knizova, P. (2012). Analysis of wave-like oscillations in parameters of sporadic E layer and neutral atmosphere. *Journal of Atmospheric and Solar-Terrestrial Physics*, 90-91, 172-178, <https://doi.org/10.1016/j.jastp.2012.04.007>.

Mo, X. H., & Zhang, D. H. (2018). Lunar tidal modulation of periodic meridional movement of equatorial ionization anomaly crest during sudden stratospheric warming. *Journal of Geophysical Research: Space Physics*, 123, 1488-1499,
<https://doi.org/10.1002/2017JA024718>.

Newell, P. T., Liou, K., Zhang, Y., Sotirelis, T., Paxton, L. J., & Mitchell, E. J. (2014). OVATION Prime-2013: Extension of auroral precipitation model to higher disturbance levels. *Space Weather*, 12(6), 368-379, <https://doi.org/10.1002/2014SW001056>.

Nishioka, M., Tsugawa, T., Kubota, M., & Ishii, M. (2013). Concentric waves and short-period oscillations observed in the ionosphere after the 2013 Moore EF5 tornado. *Geophysical Research Letters*, 40(21), 5581-5586, <https://doi.org/10.1002/2013GL057963>.

Oberheide, J., Forbes, J. M., Häusler, K., Wu, Q., & Bruinsma, S. L. (2009). Tropospheric tides from 80 to 400 km: Propagation, interannual variability, and solar cycle effects. *Journal of Geophysical Research: Atmospheres*, 114(D1), <https://doi.org/10.1029/2009JD012388>.

Oberheide, J., Pedatella, N. M., Gan, Q., Kumari, K., Burns, A. G., & Eastes, R. W. (2020). Thermospheric Composition O/N Response to an Altered Meridional Mean Circulation During Sudden Stratospheric Warmings Observed by GOLD. *Geophysical Research Letters*, 47(1), e2019GL086313, <https://doi.org/10.1029/2019GL086313>.

Olson, M. E., Fejer, B. G., Stolle, C., Lühr, H., & Chau, J. L. (2013). Equatorial ionospheric electrodynamic perturbations during Southern Hemisphere stratospheric warming events. *Journal of Geophysical Research: Space Physics*, 118(3), 1190-1195,
<https://doi.org/10.1002/jgra.50142>.

Owolabi, C., Lei, J., Bolaji, O. S., Jimoh, O., Ruan, H., Li, N., et al. (2019). Investigation on the variability of the geomagnetic daily current during sudden stratospheric warmings. *Journal of Geophysical Research: Space Physics*, 124, 6156-6172,
<https://doi.org/10.1029/2019JA026667>.

Oyama, K. I., Jhou, J. T., Lin, J. T., Lin, C., Liu, H., & Yumoto, K. (2014). Ionospheric response to 2009 sudden stratospheric warming in the Northern Hemisphere. *Journal of Geophysical Research: Space Physics*, 119(12), 10-260,
<https://doi.org/10.1002/2014JA020014>.

- Paes, R. R., Batista, I. S., Candido, C. M. N., Jonah, O. F., and Santos, P. C. P. (2014), Equatorial ionization anomaly variability over the Brazilian region during boreal sudden stratospheric warming events, *J. Geophys. Res. Space Physics*, 119, 7649–7664, <https://doi.org/10.1002/2014JA019968>.
- Pal, S., Hobara, Y., Chakrabarti, S. K., & Schnoor, P. W. (2017). Effects of the major sudden stratospheric warming event of 2009 on the subionospheric very low frequency/low frequency radio signals. *Journal of Geophysical Research: Space Physics*, 122(7), 7555-7566, <https://doi.org/10.1002/2016JA023813>.
- Pancheva D, Lastovicka J, de La Morena B A. (1991) Quasi-periodic fluctuations in ionospheric absorption in relation to planetary activity in the stratosphere. *J Atmos Sol Terr Phys*, 53: 1151–1155, doi: 10.1016/0021-9169(91)90065-F, [https://doi.org/10.1016/0021-9169\(91\)90065-F](https://doi.org/10.1016/0021-9169(91)90065-F).
- Pancheva, D., & Mukhtarov, P. (2011). Stratospheric warmings: The atmosphere–ionosphere coupling paradigm. *Journal of Atmospheric and Solar-Terrestrial Physics*, 73(13), 1697-1702, <https://doi.org/10.1016/j.jastp.2011.03.006>.
- Pancheva, D., Y. Miyoshi, P. Mukhtarov, H. Jin, H. Shinagawa, and H. Fujiwara (2012), Global response of the ionosphere to atmospheric tides forced from below: Comparison between COSMIC measurements and simulations by atmosphere-ionosphere coupled model GAIA, *J. Geophys. Res.*, 117, A07319, <https://doi.org/10.1029/2011JA017452>.
- Pancheva, D., Mukhtarov, P., & Siskind, D. E. (2018). The quasi-6-day waves in NOGAPS-ALPHA forecast model and their climatology in MLS/Aura measurements (2005–2014). *Journal of Atmospheric and Solar-Terrestrial Physics*, 181, 19-37, <https://doi.org/10.1016/j.jastp.2018.10.008>.
- Park, J., Lühr, H., & Min, K. (2011). Climatology of the inter-hemispheric field-aligned current system in the equatorial ionosphere as observed by CHAMP. *Ann. Geophys.*, 29, 573–582, <https://doi.org/10.5194/angeo-29-573-2011>.
- Park, J., H. Lühr, M. Kunze, B. G. Fejer, and K. W. Min (2012), Effect of sudden stratospheric warming on lunar tidal modulation of the equatorial electrojet, *J. Geophys. Res.*, 117, A03306, <https://doi.org/10.1029/2011JA017351>.
- Park, J., and H. Lühr (2012), Effects of sudden stratospheric warming (SSW) on the lunital modulation of the F-region dynamo, *J. Geophys. Res.*, 117, A09320, <https://doi.org/10.1029/2012JA018035>.
- Park, J., Noja, M., Stolle, C., & Lühr, H. (2013). The Ionospheric Bubble Index deduced from magnetic field and plasma observations onboard Swarm. *Earth, Planets and Space*, 65(11), 1333-1344, <https://doi.org/10.5047/eps.2013.08.005>.
- Park, J., Lühr, H., Kervalishvili, G., Rauberg, J., Michaelis, I., Stolle, C., & Kwak, Y. S. (2015). Nighttime magnetic field fluctuations in the topside ionosphere at midlatitudes and their relation to medium-scale traveling ionospheric disturbances: The spatial structure and scale sizes. *Journal of Geophysical Research: Space Physics*, 120(8), 6818-6830, <https://doi.org/10.1002/2015JA021315>.

- Patra, A. K., P. Pavan Chaitanya, S. Sripathi, and S. Alex (2014), Ionospheric variability over Indian low latitude linked with the 2009 sudden stratospheric warming, *J. Geophys. Res. Space Physics*, 119, 4044–4061, <https://doi.org/10.1002/2014JA019847>.
- Paulino, A. R., Batista, P. P., Clemesha, B. R., Buriti, R. A., & Schuch, N. (2012). An enhancement of the lunar tide in the MLT region observed in the Brazilian sector during 2006 SSW. *Journal of Atmospheric and Solar-Terrestrial Physics*, 90, 97-103, <https://doi.org/10.1016/j.jastp.2011.12.015>.
- Pedatella, N. M., & Forbes, J. M. (2009). Interannual variability in the longitudinal structure of the low-latitude ionosphere due to the El Niño-Southern Oscillation. *Journal of Geophysical Research: Space Physics*, 114(A12), <https://doi.org/10.1029/2009JA014494>.
- Pedatella, N. M., and J. M. Forbes (2010), Evidence for stratosphere sudden warming-ionosphere coupling due to vertically propagating tides, *Geophys. Res. Lett.*, 37, L11104, <https://doi.org/10.1029/2010GL043560>.
- Pedatella, N. M., H.-L. Liu, A. D. Richmond, A. Maute, and T.-W. Fang (2012), Simulations of solar and lunar tidal variability in the mesosphere and lower thermosphere during sudden stratosphere warmings and their influence on the low-latitude ionosphere, *J. Geophys. Res.*, 117, A08326, <https://doi.org/10.1029/2012JA017858>.
- Pedatella, N. M., and H.-L. Liu (2013a), The influence of atmospheric tide and planetary wave variability during sudden stratosphere warmings on the low latitude ionosphere, *J. Geophys. Res. Space Physics*, 118, 5333–5347, <https://doi.org/10.1002/jgra.50492>.
- Pedatella, N. M., and Liu, H. L. (2013b). Influence of the El Niño Southern Oscillation on the middle and upper atmosphere. *Journal of Geophysical Research: Space Physics*, 118(5), 2744-2755, <https://doi.org/10.1002/jgra.50286>.
- Pedatella, N. M. (2014). Observations and simulations of the ionospheric lunar tide: Seasonal variability. *Journal of Geophysical Research: Space Physics*, 119(7), 5800-5806, <https://doi.org/10.1002/2014JA020189>.
- Pedatella, N. M., Fuller-Rowell, T., Wang, H., Jin, H., Miyoshi, Y., Fujiwara, H., & Goncharenko, L. (2014a). The neutral dynamics during the 2009 sudden stratosphere warming simulated by different whole atmosphere models. *Journal of Geophysical Research: Space Physics*, 119, 1306–1324, <https://doi.org/10.1002/2013JA019421>.
- Pedatella, N. M., Liu, H. L., Sassi, F., Lei, J., Chau, J. L., & Zhang, X. (2014b). Ionosphere variability during the 2009 SSW: Influence of the lunar semidiurnal tide and mechanisms producing electron density variability. *Journal of Geophysical Research: Space Physics*, 119(5), 3828-3843, <https://doi.org/10.1002/2014JA019849>.
- Pedatella, N. M., Fuller-Rowell, T., Wang, H., Jin, H., Miyoshi, Y., Fujiwara, H., & Matthias, V. (2014). The neutral dynamics during the 2009 sudden stratosphere warming simulated by different whole atmosphere models. *Journal of Geophysical Research: Space Physics*, 119(2), 1306-1324, <https://doi.org/10.1002/2013JA019421>.
- Pedatella, N. M., & Maute, A. (2015). Impact of the semidiurnal lunar tide on the midlatitude thermospheric wind and ionosphere during sudden stratosphere warmings. *Journal of*

Geophysical Research: Space Physics, 120(12), 10-740,

<https://doi.org/10.1002/2015JA021986>.

Pedatella, N. M., Fang, T. W., Jin, H., Sassi, F., Schmidt, H., Chau, J. L., Siddiqui, T. A., & Goncharenko, L. (2016a). Multimodel comparison of the ionosphere variability during the 2009 sudden stratosphere warming. *Journal of Geophysical Research: Space Physics*, 121(7), 7204-7225, <https://doi.org/10.1002/2016JA022859>.

Pedatella, N. M., Richmond, A. D., Maute, A., & Liu, H. L. (2016b). Impact of semidiurnal tidal variability during SSWs on the mean state of the ionosphere and thermosphere. *Journal of Geophysical Research: Space Physics*, 121(8), 8077-8088, <https://doi.org/10.1002/2016JA022910>.

Pedatella, N., Chau, J., Schmidt, H., Goncharenko, L., Stolle, C., Hocke, K., & Siddiqui, T. (2018). How sudden stratospheric warming affects the whole atmosphere. *Eos*, 99, 35-38, <https://doi.org/10.1029/2018EO092441>.

Picone, J. M., Hedin, A. E., Drob, D. P., and Aikin, A. C., NRLMSISE-00 empirical model of the atmosphere: Statistical comparisons and scientific issues (2002), *J. Geophys. Res.*, 107(A12), 1468, <https://doi.org/10.1029/2002JA009430>.

Pilinski, M. D., & Crowley, G. (2015). Seasonal variability in global eddy diffusion and the effect on neutral density. *Journal of Geophysical Research: Space Physics*, 120(4), 3097-3117, <https://doi.org/10.1002/2015JA021084>.

Polyakova, A. S., Chernigovskaya, M. A., & Perevalova, N. P. (2014). Ionospheric effects of sudden stratospheric warmings in eastern Siberia region. *Journal of Atmospheric and Solar-Terrestrial Physics*, 120, 15-23, <https://doi.org/10.1016/j.jastp.2014.08.011>.

Qian, L., A. G. Burns, B. A. Emery, B. Foster, G. Lu, A. Maute, A. D. Richmond, R. G. Roble, S. C. Solomon, and W. Wang, The NCAR TIE-GCM: A community model of the coupled thermosphere/ionosphere system, in *Modeling the Ionosphere-Thermosphere System*, AGU Geophysical Monograph Series, 2014, <https://doi.org/10.1002/9781118704417.ch7>.

Rao, J., Ren, R., Chen, H., Yu, Y., & Zhou, Y. (2018). The stratospheric sudden warming event in February 2018 and its prediction by a climate system model. *Journal of Geophysical Research: Atmospheres*, 123(23), 13-332, <https://doi.org/10.1029/2018JD028908>.

Reigber, C., Lühr, H., Schwintzer, P. (2002). CHAMP mission status. *Adv. Space Res.*, 30(2), 129-134, [https://doi.org/10.1016/S0273-1177\(02\)00276-4](https://doi.org/10.1016/S0273-1177(02)00276-4).

Richmond, A. D. (1995), Ionospheric electrodynamics, in *Handbook of Atmospheric Electrodynamics*, vol. 2, edited by H. Volland, pp. 249–290, CRC Press, Boca Raton, Fla.

Richmond, A.D. (1995). Ionospheric electrodynamics using magnetic apex coordinates. *Journal of geomagnetism and geoelectricity*, 47(2), 191-212, <https://doi.org/10.5636/jgg.47.191>.

Richmond, A. D., & Lu, G. (2000). Upper-atmospheric effects of magnetic storms: a brief tutorial. *Journal of Atmospheric and Solar-Terrestrial Physics*, 62(12), 1115-1127, [https://doi.org/10.1016/S1364-6826\(00\)00094-8](https://doi.org/10.1016/S1364-6826(00)00094-8).

- Richmond, A. D. (2011). Electrodynamics of ionosphere–thermosphere coupling. In *Aeronomy of the Earth's Atmosphere and Ionosphere* (pp. 191-201). Springer, Dordrecht, https://doi.org/10.1007/978-94-007-0326-1_13.
- Rienecker, M.M., M.J. Suarez, R. Gelaro, R. Todling, J. Bacmeister, E. Liu, M.G. Bosilovich, S.D. Schubert, L. Takacs, G. Kim, S. Bloom, J. Chen, D. Collins, A. Conaty, A. da Silva, W. Gu, J. Joiner, R.D. Koster, R. Lucchesi, A. Molod, T. Owens, S. Pawson, P. Pegion, C.R. Redder, R. Reichle, F.R. Robertson, A.G. Ruddick, M. Sienkiewicz, and J. Woollen (2011). MERRA: NASA's Modern-Era Retrospective Analysis for Research and Applications. *J. Climate*, 24, 3624–3648, <https://doi.org/10.1175/JCLI-D-11-00015.1>.
- Rishbeth, H., Müller-Wodarg, I.C.F., Zou, L. et al. (2000) Annual and semiannual variations in the ionospheric F2-layer: II. Physical discussion. *Annales Geophysicae* 18, 945–956, <https://doi.org/10.1007/s00585-000-0945-6>.
- Ritter, P., Lühr, H., & Rauberg, J. (2013). Determining field-aligned currents with the Swarm constellation mission. *Earth Plan. Space*, 65(11), 9, <https://doi.org/10.5047/eps.2013.09.006>.
- Roble R, Ridley E. An auroral model for the NCAR thermospheric general circulation model (TGCM) *Ann Geophys.* 1987;5A:369–382.
- Rodrigues, F. S., G. Crowley, S. M. I. Azeem, and R. A. Heelis (2011), C/NOFS observations of the equatorial ionospheric electric field response to the 2009 major sudden stratospheric warming event, *J. Geophys. Res.*, 116, A09316, <https://doi.org/10.1029/2011JA016660>.
- Rodríguez-Zuluaga, J., Stolle, C., Yamazaki, Y., Lühr, H., Park, J., Scherliess, L., & Chau, J. L. (2019). On the balance between plasma and magnetic pressure across equatorial plasma depletions. *Journal of Geophysical Research: Space Physics*, 124(7), 5936-5944, <https://doi.org/10.1029/2019JA026700>.
- Rother, M., Schlegel, K., Lühr, H. (2007). CHAMP observation of intense kilometer-scale field-aligned currents, evidence for an ionospheric Alfvén resonator. *Ann. Geophys.*, 25, 1603–1615, <https://doi.org/10.5194/angeo-25-1603-2007>.
- Sarris, T. E., Talaat, E. R., Palmroth, M., Dandouras, I., Armandillo, E., Kervalishvili, G., Buchert, S., Tourgaidis, S., Malaspina, D., Jaynes, A. N., Paschalidis, N., Sample, J., Halekas, J., Doornbos, E., Lappas, V., Jørgensen, T. M., Stolle, C., Cliverd, M., Wu, Q., Sandberg, I., Pirnaris, P., & Aikio, A. (2020). Daedalus: a low-flying spacecraft for in situ exploration of the lower thermosphere-ionosphere. *Geoscientific Instrumentation, Methods and Data Systems*, <https://doi.org/10.5194/gi-9-153-2020>.
- Sassi, F., H.-L. Liu, J. Ma, and R. R. Garcia (2013), The lower thermosphere during the northern hemisphere winter of 2009: A modeling study using high-altitude data assimilation products in WACCM-X, *J. Geophys. Res. Atmos.*, 118, <https://doi.org/10.1002/jgrd.50632>.
- Sathishkumar, S., and S. Sridharan (2013), Lunar and solar tidal variabilities in mesospheric winds and EEJ strength over Tirunelveli (8.7N, 77.8E) during the 2009 major stratospheric warming, *J. Geophys. Res. Space Physics*, 118, 533–541, <https://doi.org/10.1029/2012JA018236>.

- Scherliess, L., Thompson, D. C., & Schunk, R. W. (2008). Longitudinal variability of low - latitude total electron content: Tidal influences. *Journal of Geophysical Research: Space Physics*, 113(A1), <https://doi.org/10.1029/2007JA012480>.
- Schwartz, M., Lambert, A., Manney, G., Read, W., Livesey, N., and Froidevaux, L. (2008). Validation of the Aura Microwave Limb Sounder temperature and geopotential height measurements. *Journal of Geophysical Research*, 113, D15S11. <https://doi.org/10.1029/2007JD008783>.
- Schunk, R. W., Scherliess, L., Sojka, J. J., Thompson, D. C., Anderson, D. N., Codrescu, M., Minter, C., Fuller-Rowell, T. J., Heelis, R. A., Hairston, M., & Howe, B. M. (2004). Global assimilation of ionospheric measurements (GAIM). *Radio Science*, 39(1), doi: 10.1029/2002RS002794.
- Shepherd, S.G., (2014), Altitude-Adjusted Corrected Geomagnetic Coordinates: Definition and Functional Approximations, *J. Geophys. Res.*, 119, <https://doi.org/10.1002/2014JA020264>.
- Shpynev, B. G., Kurkin, V. I., Ratovsky, K. G., Chernigovskaya, M. A., Belinskaya, A. Y., Grigorieva, S. A., & Mukhtarov, P. (2015). High-midlatitude ionosphere response to major stratospheric warming. *Earth, Planets and Space*, 67(1), 18, <https://doi.org/10.1186/s40623-015-0187-1>.
- Siddiqui, T. A., H. Lühr, C. Stolle, and J. Park (2015a), Relation between stratospheric sudden warming and the lunar effect on the equatorial electrojet based on Huancayo recordings, *Ann. Geophys.*, 33(2), 235–243, <https://doi.org/10.5194/angeo-33-235-2015>.
- Siddiqui, T. A., Stolle, C., Lühr, H., & Matzka, J. (2015b). On the relationship between weakening of the northern polar vortex and the lunar tidal amplification in the equatorial electrojet. *Journal of Geophysical Research: Atmosphere*, 120, 5800–5806. <https://doi.org/10.1002/2015JA021683>.
- Siddiqui, T. A., Stolle, C., & Lühr, H. (2017). Longitude-dependent lunar tidal modulation of the equatorial electrojet during stratospheric sudden warmings. *Journal of Geophysical Research: Space Physics*, 122(3), 3760-3776, <https://doi.org/10.1002/2016JA023609>.
- Siddiqui, T. A., Yamazaki, Y., Stolle, C., Lühr, H., Matzka, J., Maute, A., & Pedatella, N. (2018a). Dependence of Lunar Tide of the Equatorial Electrojet on the Wintertime Polar Vortex, Solar Flux, and QBO. *Geophysical Research Letters*, 45(9), 3801-3810, <https://doi.org/10.1029/2018GL077510>.
- Siddiqui, T. A., Maute, A., Pedatella, N., Yamazaki, Y., Lühr, H., & Stolle, C. (2018b). On the variability of the semidiurnal solar and lunar tides of the equatorial electrojet during sudden stratospheric warmings. *Ann. Geophys.*, 36, 1545–1562, <https://doi.org/10.5194/angeo-36-1545-2018>.
- Siemes, C., da Encarnação, J. D. T., Doornbos, E., van den IJssel, J., Kraus, J., Perešty, R., Grunwaldt, L., Apelbaum, G., Flury, J., & Olsen, P. E. H. (2016). Swarm accelerometer data processing from raw accelerations to thermospheric neutral densities. *Earth, Planets and Space*, 68(1), 92, <https://doi.org/10.1186/s40623-016-0474-5>.

- Solomon, S. C., Woods, T. N., Didkovsky, L. V., Emmert, J. T., & Qian, L. (2010). Anomalous low solar extreme-ultraviolet irradiance and thermospheric density during solar minimum. *Geophysical Research Letters*, 37(16), <https://doi.org/10.1029/2010GL044468>.
- Sridharan, S., Sathishkumar, S., & Gurubaran, S. (2009). Variabilities of mesospheric tides and equatorial electrojet strength during major stratospheric warming events. *Ann. Geophys.*, 27, 4125–4130, <https://doi.org/10.5194/angeo-27-4125-2009>.
- Sridharan, S. (2017). Variabilities of low-latitude migrating and nonmigrating tides in GPS - TEC and TIMED-SABER temperature during the sudden stratospheric warming event of 2013. *Journal of Geophysical Research: Space Physics*, 122, 10,748-10,761. <https://doi.org/10.1002/2017JA024283>.
- Sripathi, S., and A. Bhattacharyya (2012), Quiet time variability of the GPS TEC and EEJ strength over Indian region associated with major sudden stratospheric warming events during 2005/2006, *J. Geophys. Res.*, 117, A05305, <https://doi.org/10.1029/2011JA017103>.
- Stening, R. J., Forbes, J. M., Hagan, M. E., & Richmond, A. D. (1997). Experiments with a lunar atmospheric tidal model. *Journal of Geophysical Research: Atmospheres*, 102(D12), 13465-13471, <https://doi.org/10.1029/97JD00778>.
- Stening, R. J. (2011), Lunar tide in the equatorial electrojet in relation to stratospheric warmings, *J. Geophys. Res.*, 116, A12315, <https://doi.org/10.1029/2011JA017047>.
- Stolle, C., Lühr, H., & Fejer, B. G. (2008). Relation between the occurrence rate of ESF and the equatorial vertical plasma drift velocity at sunset derived from global observations, *Ann. Geophys.*, 26, 3979–3988, <https://doi.org/10.5194/angeo-26-3979-2008>.
- Stolle, C., Manoj, C., Lühr, H., Maus, S., & Alken, P. (2008). Estimating the daytime equatorial ionization anomaly strength from electric field proxies. *Journal of Geophysical Research: Space Physics*, 113(A9), <https://doi.org/10.1029/2007JA012781>.
- Sutton, E. K. (2018). A new method of physics-based data assimilation for the quiet and disturbed thermosphere. *Space Weather*, 16(6), 736-753, <https://doi.org/10.1002/2017SW001785>.
- Tang, W., Xue, X. H., Lei, J., & Dou, X. K. (2014). Ionospheric quasi-biennial oscillation in global TEC observations. *Journal of Atmospheric and Solar-Terrestrial Physics*, 107, 36-41, <https://doi.org/10.1016/j.jastp.2013.11.002>.
- Themens, D.R., P.T. Jayachandran, R.B. Langley, J.W. MacDougall, and M.J. Nicolls (2013). Determining Receiver Biases in GPS-derived Total Electron Content in Auroral Oval and Polar Cap Region Using Ionosonde Measurements. *GPS Solutions*, 17(3), pp. 357-369, doi:10.1109/URSIGASS.2011.6050982.
- Themens, D. R., P. T. Jayachandran, and R. B. Langley (2015), The nature of GPS differential receiver bias variability: An examination in the polar cap region, *J. Geophys. Res. Space Physics*, 120, 8155–8175, <https://doi.org/10.1002/2015JA021639>.
- Themens, D. R., Jayachandran, P. T., Galkin, I., & Hall, C. (2017). The Empirical Canadian High Arctic Ionospheric Model (E-CHAIM): NmF2 and hmF2. *Journal of Geophysical Research: Space Physics*, 122(8), 9015-9031, <https://doi.org/10.1002/2017JA024398>.

Themens, D.R., et al. (2018). Topside Electron Density Representations for Middle and High Latitudes: A Topside Parameterization for E - CHAIM Based on the NeQuick, *Journal of Geophysical Research: Space Physics*, 123, 2, 1603-1617, <https://doi.org/10.1002/2017JA024817>.

Themens, D.R., P.T. Jayachandran, A.M. McCaffrey, B. Reid, and R.H. Varney (2019). A bottomside parameterization for the Empirical Canadian High Arctic Ionospheric Model (E-CHAIM), *Radio Sci.*, <https://doi.org/10.1029/2018RS006748>.

Themens, D. R., Jayachandran, P. T., Reid, B., & McCaffrey, A. M. (2020). The limits of empirical electron density modeling: Examining the capacity of E-CHAIM and the IRI for modeling intermediate (1-to 30-day) timescales at high latitudes. *Radio Science*, 55(4), 1-15, <https://doi.org/10.1029/2018RS006763>.

Titheridge, J. E. (1988), The real height analysis of ionograms: A generalized formulation, *Radio Sci.*, 23(5), 831–849, <https://doi.org/10.1029/RS023i005p00831>.

Torrence, C., & Compo, G. P. (1998). A practical guide to wavelet analysis. *Bulletin of the American Meteorological society*, 79(1), 61-78, [https://doi.org/10.1175/1520-0477\(1998\)079<0061:APGTWA>2.0.CO;2](https://doi.org/10.1175/1520-0477(1998)079<0061:APGTWA>2.0.CO;2).

Tulasi Ram, S., Liu, C. H., & Su, S. Y. (2010). Periodic solar wind forcing due to recurrent coronal holes during 1996–2009 and its impact on Earth's geomagnetic and ionospheric properties during the extreme solar minimum. *Journal of Geophysical Research: Space Physics*, 115(A12), <https://doi.org/10.1029/2010JA015800>.

Upadhayaya, A. K., and K. K. Mahajan (2013), Ionospheric F2 region: Variability and sudden stratospheric warmings, *J. Geophys. Res. Space Physics*, 118, 6736–6750, <https://doi.org/10.1002/2017JA024059>.

Vadas, S. L., & Liu, H. L. (2009). Generation of large-scale gravity waves and neutral winds in the thermosphere from the dissipation of convectively generated gravity waves. *Journal of Geophysical Research: Space Physics*, 114(A10), <https://doi.org/10.1029/2009JA014108>.

Valentic, T., et al. (2013), AMISR the advanced modular incoherent scatter radar," 2013 IEEE International Symposium on Phased Array Systems and Technology, Waltham, MA, pp. 659-663, doi:10.1109/ARRAY.2013.6731908.

Vieira, F., Fagundes, P. R., Venkatesh, K., Goncharenko, L. P., and Pillat, V. G. (2017), Total electron content disturbances during minor sudden stratospheric warming, over the Brazilian region: A case study during January 2012, *J. Geophys. Res. Space Physics*, 122, 2119– 2135, <https://doi.org/10.1002/2016JA023650>.

Vineeth, C., Pant, T. K., & Sridharan, R. (2009). Equatorial counter electrojets and polar stratospheric sudden warmings-A classical example of high latitude-low latitude coupling?, *Ann. Geophys.*, 27, 3147–3153, <https://doi.org/10.5194/angeo-27-3147-2009>.

Wan, W., Ren, Z., Ding, F., Xiong, J., Liu, L., Ning, B., & Zhang, M. L. (2012). A simulation study for the couplings between DE3 tide and longitudinal WN4 structure in the thermosphere and ionosphere. *Journal of Atmospheric and Solar-Terrestrial Physics*, 90, 52-60, <https://doi.org/10.1016/j.jastp.2012.04.011>.

- Wan, X., Xiong, C., Wang, H., Zhang, K., Zheng, Z., He, Y., & Yu, L. (2019). A statistical study on the climatology of the Equatorial Plasma Depletions occurrence at topside ionosphere during geomagnetic disturbed periods. *Journal of Geophysical Research: Space Physics*, 124(10), 8023-8038, <https://doi.org/10.1029/2019JA026926>.
- Wang, C., & Picaut, J. (2004). Understanding ENSO physics—A review. *Earth's Climate: The Ocean–Atmosphere Interaction*, Geophys. Monogr, 147, 21-48.
- Whitehead, J. D. (1961). The formation of the sporadic-E layer in the temperate zones. *Journal of Atmospheric and Terrestrial Physics*, 20(1), 49-58, [https://doi.org/10.1016/0021-9169\(61\)90097-6](https://doi.org/10.1016/0021-9169(61)90097-6).
- Wang, H., T. J. Fuller-Rowell, R. A. Akmaev, M. Hu, D. T. Kleist, and M. D. Iredell (2011), First simulations with a whole atmosphere data assimilation and forecast system: The January 2009 major sudden stratospheric warming, *J. Geophys. Res.*, 116, A12321, <https://doi.org/10.1029/2011JA017081>.
- Wang, H., Akmaev, R. A., Fang, T. W., Fuller - Rowell, T. J., Wu, F., Maruyama, N., & Iredell, M. D. (2014). First forecast of a sudden stratospheric warming with a coupled whole - atmosphere/ionosphere model IDEA. *Journal of Geophysical Research: Space Physics*, 119(3), 2079-2089, <https://doi.org/10.1002/2013JA019481>.
- Waters, J. W., Froidevaux, L., Harwood, R. S., Jarnot, R. F., Pickett, H. M., and Read, W. G. (2006). The Earth Observing System Microwave Limb Sounder (EOS MLS) on the Aura satellite. *IEEE Transactions on Geoscience and Remote Sensing*, 44(5), 1075–1092.
- Wolf, R. A., Spiro, R. W., Sazykin, S., & Toffoletto, F. R. (2007). How the Earth's inner magnetosphere works: An evolving picture. *Journal of Atmospheric and Solar-Terrestrial Physics*, 69(3), 288-302, <https://doi.org/10.1016/j.jastp.2006.07.026>.
- Wu, Q., Ortland, D. A., Killeen, T. L., Roble, R. G., Hagan, M. E., Liu, H. L., ... & Niciejewski, R. J. (2008). Global distribution and interannual variations of mesospheric and lower thermospheric neutral wind diurnal tide: 1. Migrating tide. *Journal of Geophysical Research: Space Physics*, 113(A5), <https://doi.org/10.1029/2007JA012543>.
- Wu, Q., & Nozawa, S. (2015). Mesospheric and thermospheric observations of the January 2010 stratospheric warming event. *Journal of Atmospheric and Solar-Terrestrial Physics*, 123, 22-38, <https://doi.org/10.1016/j.jastp.2014.11.006>.
- Wu, Q., Maute, A., Yudin, V., Goncharenko, L., Noto, J., Kerr, R., and Jacobi, C. (2016), Observations and simulations of midlatitude ionospheric and thermospheric response to the January 2013 stratospheric sudden warming event, *J. Geophys. Res. Space Physics*, 121, 8995–9011, <https://doi.org/10.1002/2016JA023043>.
- Wu, Q., Schreiner, W. S., Ho, S. P., Liu, H. L., & Qian, L. (2017). Observations and simulations of eddy diffusion and tidal effects on the semiannual oscillation in the ionosphere. *Journal of Geophysical Research: Space Physics*, 122(10), 10-502, <https://doi.org/10.1002/2017JA024341>.
- Xiong, C., Park, J., Lühr, H., Stolle, C., & Ma, S. Y. (2010). Comparing plasma bubble occurrence rates at CHAMP and GRACE altitudes during high and low solar activity, *Ann. Geophys.*, 28, 1647–1658, <https://doi.org/10.5194/angeo-28-1647-2010>.

Xiong, C., Stolle, C., Lühr, H. et al. Scale analysis of equatorial plasma irregularities derived from Swarm constellation. *Earth Planet Sp* 68, 121 (2016). <https://doi.org/10.1186/s40623-016-0502-5>.

Xu, J., Smith, A. K., Liu, H. L., Yuan, W., Wu, Q., Jiang, G., Mlynczak, M. G., Russell III, J. M., & Franke, S. J. (2009). Seasonal and quasi-biennial variations in the migrating diurnal tide observed by Thermosphere, Ionosphere, Mesosphere, Energetics and Dynamics (TIMED). *Journal of Geophysical Research: Atmospheres*, 114(D13), <https://doi.org/10.1029/2008JD011298>.

Yadav, S., Pant, T. K., Choudhary, R. K., Vineeth, C., Sunda, S., Kumar, K. K., ... Mukherjee, S. (2017). Impact of sudden stratospheric warming of 2009 on the equatorial and low - latitude ionosphere of the Indian longitudes: A case study. *Journal of Geophysical Research: Space Physics*, 122, 10,486–10,501. <https://doi.org/10.1002/2017JA024392>.

Yadav, S., Vineeth, C., Kumar, K. K., Choudhary, R. K., Pant, T. K., & Sunda, S. (2019). The role of the phase of QBO in modulating the influence of the SSW effect on the equatorial ionosphere. *Journal of Geophysical Research: Space Physics*, 124, 6047– 6063. <https://doi.org/10.1029/2019JA026518>.

Yamazaki, Y., A. D. Richmond, and K. Yumoto (2012a), Stratospheric warmings and the geomagnetic lunar tide: 1958–2007, *J. Geophys. Res.*, 117, A04301, <https://doi.org/10.1029/2012JA017514>.

Yamazaki, Y., K. Yumoto, D. McNamara, T. Hirooka, T. Uozumi, K. Kitamura, S. Abe, and A. Ikeda (2012b), Ionospheric current system during sudden stratospheric warming events, *J. Geophys. Res.*, 117, A03334, <https://doi.org/10.1029/2011JA017453>.

Yamazaki, Y., A. D. Richmond, H. Liu, K. Yumoto, and Y. Tanaka (2012c), Sq current system during stratospheric sudden warming events in 2006 and 2009, *J. Geophys. Res.*, 117, A12313, <https://doi.org/10.1029/2012JA018116>.

Yamazaki, Y. (2013), Large lunar tidal effects in the equatorial electrojet during northern winter and its relation to stratospheric sudden warming events, *J. Geophys. Res. Space Physics*, 118, 7268–7271, <https://doi.org/10.1002/2013JA019215>.

Yamazaki, Y., & Richmond, A. D. (2013). A theory of ionospheric response to upward - propagating tides: Electrodynamical effects and tidal mixing effects. *Journal of Geophysical Research: Space Physics*, 118(9), 5891-5905, <https://doi.org/10.1002/jgra.50487>.

Yamazaki, Y. (2014). Solar and lunar ionospheric electrodynamic effects during stratospheric sudden warmings. *Journal of Atmospheric and Solar-Terrestrial Physics*, 119, 138-146, <https://doi.org/10.1016/j.jastp.2014.08.001>.

Yamazaki, Y., Kosch, M. J., & Emmert, J. T. (2015). Evidence for stratospheric sudden warming effects on the upper thermosphere derived from satellite orbital decay data during 1967–2013. *Geophysical Research Letters*, 42(15), 6180-6188, <https://doi.org/10.1002/2015GL065395>.

Yamazaki, Y., & Maute, A. (2017). Sq and EEJ—A review on the daily variation of the geomagnetic field caused by ionospheric dynamo currents. *Space Science Reviews*, 206(1-4), 299-405, <https://doi.org/10.1007/s11214-016-0282-z>.

- Yamazaki, Y., Liu, H., Sun, Y. Y., Miyoshi, Y., Kosch, M. J., & Mlynczak, M. G. (2017). Quasi-biennial oscillation of the ionospheric wind dynamo. *Journal of Geophysical Research: Space Physics*, 122(3), 3553-3569, <https://doi.org/10.1002/2016JA023684>.
- Yamazaki, Y. (2018). Quasi-6-day wave effects on the equatorial ionization anomaly over a solar cycle. *Journal of Geophysical Research: Space Physics*, 123(11), 9881-9892, <https://doi.org/10.1029/2018JA026014>.
- Yamazaki, Y., Stolle, C., Matzka, J., & Alken, P. (2018). Quasi-6-day wave modulation of the equatorial electrojet. *Journal of Geophysical Research: Space Physics*, 123(5), 4094-4109. <https://doi.org/10.1029/2018JA025365>.
- Yamazaki, Y., & Matthias, V. (2019). Large Amplitude Quasi-10-day Waves in the Middle Atmosphere during Final Warmings. *Journal of Geophysical Research: Atmospheres*, <https://doi.org/10.1029/2019JD030634>.
- Yamazaki, Y., Matthias, V., Miyoshi, Y., Stolle, C., Siddiqui, T., Kervalishvili, G., Laštovička, J., Kozubek, M., Ward, W., Themens, D. R., Kristoffersen, S., & Alken, P. (2020). September 2019 Antarctic Sudden Stratospheric Warming: Quasi-6-Day Wave Burst and Ionospheric Effects. *Geophysical Research Letters*, 47(1), e2019GL086577, <https://doi.org/10.1029/2019GL086577>.
- Yasyukevich, A. S. (2018). Variations in ionospheric peak electron density during sudden stratospheric warmings in the Arctic region. *Journal of Geophysical Research: Space Physics*, 123, 3027–3038. <https://doi.org/10.1002/2017JA024739>.
- Yiğit, E., and A. S. Medvedev (2012), Gravity waves in the thermosphere during a sudden stratospheric warming, *Geophys. Res. Lett.*, 39, L21101, <https://doi.org/10.1029/2012GL053812>.
- Yiğit, E., Medvedev, A. S., England, S. L., and Immel, T. J. (2014), Simulated variability of the high - latitude thermosphere induced by small - scale gravity waves during a sudden stratospheric warming, *J. Geophys. Res. Space Physics*, 119, 357– 365, <https://doi.org/10.1002/2013JA019283>.
- Yiğit, E., & Medvedev, A. S. (2016). Role of gravity waves in vertical coupling during sudden stratospheric warmings. *Geoscience Letters*, 3(1), 1-13, <https://doi.org/10.1186/s40562-016-0056-1>.
- Yiğit, E., Knížová, P. K., Georgieva, K., & Ward, W. (2016). A review of vertical coupling in the Atmosphere–Ionosphere system: Effects of waves, sudden stratospheric warmings, space weather, and of solar activity. *Journal of Atmospheric and Solar-Terrestrial Physics*, 141, 1-12, <https://doi.org/10.1016/j.jastp.2016.02.011>.
- Yin, F., Lühr, H., Park, J., & Wang, L. (2019). Comprehensive Analysis of the Magnetic Signatures of Small - Scale Traveling Ionospheric Disturbances, as Observed by Swarm. *Journal of Geophysical Research: Space Physics*, 124(12), 10794-10815, <https://doi.org/10.1029/2019JA027523>.
- Yu, T., Ye, H., Liu, H., Xia, C., Zuo, X., Yan, X., Yang, N., Sun, Y., & Zhao, B. (2020). Ionospheric F-layer scintillation weakening as observed by COSMIC/FORMOSAT-3 during

the major sudden stratospheric warming in January 2013. *Journal of Geophysical Research: Space Physics*, e2019JA027721, <https://doi.org/10.1029/2019JA027721>.

Yue, J., & Wang, W. (2014). Changes of thermospheric composition and ionospheric density caused by quasi 2 day wave dissipation. *Journal of Geophysical Research: Space Physics*, 119(3), 2069-2078, <https://doi.org/10.1002/2013JA019725>.

Yue, X., W. S. Schreiner, J. Lei, C. Rocken, D. C. Hunt, Y.-H. Kuo, and W. Wan (2010), Global ionospheric response observed by COSMIC satellites during the January 2009 stratospheric sudden warming event, *J. Geophys. Res.*, 115, A00G09, <https://doi.org/10.1029/2010JA015466>.

Zalizovski, AV, Kashcheiev, AS, Kashcheiev, SB, Koloskov, AV, Lisachenko, VN, Paznukhov, VV, Pikulik, I, Sopin, AA, Yampolski, Yu.MA (2018), Prototype of a portable coherent ionosonde, *Space Science and Technology*, 3(112), <https://doi.org/10.15407/knit2018.03.010>.

Zhang, X., Forbes, J. M., Hagan, M. E., Russell III, J. M., Palo, S. E., Mertens, C. J., & Mlynczak, M. G. (2006). Monthly tidal temperatures 20–120 km from TIMED/SABER. *Journal of Geophysical Research: Space Physics*, 111(A10), <https://doi.org/10.1029/2005JA011504>.

Zhang, X., & Forbes, J. M. (2014). Lunar tide in the thermosphere and weakening of the northern polar vortex. *Geophysical Research Letters*, 41, 8201–8207. <https://doi.org/10.1002/2014GL062103>.

Zhang, Y., & Paxton, L. J. (2008). An empirical Kp-dependent global auroral model based on TIMED/GUVI FUV data. *Journal of Atmospheric and Solar-Terrestrial Physics*, 70(8-9), 1231-1242, <https://doi.org/10.1016/j.jastp.2008.03.008>.

List of Abbreviations

Abbreviation	Description
AACGM	Altitude-Adjusted Corrected Geomagnetic (coordinates)
AE	Auroral Electrojet
AMIE	Assimilative Mapping of Ionospheric Electrodynamics
ARTIST	Automatic Real Time Ionogram Scaler with True height algorithm
CADI	Canadian Advanced Digital Ionosonde
CAM	Community Atmosphere Model
CESM	Community Earth System Model
CHAIN	Canadian High Arctic Ionospheric Network
CHAMP	CHALLENGING Minisatellite Payload
CIR	Co-rotating Interaction Region
CME	Coronal Mass Ejection
CODE	Center for Orbit Determination in Europe
CPCP	Cross Polar Cap Potential
DE3	Diurnal Eastward-propagating tide with zonal wave number 3
DW1	Diurnal Westward-propagating tide with zonal wave number 1
DIDBase	Digital Ionogram Data Base

Abbreviation	Description
DISC	Data, Innovation, and Science Cluster
E-CHAIM	Empirical Canadian High Arctic Ionospheric Model
E-CHAIN	Expanded-CHAIN
EEF	Equatorial electric field
EEJ	Equatorial ElectroJet
ENSO	El Niño-Southern Oscillation
EPB	Equatorial Plasma Bubble
ERA5	European Centre for Medium Weather Forecast (ECMWF) Reanalysis 5
ERWIN-II	E-Region Wind Interferometer
ESA	European Space Agency
EUV	Extreme UltraViolet
FAC	Field-Aligned Current
foF2	Critical frequency of ionospheric F2 layer
GAIA	Ground-to-Topside Model of Atmosphere and Ionosphere for Aeronomy
GCM	General Circulation Model
GFZ	Deutsches GeoForschungsZentrum
GITM	Global Ionosphere Thermosphere Model
GNSS	Global Navigation Satellite System
GPH	GeoPotential Height
GPS	Global Positioning System
GRACE	Gravity Recovery and Climate Experiment
GRACE-FO	Gravity Recovery and Climate Experiment Follow-On
GSWM	Global Scale Wave Model
GW	Gravity Wave
hmF2	Height of the maximum electron density in the ionosphere
HP	Hemispheric Power
HWM07	Horizontal Wind Model, 2007 version
IAP	Institute of Atmospheric Physics
ICON	Ionospheric Connection Explorer
IHFAC	Inter-Hemispheric Field-Aligned Current
IPMC	Ionospheric Monitoring and Prediction Center
IRI	International Reference Ionosphere
IT	Ionosphere/Thermosphere
LB	Lower Boundary
JPL	Jet Propulsion Laboratory
LEO	Low-Earth-Orbit
LOS	Line Of Sight
LT	Local Time
M2	Migrating semidiurnal lunar tide with zonal wavenumber 2
MERRA	Modern-Era Retrospective Analysis for Research and Applications
MJO	Madden-Julian Oscillation
MLS	Microwave Limb Sounder
MLT	Mesosphere and Lower Thermosphere
MOZART	Model for Ozone and Related Chemical Tracers
MSTID	Medium-Scale Traveling Ionospheric Disturbance

Abbreviation	Description
NASA	National Aeronautics and Space Administration
NH	Northern Hemisphere
NCAR	National Center for Atmospheric Research
OVATION	Oval Variation, Assessment, Tracking, Intensity, and Online Nowcasting
PVW	Polar Vortex Weakening
Q2DW	Quasi-2-Day Wave
Q6DW	Quasi-6-Day Wave
Q10DW	Quasi-10-Day Wave
Q16DW	Quasi-16-Day Wave
R1	Region-1
R2	Region-2
RINEX	Receiver INdependent EXchange format
RISR	Resolute Incoherent Scatter Radar
SABER	Sounding of the Atmosphere using Broadband Emission Radiometry
SATI	Spectral Airglow Temperature Imager
SD	Specified Dynamics
SH	Southern Hemisphere
Sq	Solar quiet
SSW	Sudden Stratospheric Warming
SW2	Semidiurnal Westward-propagating tide with zonal wave number 2
Swarm	Constellation of 3 ESA satellites, http://earth.esa.int/swarm
TEC	Total Electron Content
TIE-GCM	Thermosphere Ionosphere Electrodynamic GCM
TIMED	Thermosphere Ionosphere Mesosphere Energetics and Dynamics
TIME-GCM	Thermosphere Ionosphere Mesosphere Electrodynamic GCM
TIRO	Topside Ionosphere Radio Observations from multiple LEO-missions
UFWK	Ultra-Fast Kelvin Wave
UPC	Universitat Politècnica de Catalunya
UT	Universal Time
VERA	VERTICAL coupling in Earth's Atmosphere at mid and high latitudes
vTEC	Vertical TEC
WMO	World Meteorological Organization
WACCM-X	Whole Atmospheric Climate Community Model – Extended
ZW	Zonal Wavenumber